NASA CR-120843

MICROFOG LUBRICANT APPLICATION SYSTEM FOR ADVANCED TURBINE ENGINE COMPONENTS - PHASE II

by

J. Shim and S. J. Leonardi

MOBIL RESEARCH AND DEVELOPMENT CORPORATION

prepared for

NATIONAL AERONAUTICS AND SPACE ADMINISTRATION

NASA Lewis Research Center
CONTRACT NO. NAS 3-13207
William R. Loomis, Project Manager

1. Report No.	2. Government Accession No.	3. Recipient's Catalog No.
NASA CR-120843		

4. Title and Subtitle	5. Report Date
MICROFOG LUBRICANT APPLICATION SYSTEM FOR ADVANCED TURBINE ENGINE COMPONENTS - PHASE II TASKS III, IV AND V	June 1, 1972
	6. Performing Organization Code
7. Author(s)	8. Performing Organization Report No.
J. Shim and S. J. Leonardi	
	10. Work Unit No.
9. Performing Organization Name and Address	
Mobil Research and Development Corporation Research Department Paulsboro, New Jersey 08066	11. Contract or Grant No. NAS 3-13207
	13. Type of Report and Period Covered
12. Sponsoring Agency Name and Address	Contractor Report
National Aeronautics and Space Administration Washington, D. C. 20546	14. Sponsoring Agency Code

15. Supplementary Notes

Project Manager, William R. Loomis, Fluid System Components Division
NASA Lewis Research Center, Cleveland, Ohio

16. Abstract

The wettabilities and heat transfer rates of microfog jets (oil-mist nozzle flows) impinging on a heated rotating disc were determined under an inert atmosphere of nitorgen at temperatures ranging from 600 to 800°F (589 to 700°K). The results are discussed in relation to the various factors involved in the microfog lubricant application systems. Two novel reclassifying nozzles and a vortex mist generator were also studied.

17. Key Words (Suggested by Author(s))	18. Distribution Statement
Microfog lubrication; advanced turbine lubrication; high-temperature lubricants; wettabilities of microfogs; heat transfer by microfogs	Unclassified - unlimited

19. Security Classif. (of this report)	20. Security Classif. (of this page)	21. No. of Pages	22. Price*
Unclassified	Unclassified	206	$3.00

* For sale by the National Technical Information Service, Springfield, Virginia 22151

MICROFOG LUBRICANT APPLICATION SYSTEM FOR ADVANCED TURBINE ENGINE COMPONENTS - PHASE II

TASKS III, IV AND V

WETTABILITY AND HEAT TRANSFER OF MICROFOG JETS IMPINGING ON A HEATED ROTATING DISC, AND EVALUATION OF RECLASSIFYING NOZZLES AND A VORTEX MIST GENERATOR

by

J. Shim and S. J. Leonardi

MOBIL RESEARCH AND DEVELOPMENT CORPORATION
RESEARCH DEPARTMENT, PAULSBORO LABORATORY
PAULSBORO, NEW JERSEY

Prepared for

NATIONAL AERONAUTICS AND SPACE ADMINISTRATION

August 31, 1971

CONTRACT NAS 3-13207

NASA Lewis Research Center
Cleveland, Ohio
William R. Loomis, Project Manager
Fluid System Components Division

Table of Contents

Page

I. Introduction 1

II. Summary and Conclusions 2

III. Detailed Report 7

A. Materials 7

B. Apparatus and Procedure 7

1. Wetting Rate Determinations 9

2. Heat Transfer Studies 11

3. Wettability of Impinging Lubricant Drops 12

4. Method of Data Analysis 12

C. Results and Discussion 13

1. Wettability and Heat Transfer of Microfog Jets Impinging on a Heated Rotating Disc 14

a. Analysis 14

b. Wettability Determinations 17

(1) General Comments 17

(2) Effect of (Oil/Gas) Mass Flow Ratio 19

(3) Effect of Angular Velocity 23

c. Heat Transfer Studies 32

(1) General Comments 33

(2) Heat Transfer of Microfog Jets 35

(a) Effect of (Oil/Gas) Mass Flow Ratio 38

(b) Comparison of the Heat Transfer Coefficients of Microfog Jets With Different Test Lubricants . . 41

(c) Significance of the Temperature Difference Between Hot Surface and Cooling Stream 44

Table of Contents (Continued)

Page

(3) Heat Transfer of Nitrogen Gas Jets 49

(a) Effect of Gas Flow Rate 49

(b) Effect of Angular Velocity 53

(c) Effect of Axial Spray Distance 59

(d) Radial Variations of Heat Transfer Coefficient . 62

(e) Notes on the Empirical Correlation 64

2. Wettability of Lubricant Drops Impinging on a Heated Rotating Disc 70

a. Analysis 70

b. General Comments 74

c. Drop Formation 76

d. Drop Size 80

e. Drop Velocity 80

f. Drop Breakup 91

g. Photographic Observation of Wetting Patterns 93

3. Evaluation of Reclassifying Nozzles and a Vortex Mist Generator 94

a. Pneumatic Reclassifying Nozzle 97

b. Electrostatic Reclassifying Nozzle 101

c. Vortex Mist Generator 108

IV. Notations 112

V. References 115

VI. Appendices 117

A. Statement of Work, Contract NAS3-13207, and Physical Properties of Test Lubricants 119

Table of Contents (Continued)

Page

B. Engineering Drawings of Rotating Specimen Chamber and Drive Mechanism 126

C. Wettability of Microfog Jets Impinging on a Heated Rotating Disc 137

1. Picture Frequency Calibration for a Hycam High Speed Motion Picture Camera 138

2. Wettability Data of XRM 109 F and FN 2961 139

3. Summary of the Wetting Rate Data for XRM 109 F 148

D. Heat Transfer of Microfog Jets Impinging on a Heated Rotating Disc 152

1. Operating Principle of Heat Flux Transducer 153

2. Calibration of Heat Flux Transducer 153

3. Heat Transfer Data of Microfog Jets of Different Lubricants 157

4. Axial Variation of Heat Transfer Coefficients of Nitrogen Gas Jets Impinging on a Heated Disc 169

E. Wettability of Lubricant Drops Impinging on a Heated Rotating Disc 172

F. Wettability Data of XRM 109 F with a Pneumatic Reclassifying Nozzle 186

G. Wettability Data of XRM 109 F with an Electrostatic Reclassifying Nozzle 190

H. Wettability Data of XRM 109 F with a Vortex Mist Generator 192

I. Final Reports Distribution List for Contract NAS3-13207. 195

TABLES

1. Surface Velocity and Thickness of Thin Lubricant Film at a Disc Temperature of 600°F (589°K) 30

2. Heat Transfer Rates of XRM 109 F Microfog Jets Impinging on a Heated Rotating Disc 40

Table of Contents (Continued)

Page

TABLES (Cont'd)

3. Heat Transfer Rates of Different Lubricant Microfog Jets Impinging on a Heated Rotating Disc 42

4. Heat Transfer Characteristics of Nitrogen Gas Jets Impinging on a Heated Disc 50

5. Heat Transfer Characteristics of Nitrogen Gas Jets Impinging on a Heated Rotating Disc 56

6. Relationship Between Time and Distance Traveled by Lubricant Drops 81

7. Relationship Between Total Traverse Time and Gas Stream Velocity at Different Disc Temperatures 88

8. Wettability of XRM 109 F Microfog Jets in Presence of Electrostatic Fields 106

9. Particle Size Distributions of XRM 109 F Microfog With Different Generators 111

FIGURES

1. Flow Diagram of Experimental Apparatus 8

2. Schematic of the Physical System 15

3. Wettability of XRM 109 F at 600°F (589°K) 20

4. Effect of Impactor Size on Wetting Rate at 600°F (589°K) 22

5. Wetting Rates of XRM 109 F as a Function of (Oil/Gas) Mass Flow Ratio at Different Angular Velocities 24

6. Wetting Rates of XRM 109 F as a Function of Angular Velocity at 600°F (589°K) 25

7. Wetting Rates of XRM 109 F as a Function of Angular Velocity at 700°F (644°K) 26

8. Wetting Rates of XRM 109 F as a Function of Angular Velocity at 800°F (700°K) 27

Page

FIGURES (Cont'd)

9. Effect of Angular Velocity on Mean Surface Velocity of Lubricant Film 31

10. A typical Experimental Run for Heat Transfer Study . . 37

11. Nusselt Number Versus (Oil/Gas) Mass Flow Ratio at Different Angular Velocity 39

12. Heat Transfer Rates from a Rotating Disc at Various Temperature Differences 45

13. Variation of Heat Transfer Coefficients with Temperature Differences 46

14. Heat Transfer Characteristics of Nitrogen Gas Jets Impinging on a Heated Disc 51

15. Effect of Angular Velocity on Heat Transfer Coefficient of Nitrogen Gas Jets (log-log) 57

16. Effect of Angular Velocity on Heat Transfer Coefficient of Nitrogen Gas Jets (semi-log) 58

17. Effect of Spacing Ratio (Z/D_o) on Nusselt Number at the Center Line of Impinging Gas Jet 60

18. Lateral Variation of Local Heat Transfer Coefficients of an Air Jet Impinging on a Heated Plate 63

19. Correlation of $N_{Nu} \cdot N_{Pr}^{-1/3}$ and $(N_{Re})_m$ 68

20. Variation of Heat Transfer Coefficient at the Center Line of Impinging Jet with Axial Distance Ratio (Z/D_o). 69

21. A Theoretical Model of Kinetic Drop Formation in a Gas Stream 72

22. Drop Diameter of Liquids as a Function of Gas Stream Velocity 75

23. Schematic of the High-Speed Photographs of a Kinetic Drop Formation in a Gas Stream (FN 2961) 78

24. Schematic of the High-Speed Photographs of a Kinetic Drop Formation in a Gas Stream (XRM 109 F). 79

Table of Contents (Continued)

Page

FIGURES (Cont'd)

25. Relationship Between Time and Distance Traveled by Lubricant Drops Suspended in Gas Streams - XRM 109 F and 600°F (589°K) 82

26. Relationship Between Time and Distance Traveled by Lubricant Drops Suspended in Gas Stream - XRM 109 F and 600°F (589°K) in Log-Log Scale 83

27. Relationship Between Time and Distance Traveled by Lubricant Drops Suspended in Gas Streams - XRM 109 F and 700°F (644°K) 85

28. Relationship Between Time and Distance Traveled by Lubricant Drops Suspended in Gas Streams - XRM 109 F and 800°F (700°K) 86

29. Relationship Between Time and Distance Traveled by Lubricant Drops Suspended in Gas Stream - FN 2961 and 600°F (589°K) 87

30. Effect of Capillary Size on Relationship Between Time and Distance Traveled by Lubricant Drops - XRM 109 F and 600°F (589°K) 90

31. Effect of Gas Stream Velocity on Wetting Patterns Formed by Droplets of XRM 109 F Impinging on a Rotating Disc at 295°K 95

32. Effect of Angular Velocity on Wetting Patterns Formed by Droplets of XRM 109 F Impinging on a Rotating Disc at 295°K 96

33. Experimental Microfog Reclassifying Nozzle 98

34. Photograph of Experimental Reclassifying Nozzle 99

35. Wetting Rates of XRM 109 F as a Function of (Oil/Gas) Mass Flow Ratio for Different Reclassifying Nozzles . . 100

36. Adapter Assembly for Electrostatic Reclassifying Nozzle 103

37. High Voltage Electrostatic Charger 104

38. Schematic View of a Vortex Mist Generator 109

Table of Contents (Continued)

Page

FIGURES (Cont'd)

39. Picture Frequency Versus Film Length 138

40. Operational Principle of Heat Flux Transducer 154

41. Heat Flux Data for Calibration of the Heat Flux Transducer 155

42. A Calibration Curve for EMF Recorder 156

I. INTRODUCTION

Earlier work (1, 2) initiated under Contract NAS3-9400 was successful in establishing new techniques and equipment for investigating the wetting characteristics of microfog lubricants on a static metal surface under an inert atmosphere of nitrogen at temperatures ranging from 600 to 800°F (589 to 700°K). The work also developed valuable information on the wettabilities of five potential high-temperature lubricants.

Under the present contract, additional work (3) with a static metal surface was carried out under various test conditions selected to provide broader information needed to guide the development of an advanced microfog lubricant application system. The wetting data in this work were discussed in relation to the rate of oil-mist output, impaction velocity, temperature and surface characteristics of the wetted plate, and properties of the lubricants.

The technology gained in these earlier investigations is still limited and, to an extent, insufficient to establish firm relations representing the general behavior of microfog particles, which are needed to optimize microfog lubrication. A particular area in need of further attention is the reclassification of microfog particles by means of a nozzle. Moreover, for most practical lubricating systems, information on the stability and heat transfer properties of the thin lubricant films that spread over the heated dynamic surfaces is unavailable, although the flow characteristics of a thin lubricant film, by influencing heat transfer from the heated surface, may play an important role in determining the performance of the lubricant in high-temperature applications. Without effective cooling, a burden which in most high-temperature applications falls on the lubricant film, thermal excursions at lubricated contact points can lead to component failures.

The ultimate aims of the present program are, therefore, to develop additional technology needed for the advancement of reclassification through a nozzle, and to investigate the hydrodynamic phenomena and convective heat transfer characteristics of thin lubricant films spreading over a heated rotating disc situated in the forced inflow of microfog streams. The Statement of Work for this contract is attached hereto as Appendix A.

This is the final report submitted under Contract NAS3-13207, entitled "Microfog Lubricant Application System for Advanced Engine Components - Phase II," and covers Tasks III, IV, and V of this contract.

II. SUMMARY AND CONCLUSIONS

The wetting and heat transfer characteristics of microfog jets impinging on a heated rotating surface of high carbon steel (WB-49) were determined under a variety of test conditions. This work was supplemented by a brief study of the kinetic formation and impingement dynamics of single lubricant drops. The present program also included an evaluation of a vortex mist generator and two novel types of reclassifying nozzles. Most of the work with microfog jets, except as otherwise specified, was conducted at 45 psig (40 N/cm^2) in an inert atmosphere of nitrogen, which was employed as the atomizing and carrier gas.

A. Wetting Rate Determinations

The wetting rates of microfog jets of two high temperature lubricants, FN 2961 and XRM 109 F, on a disc (4" diameter) were investigated with an axial spray distance ratio [ratio of spray distance to nozzle orifice diameter, (Z/D_O)] of 5.85 at disc temperatures of 600, 700, and 800°F (589, 644, and 700°K), at angular velocities ranging from 0 to 312 rad/s. Wetting rates obtained with gas flow rates of 3, 4, and 5 cfm (1.4×10^{-3}, 1.9×10^{-3}, and 2.4×10^{-3} m^3/s) vary considerably for a given test condition: for a given combination of disc temperature and rotational velocity, the wetting rates increase with increasing (oil/gas) mass flow ratios established by varying gas flow rate to the microfog generator. For a given mass flow ratio, increasing angular velocity of the disc greatly enhances the wetting rates by increasing the mean surface velocity of the thin lubricant films spreading over it, induced by the action of centrifugal forces at free surface. The increase in wetting rate by this means appears to be brought about at the expense of film thickness.

FN 2961, sprayed as microfog jets on a heated rotating disc, fails to form a uniform film spreading over the disc surface, even at high (oil/gas) mass flow ratios and regardless of the disc temperature. Much of the film flow is characterized by heavy streaking. On the other hand, XRM 109 F exhibits excellent inherent wetting properties by forming a continuous lubricant film on the disc under most conditions. However, at a disc temperature of 800°F (700°K) and an angular velocity of 104 rad/s or higher, XRM 109 F forms a continuous film over the disc to only a radial distance of 1-3/4 inches (4.45 cm), beyond which heavily streaked flow develops under the test conditions employed.

B. Heat Transfer Studies

The heat transfer characteristics of microfog jets of four test lubricants impinging normal to a heated rotating disc were investigated under various test conditions, with a convergent nozzle

(4.34 mm orifice diameter) at entrance pressure up to 67 psig ($56\ N/cm^2$). The test oils comprised FN 2961 (super-refined naphthenic mineral oil), XRM 109 F (synthesized hydrocarbon), XRM 109 F plus 10% (by weight) Kendall super-refined paraffinic resin, and XRM 109 F blended with 10% (by weight) XRM 126 A (less viscous synthesized hydrocarbon).

The heat transfer rates of the microfog jets indicate that the convective heat transfer coefficient is largely controlled by the gas phase alone. Only the microfog lubricant drops that impinge on the disc seem to have a slight cooling effect, while the microfog stream of non-impinging drops appears to behave as a single gas phase stream. The heat transfer coefficient is insensitive to variation of other factors tested, such as angular velocity of the disc, the rate of oil-mist output, and physical properties of the lubricants. This insensitivity may be related to a thermal boundary layer formed along the cooling surface, which seems to be unaffected by the factors listed, although their effect on the hydrodynamic boundary layer may be significant.

The temperature effects on the heat transfer coefficient were analyzed from the heat transfer data for XRM 109 F microfog jets at disc temperature ranging from 600 to 800°F (589 to 700°K). The heat transfer coefficient tends to decrease with the increasing temperature difference between the disc surface and the impinging jet. The large property variations of the impinging jets and of the thin lubricant films flowing over the disc, causing "laminarization," inverse transition from the turbulent to the laminar regime for forced convective flow, are cited as a possible reason for the decrease in heat transfer coefficient.

The heat transfer coefficients obtained with nitrogen gas jets (without microfog) impinging on a heated disc increase slightly with increasing angular velocity of the disc, but at only low forced inflows. The coefficients decrease rapidly with increasing radial distance from the stagnation point of the jet, but they seem to gradually approach asymptotic values, beginning at a radial distance ratio (r/D_o) of around 8.

The heat transfer coefficients were found to increase also with increasing rates of forced inflow and to decrease as the axial spray distance ratio (Z/D_o) increases. These results are empirically correlated by means of the dimensionless equation of the Nusselt type:

$$N_{Nu} = 1.9\left[(N_{Re})_m \cdot (N_{Pr}) \cdot \left(\frac{D_o}{Z}\right)\right]^{1/3}$$

This relation gives fairly good agreement with the experimental data.

C. Kinetic Drop Formation

Using a dropwise lubricant feed system, which forms and projects a drop of known size with a gas stream of given velocity onto a solid surface, the formation, size, velocity, and impingement dynamics of XRM 109 F and FN 2961 drops impinging on a heated rotating disc were studied with the aid of high-speed photography. Drop sizes were varied by the use of two different capillary tube sizes in the drop-forming section. Gas stream velocities of 11, 15, and 19 m/s were employed.

The mechanisms of kinetic drop formation are briefly described for XRM 109 F and FN 2961 from photographic observation. The drops of these lubricants differ markedly in the shapes and sizes of the ligaments (thin filaments) formed on the drop surfaces when the drops separate from the tip of a capillary tube. The lower viscosity of FN 2961 appears to reduce the stability of the ligaments, resulting in a greater number of satellite drops, a larger proportion of drops that are free of ligaments, and a larger number of drops overall, than for XRM 109 F under corresponding conditions.

The estimated values of drop size with a capillary tube of 1 mm diameter for these lubricants range from 1.3 to 1.7 mm at the gas stream velocities tested. For the effect of gas stream velocity on drop size, the general trend, though inconclusive, seems to be to smaller drop sizes at the higher gas stream velocities.

The drops detached from the capillary tip are not fully entrained by the gas streams because of the significant differences in density between the lubricant drops and the gas. The terminal velocities of the drops do, however, increase with increasing gas stream velocity. The velocities acquired by drops seem to be largely dependent on the sizes and shapes of ligaments on the drop surfaces, which, in turn, depend on the mechanisms of kinetic drop formation.

When a drop undergoes aerodynamic breakup, the most critical factor controlling the break appears to be the relative velocity (velocity difference between drop and gas stream). Other factors are surface tension, viscosity, and density of the drop.

The tangential velocity of a surrounding gas near a disc rotating at 312 rad/s appears to have some complex effects on the impinging velocity of drops moving toward the disc. But the effects of drop size, angular velocity of the disc, and the velocities of gas jets impinging on the disc, particularly those of wall jets, are strongly coupled and difficult to separate. Hence, the present test rig can not provide information of sufficient accuracy to draw any quantitative conclusions regarding a possible windage effect caused by the action of centrifugal forces generated by the rotating disc.

For a given drop, the gas stream velocity and angular velocity of a disc have a pronounced effect on the wetted area and wetting patterns formed by the drop; as both gas stream velocity and angular velocity of the disc increase, the wetted area formed by the drop upon impingement becomes wider and the ligaments (streaks) formed are much smaller.

D. Reclassifying Nozzles and a Vortex Mist Generator

Experimental "reclassifying" nozzles of two different types - pneumatic and electrostatic - have been developed and evaluated by comparing their wetting rate data with those obtained from a conventional (convergent) nozzle. Their advantages and limitations are briefly discussed in terms of wetting rate and several desirable parameters of microfog lubrications.

A pneumatic nozzle, basically consisting of a conventional convergent nozzle with one layer of stainless steel screen (150 mesh) inserted in a converging section and a secondary gas nozzle which is mounted axially outside of the convergent nozzle, is extremely successful in enhancing the wetting rates of XRM 109 F microfog jets. The effectiveness of this nozzle is attributed to efficient particle size reclassification through the action of the screen within the nozzle. Another potential advantage of this nozzle, which the test conditions could not properly evaluate, is reduction (by the surrounding air jet) of the amount of lubricant which escapes the main microfog stream.

One of two novel electrostatic nozzles which were briefly examined was designed to enhance the collection of microfog particles by an impactor through the action of an electrostatic field external to the nozzle. With this nozzle, the electrostatic field, regardless of its polarity, had no beneficial effect on wetting rate, but disrupted lubricant film formation by causing heavy streaking of the film flow.

A second electrostatic nozzle, which applied the field internally, was designed to promote size reclassification of the microfog particles. The electrostatic field in this case seemed to produce a slight trend toward improved wetting rate.

The results obtained with electrostatic nozzles in general indicate the need for further refinements of their designs before their anticipated advantages can be firmly demonstrated and quantitatively evaluated.

An effort was made to evaluate a microfog generator having a pneumatic vortex atomizing nozzle for which significant advantages of low maintenance and high efficiency of mist generation are claimed. The vortex mist generator evaluated was considerably smaller than the conventional venturi-type generator used in all of the other work. Because of this difference in the capacities of the two generators, it is difficult to draw from the existing data any conclusions on their relative capabilities. While a comparison of the particle size distribution data obtained with the two generators seems to indicate little difference in atomization, data for a vortex mist generator of comparable size are needed for a more proper comparison.

III. DETAILED REPORT

A. Materials

The two high-temperature lubricants tested and the two blended test lubricants were:

- FN 2961, Humble Oil and Refining Co.
- XRM 109 F, Mobil Research and Development Corp.
- XRM 109 F plus 10% (by wt.) Kendall super-refined paraffinic resin [~20,000 SUS at 100°F (311°K)]
- XRM 109 F blended with 10% (by wt.) Mobil XRM 126 A

Identification by chemical type, and physical properties for each lubricant, are listed in Appendix A.

The test specimen was a circular plate, 4 inches (10.1 cm) in diameter and 1/4 inch (0.63 cm) in thickness, made of hardened CVM WB-49 material and finished circumferentially ground to 4 to 8 μin. (0.1 to 0.2 μm) RMS. A disc with a freshly ground surface was used for each run.

Nitrogen gas employed in this work was "purified grade," stated by the supplier (the Airco Industrial Gases Division of the Air Reduction Co.) to have a minimum purity of 99.98 mole percent with a maximum of 10 ppm oxygen.

B. Apparatus and Procedure

A schematic flow diagram of the basic apparatus used for all of the experimental works is shown in Figure 1. Detailed descriptions of the major components and related procedures were reported elsewhere (1, 2), except for a new rotating specimen test chamber (E) which was designed specifically for the present investigation (Tasks III, IV, and V) and was employed in wetting rate and heat transfer studies of microfog jets. Engineering details and the materials list for the new test chamber are shown in Appendix B.

The test chamber, which is essentially a stainless steel shell 10 inches (25.4 cm) in diameter, wrapped with a 3,200 W heater, is insulated with diatomaceous earth and is equipped with three view-ports through which photographic observations of the test specimen can be made. Relative angles of the view-ports are described in our earlier report (1). The test chamber can be controlled to pressures to 80 psia (55 N/cm^2) and to temperatures of 1000°F (811°K) by a current-proportioning Barber-Coleman capacitrol in conjunction with a silicon control rectifier (SCR).

Figure 1

FLOW DIAGRAM OF EXPERIMENTAL APPARATUS

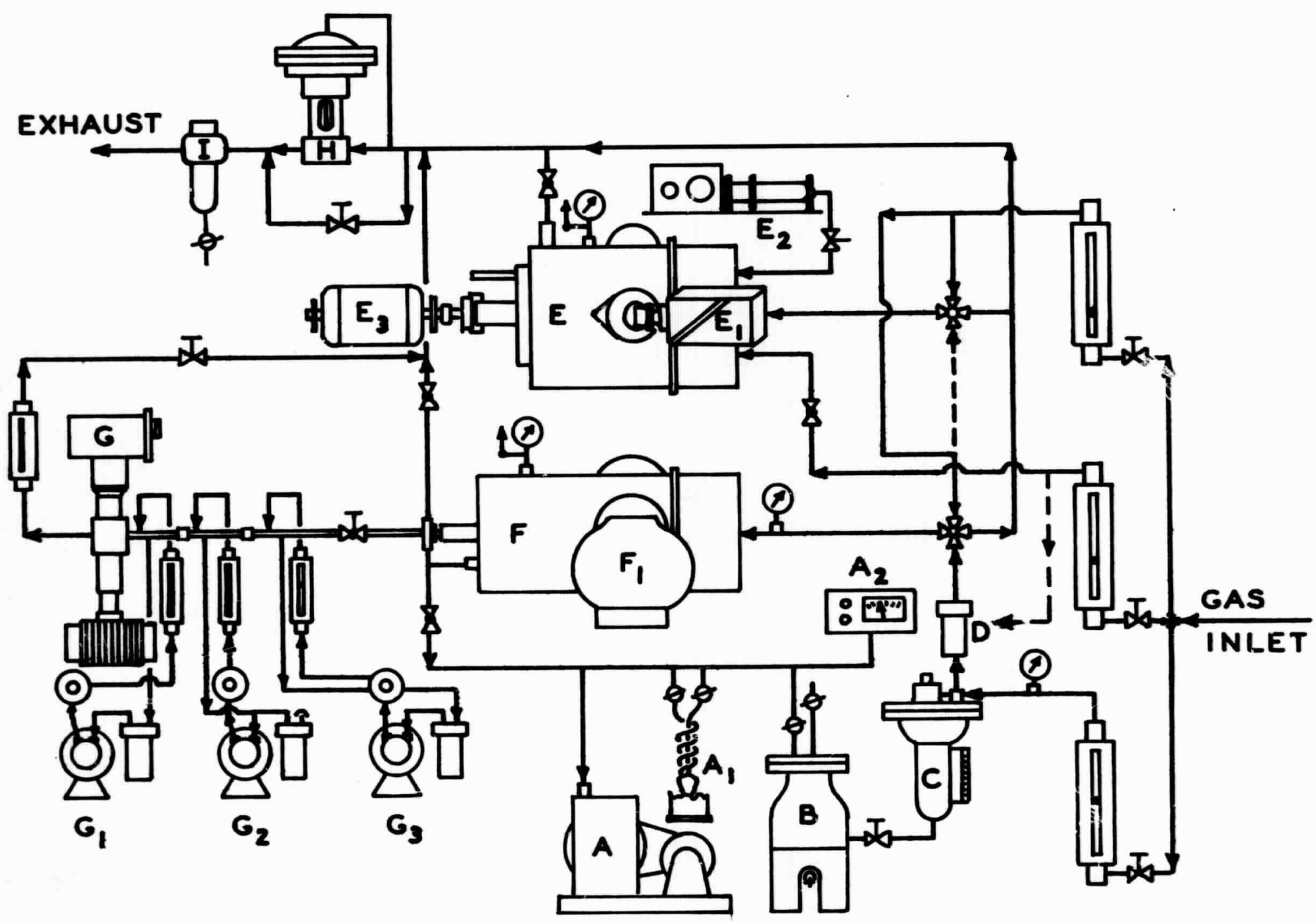

The test specimen is a disc composed of CVM WB-49 tool steel. The test surface (the disc face) is circumferentially ground to 4 to 8 μin. (0.1 to 0.2 μm) RMS. The rear surface of the disc is recessed to accept a heat flux transducer and two thermocouples in contact with the disc. The removable disc is vertically mounted by two set-screws [1/4 in. (6.3 mm) from the edge] to a head assembly containing a 1,000 W spiral Calrod heater capable of heating the disc to 1,000°F (811°K). The entire head assembly is rotated at angular velocities up to 520 rad/s by a 3/4 HP (560 W) Boston Gear Works DC motor regulated by a ratiotrol controller (SCR type). The actual angular velocity of the test specimen is measured by means of an Airpax electronic tachometer, which is accurate within 0.25 percent.

The drive shaft is sealed by a special magnetic carbon ring shaft seal, supplied by the Magnetic Seal Corporation, which allows the test chamber to be evacuated or pressurized to specified conditions. The seal is comprised of a carbon ring, backed with type 416 stainless steel, sliding against the surface of an Alnico-5 magnetic ring. The carbon ring is coupled to the rotating shaft by means of an "O" ring, while the magnetic ring is fixed to the stationary housing. To secure at high test chamber temperatures the satisfactory operation of the magnetic seal and a 55 mm-bore ball bearing on the spindle, the drive mechanism is cooled by running water through a hollow collar, or jacket, surrounding the rear section of the rotating head, and is lubricated with a small recycling lubricant spray system.

The temperature of the disc is sensed by two iron-constantan parallel thermocouples situated 1/8 in. (3.18 mm) behind the face of the disc and symmetrically spaced at 1 in. (2.54 cm) radial distance from the center of the disc. The disc temperature is regulated by a Barber-Coleman nonsaturating reset temperature controller, and is recorded by a Barber-Coleman autronic single pen recorder. The output signal of the heat flux transducer, a special design fabricated to specifications by Heat Technolog Laboratory, is recorded by a Leeds and Northrup high-speed Speedomax G millivolt recorder. Electrical connections to the heater, thermocouples, and heat flux transducer are made through a brush-ring assembly, comprised of carbon brushes sliding on silver rings, and supplied by the Electro-tech Corporation.

The gas and microfog streams are introduced at one end of the test chamber and are directed to the disc surface by way of a spray (or reclassifying) nozzle, positioned at a right angle to the disc surface and at 1 in. (2.54 cm) from that surface.

1. Wetting Rate Determinations

Wetting rates under a variety of test conditions are determined in the rotating specimen chamber (E). The progressive wetting of the heated disc surface by a microfog stream is photographed by a Hycam high-speed movie camera (F_1) operating at framing speeds of 20, 200, and 800 frames per second (fps), depending upon the angular velocity of the disc. The camera with a 25 mm, f/2.8 lens is focussed on the disc through one view-port and illumination at two other ports is provided by GE 650 W DVY lamps in silvered reflectors. The relative angles of these view-ports are identical to those already described in our earlier report (1).

To start a typical wettability test, heat the test chamber, the microfog generator, and the incoming nitrogen gas stream to the desired temperatures and start the flow of tap water through the water jacket. While heating these components, clean a fresh test disc as specified in Section e, Task I, by rinsing with acetone, scrubbing with moist levigated alumina and a soft polishing cloth, then rinsing successively with tap water, distilled water, and ethyl alcohol. Load the Hycam high-speed movie camera (F_1) with 400 ft. of Eastman Kodak Ektachrome color reversal film, type 7242, and set the framing speeds at 20 to 800 fps, depending on the angular velocity of the disc. After establishing steady-state conditions of temperature at the chamber, microfog generator, and incoming gas line, fasten the test disc to the front of the rotating head assembly, install the cleaned spray nozzle at 1 in. (2.54 cm) axial distance from the center of the disc, and quickly close the test chamber door. Purge the test chamber with fresh nitrogen gas for 10 minutes and slowly raise the chamber pressure to 45 psig (40 N/cm^2). Heat the test disc to the required test temperatures of 600, 700, and 800°F (589, 644, and 700°K) while continuing to purge at a nitrogen gas flow rate of 1 cfm (0.5×10^{-3} m^3/s). Start the circulation of lubricant from the small recycling lubricant spray system to the front spindle ball bearing, then rotate the disc at the required angular velocity. Readjust the temperature of the disc, if necessary, and start the required flow rate of heated nitrogen gas to the microfog generator with the microfog stream diverted directly to the exhaust line via the 4-way valve. When the run conditions of temperature, pressure, gas flow rate, and angular velocity reach equilibrium, illuminate the disc with the two lights, and actuate the control solenoid, setting the Hycam high-speed movie camera in operation and simultaneously delivering an electrical signal to a relay switch, which after a 1 or 1.5 second time delay, reverses the 4-way directional valve. This sends the microfog stream from the generator through the spray nozzle to the disc surface, while diverting the nitrogen gas stream directly to the exhaust line. Starting the camera 1 or 1.5 seconds in advance allows it to accelerate to the desired framing speed before the microfog stream is introduced to the disc. At the end of the run, usually between 5 to 15 seconds, deactivate the control solenoid, stopping the camera and switching the 4-way valve to return the nitrogen gas stream to the test chamber and the microfog stream to the exhaust line. Turn off the illuminating lights and the disc heater, stop rotation of the disc and gas flows, exhaust the system pressure, and remove the spray nozzle and the disc.

2. Heat Transfer Rates

Heat transfer studies employ the same experimental apparatus and test specimen as the wettability studies do. Instead of photographing wetting phenomena, however, the heat transfer rates of gas or microfog jets impinging on a heated rotating disc are measured by using a heat flux transducer.

In order to obtain the corresponding convective heat transfer coefficient, it is necessary to accurately determine the total heat transferred away from the heated rotating disc, the surface temperature of the disc, and the temperature of the incoming nitrogen gas stream far removed from the disc. It also is necessary to minimize heat transfer by radiation and conduction. Micalex insulation on the back and edge of the disc reduces conduction loss and suppresses radial temperature differences within the disc; and great care is exercised in controlling the temperatures of the disc and the gas stream. Local heat transfer rates are measured with the heat flux transducer mounted 1/8 in. (3.18 mm) behind the disc surface. This produces an emf proportional to the heat flux from a test area [1/2 in. (1.27 cm) diameter], without significantly disturbing the isothermal condition of the heat transfer surface. The principle of the heat flux transducer and the method of its calibration are fully described in Appendices D-1 and D-2, respectively.

The procedure for introducing the gas and microfog streams to the disc surface is identical to that for wettability studies, except that an additional gas stream, bypassing the microfog generator, is allowed to flow through the spray nozzle to the disc surface before introduction of the microfog stream. This is done to measure the heat transfer rates of gas jets as references before determining the rates for microfog jets.

For a typical series of tests, the procedure to establish the steady-state conditions of temperatures, pressure, and gas flow rates is identical to that described for wettability studies. Once the steady-state conditions are reached, start the required nitrogen gas flow, bypassing the microfog generator and venting directly to the exhaust line via the 4-way directional valve, and start the calibrated L&N millivolt recorder for the transducer output to establish the base line for a flow of 1 cfm (0.5×10^{-3} m^3/s). When the recorder shows a steady-state convective heat transfer, energize the control solenoid which reverses the 4-way valve and directs the reference gas stream to the disc surface, and the nitrogen purge gas (1 cfm) to the exhaust line. When the run is completed (usually in 30 to 35 seconds), as indicated by a constant millivolt read-out, deactivate the solenoid which controls the 4-way valve to switch the reference nitrogen stream to the exhaust and the nitrogen purge gas to the disc. Readjust the temperatures of the disc and the nitrogen gas stream, if necessary. As soon as a new steady-state condition is established with 1 cfm (0.5×10^{-3} m^3/s) nitrogen gas flow, repeat the same operations with the microfog stream by directing the required nitrogen gas stream to the microfog generator. When the test run with the microfog stream is finished, turn off the recorder and the disc heater, stop rotation of the disc and the gas flows, relieve system pressure, and remove the disc and spray nozzle.

3. Wettability of Impinging Lubricant Drops

Wettability studies of single lubricant drops impinging on a heated rotating disc employ basically the same test apparatus described for the wettability and heat transfer studies of microfog jets. The convergent spray nozzle is replaced by a dropwise applicator which is described in Attachment 7, Appendix B. The applicator is essentially a capillary tube around which a well-defined gas stream flows. The well-defined gas stream is secured by passing the nitrogen gas stream through a calming zone consisting of multilayers of fine screen. The gas stream entrains the drops formed at the tip of the tube and carries them to the surface of the rotating disc. The rate of lubricant volume delivered to the disc is metered by use of a Harvard infusion-withdrawal pump (E_2) supplied by Harvard Apparatus. The pump with a 50 ml stainless steel syringe provides pumping rates ranging from 0.0001 to 0.65 ml/s at accuracies to ±0.5 percent.

The kinetics of drop formation, the sizes and velocities of suspended lubricant drops, and the dynamics of lubricant drops impinging on the heated rotating disc are photographed by the Hycam high-speed motion picture camera with a 63 mm, f/2.7 lens, plus a 7 mm extension, which is focussed on the tip of the capillary tube.

The operating procedure for this series of tests differs from those described before only in that single lubricant drops, instead of microfog streams, are introduced to the disc. The dropwise applicator is located at a 1 in. (2.54 cm) axial distance from the disc surface and directed normal to that surface at a radial distance of 1 in. (2.54 cm) from the center of the disc. The remainder of the operating procedure is identical to that described for wettability studies except that the microfog generator contains no lubricant.

4. Method of Data Analysis

a. Wettability

The filmed results of wetting studies were analyzed with the aid of a Photo Optical Data Analyzer (L-W Photo Corp.) and a Photo Data Quantitative Comparator, or "PDQ" screen (Photographic Analysis Co.). Images were projected at a 1:1 magnification ratio. After projecting the photographic images, progressive advancement of a circular uniform lubricant film on the disc was followed at six index marks corresponding to the disc area coverages of 0.14, 0.25, 0.39, 0.55, 0.76, and 1.00 fractions. At the known film speeds of 20, 200, and 800 fps, the wetting times for these coverages are readily determined from the frame number recorded as the edge of the lubricant film advances across the appropriate index line on the screen.

b. Single Lubricant Drop

Analyses of the filmed kinetic drop formation employ the same analyzer and PDQ screen that are used in wettability studies. Images were projected on the screen at a 7:1 magnification ratio. After a system appeared to be at equilibrium, the sizes of selected individual drops were measured, their velocities were determined from the number of frames required to traverse the distances between grid lines on the screen, and their wetting patterns were observed as they impinged on the disc surface.

c. Heat Transfer Study

Total heat transfer rates were estimated from the millivolt recorder read-out with a gauge constant for the heat flux transducer of 0.752 $Btu/ft^2 \cdot s \cdot mv$ (0.855 $W/cm^2 \cdot mv$) (see Figure 41), and their corresponding heat transfer coefficients were calculated by using the following equation:

$$h = \frac{(Q/A)}{T_W - T_\infty}$$

where (Q/A) represents the total heat flux and $(T_W - T_\infty)$ the temperature difference between the disc and the gas stream.

C. Results and Discussion

For convenience in analyzing the results of different phases of this investigation, this section is divided into three parts:

1. Wettability and heat transfer of microfog jets impinging on a heated rotating disc
2. Wettability of lubricant drops impinging on a heated rotating disc
3. Evaluation of reclassifying nozzles and a vortex mist generator

1. Wettability and Heat Transfer of Microfog Jets Impinging on a Heated Rotating Disc

Since the key to microfog lubrication is the effective wetting of the surface to be lubricated, the wetting characteristics of the microfog particles, in relation to the thin lubricant film flow and heat transfer on the surface, are of fundamental importance. Impaction of a microfog stream on a heated rotating disc may be chosen as a model system for study of the effects of centrifugal forces generated by the rotating disc on the microfog stream and on the flow of a thin lubricant film spreading over the disc, and its effect on heat transfer.

a. Analysis

The system to be studied for this phase of the contract, as shown schematically in Figure 2, is a heated rotating disc at uniform surface temperature, T_w, situated in a forced inflow of the microfog stream which has velocity, U_∞, and temperature, T_∞. This microfog stream forms, upon impingement on the rotating disc, a continuous lubricant film having a film thickness, δ, along the radial distance, r, of the disc surface. This continuous lubricant film moves radially outward along the disc at velocity u_r under the action of the centrifugal forces generated by the disc rotating at angular velocity, ω, and of the interfacial shear, τ_i, caused by the adjacent microfog streams at a lubricant-microfog interface.

The prime targets of this investigation are the thin film flow and heat transfer of the system. In order to achieve these goals, it is first necessary to analyze in detail the velocity and temperature distributions in both lubricant and microfog boundary layers on a rotating disc. The problem is, of course, governed by the basic conservation laws: momentum and energy equations. Solving such a set of mathematical equations would appear a formidable task, although the equations can be tractable by use of van Karman's transformation, and is not within the scope of this investigation. With several assumptions, however, the equations can be reduced and simplified, and still be applied to the physical model as defined in Figure 2.

For the case of laminar film flow on a rotating disc with viscous friction, no slippage, and sufficiently large distance along r, a simplified solution for the radial surface velocity of lubricant film can be expressed as:

$$u_r = \frac{\omega^2 \rho_\ell}{2\mu_\ell r} (Z^2 - 2Z\delta) + \frac{\tau_i Z}{\mu_\ell} \qquad (1)$$

Figure 2

SCHEMATIC OF THE PHYSICAL SYSTEM

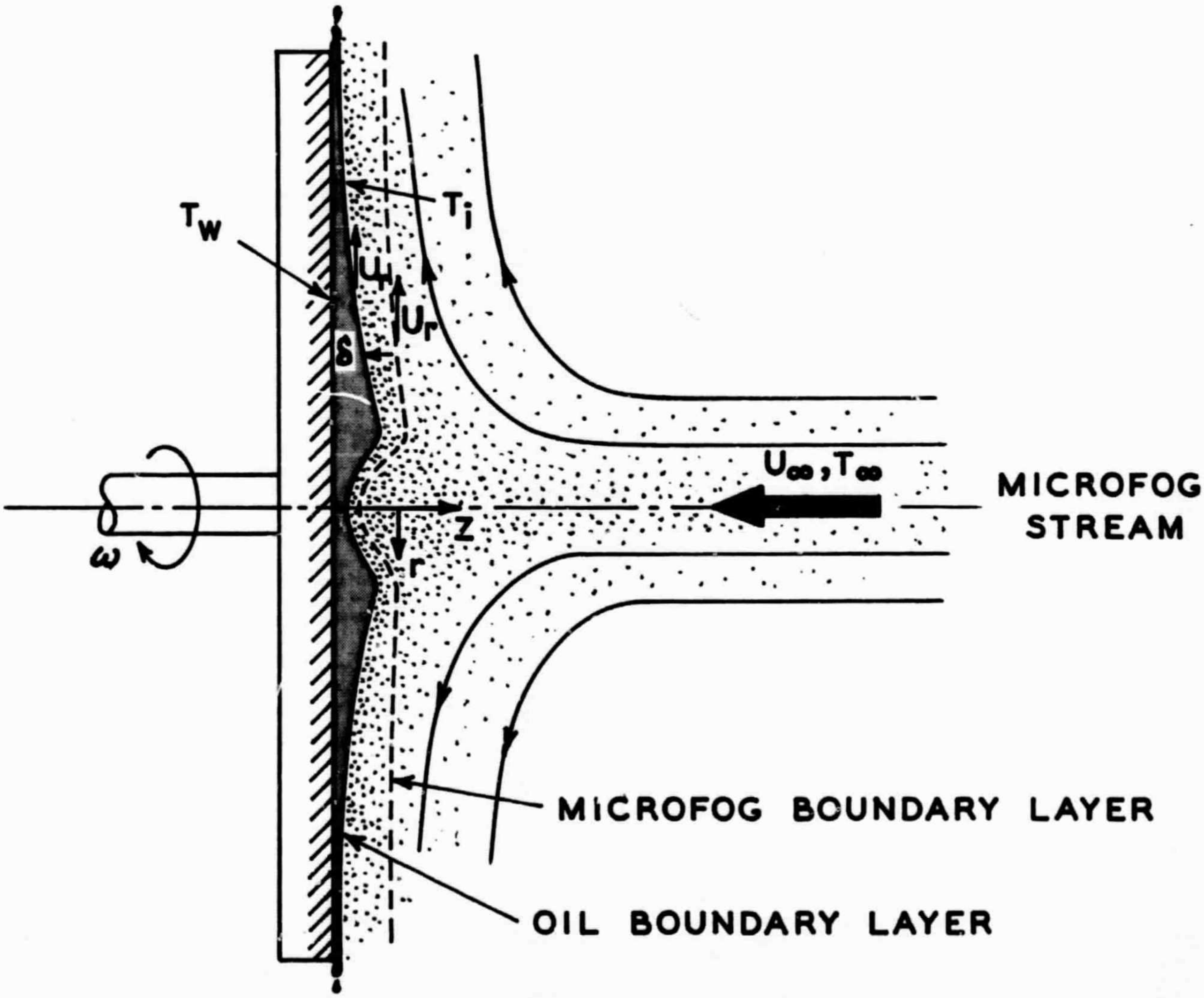

By integrating Equation (1) over the film thickness, δ, the mean radial velocity is found to be

$$\langle \bar{u}_r \rangle = \frac{1}{\delta}\int_0^\delta u_r(Z)\,dZ = \frac{\tau_i \delta}{2\mu_\ell} + \left[\left(\frac{\omega V}{2\pi r}\right)^2 \frac{\rho_\ell}{3\mu_\ell}\right]^{1/3} \qquad (2)$$

where

$$\tau_i = \left[\mu_\ell \frac{\partial u_r}{\partial Z}\right]_{Z=\delta} = \left[\mu_g \frac{\partial U_r}{\partial Z}\right]_{Z=\delta}$$

The first term on the right designates the velocity motivated by interfacial shear and the second term represents the action of the centrifugal forces.

The most important results of practical interest are the heat transfer characteristics of the system. The local heat flux, Q, from the heated disc may be expressed by Fourier's law:

$$Q = k\left(A_1 \frac{\partial T}{\partial Z}\right)_{Z=o} \qquad (3)$$

Introducing the overall heat transfer coefficient, h, the expression for Q becomes:

$$Q = hA_2(T_w - T_\infty) \qquad (4)$$

It is customary to rephrase the heat transfer results as a heat transfer coefficient, which is defined as follows:

$$h \equiv \frac{k\left(A_1 \frac{\partial T}{\partial Z}\right)_{Z=o}}{A_2(T_w - T_\infty)} \quad (A_1 \neq A_2) \qquad (5)$$

To relate δ to known physical quantities, an overall energy balance is expressed in the following form:

$$k\left(A_1 \frac{\partial T}{\partial Z}\right)_{Z=o} = \int_0^\delta 2\pi r \rho_\ell u_r Cp_1 (T_i - T_\infty)\,dZ$$
$$+ M_\ell \{Cp_1(T_B - T_\infty) + \lambda\}$$
$$+ W\,Cp_2\,(T_G - T_\infty) \qquad (6)$$

where Cp_1 and Cp_2 are the heat capacities of the lubricant and microfog streams, respectively; M_ℓ, the amount of lubricant evaporated; λ, the heat of vaporization; and W, the total mass flow rate of the microfog stream. The first term on the right is the heat absorbed by the lubricant film flowing over the disc; the second term accounts for evaporative cooling; and the third term is heat taken away by the microfog stream at the lubricant-microfog interface. The left hand side, of course, represents the total heat transferred from the disc surface to the lubricant film and the microfog stream. The various terms in Equations (5) and (6) will be used for the reduction and comparison of experimental data.

b. Wettability Determinations

Determinations of the wetting rates of the two base lubricants, FN 2961 and XRM 109 F, which were selected because of their performance shown in Tasks I and II, were made with No. 1 spray nozzle (4.34 mm orifice diameter) under test conditions as specified in Task III.

Test results, reporting wetting times at different radial distances, are listed in Appendix C-2 under a variety of test conditions. Discussion of the test results will employ the specific wetting rate concepts as defined in our previous work (2). Because discussion or comparison of the great mass of wetting rate data would be exceedingly cumbersome, it will be confined to significant factors which may have an important bearing in microfog lubrication, citing typical examples to illustrate general trends. Any test results deviating from the general trend will be pointed out and discussed separately.

(1) General Comments

When wettabilities of microfog streams of different lubricants on a static metal surface were determined under a variety of test conditions, a movie camera operating at 64 fps was successfully used to photograph the progressive movement of a thin lubricant film spreading on the metal surface (2). In this case, the picture frequency of the camera was sufficiently fast to stop the dynamic behavior of the lubricant film. However, in the present contract, a heated rotating disc was chosen as a test plate for study of the effects of centrifugal forces generated by the rotating disc on the incoming microfog streams and on the flow of thin lubricant films formed by the microfog streams. The added motion of the rotating disc, however, greatly complicated efforts to record wettability data on motion picture film. To achieve the very short exposure times required to "freeze" the rapid action of lubricant film flow on the rotating disc, Hycam high-speed motion picture camera was employed. A high-speed photographic system with large, controlled electronic flash units, and with special optical systems, was also considered. This approach, which might provide better image quality, was, however, rejected on the basis of the limited funds and time available to complete the study.

Satisfactory picture quality with the Hycam high-speed camera depended on the following information based on the nature of the subject and the degree of subject resolution:

- The maximum allowable exposure time that would limit blur or loss of resolution to acceptable proportions.

- The amount of light energy required by the subject at the maximum allowable exposure time.

As the result of many calculations and extensive photographic experiments to answer these questions, the shutter duration-period ratio was decreased from 1/2.5 to 1/100 by installing a slit-shutter in the Hycam high-speed camera, electrical power around 1.3 KW was provided for illumination of the subject area, and a lens aperture of f/4 was set. Established relations between picture frequency and peripherial velocity of the disc calculated at a maximum radius of 2 inches (5.08 cm) are as follows:

Angular Velocity (rad/s)	Subject Velocity (m/s)	Picture Frequency (fps)	Effective Exposure Time (s)	Time Delay (s)
0	0	20	5.0×10^{-4}	0
26	1.32	200	5.0×10^{-5}	1
52	2.64	200	5.0×10^{-5}	1
104	5.28	800	1.2×10^{-5}	1.5
312	15.84	800	1.2×10^{-5}	1.5

During the development of the photographic techniques, we found that at these picture frequencies, prestarting of the Hycam high-speed movie camera by a time delay mechanism was needed because of its acceleration period requirement (refer to Figure 39). Best results were consistently obtained with 400-foot rolls of Ektachrome Film 7242 EF. Although the quality of the high-speed movies was at a satisfactory level for the analysis of photographically recorded experimental results, it was generally not as good as that of the movies for the static test plates obtained in the previous contract. Images of the dynamic behavior of thin lubricant films recorded on movie film were not completely free from blur, even with a blur limit of 0.001 in. (0.0025 cm), when the disc rotated at 312 rad/s. Further improvement was prevented by the photographic limitations imposed by geometry of the test chamber and reduction of the light intensity by fog which accumulated in the test chamber during the longer test times required for the 4" disc compared with the 2" square test plate used in the previous study. The effects of the changed geometry will be discussed in greater detail in a later section.

The photographic limitations sometimes cast uncertainty on experimental results at high angular velocities of the disc. In these cases, duplicate runs were made to ensure reliability of the test data. Typical experimental results, illustrated by the wetting data for XRM 109 F with the disc at an angular velocity of 312 rad/s and a temperature of 600°F (589°K), are shown in Figure 3. The plots exhibit an excellent straight line relationship. The same relationship was observed in the previous study with the static test plate, although the data points scatter considerably more in the present investigation. In general, the results are satisfactory, and the test data at other conditions yield similar relations except for FN 2961 which, under all test conditions, forms a uniform lubricant film spreading over the heated disc to only a 1 in. (2.54 cm) radial distance beyond which a streaky flow occurs (refer to Appendix C-2). Thus, subsequent discussion will not apply to the results of FN 2961 because it failed to yield complete sets of data points.

The filmed wetting rate data for XRM 109 F also revealed that under the present test conditions at a disc temperature of 600°F (589°K), a continuous lubricant film generally spread to the edge of the disc. On the other hand, at higher disc temperatures, and particularly at 800°F (700°K) with the disc rotating at angular velocities of 104 rad/s or higher, XRM 109 F formed a continuous lubricant film flowing over the disc to only approximately a 1-3/4 in. (4.44 cm) radial distance, beyond which the lubricant flow was characterized by heavy streaking. This streaky flow may be initiated and controlled partly by shear of the lubricant film by the high-speed gas stream and the centrifugal forces created by the rotating disc, and partly by evaporation of the lubricant film. The thermocapillary effects (variation of surface tension of the film with temperature) also may be a contributing factor (2).

(2) Effect of (Oil/Gas) Mass Flow Ratio

In order to illustrate the effect of (oil/gas) mass flow ratio on wetting rate, the wetting rates for XRM 109 F with a stationary heated disc (4" circular plate) at gas flow rates of 3, 4, and 5 cfm (1.4×10^{-3}, 1.9×10^{-3}, and 2.4×10^{-3} m^3/s) are shown in Figure 4, which also includes the wetting rates of XRM 109 F with a 2" square plate taken from our previous work (3).

With increasing (oil/gas) mass flow ratios, the wetting rates, as expected, increase linearly. However, the increased (oil/gas)

Figure 3

WETTABILITY OF XRM 109 F AT 600°F (589°K)

Angular Velocity : 312 rad/s
Surface Area of Disc : 80.8 cm^2

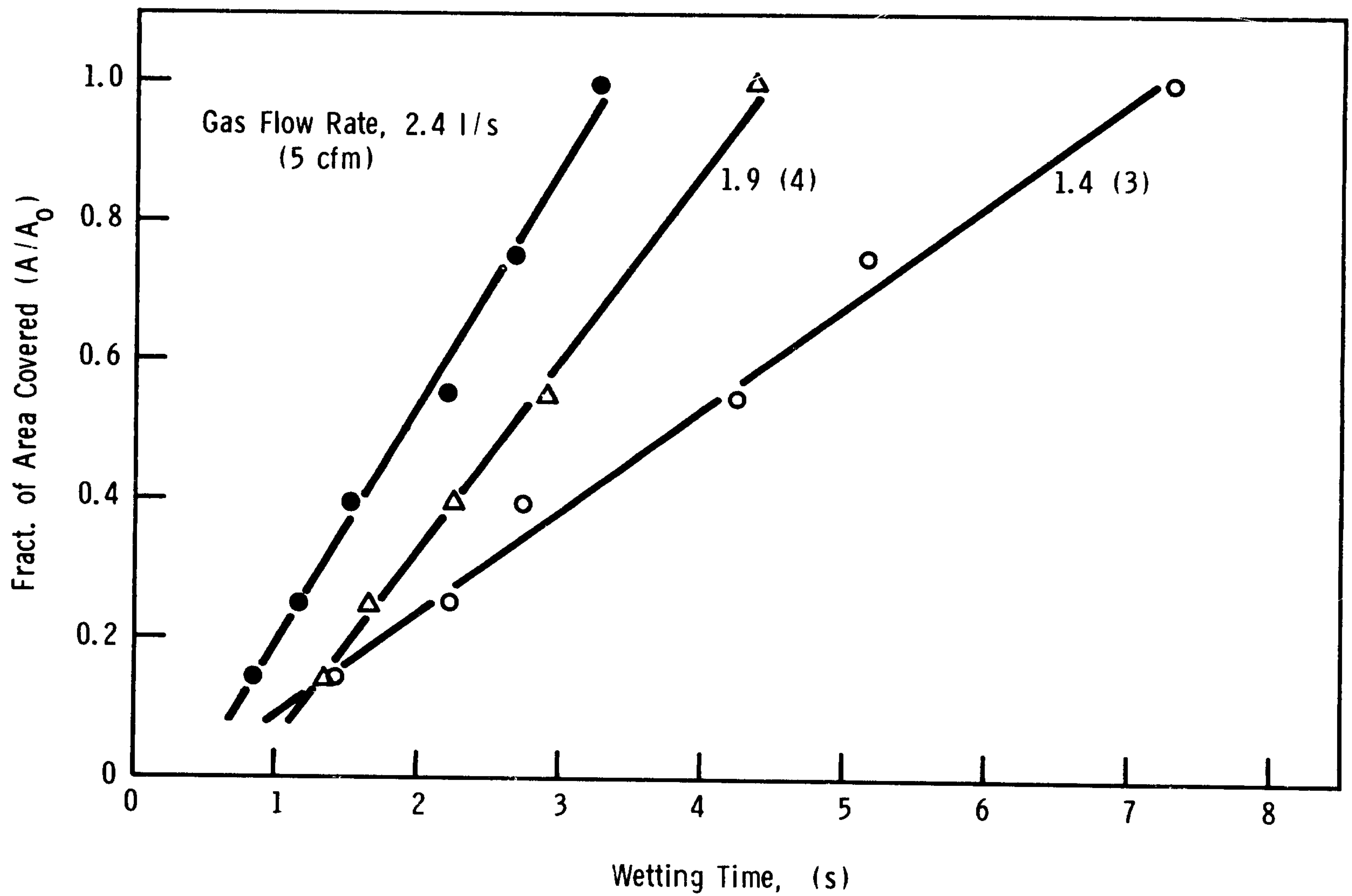

mass flow ratios are established by increasing gas flow rates to the microfog generator, a procedure which also increases the impaction velocity for a given nozzle. Hence, the increases in wetting rate shown in Figure 4 are due not entirely to the increase in (oil/gas) mass flow ratio, but to a combination of increases in impaction velocity and mass flow ratio. The effects of these factors on wetting rate has been discussed in greater detail elsewhere (2).

Of particular interest are the wetting rates of XRM 109 F with two impactors of different size. As shown in Figure 4, the rates with the 4" circular test plate are considerably lower than those with the 2" square plate under the identical test conditions. A comparison of the specific wetting rates (the slopes of the straight lines in Figure 4) for these plates is shown as below:

Test Plate	Specific Wetting Rate
	(cm^2/s/mass flow ratio) x 10^{-3}
2" square plate	17.0
4" circular plate	5.3

The straight lines for both plates also give a nearly identical value (2.0 x 10^{-3}) of the minimum wetting rate [minimum (oil/gas) mass flow ratio required to wet a test plate], which are determined by taking the intercept at zero wetting rate.

Reduction of the wetting rates of XRM 109 F with the 4" circular test plate is probably caused by a decrease in collection efficiency of microfog particles. This decrease may be explained by examining the relationship between collection efficiency and impactor (test plate) size, as expressed in the mathematical form of

$$\eta = \frac{\rho_\ell \bar{d}^2 U_\infty}{72 \mu_g D} \tag{7}$$

Provided that all operating parameters are equal for a spray system except for impactor size, the collection (inertial) efficiency of the system, η, is inversely related to only the impactor size, D; that is

$$\eta \propto \frac{1}{D} \tag{8}$$

It is apparent from Equation (8) that η decreases with increasing value of D, as demonstrated in Figure 4. According to Equation (8), the ratio of the specific wetting rates between the two test plates

Figure 4

EFFECT OF IMPACTOR SIZE ON WETTING RATE AT 600°F (589°K)

Test Oil : XRM 109 F
Angular Velocity : 0 rad/s

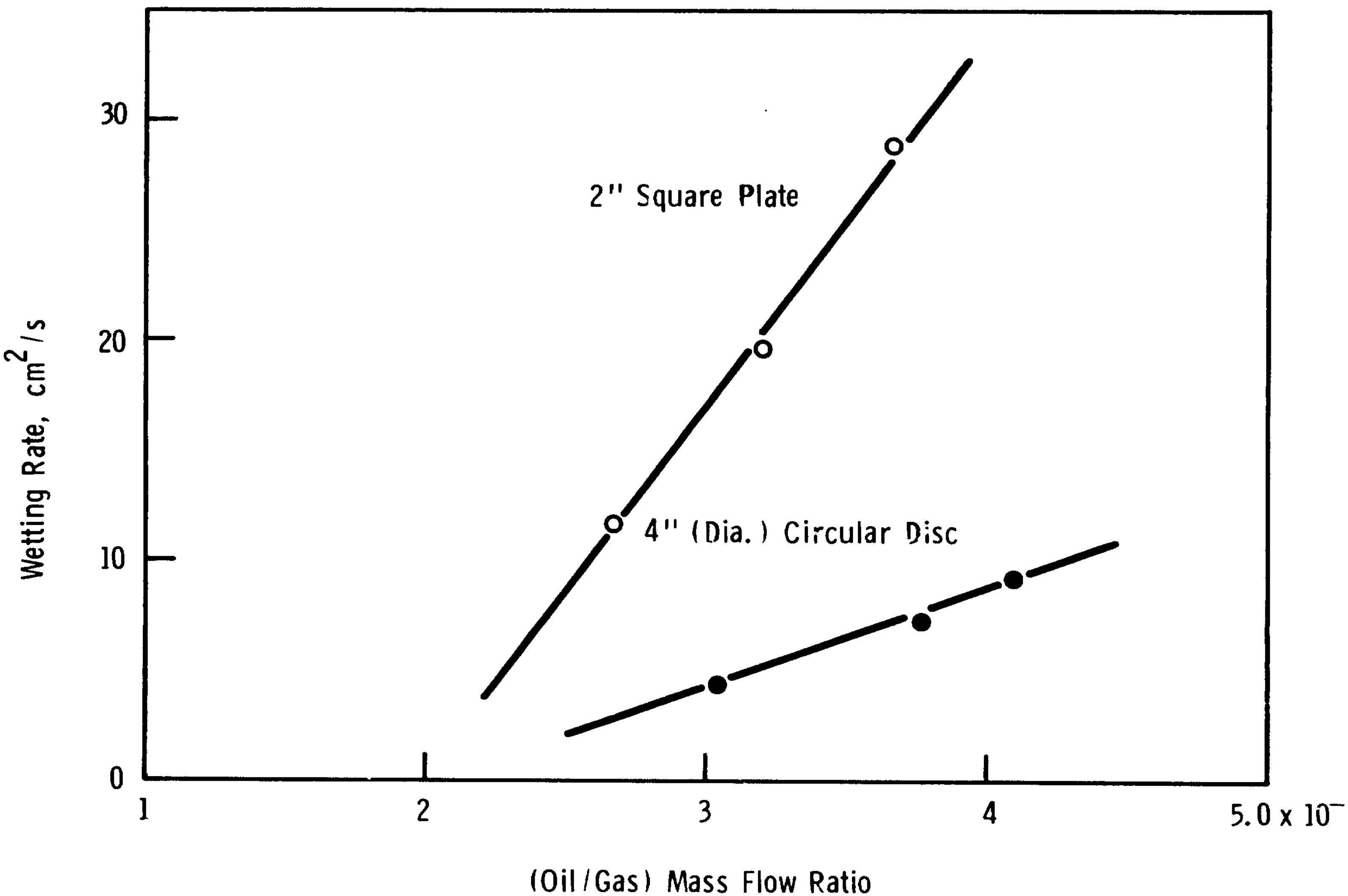

should be 2:1 (2" square plate : 4" circular plate), assuming that thickness of thin lubricant films spreading on the plates is identical; however, the ratio taken from the experimental results is about 3.2:1. This difference in the predicted and experimentally determined ratios of specific wetting rates for the two test plates may be explained in part by the geometric differences between the square and circular plates. In addition, the effective impactor size of the 4" circular test plate actually is close to 6" (15.24 cm) because of a one-inch (2.54 cm) band of insulation surrounding the test plate. A possible difference in the evaporation losses of thin lubricant films spreading on the two plates also may be a contributing factor.

The importance of (oil/gas) mass flow ratio can be demonstrated at dynamic as well as static disc conditions. In Figure 5, wetting rates of XRM 109 F are plotted as a function of (oil/gas) mass flow ratio at angular velocities of 0, 52, and 312 rad/s [the corresponding values of $(N_{Re})_\omega$ are 0, 3.9×10^3, and 23.2×10^3]. With increasing (oil/gas) mass flow ratios, the wetting rates, once again, increase linearly in all cases at varying slopes, indicating that the wettabilities of XRM 109 F under these test conditions are strongly dependent on angular velocity. To illustrate this behavior, the specific wetting rates, which are determined from the slopes of the linear relations presented in Figure 5, are compared below at different angular velocities:

Angular Velocity (rad/s)	Specific Wetting Rate (cm^2/s/mass flow ratio) $\times 10^{-3}$
0	5.3
52	12.0
312	16.0

It is clear from the above table that for a unit (oil/gas) mass flow ratio, the angular velocity has a pronounced effect on wetting rate.

(3) Effect of Angular Velocity

Discussion in the preceding section has indicated important effects of angular velocity on wetting rate. In order to facilitate discussion of these effects, the wetting rates for XRM 109 F at 600°F (589°K) with varying angular velocities of 0, 26, 52, 104, and 312 rad/s, are shown in Figure 6. Gas flow rates used are 3, 4, and 5 cfm (1.4×10^{-3}, 1.9×10^{-3}, and 2.4×10^{-3} m^3/s). In a similar manner, the wetting rates at 700 and 800°F (644 and 700°K), constructed from Appendix C-3, are presented in Figures 7 and 8, respectively. The wetting rates at gas flow rates of 4 and 5 cfm (1.9×10^{-3} and 2.4×10^{-3} m^3/s) increase sharply, as anticipated, with increasing

Figure 5

WETTING RATES OF XRM 109 F AS A FUNCTION OF (OIL/GAS) MASS FLOW RATIO AT DIFFERENT ANGULAR VELOCITY

$(N_{Re})_\omega = \frac{\omega r^2 \rho_g}{\mu_g}$

○ 0
△ 3.9×10^3
● 23.2×10^3

T_W : 600 °F (589 °K)

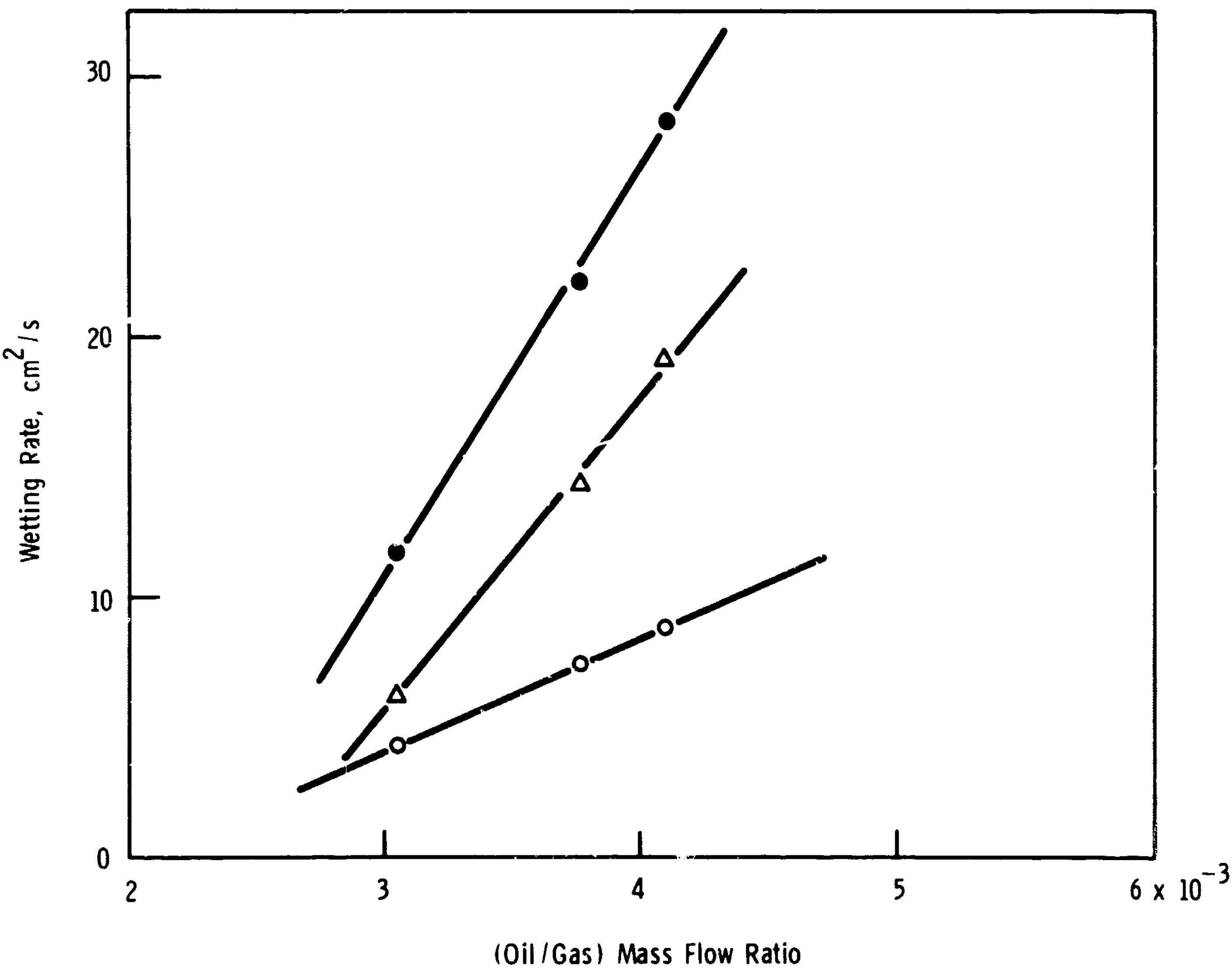

Figure 6

WETTING RATES OF XRM 109 F AS A FUNCTION OF ANGULAR VELOCITY AT 600°F (589°K)

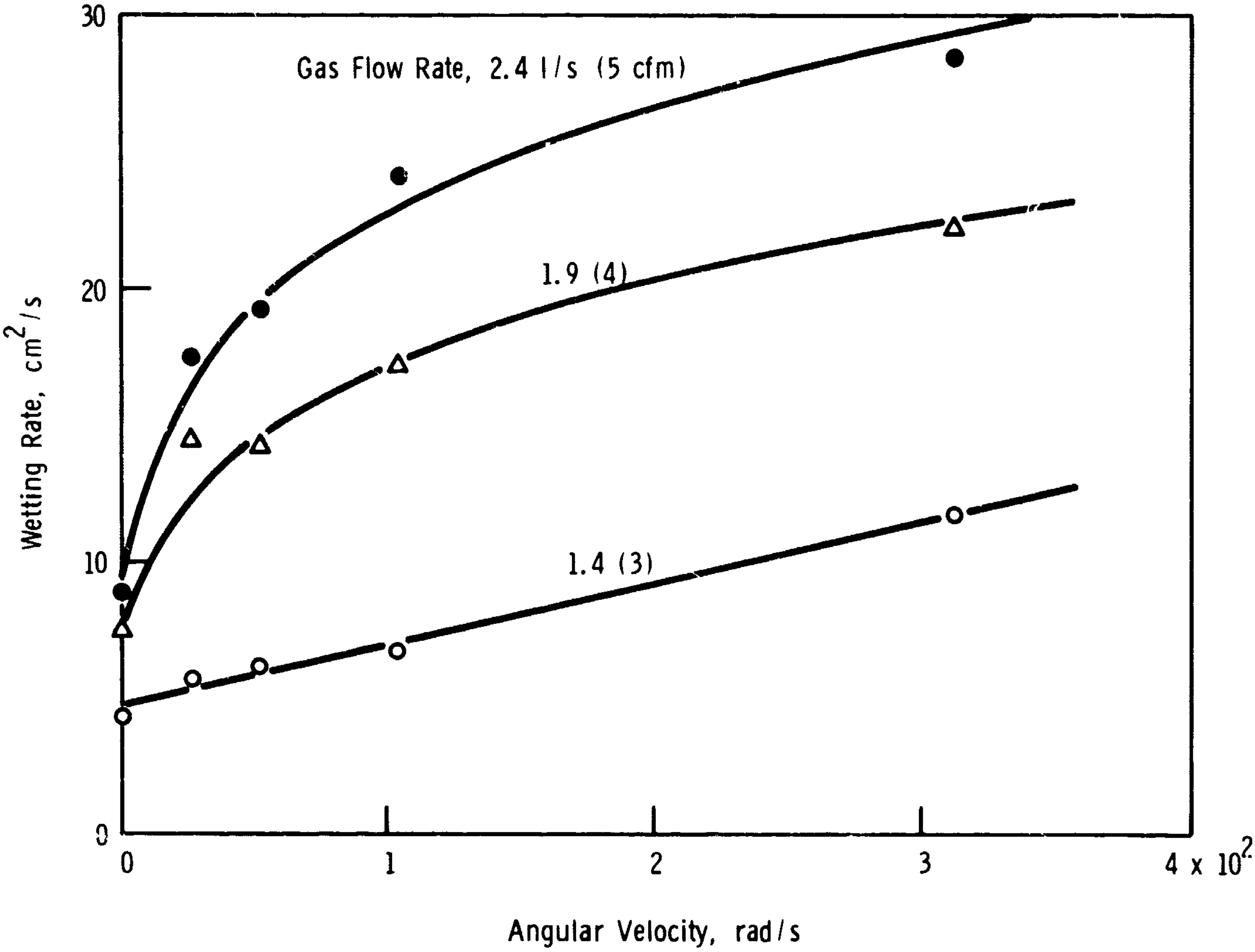

Figure 7

WETTING RATES OF XRM 109 F AS A FUNCTION OF ANGULAR VELOCITY AT 700°F (644°K)

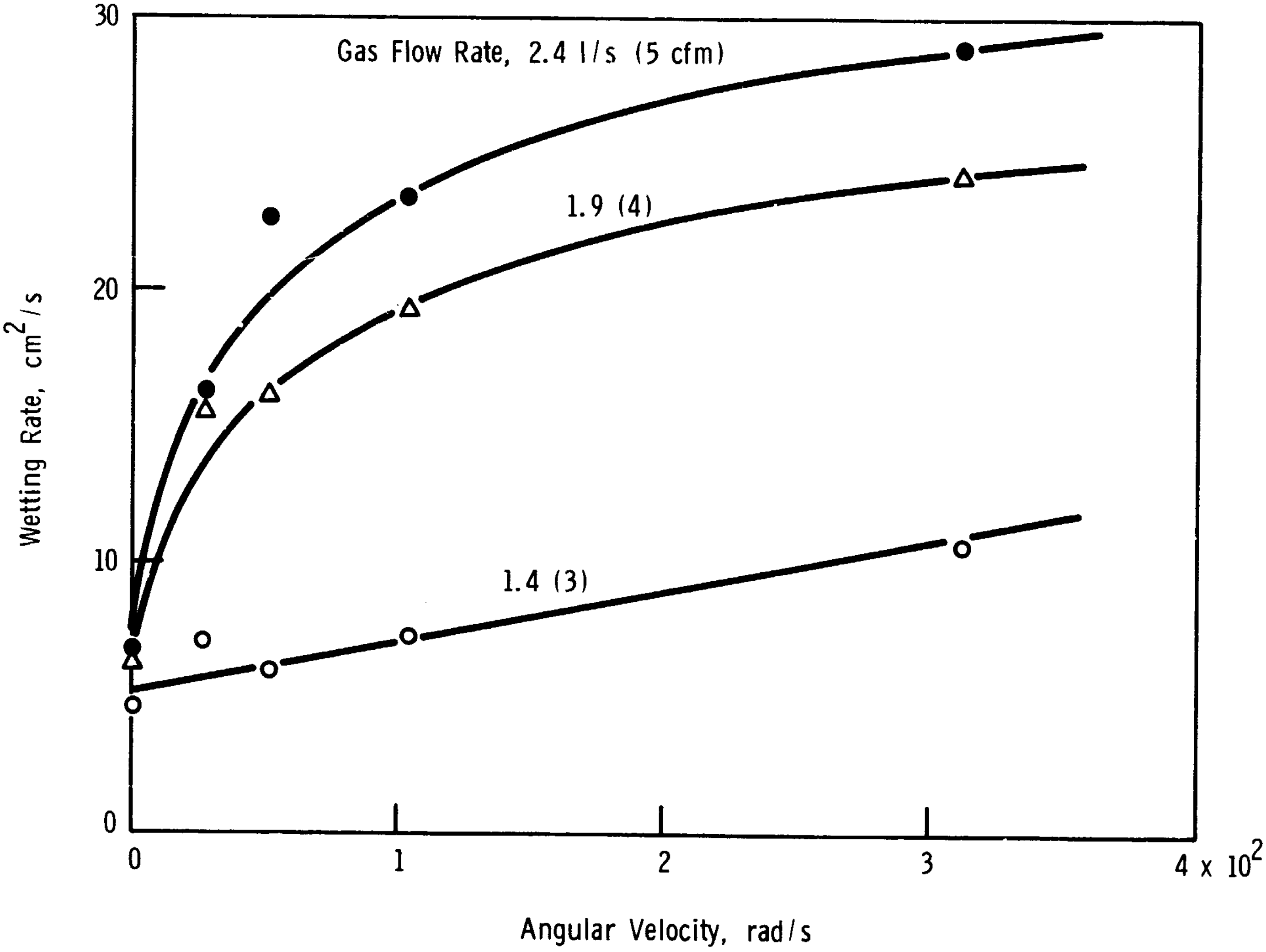

RE

Figure 8

WETTING RATES OF XRM 109 F AS A FUNCTION OF ANGULAR VELOCITY AT 800°F (700°K)

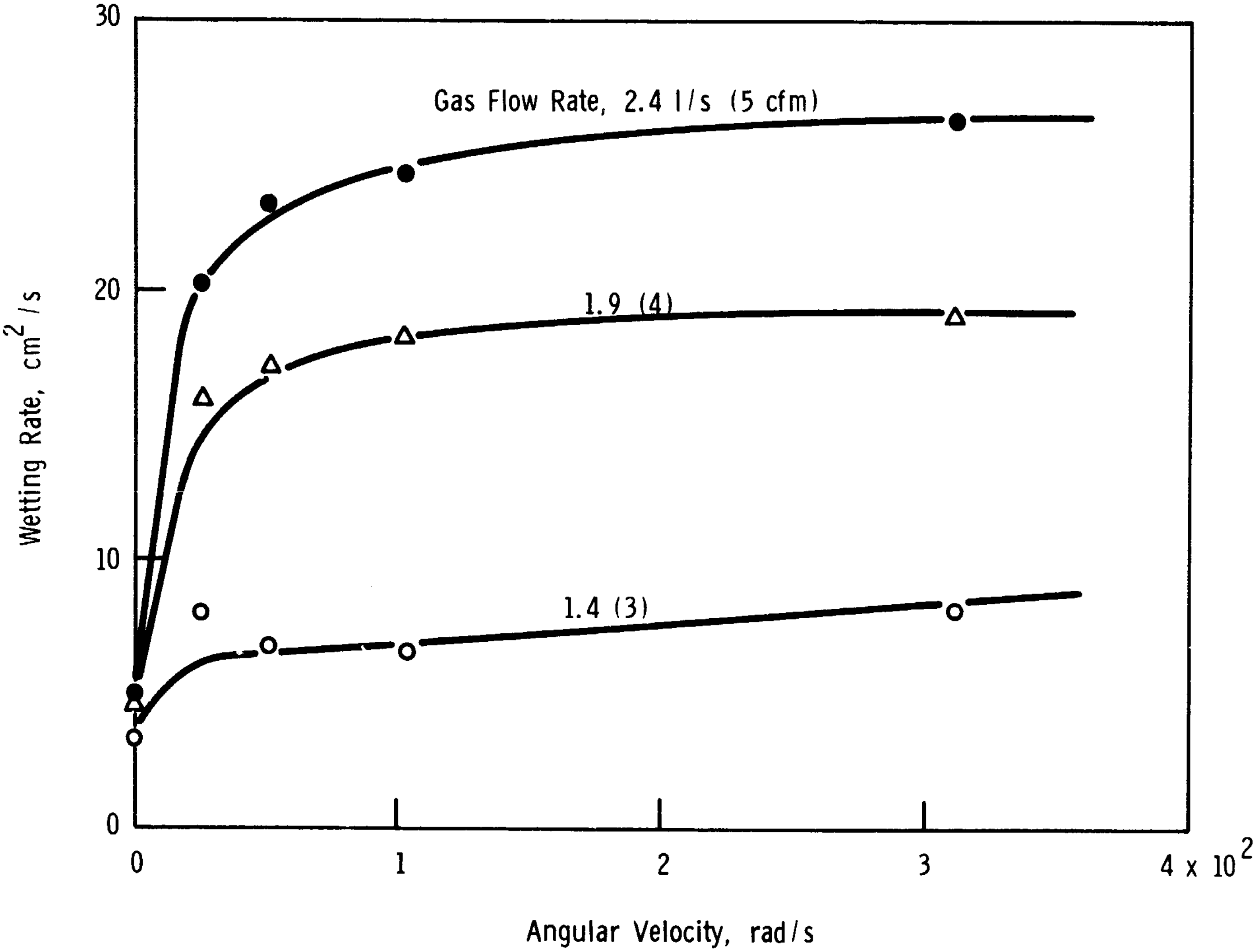

angular velocity; but the rates of increases in wetting rate in terms of angular velocity gradually diminish. It is also noted from Figure 6 that when the disc rotates at angular velocities of 312 rad/s or higher, the wetting rates for XRM 109 F in the present test apparatus seem to have only a slight dependence on angular velocity. Hence, efforts to further increase the wetting rate of the fluid by increasing angular velocity may be impractical. The wetting rates at 3 cfm (1.4×10^{-3} m^3/s) also show little influence of angular velocity, suggesting that the amount of fluid accumulated on the disc is too limited to be greatly influenced by either the interfacial shear generated by the gas stream along the disc or the action of centrifugal forces created by the rotating disc. Instead, the flow of lubricant film may be principally controlled by the fundamental properties of the lubricant film. This type of behavior is more apparent when the wetting rate data at 800°F (700°K), shown in Figure 8, are analyzed. Here, the wetting rates at 4 and 5 cfm (1.9×10^{-3} and 2.4×10^{-3} m^3/s) increase markedly with angular velocity up to 52 rad/s, beyond which they show practically no further change despite an additional 6-fold increase in angular velocity. This suggests the conclusion that when the specific flow rate of lubricant drops to the disc is limited, then the wetting rate is affected by angular velocity of the disc only up to a certain point, beyond which the rate is no longer a function of the action of centrifugal forces.

The data discussed thus far have not indicated whether the increase in wetting rate with angular velocity may be attributed either to an increase in the specific flow rate of lubricant drops or to the decrease in lubricant film thickness. To investigate this aspect of angular velocity effects, and to analyze these effects in terms of the surface radial velocity and thickness of a thin lubricant film, we determined the specific flow rates of lubricant drops to the disc. From these specific flow rates, the mean surface velocities and thicknesses of lubricant films were calculated. The determinations of the specific flow rates of lubricant drops to the disc were made with a cascade impactor technique, described in our previous work (2), at a spray distance of 1 in. (2.54 cm). Calculations of the surface radial velocities and thicknesses were made with the use of the following equations:

For the average (log-mean) surface velocity

$$\langle \bar{u}_r \rangle = \frac{1}{r_2 - r_1} \int_{r_1}^{r_2} u(r)\,dr = \frac{(dA/dt)}{2\pi \left\{ \dfrac{r_2 - r_1}{\log\left(\frac{r_2}{r_1}\right)} \right\}} \tag{9}$$

For the film thickness

$$\delta = \frac{\Gamma}{\rho_\ell \langle \bar{u} \rangle} \tag{10}$$

where $\langle\bar{u}\rangle = \langle\bar{u}_r\rangle/2$. In derivations of these equations, it is assumed that the temperature of the lubricant film is in equilibrium with the disc temperature, and that no lubricant is lost through evaporation. The value of density at 600°F (589°K) is extrapolated by taking a straight line relation, even though the validity of this type of extrapolation to this temperature is in doubt.

The results listed in Table 1, calculated from the wetting rate data for XRM 109 F at a disc temperature of 600°F (589°K), reveal that mean surface velocity increases with increasing angular velocity and gas flow rate. The tabulated results also show that the specific flow rate of lubricant drops to the disc increases with increasing gas flow rate, but not with increasing angular velocity. This finding suggests that an increase in angular velocity may improve the wetting rate of a lubricant not by increasing specific flow rate, but by increasing mean surface velocity through the action of centrifugal forces at the free interface. An increase in wetting rate by this means is, of course, brought about at the expense of lubricant film thickness. It is clearly demonstrated in Table 1 that the calculated film thicknesses decrease with increasing angular velocity.

Since the velocity distribution of a lubricant film is expressed in mathematical form for the case of laminar film flow motivated by interfacial shear and the action of centrifugal forces [refer to Equations (1) and (2)], it is of interest to compare these relations in a limited way with existing experimental data. To do so, the surface velocities of lubricant films, from Table 1, are plotted in Figure 9 against angular velocity at gas flow rates of 3, 4, and 5 cfm (1.4×10^{-3}, 1.9×10^{-3}, and 2.4×10^{-3} m^3/s). Keeping in mind that the surface velocities plotted are motivated only by rotation of the disc, it is evident from Figure 9 that the surface velocity induced by the action of centrifugal forces, as expected, increases with increasing angular velocity. But, it is somewhat surprising to find, at angular velocities ranging from 0 to 312 rad/s the increases in surface velocity with respect to angular velocity are considerably lower than those predicted by Equation (2). For convenience in comparing the experimental data with the theoretical, the mean surface velocities of lubricant films at the gas flow rate of 4 cfm (1.9×10^{-3} m^3/s) are chosen for discussion. Here, the experimental mean surface velocity, represented as a straight line in Figure 9, may be expressed in the form of

$$\langle\bar{u}_r\rangle = 3.2 + 0.92\left(\omega\right)^{1/3} \tag{11}$$

whereas the theoretical surface velocity, predicted by Equation (2) is related to the angular velocity by

Table 1

Surface Velocity and Thickness of Thin Lubricant Film at a Disc Temperature of 600°F (589°K)

Item	Run No.	Gas Flow Rate	Rat of Oil-Mist Output	Angular Velocity	Wetting Rate	Mean Surface Velocity	Specific Flow Rate	Lubricant Film Thickness
		$(m^3/s) \times 10^3$ @ 40 N/cm^2 & 366°K	$(cm^3/s) \times 10^2$	(rad/s)	(cm^2/s)	$(cm/s) \times 10'$	$(g/cm - s) \times 10^4$	(μm)
1	XRM 15-1	1.4 (3 cfm)	2.0	0	4.4	1.9	2.2	33.6
2	XRM 16-1	1.4	2.0	26	5.7	2.5	1.9	22.0
3	XRM 17-1	1.4	2.0	52	6.2	2.7	2.0	21.5
4	XRM 17-2	1.4	2.0	104	7.1	3.1	1.9	17.8
5	XRM 20-5	1.4	2.0	312	11.8	5.1	2.4	13.7
6	XRM 15-2	1.9 (4 cfm)	3.3	0	7.5	3.2	5.5	50.0
7	XRM 16-2	1.9	3.3	26	14.5	6.2	5.2	24.3
8	XRM 16-5	1.9	3.3	52	14.3	6.2	5.4	25.2
9	XRM 17-3	1.9	3.3	104	17.2	7.4	5.3	20.8
10	XRM 21-1	1.9	3.3	312	22.2	9.6	5.2	15.7
11	XRM 15-3	2.4 (5 cfm)	4.3	0	8.8	3.8	5.8	44.3
12	XRM 16-3	2.4	4.3	26	17.5	7.5	6.0	24.2
13	XRM 16-4	2.4	4.3	52	19.2	8.3	6.1	21.8
14	XRM 17-4	2.4	4.3	104	24.2	10.2	6.3	17.9
15	XRM 21-2	2.4	4.3	312	28.4	12.2	6.2	14.7

Test Conditions - Generator Temp.: 200°F (366°K)
Spray Nozzle: No. 1 (4.34 mm orifice dia.)
Disc Size: 10.2 cm dia.
Lubricant: XRM 109 F

Figure 9

EFFECT OF ANGULAR VELOCITY
ON MEAN SURFACE VELOCITY OF LUBRICANT FILM

Lubricant : XRM 109 F
T_W : 600 °F (589 °K)

Gas Flow Rate, $(m^3/s) \times 10^3$

○ 1.4 (3 cfm)
△ 1.9 (4)
● 2.4 (5)

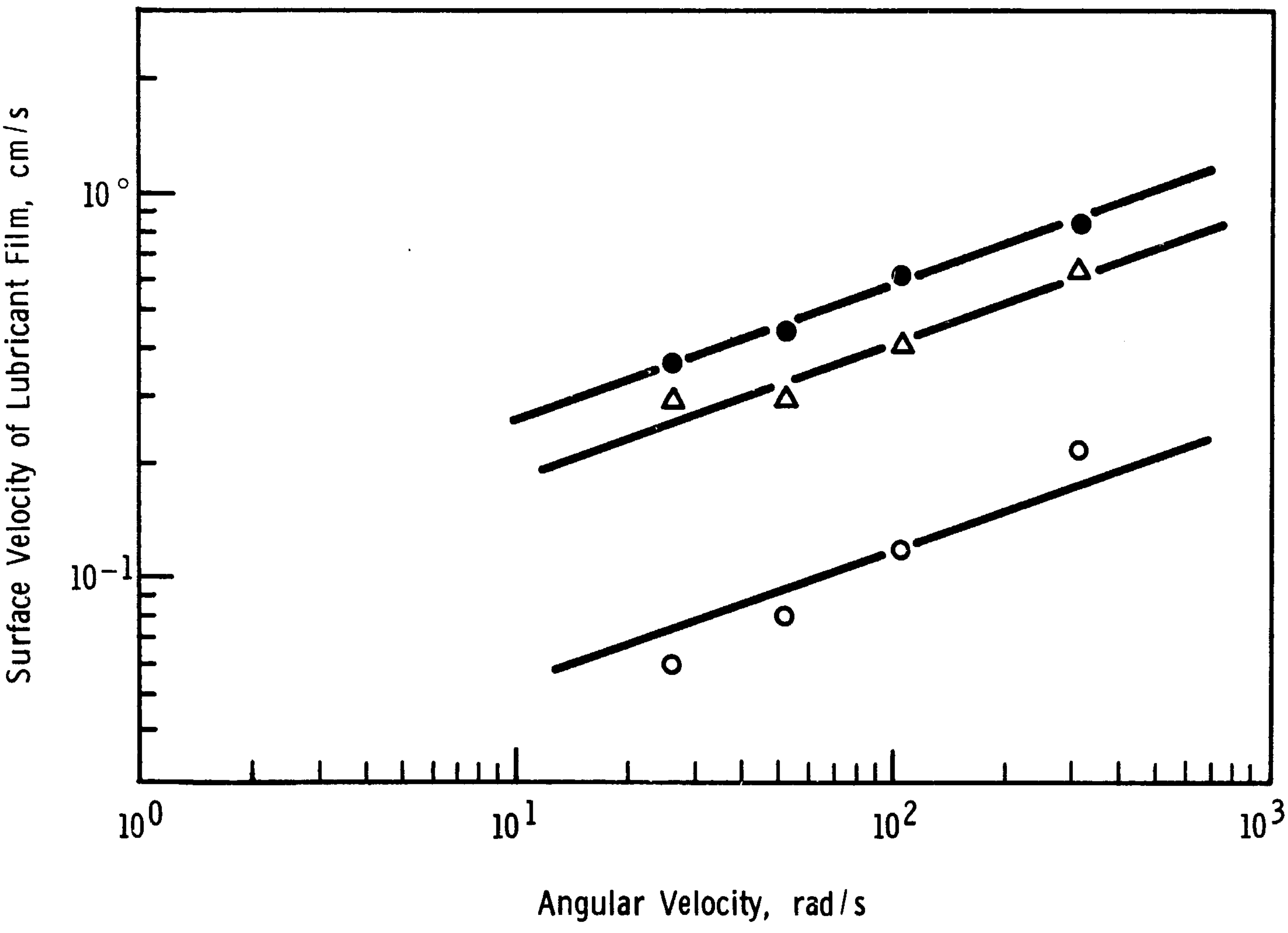

$$\langle \bar{u}_r \rangle = a + b(\omega)^{2/3} \tag{12}$$

where $a = \left(\frac{\tau_i \delta}{2\mu_\ell}\right)$

$$b = \left[\left(\frac{V}{2\pi r}\right)^2 \frac{\rho_\ell}{3\mu_\ell}\right]^{1/3}$$

Of particular interest is the higher exponential value of angular velocity for Equation (12) than for Equation (11). This implies that the effect of angular velocity on surface velocity is more apparent in the theoretical equation than in the experimental. While the reason for the difference is not evident from this study, evaporative loss from the thin lubricant film may be a factor. Of course, the validities of the assumptions made in deriving the equations may be open to question inasmuch as the lubricant films studied seem to be much thinner than for laminar flow of hydrodynamic boundary layers, on which the derivation is based. Obviously, a more extensive experimental study is needed to resolve these questions.

c. Heat Transfer Studies

Heat transfer properties of gas- and microfog-jets impinging normal to a heated rotating disc were studied under various test conditions with a convergent nozzle (4.34 mm orifice diameter) at entrance pressure up to 82 psia (56 N/cm^2).

Test results, reporting total heat fluxes at different conditions, are listed in Appendix D-3 with other pertinent data. Also included are the heat transfer rates estimated from calibration data of the heat flux transducer and the corresponding coefficients calculated by using Equation (5).

In discussing the test results summarized in Appendix D-3, the heat transfer coefficient and its corresponding Nusselt number, $(hD_o/kg)_f$, are used interchangeably. The Nusselt number was evaluated at the arithmetic average of the disc surface and bulk temperatures (often referred to as the film temperature), and with a characteristic heat transfer path of length D_o; whereas the mass-flow Reynolds number, $(D_oG/\mu_g)_b$, was evaluated at bulk temperatures. In addition, the rotational Reynolds number, $(\omega Ro^2\rho_g/\mu_g)$, was calculated at a maximum circumferential velocity of ωRo. Using these terms as references, discussion of the heat transfer data will be based only on significant factors which may play an important role in microfog lubrication, instead of specific experimental runs.

(1) General Comments

In heat transfer studies with the present apparatus, the total electrical-energy input to the heated disc and the electrical feedbacks from a heat flux transducer and thermocouples were made through a brush-ring assembly, as illustrated in Attachment 3, Appendix B. We were initially concerned with the fact that the added junctions for these electrical circuits, particularly for the heat flux transducer, may introduce a considerable error to the studies. Preliminary surface cooling studies with nitrogen gas jets, after calibrating the L&N Speedomax G recording potentiometer and the heat flux transducer (principle and method of calibrating the heat flux transducer are described in Appendices D-1 and D-2), showed that the electrical resistance of the brush-ring assembly was relatively small compared to that of the transducer electrical circuit. This small electrical resistance added to that of the transducer was satisfactorily stable once the rings and brushes had been fitted carefully. But, when the disc was heated to 800°F (700°K) and rotated at 104 rad/s or higher, the brush-ring assembly appeared to introduce error in the total output of the transducer, showing a considerable oscillation in the recording potentiometer. The maximum oscillation was, however, less than 0.6 mv and, in such cases, an arithmetic mean value was reported. All in all, the studies indicated that the transducer, with a heat flux range to 10 $Btu/ft^2 \cdot s$ (11.35 W/cm^2), performed reasonably well, and its sensitivity was satisfactory. The running time required for the transducer to reach a steady-state condition was approximately 30 seconds for each test.

After continuous satisfactory use for one month, the transducer appeared to gradually lose its sensitivity because of the extended exposure to severe environment, although its manufacturer had claimed a longer life. When it was apparent that the transducer was no longer accurate enough to be used for heat transfer study, it was replaced with a new one which was, of course, calibrated as described in Appendix D-2. Some heat transfer runs were repeated with the new transducer, and agreement between pairs of repeated data was, in general, excellent.

The gradual loss of transducer sensitivity is believed to be caused by surface oxidation of the very fine wires used in the transducer's electrical circuits and by heat stresses, both in time changing resistance of the circuits. Deterioration of the heat transfer medium inserted in the transducer also may be a contributing factor. Hence, improved life in a high-temperature environment probably could be gained by better sealing of the transducer under vacuum.

Another concern during the heat transfer studies was temperature control of the disc surface and of the microfog (or nitrogen gas) jets impinging on the disc. Average temperature variations of the test plate from the desired temperature in most cases were less than ±10°F (5.5°K), except for the runs at 800°F (700°K). Total plate temperatures at high gas flow rates dropped sharply by about 50°F (27.8°K). In such cases, it was felt that the source of heat energy (1,000 Watt Calrod heater) to the disc was not quite of sufficient capacity to maintain the disc temperature constant because of the comparatively long time required to establish a steady-state condition with the heat flux transducer. As the heater aged, its response to the controller was more erratic and the rate of heat input to the disc was slower, resulting in a non-isothermal disc surface and, consequently, test data of less certainty. In minimizing the errors caused by these difficulties, the total electrical energy input to the disc heater was deliberately raised just before introducing the desired gas or microfog stream to the disc surface so that the added heat energy compensated for the anticipated temperature drop. This operation was essentially a trial-and-error process aided by immediately preceding experience with the test apparatus, and, therefore, no general rule was applied for a given test condition.

The temperature control of the microfog jets impinging on the heated disc was, for this study, a matter of greater importance and complexity, and thus became the subject of much serious attention. As described in Appendix A, the jets were in all cases heated to 200°F (366°K), unless otherwise specified. Their temperature was controlled by manually regulating the voltage to a 600 W line heater in a transporting pipe ahead of the microfog generator. The system was originally designed for wetting rate studies for which accurate temperature control of the gas stream is less important. As a result of this, the temperatures of the gas stream to the microfog generator varied somewhat more than desired for some of the heat transfer tests, depending upon gas flow rates and the times required to bring the entire system to a steady-state condition.

Another factor to be considered in the present heat transfer study is the effect of wall proximity on heat transfer. In usual applications of impinging jets for cooling, jets at room temperature are generally used, so that the entrainment of surrounding gas does not affect their temperature. For this simple case the mean effective temperature difference is proportional (or in some cases equal) to the overall temperature difference between the hot surface and the incoming jet. In the case of cooling applications where a hot surface is situated in a heated test chamber, as in this project, matters are usually more complicated in that cool jets discharge into a hotter atmosphere so that turbulent mixing, both before and after impingement, raises their temperature. Accordingly, for a given overall temperature difference the effective temperature difference for heat transfer now depends on not only the gas flow rates, but also the geometry of the system. Therefore, when the overall temperature difference is used in calculating heat transfer coefficients with Equation (5), the temperature effects on the heat transfer coefficients, as will be later discussed, are uncertain. This uncertainty in the heat transfer data probably is the greatest weakness of the present study, although the prime objective is to determine the heat transfer rates of impinging gas jets with and without the presence of microfog particles, where only the differences in heat transfer rates are important. Nevertheless, in cooling applications entailing large temperature differences between the heated surface and impinging jets, it may be desirable to make adjustment for evaluating the mean effective temperature difference and to allow for the variation of the transport properties of gas across the boundary layer around the surface.

Recognizing the importance of ΔT, $(T_w - T_\infty)$, used for calculations, some efforts were made to measure temperatures of the microfog stream leaving the disc surface after impingement, with a thermocouple placed 1/2 inch off the disc in the radial direction, but in the same plane. The measured temperatures under different chamber and disc temperatures varied considerably depending on microfog flow rates and the times required to bring the system to a desired condition. Average ranges of the temperature variation were as follows:

Disc and Chamber (°F)	Microfog Off-Stream (°F)
600 (589°K)	420 (489°K) – 480 (522°K)
700 (644°K)	460 (511°K) – 540 (555°K)
800 (700°K)	500 (533°K) – 610 (594°K)

As indicated in the above table, the widest variation, 110°F (61°K), occurred at 800°F (700°K). In general, although the temperature data scattered markedly, increasing the microfog flow rate to the disc surface decreased the temperature of the microfog off-stream for a given overall temperature difference between the disc and the incoming microfog jets.

(2) Heat Transfer of Microfog Jets

Increasing emphasis is currently being directed toward reducing the size and weight of heat transfer equipment used in advanced turbine engines. A segment of this study is focussed on the possible increase in heat transfer from a rotating disc when microfog lubricant drops are present in a nitrogen gas stream. Lubricant drops suspended in the gas stream as illustrated in Figure 2 may increase heat transfer from the disc surface by sensible heating and by evaporation of the lubricant in the thin film. (The lubricant and gas boundary layers shown in Figure 2 are disproportionately large.) This cooling technique is closely related to modern cooling applications such as film, ablation, and transpiration cooling.

In order to study the heat transfer from a geometrically simple dynamic surface exposed to an incoming microfog jet, and to determine the relative contributions to total heat transfer of sensible heating of the lubricant film, evaporative convection cooling by the lubricant film-microfog stream, and forced convection cooling by the microfog stream alone, the heat transfer rates of microfog jets of four different lubricants were determined. These experiments employed the No. 1 nozzle (4.54 mm orifice diameter, spray distance ratio of 5.85) at a variety of test conditions as specified in Task IV. The four test lubricants used were:

- XRM 109 F
- FN 2961
- XRM 109 F plus 10% (by weight) Kendall super-refined paraffinic heavy resin (~20,000 SUS at 100°F)
- XRM 109 F blended with 10% (by weight) XRM 126 A

The total heat fluxes and the calculated coefficients of the microfog jets are summarized in Appendix D-3, which also includes the total heat fluxes of gas jets alone. A typical experimental run, shown in Figure 10, is illustrated by the data for XRM 109 F with a disc heated to 700°F (644°K) and rotating at 104 rad/s, and a gas flow rate of 4 cfm (1.9×10^{-3} m^3/s). In general, similar curves represent the test data for other runs.

The values of ΔQ were estimated from the experimental data by using the following equation:

$$\Delta Q = Q_f - Q_g \tag{13}$$

$$\cong (Q_f - Q_g) - \underbrace{(Q''_g - Q'_g)}_{\text{a correction factor for the reference line}} \tag{14}$$

In determining the total heat fluxes of microfog jets, we found that a reference heat flux with 1 cfm (0.5×10^{-3} m^3/s) varied measurably from run to run. Thus, a correction factor was introduced in Equation (13) to adjust this variation. The correction factor can, of course, be eliminated if the reference line for each run is established at the same point. Since this would require a long and

Figure 10

A TYPICAL EXPERIMENTAL
RUN OF HEAT TRANSFER STUDY

Angular Velocity : 104 rad/s
Gas Flow Rate : 1.9×10^{-3} m^3/s
Disc Temp. : 644 °K
Gas Temp. : 366 °K

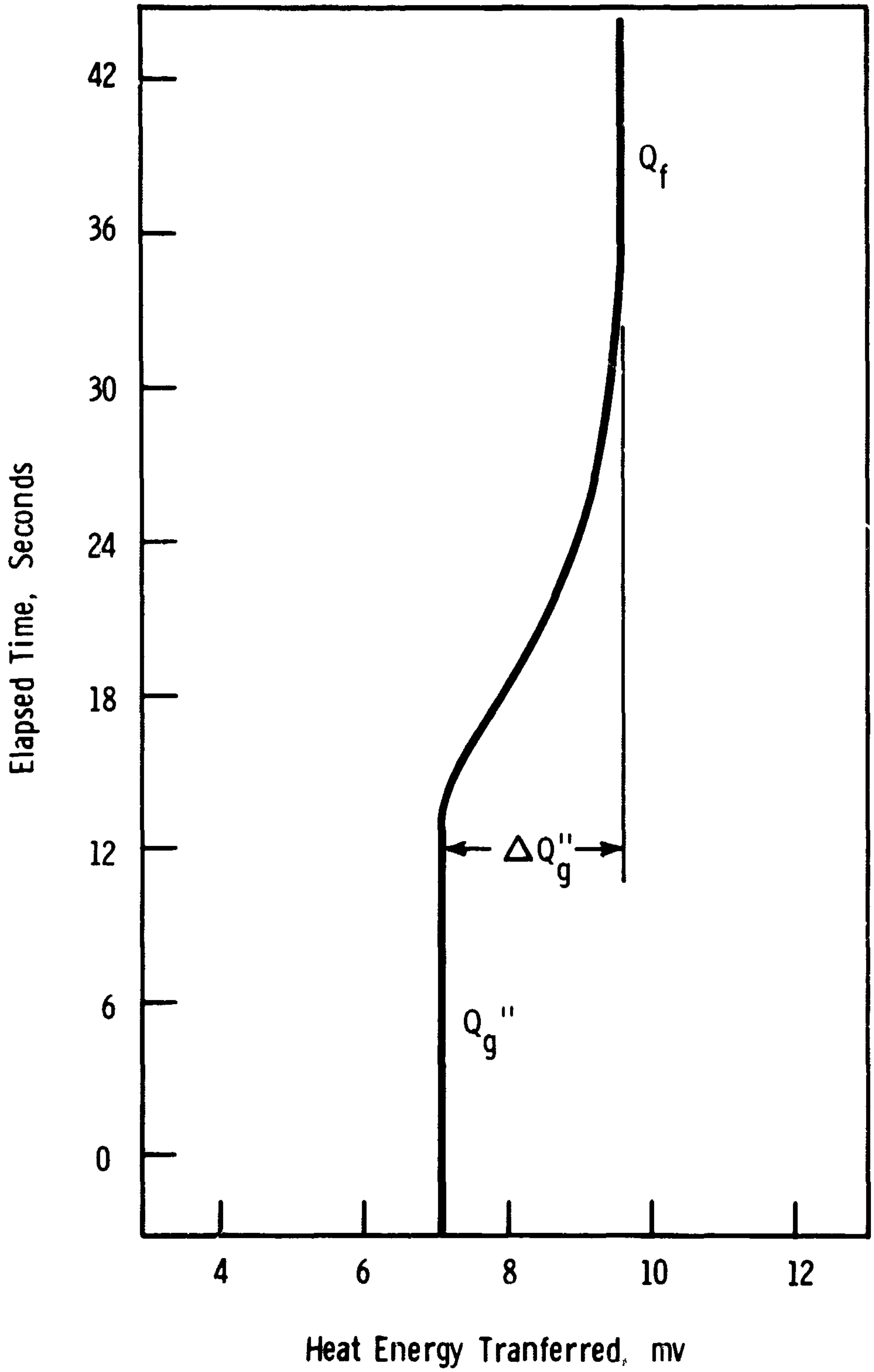

tedious effort, Equation (14) is used in this work as a matter of convenience.

(a) Effect of (Oil/Gas) Mass Flow Ratio

Since three gas flow rates to the microfog generator are employed in the heat transfer study, it is of interest to investigate how the rates of oil-mist output affect the heat transfer coefficients of a test lubricant at different angular velocities. When discussing the effect of (oil/gas) mass flow ratio on heat transfer coefficients for a microfog (two-phase) flow, we must recognize that impaction efficiency, which depends principally on impaction velocity and particle size, has important effects on heat transfer because of its strong influence on wetting rate. Heat transfer must, therefore, be considered in conjunction with wetting rate, which has already been treated in Task III.

Results representing the effect of (oil/gas) mass flow ratio on the heat transfer coefficient, summarized from the experimental data obtained for XRM 109 F at 600°F (589°K), are shown in Figure 11. It can be seen from Figure 11 that the heat transfer coefficient increases slightly with increasing (oil/gas) mass flow ratio for all the angular velocities tested. The increase seems to be more apparent at a rotational Reynolds number of 2.32×10^4 than one of 0 (a stationary heated disc). In analyzing the results presented in Figure 11, it must be remembered that the increase in wetting rate probably is caused by increases in two variables - the rate of oil-mist output and gas flow rate - which, with the generator used in this study, are interrelated so that one variable cannot be changed without affecting the other. For this reason, it is extremely difficult to study independently the effect of (oil/gas) mass flow ratio on a heat transfer coefficient. However, since the reference lines for the heat transfer study have been established with only nitrogen gas flow under various test conditions, it is at least possible to determine the effect of microfog particles by simply comparing the heat transfer data of microfog jets with those of nitrogen gas jets. The comparison is listed in Table 2.

Comparison of the data in Table 2 indicates that the heat transfer rates with microfog jets of XRM 109 F improve about 4 to 8% over the corresponding cases for nitrogen gas jets only. However, because these improvements are not only small, but also often masked in experimental error, it is difficult to draw any quantitative conclusion from this comparison. It is somewhat unexpected that the heated disc is cooled mostly by the gas stream at the interface (lubricant film-gas stream), and only a little by the thin lubricant films spreading over the disc. Following Equation (6), it may be concluded from this comparison that the sensible heat absorbed by the thin lubricant films and the heat carried away by evaporative cooling are relatively small, as compared with the heat taken away by the gas

Figure 11

NUSSELT NUMBER VERSUS (OIL/GAS) MASS FLOW RATIO
AT DIFFERENT ANGULAR VELOCITY

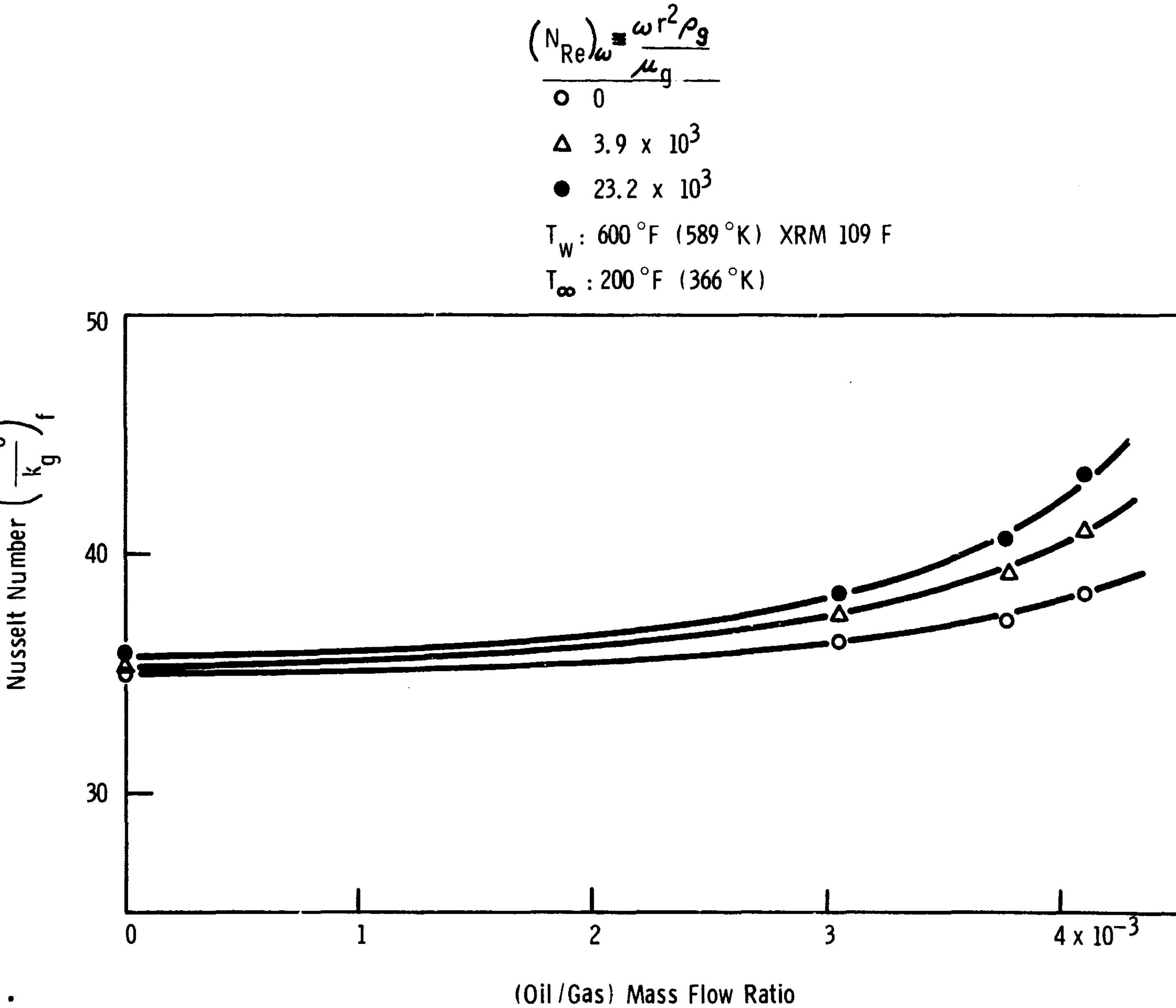

Table 2

Heat Transfer Rates of XRM 109 F Microfog Jets Impinging on a Heated Rotating Disc

Item	Run No.	Gas Flow Rate	Rate of Oil-Mist Output	Angular Velocity	Temperature (°F)		Heat Energy Transferred (mv)			Total Heat Flux	Heat Transfer Coefficient
		(m^3/s) x 10^3 @ 40 N/cm^2 & 366°K	(cm^3/s) x 10^2	(rad/s)	T_w	T_∞	Q_f	Q_E	ΔQ	(Btu/hr - ft^2) x 10^{-3}	(Btu/hr - ft^2 - °F)
1	TX-1	1.4 (3 cfm)	2.0	0	600 (589°K)	200 (366°K)	8.6	8.3	0.3	23.2 (74 x 10^3 W/m^2)	58.0 (333 W/m^2 - °K)
2	TX-2	1.9 (4)	3.3	0	600	195	8.9	8.5	0.4	24.0	59.3
3	TX-3	2.4 (5)	4.3	0	600	195	9.2	8.7	0.5	24.8	6.13
4	TX-4	1.4	2.0	26	600	200	8.8	8.4	0.4	23.8	59.5
5	TX-5	1.9	3.3	26	600	200	8.9	8.5	0.4	24.0	60.0
6	TX-6	2.4	4.3	26	600	210	9.3	8.7	0.6	25.1	64.4
7	TX-7	1.4	2.0	52	600	220	8.4	8.0	0.4	22.7	59.8
8	TX-8	1.9	3.3	52	600	220	8.8	8.3	0.5	23.8	62.6
9	TX-9	2.4	4.3	52	600	220	9.2	8.6	0.6	24.8	65.3
10	TX-1C	1.4	2.0	104	600	210	8.3	8.0	0.3	22.4	57.5
11	TX-11	1.9	3.3	104	600	210	8.5	8.2	0.3	22.9	58.8
12	TX-12	2.4	4.3	104	600	210	9.3	8.7	0.6	25.1	64.4

Oil Temperature: 200°F (366°K)
Nozzle: No. 1 (4.34 mm orifice dia.)

stream, and that the microfog stream of non-impinging lubricant drops seems to behave as a single gas-phase stream.

Before the present investigation, it was considered possible that a thin lubricant film on the heated disc, or lubricant vapor at the interface of the disc surface and the lubricant film, might act as an insulating barrier to heat transfer from the disc surface. Contrary to this view, the experimental data revealed no case where the heat transfer rate actually was reduced by the presence of the thin lubricant film. The data of Table 2 also suggest there is little difference in thermal properties between microfog and gas streams. To verify this, determination of their thermal properties should be made experimentally.

Although we discussed here only the results of XRM 109 F at 600°F (589°K), the test results of other lubricants indicated, to a greater or lesser degree, a similar general trend in the effects of (oil/gas) mass flow ratio on heat transfer.

(b) Comparison of the Heat Transfer Coefficients of Microfog Jets With Different Test Lubricants

For convenience in comparing the heat transfer rates of the four test lubricants having similar properties except for viscosity, their heat transfer coefficients, obtained with a disc heated to 600°F (589°K) and rotating at 104 rad/s, have been chosen for discussion. Results including heat transfer rates, constructed from Appendix D-3, are presented in Table 3.

The heat transfer studies with the four lubricants, in general, show that the heat transfer coefficients of microfog jets seem to vary little from those of nitrogen gas jets. This, once again, affirms the conclusion drawn in the preceeding section that the heat taken away by the thin lubricant films formed in the impinging region of the disc is relatively small in comparison with the heat transferred by the gas stream. This can be more clearly demonstrated when the heat transfer results of XRM 109 F microfog jets are compared with the corresponding cases of FN 2961, as shown in the series of test runs represented by Items (1) to (6). These test data illustrate the effect of particle concentration (the number of microfog particles suspended in the gas stream) on heat transfer. It is somewhat surprising to find that the increased particle concentration for FN 2961 has little effect on the heat transfer coefficient. This seems to contradict the earlier conclusion that the heat transfer coefficient tends to increase with increase of the (oil/gas) mass flow ratio. For example, when Items (1) and (4) are compared, the rates of oil-mist output with a gas flow rate to the generator of 3 cfm (1.4×10^{-3} m^3/s) are 2.0×10^{-2} cm^3/s for XRM 109 F and 3.5×10^{-2} cm^3/s for FN 2961; but the corresponding heat transfer coefficients are 57.5 Btu/hr·ft^2·°F (325 W/m^2·°K) for

Table 3

Heat Transfer Rates of Various Microfog Lubricant Jets Impinging on a Heated Rotating Disc

Item	Test Fluid	Gas Flow Rate	Rate of Oil-Mist Output	Temperature °F		Heat Energy Transferred	Total Heat Flux	Heat Transfer Coefficient
		$(m^3/s) \times 10^{+3}$ @ 40 N/cm^2 & 366°K	$(cm^3/s) \times 10^2$	T_w	T_∞	(mv)	$(Btu/hr - ft^2) \times 10^{-3}$	$(Btu/hr - ft^2 - °F)$
	XRM 109 F							
1		1.4 (3 cfm)	2.0	600	210	8.3	22.4 (72×10^3 W/m^2)	57.5 (330 W/m^2 - °
2		1.9 (4)	3.3	600	210	8.5	22.9	58.8
3		2.4 (5)	4.3	600	210	9.3	25.1	64.4
	FN 2961							
4		1.4	3.5	600	200	8.5	23.0	57.5
5		1.9	7.0	600	190	8.8	23.8	58.0
6		2.4	9.0	600	210	9.2	24.8	63.6
	XRM 109 F + 10% Kendall Paraffinic Resin (~ 20,000 SUS)							
7		1.4	2.5	610	210	8.5	23.0	57.5
8		1.9	4.0	605	210	8.8	23.8	60.3
9		2.4	5.1	595	205	9.1	24.6	63.1
	XRM 109 F + 10% XRM 126 A							
10		1.4	2.3	610	230	8.4	22.7	59.7
11		1.9	3.8	600	210	8.9	24.0	61.5
12		2.4	4.7	590	195	9.1	24.6	62.3

Angular Velocity: 104 rad/s
Spacing Ratio: 5.85

both cases. In a similar manner, the gas flow rates of 4 and 5 cfm (1.9×10^{-3} and 2.4×10^{-3} m^3/s) can be compared to show the insensitivity of heat transfer coefficients to variations of particle concentration.

This insensitivity may be related to the thermal boundary layers formed in the region of lubricant particle impingement. According to this view, although it has not been experimentally confirmed, the flow characteristics of thin lubricant films in the impinging zone are still mainly controlled by impinging jets so that thickness of the films may vary little despite a considerable increase in the amount of lubricant accumulated on the disc. Such a situation may only exist because of difference in viscosity between FN 2961 and XRM 109 F. This may account, at least in part, for the insensitivity of heat transfer coefficients. In connection with this line of reasoning, the great difference in the wetting patterns of the two lubricants must be recalled. XRM 109 F forms a continuous lubricant film, while FN 2961 has a streaky wetting pattern, as illustrated briefly in Section b(1) and in more detail in the previous work (2, 3).

In Table 3, comparison of items (7) to (12) with items (1) to (4) reveals once again that the heat transfer coefficient is unaffected by the presence of added fractions in XRM 109 F. In reference to Items (7) to (9), it has been demonstrated that addition of 10% Kendall paraffinic resin (~20,000 SUS) to XRM 109 F enhances the wettability of the fluid (3), as well as its performance in a full-scale bearing test rig (4). Thus the purpose of the heat transfer test was to show whether this improved wettability has any effect on heat transfer. It is apparent from Table 3 that the Kendall paraffinic resin neither enhances nor hinders heat transfer in this series of tests. Items (10) to (12) were aimed to study the effect of transpirational cooling by deliberately adding a light fraction of similar chemical composition (XRM 126 A) to XRM 109 F. Evaporation of the fraction during wetting was thought to be potentially capable of increasing heat transfer rates from the disc surface (5, 6). However, no effect on the heat transfer coefficients was observed. Although the reason for this behavior is unknown at present, it could be related to the thermal boundary layer concept in the manner already explained; i.e., the amount of lubricant accumulated on the disc in these experiments may still be insufficient to form a lubricant film thick enough to influence the thermal boundary layer. A detailed investigation of the system would, therefore, be of great interest.

Similar comparisons showing that lubricants of different properties in microfog jets have little influence on heat transfer at other temperatures and angular velocities of the disc can be made by selecting appropriate data from Appendix C-3 in relation to gas flow rates and rates of oil-mist output.

Analysis of the heat transfer data for microfog jets of four different lubricants impinging on a heated rotating disc via a convergent nozzle at entrance pressures up to 82 psia (55 N/cm^2), can be summarized as follows: The local heat transfer coefficient is mostly controlled by the gas phase alone. Only the impinging lubricant drops contriubte to cooling, and their effect is slight. The microfog stream of non-impinging drops behaves as a single gas phase stream. It is also found that the local heat transfer coefficient is affected little by other factors tested, such as angular velocity of the disc, the rate of oil-mist output, and physical properties of the test lubricants, most notably viscosity. Insensitivity of the heat transfer coefficient toward variation of these factors suggests that the thermal boundary layer thickness is largely unaffected by them, although their effect on the momentum boundary layer may be significant. This insensitivity may be related to thinness of the lubricant films formed by impingement of microfog lubricant drops; i.e., the films may be so thin that they have almost no effect on the thermal boundary layer. Thus, in order to utilize microfog nozzle flows for more effective cooling, it appears essential that the microfog concentration in the gas stream be increased by perhaps 10-fold or more over the microfogs produced by the current generator. Hence, of prime importance in developing a successful microfog lubricant application system for high-temperature lubrication is the development of a microfog generator capable of delivering much higher (oil/gas) mass flow ratios than currently available commercial generators. The second requirement is the proper system design for a specific application. Research endeavors in these areas are urgently needed for successful adaptation of microfog lubrication systems to advanced turbine engines.

(c) Significance of the Temperature Difference Between Hot Surface and Cooling Stream

To aid discussion of temperature effects on heat transfer coefficients, the total heat transfer rates from a rotating disc at various temperature differences between the disc and the cooling stream, and the corresponding heat transfer coefficients, are presented in Figures 12 and 13, respectively. For convenience in illustrating the temperature difference effects, the (oil/gas) mass flow ratios of 3.05×10^{-3} and 4.1×10^{-3}, which correspond to gas flow rates of 3 and 5 (2.4×10^{-3} m^3/s) cfm to the microfog generator, were selected from Appendix D-3. Furthermore, the heat transfer results are plotted indiscriminately with regard to angular velocity of the disc because the angular velocity at these mass flow ratios seems to have little effect on the heat transfer coefficient. The heat transfer data for nitrogen gas at a forced inflow of 1 cfm (0.5×10^{-3} m^3/s) are also included in these plots. It is noted from Figures 12 and 13 that at any given gas flow rate, an increase in temperature difference between the disc surface and the bulk

Figure 12

HEAT TRANSFER RATES FROM A
ROTATING DISC AT VARIOUS TEMPERATURE DIFFERENCES

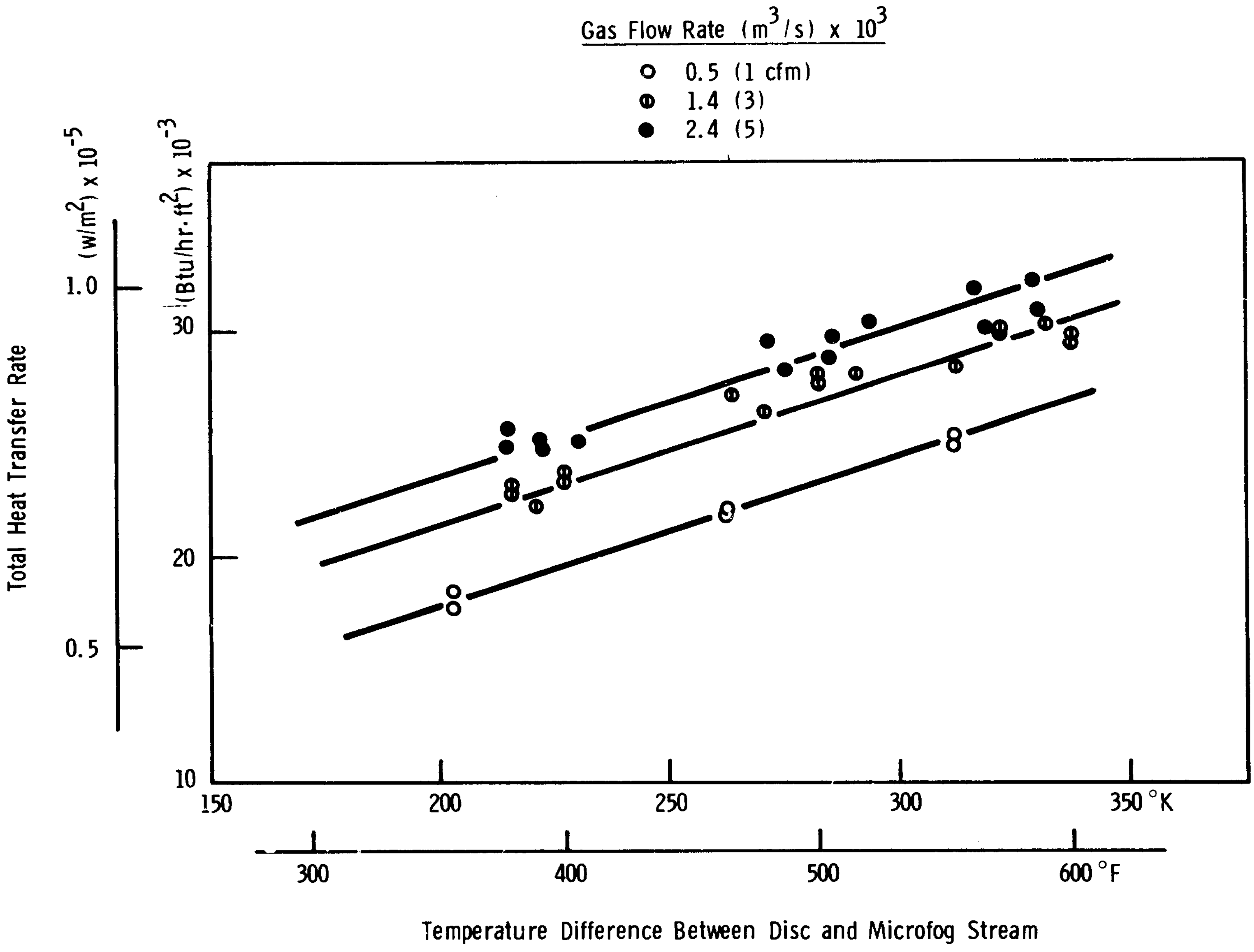

Figure 13

VARIATION OF HEAT TRANSFER COEFFICIENTS WITH TEMPERATURE DIFFERENCES

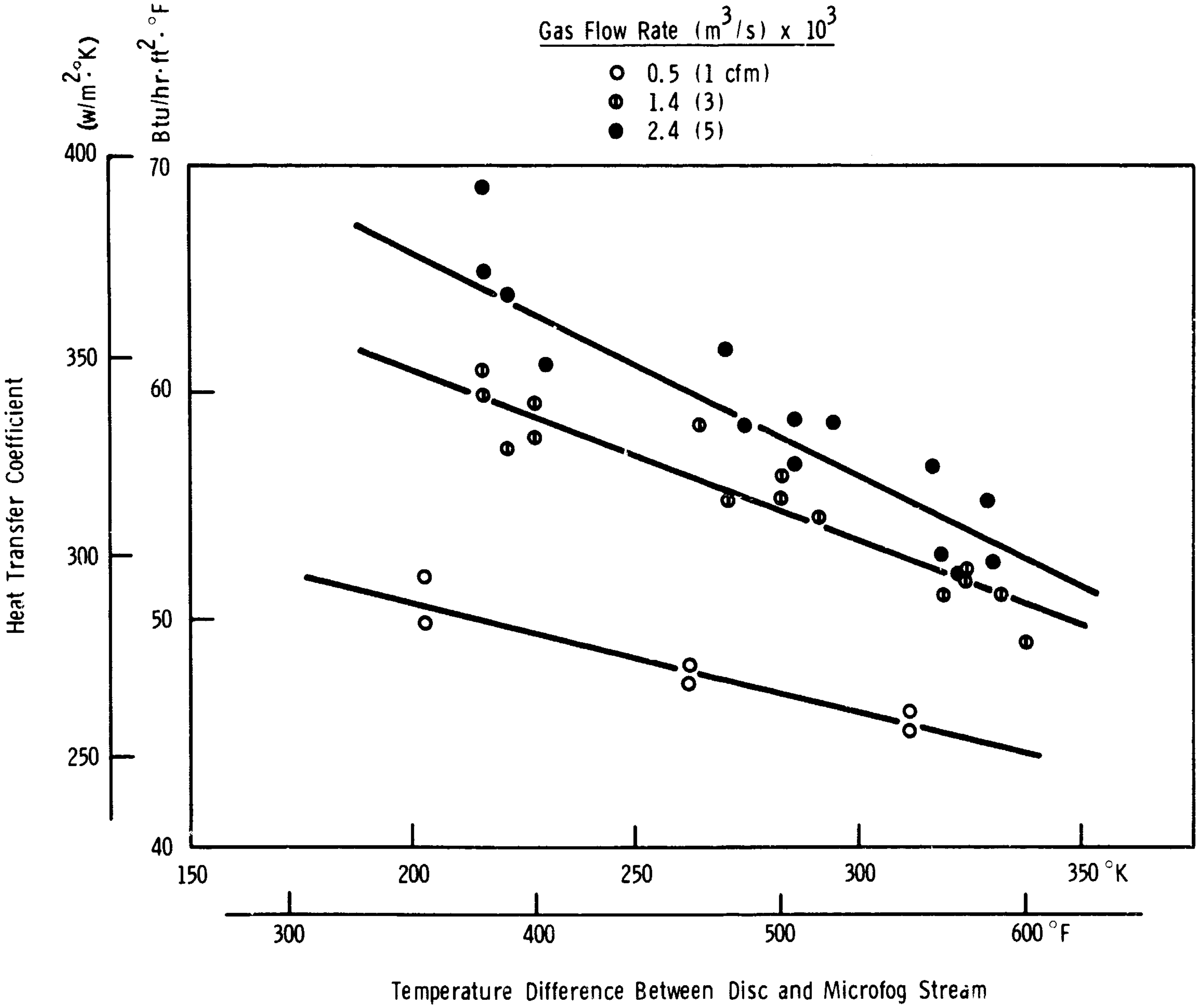

microfog stream causes an increase in the total amount of heat transferred from the disc and a decrease in the corresponding heat transfer coefficient. However, an increasing mass flow ratio at any given temperature difference seems to increase both the heat transfer rate and its corresponding coefficient, although the heat transfer data with microfog flow are more scattered than those with nitrogen gas flow.

When a stationary heated solid surface is exposed to a still gas, it increases the natural convection of gas flow as a result of density differences in the fluid, and the intensity of this circulation is proportional to ΔT, $(T_W - T_\infty)$; but when it is subjected to a forced inflow of gas, the forced convective heat transfer is only a function of the intensity of the gas movement. For this reason, a significant finding of this work is the decrease of the heat transfer coefficient with increasing ΔT. This observed phenomenon may be the result of reverse transition, defined as a transition from a turbulent flow to a laminar flow. Based on the phenomenon of reverse transition, the unexpected decrease in heat transfer coefficient may be explained as follows: when the temperature difference between disc surface and cooling microfog stream is sufficiently large, the actions of large heat transfer rates cause significant transport property variations, especially in the viscosity of fluids within the thermal boundary layers formed about the disc surface (7). The viscosity increases with increasing ΔT such that the Reynolds number decreases sufficiently for the flow to undergo a transition from turbulent to laminar, which in turn decreases the forced convective heat transfer coefficient.

A careful analysis of Figure 13 suggests that since the heat transfer coefficient is still a function of ΔT, the fluid motion characteristic of natural convection may be significant. Unlike the conventional natural convection, the fluid motion appears to adversely affect the coefficient. Owing to lack of information about the flow characteristics of fluids near the rotating disc, it is extremely difficult to present a more positive explanation for the decrease in heat transfer coefficient. In addition, the task is made still more formidable by the formation of thin lubricant films spreading on the disc surface by the impingement of microfog particles.

For any given system with a large temperature difference, one may expect that the reverse transition from turbulent to laminar flow in a cooling fluid causes a sharp decrease in the heat energy transfer to the cooling fluid and a consequent rise in the surface temperature. The effects of the large temperature difference can also be expected to be reversed for the heating of the surface by the fluid because the temperature and velocity distributions react to the large temperature difference in opposite ways when the direction of the heat flow is changed.

A question of particular interest is that of lubricant film temperature, T_i; i.e., do the lubricant drops immediately heat up to the disc temperature upon impingement? Although no effort was made to determine the film temperature, it can be said from a further analysis of the general conclusions drawn in the preceding section, with the aid of Equation (6), that the temperature of a thin lubricant film spreading on a heated rotating disc probably is very close to that of the disc surface. This finding can be more clearly demonstrated by combining Equations (5) and (6):

$$h = \frac{\int_0^{\delta} 2\pi r \rho_\ell u_r Cp_1 (T_i - T_\infty) dZ + M_\ell \{Cp_1 (T_B - T_\infty) + \lambda\} + WCp_2 (T_G - T_\infty)}{A_2 (T_w - T_\infty)} \tag{15}$$

Recognizing that $WCp_2(T_G - T_\infty) = hg\ A_3(T_i - T_\infty)$ and that the contributions of sensible and evaporative heat by the lubricant film to the overall heat transfer rates are relatively small, Equation (15) then becomes:

$$h = \frac{hg\ A_3 (T_i - T_\infty)}{A_2 (T_w - T_\infty)} \tag{16}$$

Since $A_2 = A_3$, Equation (16) yields:

$$\frac{h}{hg} = \frac{T_i - T_\infty}{T_w - T_\infty} \tag{17}$$

The experimental results listed in Table 2 have, however, shown that $h \cong hg$, implying that:

$$T_i \cong T_w \tag{18}$$

Equation (18) suggests several interesting points:

- The thin lubricant film formed by microfog particles seems to be heated to the disc temperature immediately upon impingement of the particles.
- The heat transfer coefficient is controlled by gas film resistance at the gas-liquid interface and not at the liquid-solid interface.
- The thermal boundary layer seems to be formed over the lubricant film rather than through the liquid film.

These remarks merely confirm the previous conclusions on the insensitivity of the heat transfer coefficient to the presence of thin lubricant films formed by impinging microfog jets.

(3) Heat Transfer of Nitrogen Gas Jets

When it became evident that the heat transfer coefficient of microfog jets impinging on a heated rotating disc was affected little by different operating variables tested under a variety of conditions as specified in Task IV, heat transfer data for nitrogen gas jets were obtained under more expanded test conditions. This, although not required by the contract, was done to aid discussion of heat transfer phenomena in terms of pertinent factors for the present system, and to gain more knowledge of the heat transfer phenomena for impinging jets.

Accordingly, these heat transfer data for nitrogen gas jets only were obtained under test conditions specified in the contract unless otherwise indicated.

(a) Effect of Gas Flow Rate

In establishing the reference lines for the heat transfer study, the surface cooling rates from a heated rotating disc were measured with only nitrogen gas jets and were reported in Section c(2). Further efforts were made to study the effect of gas flow rate on heat transfer coefficient by extending the surface cooling studies of a heated disc at lower gas flow rates. In this series of experiments the heat transfer rates at the stagnation point and their corresponding heat transfer coefficients were determined with a stationary disc heated to 600°F (589°K), and at a spray distance ratio of 5.85. The gas flow rates used varied from 0 to 4 cfm (1.9×10^{-3} m^3/s), and the pressure of the test chamber, unlike the studies discussed in Section c(2), was maintained at 1 atmosphere (10 N/cm^2) during the experiments.

The experimental and calculated results are listed in Table 4, and are graphically presented in Figure 14 by plotting the Stanton number or heat transfer coefficient versus the mass-flow Reynolds number. The result designated as Item 1 in Table 4 probably represents the natural convective heat transfer for nitrogen gas, which is similar to the Graetz-Nusselt problem. Since no forced inflow is introduced to the disc surface, the corresponding mass-flow Reynolds number cannot be obtained, although there exists the flow of gas generated by the thermal fluxes at the interface. For this reason, the heat transfer result for the case of Item 1 indicated in Figure 14 is based on the value of the heat transfer coefficient, and not on the value of the mass-flow Reynolds number. Also, the gas flow rates reported in Table 4 are corrected for pressure, but the correction does not include the compressibility factor of nitrogen gas at this pressure.

C2

Table 4

Heat Transfer Characteristics of Nitrogen Gas Jets Impinging on a Heated Disc

Item	Run No.	Gas Flow Rate	Temperature, °F		Heat Energy Transferred	Total Heat Flux	Heat Transfer Coefficient	$(N_{Re})_m$	N_{Nu}	N_{St}
		$(m^3/s) \times 10^3$ @ 40 N/cm^2 & 366°K	T_w	T_∞	(mv)	$(Btu/hr - ft^2) \times 10^{-3}$	$(Btu/hr - ft^2 - °F)$	$(D_oG/\mu_g)_B \times 10^{-4}$	$(hD_o/k_g)_f$	$(h/C_pG)_B \times 10^4$
1	X1-1	0	600 (589°K)	140 (333°K)	1.8	4.9 (12.3×10^3 W/m^2)	10.7 (48 W/m^2 - °K)	Free stream	6.8	?
2	X1-2	0.1	600	145	4.0	10.8	23.7	0.5	14.9	56.5
3	X1-3	0.25	600	185	5.3	14.3	34.4	1.2	21.6	32.8
4	X1-4	0.3	595	145	6.4	17.3	38.4	1.4	24.1	30.5
5	X4-1	0.5 (1 cfm)	600	235	6.6	17.8	48.7	2.4	30.5	23.2
6	X4-2	1.0	600	200	8.1	21.9	54.8	4.8	34.4	13.0
7	TX-1	1.4	600	200	8.3	22.4	56.0	7.2	35.1	8.9
8	TX-2	1.9	600	195	8.5	23.0	56.8	9.1	35.6	7.1
9	TX-3	2.4	600	195	8.7	23.5	58.0	11.0	36.4	6.0

Spacing Ratio (Z/D_o): 5.85

Spray Nozzle: No. 1 (4.34 mm dia.)

Angular Velocity: 0 rad/s

Figure 14

HEAT TRANSFER CHARACTERISTICS
OF NITROGEN GAS JETS IMPINGING ON A HEATED DISC

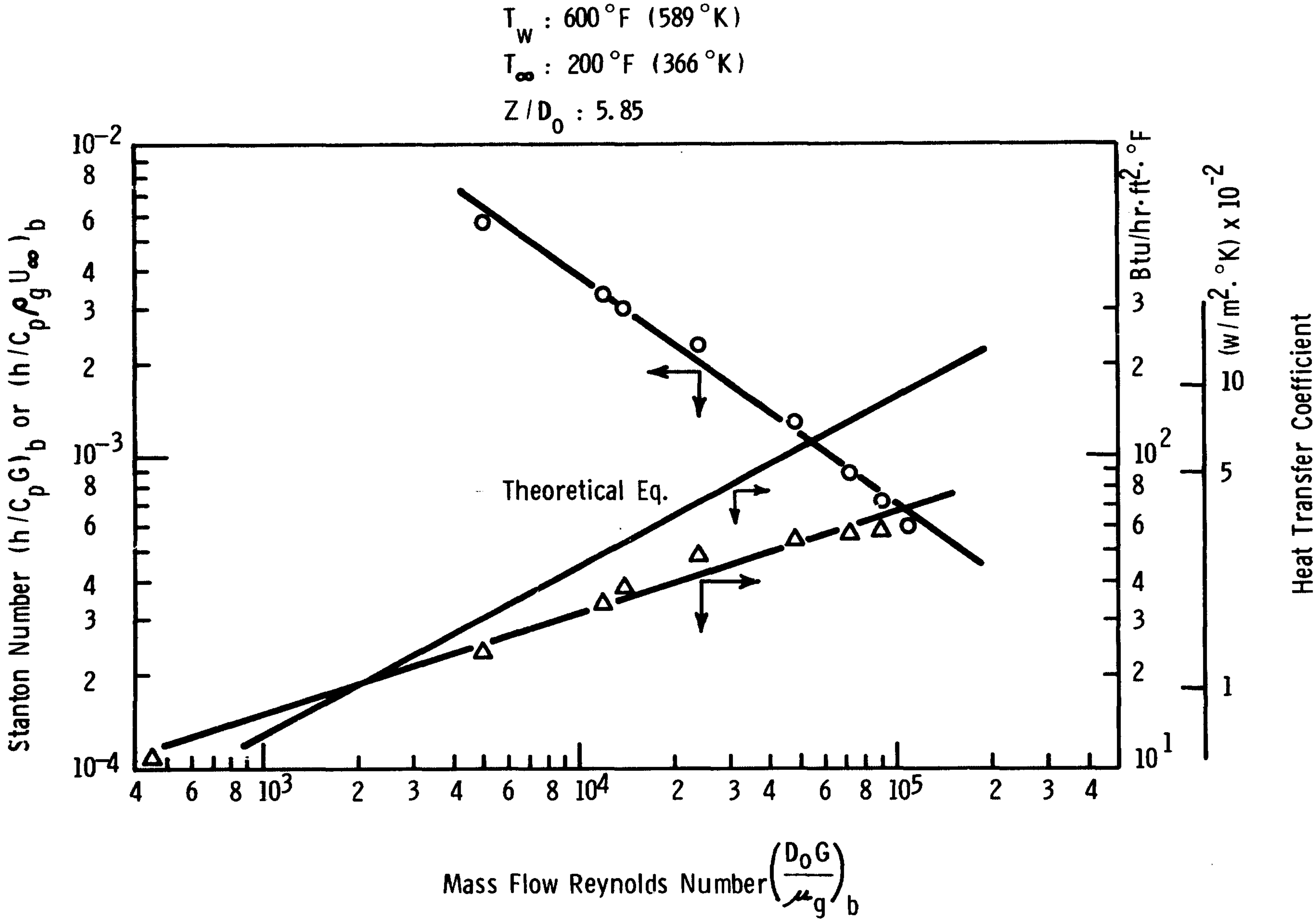

The results presented in Figure 14 clearly demonstrate that the heat transfer coefficient increases with increasing gas flow rate, but not as much as the Reynolds analogy predicts. This can be more clearly seen when these straight lines are expressed:

$$h = 1.5\left(N_{Re}\right)_{m,b}^{1/3} \quad \text{(from the experimental data)} \tag{19}$$

and

$$h = 0.47\left(N_{Re}\right)_{m,b}^{1/2} \quad \text{(from the theoretical treatment)} \tag{20}$$

The reason for the discrepancy in the exponents to the Reynolds number is unclear. The theoretical treatment for the heat transfer coefficient along a flat plate with a laminar boundary layer also reveals that the slope of the generalized surface temperature curve, $(d\Theta/d\eta)_{\eta=o}$, is equal to the Nusselt number divided by the square root of the Reynolds number (8); i.e.:

$$\left(\frac{d\Theta}{d\eta}\right)_{\eta=o} = \frac{N_{Nu}}{\left(N_{Re}\right)_m^{1/2}} \tag{21}$$

where $\Theta = \frac{T - T_\infty}{T_w - T_\infty}$, which signifies the thickness of thermal boundary layer. $(d\Theta/d\eta)_{\eta=o}$ varies only with the Prandtl number and, therefore, for a given system it is a constant. In the light of Equation (21), and from comparison of Equations (19) and (20), the difference in values of $(d\Theta/d\eta)_{\eta=o}$, 1.5 and 0.47, suggests that the thermal boundary layer may be thicker for our system than for the theoretical treatment. This further suggests that the fluid motion characterisitcs of forced convection around the heated disc may be less significant than Equation (21) indicates.

In order to further pursue this line of reasoning for the correlation, the heat transfer data are replotted in the form of the Colburn equation (9), as presented in Figure 14. It may be observed that

$$h \cdot \left(\frac{\pi D^2}{4}\right) \cdot (T_w - T_\infty) = Cp_2 \cdot G\left(\frac{\pi D^2}{4}\right)(T_G - T_\infty) \tag{22}$$

so that the Stanton number

$$\frac{h}{Cp_2 G} = \left(\frac{D_o}{D}\right)^2 \left(\frac{T_G - T_\infty}{T_w - T_\infty}\right) \quad (23)$$

may be evaluated directly from temperature data without determination of any physical properties. As indicated by Equation (23), where values of D_O, D, T_W, and T_∞ are known, as in the present system, the Stanton number can easily be calculated with a simple determination of T_G. This was done for this contract, although the values of T_G were not particularly accurate. As a matter of interest, using the temperature data from Section c(2), the Stanton number at an average outlet temperature of gas of 460°F (511°K) is calculated to be 1.19×10^{-3}, and its corresponding mass-flow Reynolds number from Figure 14 is 5×10^4, which is equivalent to a gas flow rate of 2 cfm (1.0×10^{-3} m^3/s) at 40 N/cm^2 and 366°K. The Stanton number calculated by this method is in fairly good agreement with the experimental, considering the accuracy of temperature measurements with the present apparatus.

Since the Stanton number is defined as the ratio of actual heat transferred to thermal capacity of a fluid, it gives some indication of how effectively heat is transferred from a heated surface by the fluid. It is very interesting to examine this point from Figure 14 by taking some value of the Stanton number. For example, at a mass-flow Reynolds number of 1.0×10^4, the Stanton number is 3.8×10^{-3}, thus suggesting that the efficiency of heat transfer for this particular case may be less than 0.4 percent, which is surprisingly low.

(b) Effect of Angular Velocity

When a heated disc rotates, it develops a "pumping action" or Goerther vortexes, pulling a surrounding fluid toward its surface and thus inducing forced convection heat transfer. The intensity of this fluid movement obviously increases as the angular velocity of the disc increases. By extending von Karman's solution, Wagner (10) first developed an equation for the surface coefficient of heat transfer by convection from a heated plate rotating in still air, and expressed it as follows:

$$h = 0.333\ k_g \left(\frac{\omega \rho_g}{\mu_g}\right)^{1/2} \quad (24)$$

Since his work, the heat transfer phenomena for laminar flow around a rotating disc have been studied in great detail (11, 12, 13), and their coefficient is given in a more general form of

$$h = \text{constant} \cdot k_g \cdot N_{Pr} \cdot \left(\frac{\omega \rho_g}{\mu_g}\right)^{1/2} \quad (25)$$

Even with these studies, when a system involves the more general and practical problem of heat transfer for forced inflows against a rotating disc, Equations (24) and (25) have a limited use, and the problem naturally becomes considerably more complicated. Here, the heat transfer rates are affected not only by induced flow due to rotation, but also by forced inflow. Since these flows compete with each other, the rates, of course, may be predominantly controlled by either the induced flow or the forced inflow depending upon conditions of the system.

According to the theoretical analysis of heat transfer by forced flow against a rotating disc (14), the corresponding heat transfer coefficient can be given by:

$$N_{Nu} = (1 + \chi)^{1/4} \cdot \left(N_{Re}\right)_m^{1/2} \cdot \Theta'(o) \qquad (26)$$

where $\chi \equiv \left(\frac{\omega Ro}{U_\infty}\right)^2$ and $\Theta'(o) = \left[\frac{\partial}{\partial \eta}\left(\frac{T - T_\infty}{T_w - T_\infty}\right)\right]_{\eta=o}$ = constant

Equation (26) clearly shows that the heat transfer coefficient is certainly a function of the mass-flow Reynolds number, and of the ratio of circumferential velocity (ωRo) to free stream velocity, although the contribution of each group to the heat transfer coefficient is considerably different. The computer-aided calculations from the analysis indicate that the values of $N_{Nu} \cdot (N_{Re})_m^{-1/2}$ are unaffected by variation of χ at least up to 5 for air. This means that as long as the values of ($\omega Ro/U_\infty$) do not exceed $\sqrt{5}$, the heat transfer coefficient is controlled mainly by the forced inflow, and little by the induced flow due to rotation.

Inasmuch as the dependence of the heat transfer coefficient on angular velocity predicted by Equation (26) was not confirmed by the heat transfer data presented in Table 2 and Figure 11, an effort was made to determine whether, indeed, the heat transfer coefficient is affected by angular velocity at all.

In studying this aspect of heat transfer phenomena, the heat transfer coefficients of nitrogen gas jets impinging on a disc were determined at angular velocities ranging from 0 to 312 rad/s with the gas flow rates of 1/4, 1/2, and 3 cfm (1.4 x 10^{-3} m^3/s), which are considerably lower than those specified by the contract. The tests were made at a disc temperature of 600°F (589°K) with a fixed spray distance ratio of 5.85.

The test results are summarized in Table 5, and presented in Figure 15 by plotting heat transfer coefficient against angular velocity at different gas flow rates. The heat transfer coefficients actually obtained with a stationary disc are plotted against an angular velocity of 1 rad/s. It is apparent from Figure 15 that the heat transfer coefficient increases slightly with increasing angular velocity at forced inflows of 0.25 and 0.5 cfm (0.2×10^{-3} m^3/s), but the effect of angular velocity on the coefficient virtually vanishes when the forced inflow is further increased to 3 cfm (1.4×10^{-3} m^3/s). At this point, it should be recalled that angular velocity had no effect on the heat transfer coefficient at gas flow rates of 4 and 5 cfm (2.4×10^{-3} m^3/s), as already indicated in Section c(2). From the results illustrated in Figure 15, it may, therefore, be concluded that the free induction flow generated by the angular motion enhances the heat transfer coefficient by promoting gas turbulence at relatively low forced inflow of nitrogen gas, but has negligible influence at sufficiently high forced inflow. Even with forced inflows as low as 0.25 and 0.5 cfm (0.2×10^{-3} m^3/s), Figure 15 demonstrates that the heat transfer coefficient seems to be more influenced by the forced inflow than by the induction flow. This is clearly indicated by the fact that the coefficient is related to the angular velocity by

$$h \propto \omega^{0.13} \tag{27}$$

which indicates quite a low exponential value compared with that of Equation (25). A more detailed study may be required to find the cause of this discrepancy between experimental and theoretical values of the exponent.

Some efforts were also made to determine values of the transition region separating the free induction flow from the forced inflow, which control heat transfer characterisitcs of the system. In order to determine these values, Figure 15 is replotted in a semi-log scale, as shown in Figure 16. Of particular interest are the curves representing the low forced inflows. Examination of the curves in Figures 15 and 16 shows at first the characteristic no effect of an angular velocity which is then followed by a transition regime. In estimating the values of transition region, the joining points of straight line are taken and found to be about 15 and 26 rad/s for forced inflows of 0.25 and 0.5 cfm (0.2×10^{-3} m^3/s), respectively. With higher forced inflows, the joining point may appear at higher angular velocity, although in this series of tests, it is not found at 1 and 3 cfm (1.4×10^{-3} m^3/s).

The values of ($\omega Ro/U_\infty$) at these breaking points are less than 0.1 even with the extreme value of Ro [2 inches (5.08 cm) for this work]. This result, which contrasts with the earlier discussed prediciton of Equation 26, is quite surprising. The theoretical

Table 5

Heat Transfer Characteristics of Nitrogen Gas Jets Impinging on a Heated Rotating Disc

Item	Run No.	Gas Flow Rate (m^3/s) x 10^{-3} @ 40 N/cm^2 & 366°K	Angular Velocity (rad/s)	Temperature, °F T_w	Temperature, °F T_∞	Heat Energy Transferred (mv)	Total Heat Flux (Btu/hr - ft^2) x 10^{-3}	Heat Transfer Coefficient (Btu/hr - ft^2 - °F)
1	X1-2	0.1 (0.25 cfm)	0	600 (589°K)	145 (336°K)	4.0	10.8 (34 x 10^3 W/m^2)	23.7 (134 W/m^2 - °K)
2	X2-1	0.1	15	600	210	3.8	10.3	26.4
3	X2-2	0.1	52	600	220	4.4	11.9	31.3
4	X2-3	0.1	104	600	220	4.7	12.8	33.9
5	X2-4	0.1	208	600	220	5.0	13.4	35.2
6	X1-3	0.25 (0.5 cfm)	0	600	185	5.3	14.3	34.4
7	X3-1	0.25	26	600	185	5.4	14.6	35.2
8	X3-2	0.25	52	600	185	5.7	15.4	37.1
9	X3-3	0.25	104	600	185	6.4	17.3	41.7
10	X3-4	0.25	312	600	185	7.2	19.4	46.8
11	X4-1	0.5 (1 cfm)	0	600	235	6.6	17.8	48.7
12	X4-3	0.5	26	600	245	6.7	18.1	50.1
13	X4-4	0.5	52	600	245	6.8	18.4	51.9
14	X4-5	0.5	104	600	245	6.8	18.4	51.9
15	X5-1	1.4 (3 cfm)	0	600	200	8.3	22.4	56.0
16	X5-2	1.4	26	600	200	8.5	23.0	57.5
17	X5-3	1.4	52	600	220	8.3	22.4	59.0
18	X5-4	1.4	104	600	220	8.0	21.6	57.0
19	X5-5	1.4	312	600	220	8.5	23.0	60.5

Spacing Ratio (Z/D_o): 5.85 (D_o = 4.34 mm)

Figure 15

EFFECT OF ANGULAR VELOCITY
ON HEAT TRANSFER COEFFICIENTS OF NITROGEN
GAS JETS IMPINGING ON A HEATED ROTATING DISC

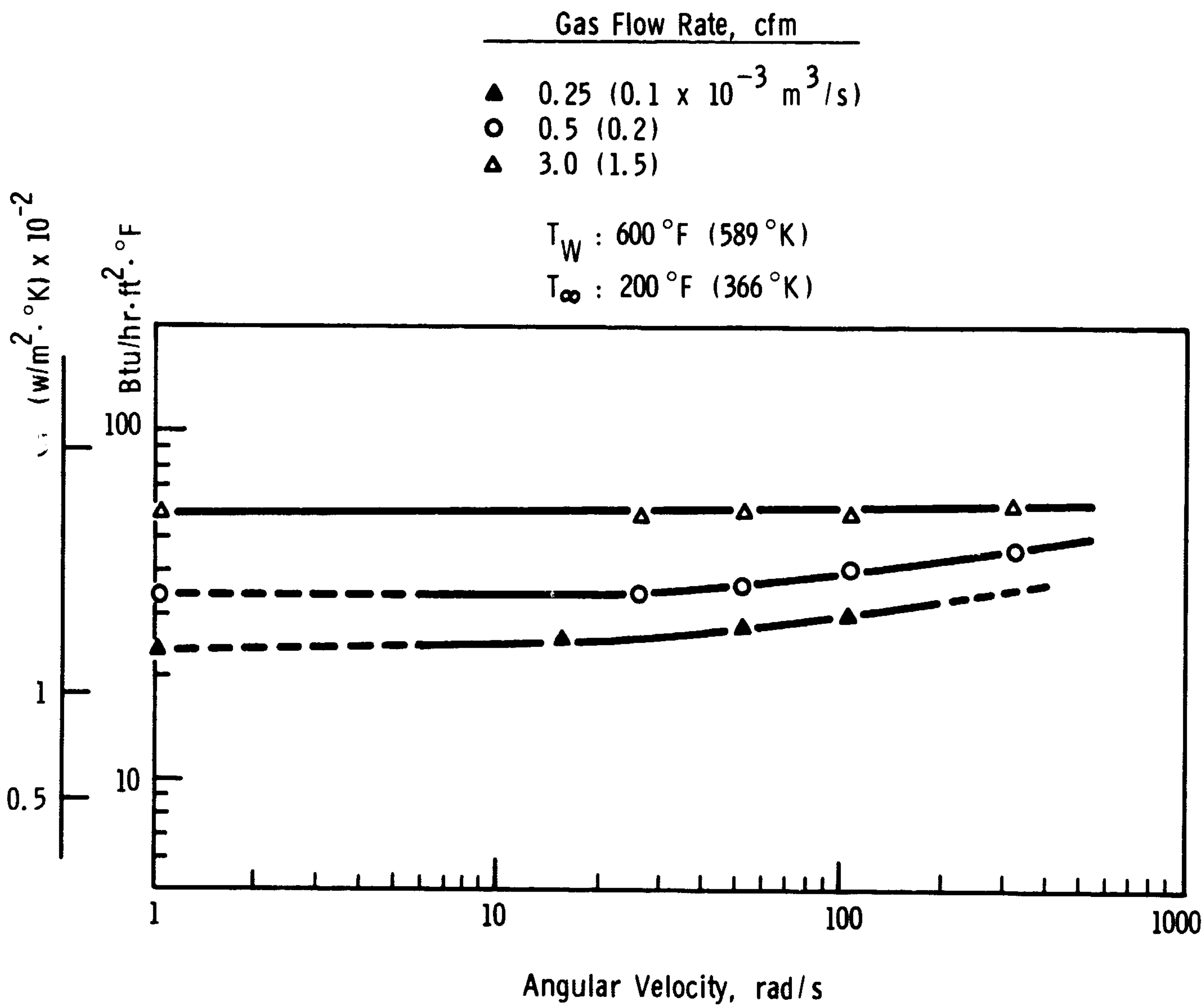

Figure 16

EFFECT OF ANGULAR VELOCITY ON HEAT TRANSFER COEFFICIENT OF NITROGEN GAS JETS

T_w : 600 °F (589 °K)

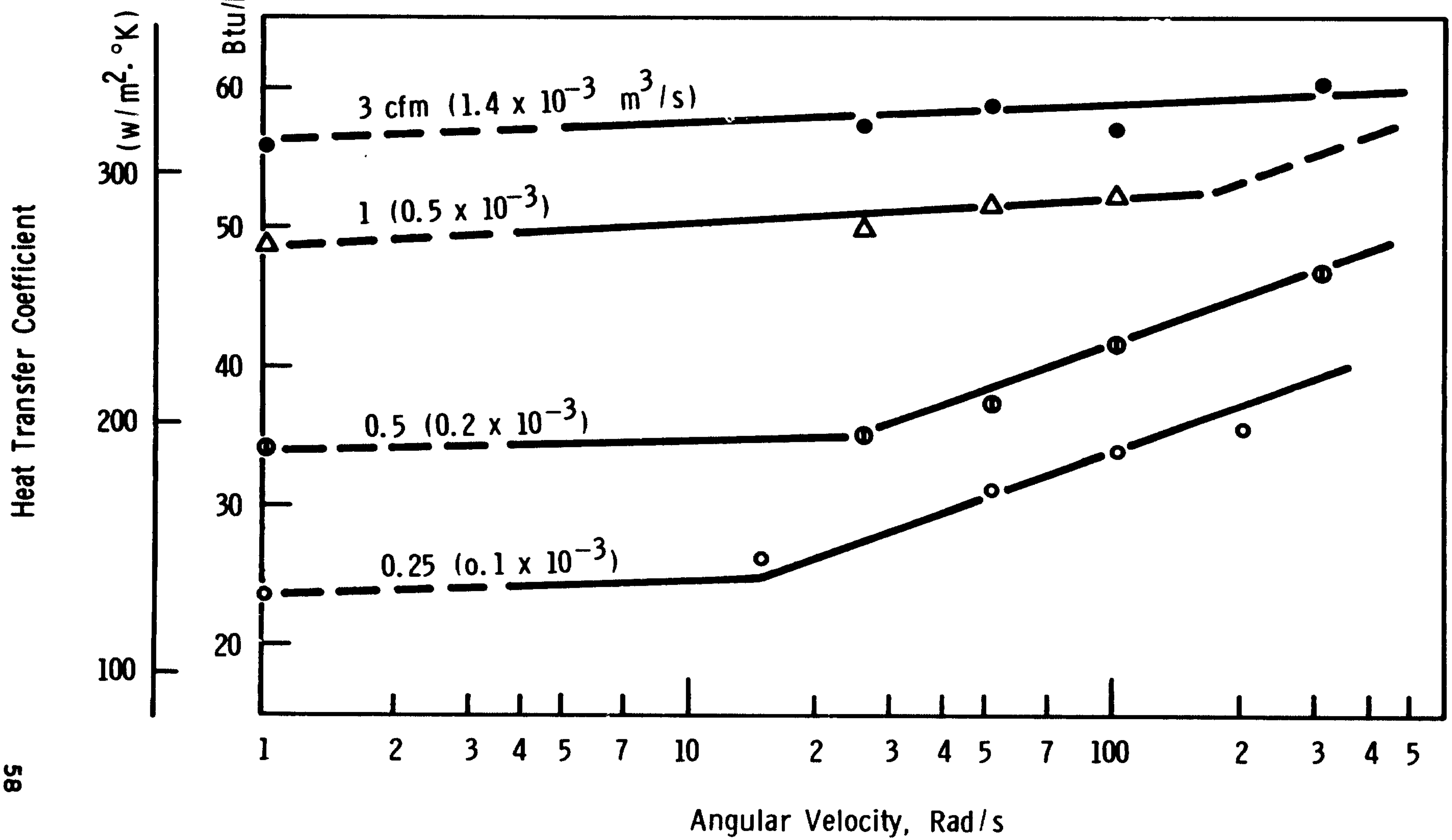

analysis based on Equation (26) indicated that the induction flow generated by rotation of the disc has no contribution to the heat transfer coefficient in this region. The reason for this contrasting result is not apparent, except that the analysis assumes a uniform forced inflow of incompressible fluid over an infinitely extended disc rotating at a constant angular velocity. The physical difference between two systems, which varies the characteristics of flow at their interfaces, may be considered a contributing factor.

In summary, the foregoing theoretical analyses and experimental data suggest that the effect of angular velocity on heat transfer coefficient in this investigation is not as dominant as Equation (25) predicts, but it is larger than that expected from Equation (26).

(c) Effect of Axial Spray Distance

From the preceding sections, it is apparent that the heat transfer coefficient of gas jets impinging on a heated rotating disc is insensitive to the variations of angular velocity of the disc and the mass-flow Reynolds number (the rates of forced gas inflow). The insensitivity of the heat transfer coefficient to these two parameters prompted an investigation of the effect of axial spray distance. It is also known that for any jets with a fixed nozzle and a given forced inflow, the impaction velocity of the jets varies dramatically as the axial spray distance changes. Hence, it is of great value to determine how the spray distance (or impaction velocity) affects the heat transfer coefficient for our system.

In this study of spray distance effects, the heat transfer rates were measured with two spray nozzles (Nos. 1 and 3) and three gas flow rates providing a range of mass-flow Reynolds numbers from 5.5×10^3 to 31.2×10^3. Axial spray distance ratios ranged from 1.78 to 23.4. For convenience in controlling the temperatures more accurately, the incoming gas and disc temperatures were chosen at 70°F (294°K) and 450°F (506°K), respectively, and the test chamber was maintained at 72°F (295°K). A stationary disc was employed for the entire series.

The heat transfer data are summarized in Appendix D-4, and the Nusselt numbers for No. 1 nozzle are plotted against the axial spray distance ratios at different Reynolds numbers in a log-log scale, as shown in Figure 17. The results in Figure 17 clearly demonstrate that for a given mass-flow Reynolds number, the heat transfer coefficient produced by an impinging jet at the stagnation point decreases monotonically with increasing spray distance; but the monotonic decrease seems to be subject to some disturbances at a distance ratio of about 20. This indicates not only that the impaction velocity of a gas jet has a profound effect on the thickness of the momentum boundary layer along the disc surface, but also that turbulence generated during the emergence of jets from a spray nozzle

Figure 17

EFFECT OF SPACING RATIO (Z/D_0) ON NUSSELT NUMBER AT THE CENTER LINE OF IMPINGING GAS JET

r/D_0 : 0

T_W : 507 °K

T_∞ : 294 °K

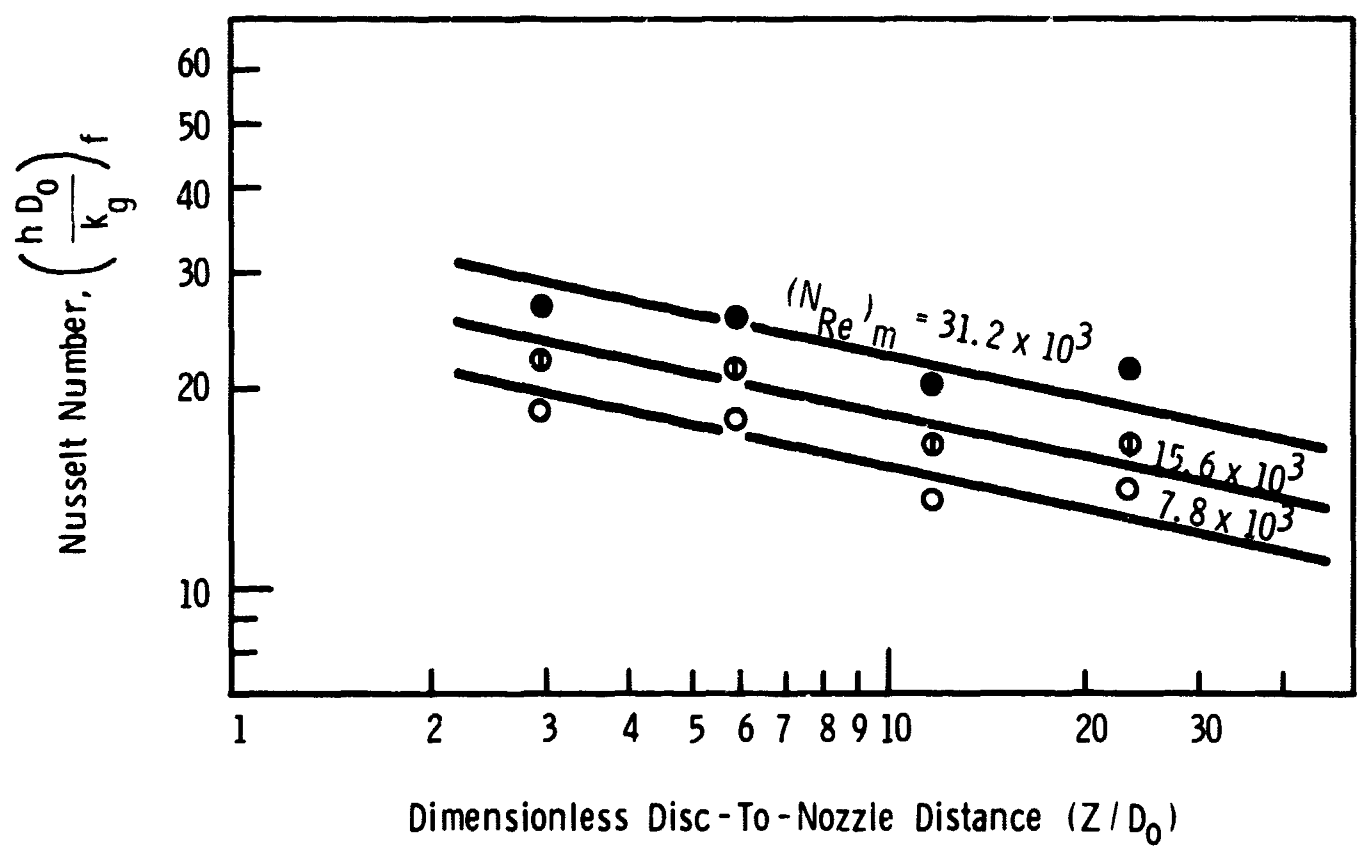

seems to influence the heat transfer coefficient by thinning out the thermal boundary layers.

According to Schrader's theoretical treatment of boundary layer thickness of gas jets impinging on a flat plate (15), it would be expected that the heat transfer coefficient is inversely proportional to axial spray distance along the center of the gas jet and directly proportional to the impaction velocity of the jet. An analysis of his theoretical treatment further suggests that based on just flow considerations of free jets, the heat transfer coefficient should remain constant in the region of potential core of the jets; i.e., $(Z/D_o) < 4$, and the coefficient should decrease in proportion to (D_o/Z) for $(Z/D_o) > 4$. In turning from free jets to impinging jets, it has been proved by several investigators (16, 17, 18) that a submerged circular jet propagates as a free jet to within a distance of roughly 1.2 nozzle diameters from the impactor surface, where its deceleration begins.

Adapting this treatment to jets of a finite size, such as the system employed in this work, careful review of the experimental results reveals that:

- The heat transfer coefficient, in fact, remains relatively unchanged in the region of potential core.
- The Nusselt number in this study is related by

$$N_{Nu} \propto (D_o/Z)^{0.2} \tag{28}$$

for $(N_{Re})_m$ up to 3.1×10^4 and $(Z/D_o) < 23.4$.

The first result can be easily demonstrated by comparison of the results summarized in Appendix D-4. For example, for a mass-flow Reynolds number the heat transfer coefficient varies from 21.0 (119 $W/m^2 \cdot {}^\circ K$) to 20.7 $Btu/hr \cdot ft^2 \cdot {}^\circ F$ (117 $W/m^2 \cdot {}^\circ K$) for distance ratios of 1.78 and 3.56, respectively. In the same manner the coefficient for other Reynolds numbers can be compared. It is quite surprising to find the exponential value of the distance ratio so low in comparison with that suggested by Schrader's treatment. While the reason for this discrepancy is not clearly revealed by the currently available information, it may be suggested that the turbulence generated by mixing of impinging jets with the surrounding fluid is much more intense than that usually encountered in pipe flow, and its intensity increases continuously with jet length. These factors may cause a sufficiently large increase in the heat transfer coefficient to compensate for a decrease brought about by decreased impaction velocity. This may explain why the heat transfer coefficient is relatively independent of (D_o/Z). In addition, the uncertainty of the temperature difference used in calculation of the heat transfer coefficient may be a contributing factor, as was explained in Section c(2).

(d) Radial Variations of Heat Transfer Coefficients

In this contract, no attempt was made to determine experimentally the variation of heat transfer coefficients with radial distance from the stagnation point of the disc. However, according to Gardon and Akfirat (18, 19), when a gas jet impinges on a heated flat plate, the heat transfer coefficient varies markedly along the radial distance of the plate, as shown in Figure 18. Typical of turbulent gas jets impinging on a flat plate, Figure 18 illustrates two distinct patterns in the variation of heat transfer coefficient with the dimensionless radial distance, (r/D_O):

- As the axial spray distance ratio, (Z/D_O), is reduced below 8, two "humps" begin to form at about the radial distance ratios, $(r/D_O) = \pm 7$; and, for $(Z/D_O) < 6$, they become well-defined secondary peaks in the heat transfer coefficient, as clearly illustrated by the curves for $(Z/D_O) = 5$ and 2 in the part (a) of Figure 18.

- For $(Z/D_O) \gtrsim 16$, the radial variation of heat transfer coefficients has a bell shape and a single low peak, as shown in part (b) of Figure 18; but for $16 \gtrsim (Z/D_O) \gtrsim 8$, the bell shape seems to be modified by an abrupt change in slope, or inflection point, in the vicinity of $(r/D_O) = 4$.

It is also apparent from Figure 18 that the heat transfer coefficients in most cases decrease rapidly with increasing radial distances from the stagnation point and seem to gradually approach asymptotic values, beginning at $(r/D_O) \gtrsim 8$. It is interesting to note that for $(Z/D_O) \gtrsim 80$ the heat transfer coefficient is remarkably unaffected by variation of the radial distance from the stagnation point.

Gardon and Akfirat have attempted to explain these complex phenomena involved in the radial variation of heat transfer coefficients for turbulent gas jets impinging on a heated plate by the sole consideration of the laminar- and turbulent-boundary layer flows of wall jets*, and found that the heat transfer characteristics of impinging jets cannot be explained simply by the velocity- and position-dependent boundary layer thicknesses alone. They can be explained, however, if one also takes into account the influence

---

*Whenever a jet impinges on a surface, the flow outward from the impinging region is termed a wall jet.

Figure 18

RADIAL VARIATION OF LOCAL HEAT TRANSFER COEFFICIENTS
OF AN AIR JET IMPINGING ON A HEATED PLATE

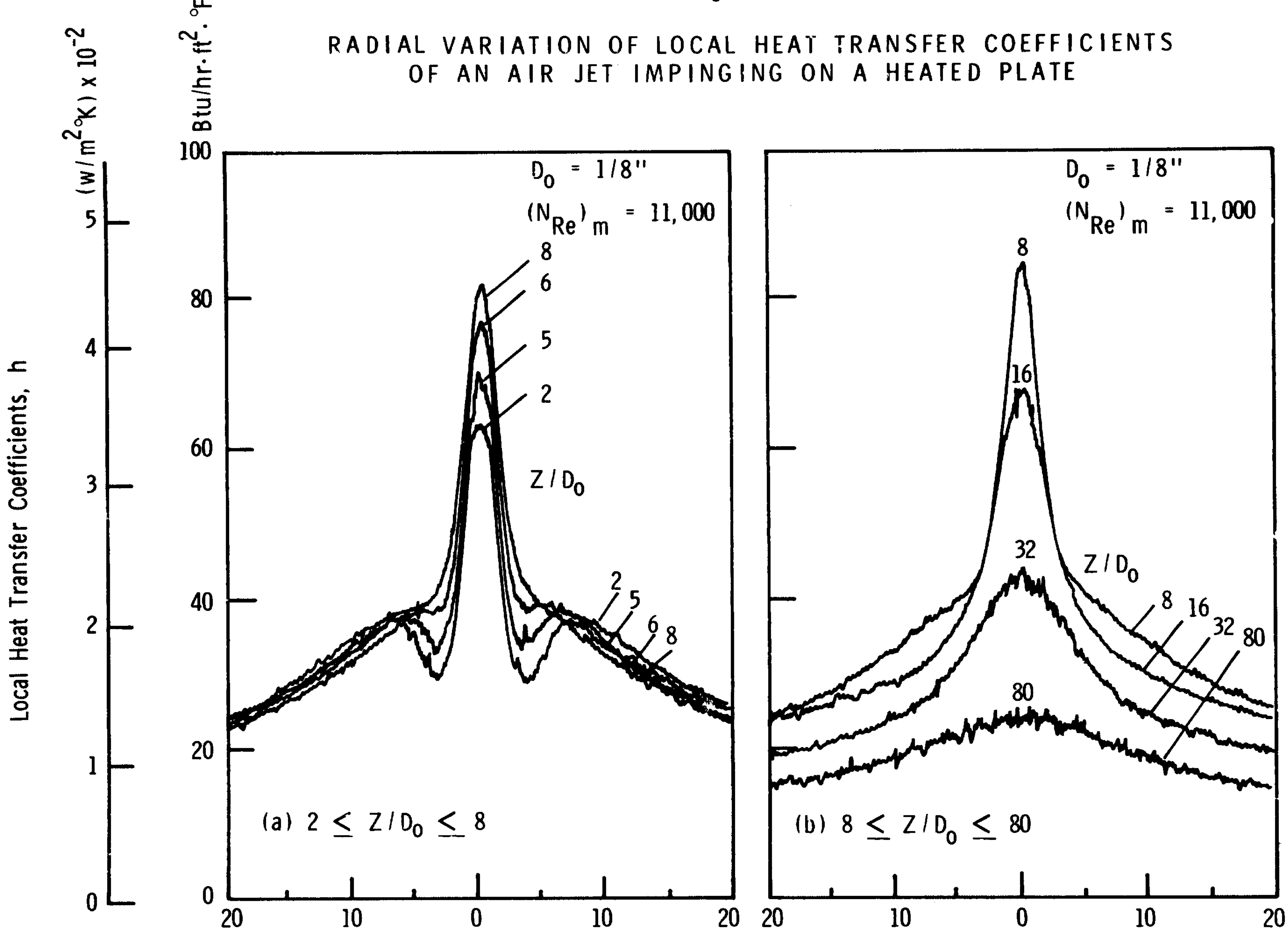

of turbulent intensity and, more importantly, turbulent scale. Owing to lack of information on the flow characteristics of impinging jets in the impingement and wall jet region, no full explanation is available for the corresponding heat transfer phenomena.

(e) Notes on the Empirical Correlation

Since analytical treatment of the problem in the impingement region would be not only exceedingly complex, but also beyond the scope of this project, there has been no sustained effort toward a solution to a mathematical model representing this study. Nevertheless, the heat transfer data may still be empirically correlated by means of a dimensionless equation of the Nusselt type:

$$\frac{hD_o}{k_g} = \text{some function of } \frac{D_oG}{\mu_g},\ \frac{Cp_2\mu_g}{k_g},\ \frac{Z}{D_o},\ \frac{\omega Ro^2\rho_g}{\mu_g},$$

$$\frac{\mu_g Ro}{\rho_\ell U_\infty^2 Dp^2},\ \frac{\Delta P}{\rho U_\infty^2},\ \frac{T - T_\infty}{T_w - T_\infty} \qquad (29)$$

The group $\Delta P/\rho U_\infty^2$ may be omitted from this expression because it is a function of the groups D_oG/μ_g and Z/D_o. Also the group $(T - T_\infty/T_w - T_\infty)$ may be omitted because it is an implicit function of the groups hD_o/k_g, D_oG/μ_g, $Cp_2\mu_g/k_g$, and Z/D_o. As a result of the preceding arguments, Equation (29) may be rewritten:

$$\frac{hD_o}{k_g} = \phi_1\left[\frac{D_oG}{\mu_g},\ \frac{Cp_2\mu_g}{k_g},\ \frac{Z}{D_o},\ \frac{\omega Ro^2\rho_g}{\mu_g},\ \frac{\mu_g Ro}{\rho_\ell U_\infty^2 Dp^2}\right] \qquad (30)$$

or

$$N_{Nu} = \phi_1\left[\left(N_{Re}\right)_m,\ N_{Pr},\ \frac{Z}{D_o},\ \left(N_{Re}\right)_\omega,\ N_{Stk}\right] \qquad (31)$$

where $(N_{Re})_m$ signifies the character of mass-flow impinging on a disc; N_{Pr}, the properties of the fluid; Z/D_o, the axial spray distance; $(N_{Re})_\omega$, the characteristics of a rotating disc; and N_{Stk}, the inertial impaction of microfog particles. According to Equation (30), for the heat transfer of microfog jets impinging on a heated rotating disc, the heat transfer coefficient for cooling may be correlated by a relation among the dimensionless groups of the mass-flow Reynolds number, the Prandtl number, a geometrical factor, the rotational Reynolds number, and the Stokes number.

Earlier experimental results, however, have shown that the heat transfer coefficient is insensitive to variation of the rotational Reynolds number at high values of the mass-flow Reynolds number. This means that the angular velocity of the disc has little effect on the coefficient as long as the rates of forced inflow are sufficiently high. Moreover, for a case where the values of the Stokes number remain constant (i.e., the microfog spray system is fixed), Equation (31) then becomes:

$$N_{Nu} = \phi_2 \left[\left(N_{Re}\right)_m , \quad N_{Pr} , \quad \frac{Z}{D_o} \right] \tag{32}$$

Keep in mind that Equation (32) was derived on the assumptions of (a) constant fluid physical properties, (b) no gravity forces, and (c) no viscous dissipation effects.

Up to this point, it has been assumed that the fluid properties are independent of temperature variation. Actually this is far from true in most physical situations, particularly in this study. The temperature dependence of viscosity may be handled empirically by including (μ_W/μ_B)*, in which μ_B is the viscosity of the fluid at some bulk temperature and μ_W is that at the temperature of the solid surface. Hence, for this study where temperature differences between the disc and the incoming gas stream are very large, the following relation can be used:

$$N_{Nu} = \phi_3 \left[\left(N_{Re}\right)_m , \quad N_{Pr} \cdot \quad \frac{Z}{D_o} , \quad \frac{\mu_W}{\mu_B} \right] \tag{33}$$

It must be remembered that relations of this type, in order to be useful, must be accompanied by (a) the specification of temperature

---

*A group of this type also can be arrived at by inserting in the equation of change a temperature-dependent coefficient of viscosity, described by a Taylor expansion of μ as a function of T,

$$\mu = \mu_B + \left(\frac{\partial \mu}{\partial T}\right)_{T=T_\infty} (T - T_\infty) + ----$$

The differential quotient is approximated by a difference quotient by

$$\frac{\mu}{\mu_B} = 1 + \left(\frac{\mu_W}{\mu_B} - 1\right) \left(\frac{T - T_\infty}{T_W - T_\infty}\right) + ----$$

which is rearranged to obtain a dimensionless viscosity. This group (μ_W/μ_B) then appears naturally in the equation of change.

drop used in the definition of h, and (b) a statement of the choice of average temperature for computing the physical properties contained in the dimensionless groups. A considerable divergence of opinion exists in the engineering literature on both of these points, particularly the temperature basis at which the physical properties of fluid must be evaluated. Some authors (20, 21) recommend the bulk temperature, others (9) the film temperature, T_i, defined as 0.5 $(T_W + T_\infty)$. Theoretically, if the temperature distribution is known, the physical properties must be evaluated at the temperature which is integrated through the boundary layers; i.e.,

$$\langle \overline{T}_i \rangle = \frac{1}{(\pi R_o^2) \cdot \delta} \int_o^{\delta_t} \int_o^{R_o} T\ (Z,r)\ dZ \cdot 2\pi r dr \qquad (34)$$

where δ_t represents the thickness of the thermal boundary layer.

Following the classical forced flow convective heat transfer approach, Equation (33) can now be written as products of powers of the dimensionless groups:

$$N_{Nu} = K \left(N_{Re}\right)_m^{\alpha} \cdot \left(N_{Pr}\right)^{\beta} \cdot \left(\frac{Z}{D_o}\right)^{\gamma} \cdot \left(\frac{\mu_B}{\mu_w}\right)^{\delta} \qquad (35)$$

where β and δ are usually assumed to be, respectively, 1/3 and 0.14 for gases. To further develop a correlation, the heat transfer data for nitrogen gas jets impinging on a stationary disc heated at 600°F (589°K), summarized in Table 4, are shown in Figure 19, where $N_{Nu} \cdot N_{Pr}^{-1/3}$ is plotted against the mass-flow Reynolds number in a log-log scale. Also included in the plot are the limited data taken at an axial spray distance ratio of 3.56 and a theoretical equation for the laminar flow convective heat transfer coefficient, which was first given by Pohlhausen (8) and used successfully in the following form:

$$N_{Nu} = 0.332 \left(N_{Re}\right)_m^{1/2} \cdot N_{Pr}^{1/3} \qquad (36)$$

It must be pointed out that the definition of characteristic size in Equation (36) differs from that of the experimental data in that the distance along the heat transfer surface from the center line of the impinging jet is used in Equation (36), while the orifice size of the spray nozzle is applied in calculations of the experimental data.

The Prandtl number, being practically constant in the temperature ranges investigated ($0.66 < N_{Pr} < 0.69$), was not considered during the processing of the experimental data, but was included at the end to generalize the correlations.

Figure 19 shows that the value of α is about 1/3, that the Nusselt number is affected by variation of the axial spray distance ratio, and that, apparently, the heat transfer coefficients derived from the theoretical equation are higher than the experimental values with mass-flow Reynolds number exceeding 2.0×10^3. The values of $(\mu_B/\mu_W)^{0.14}$ are not included here because their contributions to the Nusselt number for this study never amount to more than 6 percent of the total values. For this reason, the group (μ_B/μ_W) can be omitted from Equation (35).

Figure 20 shows the variation of heat transfer coefficient with axial spray distance ratio (Z/D_O) at the centerline of a jet. The value of the exponent of (D_O/Z) once again is about 1/3. It is, therefore, found from the heat transfer data that the empirical equation for a nitrogen gas jet impinging on a heated disc can be given by:

$$N_{Nu} = 1.9\left[\left(N_{Re}\right)_m \cdot N_{Pr} \cdot \frac{D_o}{Z}\right]^{1/3} \tag{37}$$

For nitrogen gas, Equation (37) can be further simplified to:

$$N_{Nu} = 1.67\left[\left(N_{Re}\right)_m \cdot \frac{D_o}{Z}\right]^{1/3} \tag{38}$$

Comparing with an empirical equation experimentally obtained by Gardon and Akfirat for heat transfer characteristics of impinging air jets, Equation (38) consistently predicts lower heat transfer coefficients than their equation, which is expressed as:

$$N_{Nu} = 1.2\left(N_{Re}\right)_m^{0.58}\left(\frac{D_o}{Z}\right)^{0.62} \tag{39}$$

for $2 \times 10^3 < (N_{Re})_m < 5 \times 10^4$ and $14 < (Z/D_O) < 60$. It is evident from the two equations that the exponential values of the Reynolds number and the distance ratio, (D_O/Z), are higher for Equation (39) than for Equation (38). This implies that the effect of these dimensionless groups on heat, the transfer coefficient is more apparent in their study than in our study. While the difference in these exponential values has not been accounted for, there is

Figure 19

CORRELATION OF $N_{nu} \cdot N_{pr}^{-1/3}$ AND $(N_{Re})_m$

Z/D_o	
○	3.56
●	5.85

T_W : 600 °F (589 °K)

T_∞ : 200 °F (366 °K)

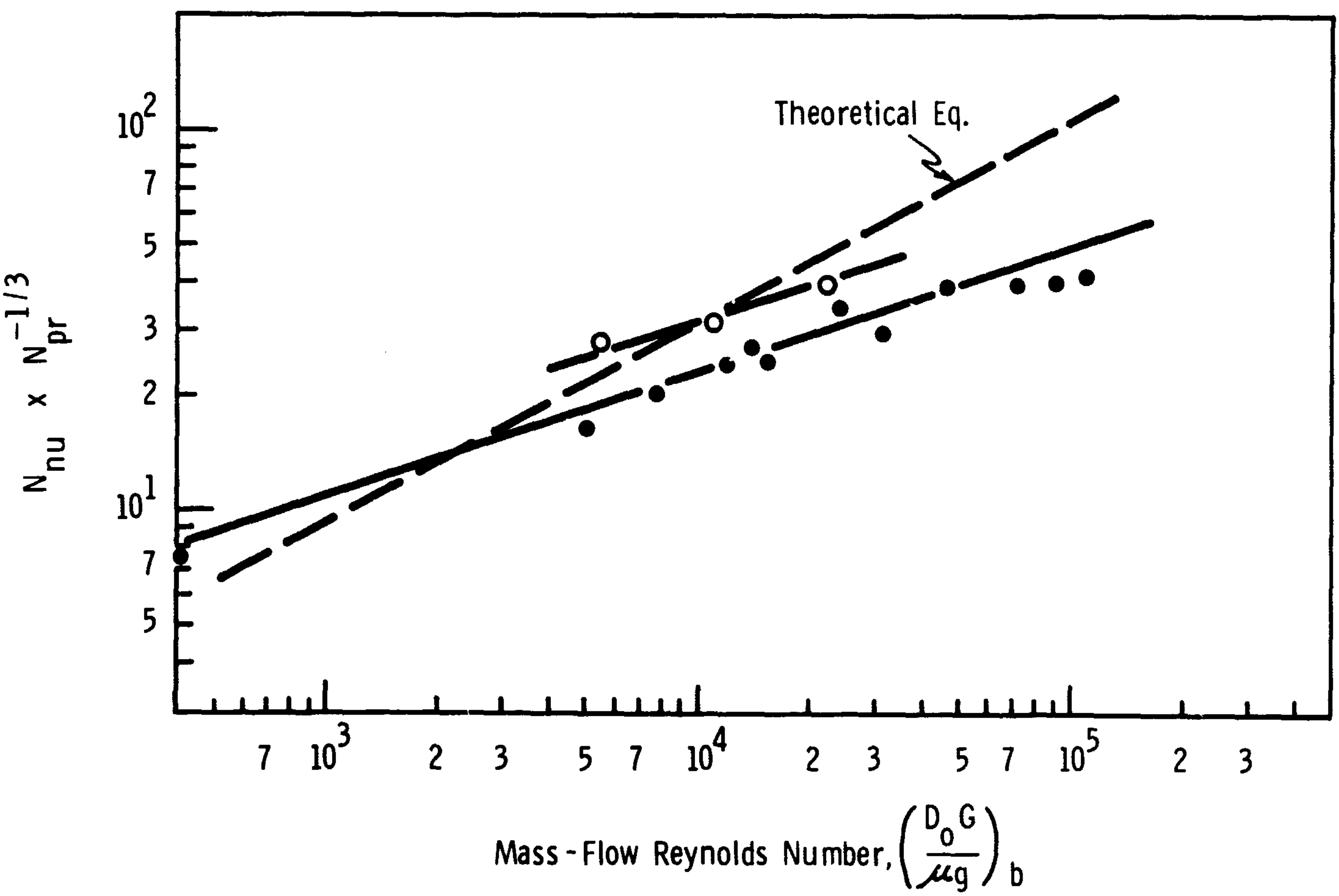

Figure 20

VARIATION OF HEAT TRANSFER
COEFFICIENT AT THE CENTER LINE OF
IMPINGING JET WITH AXIAL DISTANCE RATIO (Z/D_0)

D_0	
●	4.34 mm
Δ	7.13 mm

$(N_{re})_m$: $5 \times 10^3 \sim 1.1 \times 10^5$

T_W : 507 °K

T_∞ : 294 °K

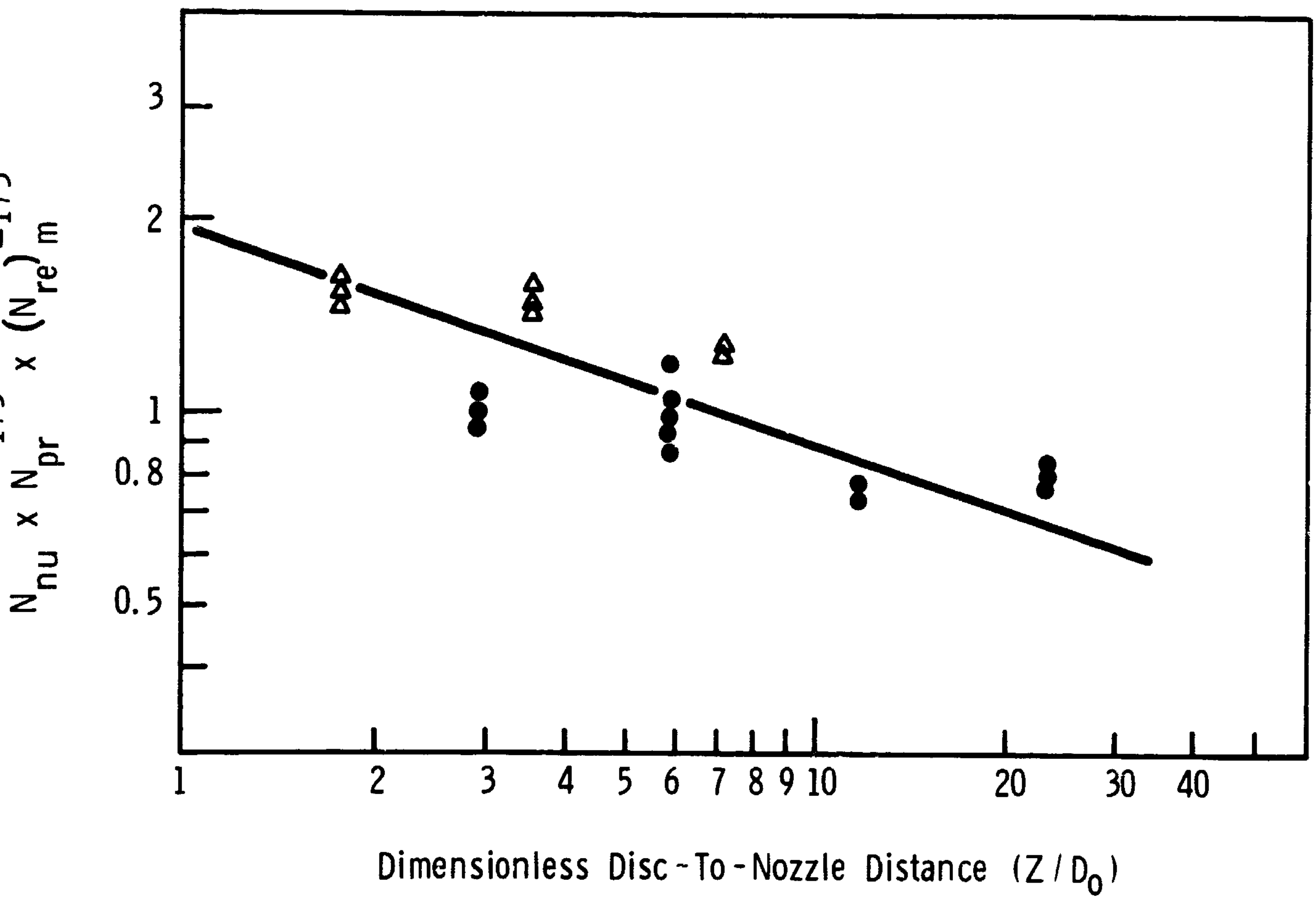

some question as to the value of $(T_W - T_\infty)$, and the effect of wall proximity on impinging gas jets, as was discussed in Section c(2). The value of $(T_W - T_\infty)$ employed for Equation (38) was 400°F (477°K), whereas the value for Equation (39) was 36°F (275°K). Moreover, Gardon and Akfirat studied their heat transfer in an open system, not in an enclosure as was the case in this study. These differences, and their apparent effects, seem to illustrate once again the importance of temperature-related variables on heat transfer.

2. Wettability of Lubricant Drops Impinging on a Heated Rotating Disc

It was found from the previous work (2) that when a microfog stream was sprayed onto a test plate through a spray nozzle for an extended period, considerable quantities of lubricant were lost; i.e., were not collected on the impactor. A part of this loss, of course, occurred in the transporting pipe lines, but some of the loss could be attributed to the loss of large lubricant drops formed at the tips of the spray nozzles. These extremely large drops (about 500~3,000 μm) normally did not impact on the test plate, but instead drifted away from the plate. Apparently, when the large drops became detached from the tip, they were not entrained back into the main stream of high velocity microfog flow. To show how such loss of large lubricant drops might be avoided, thereby increasing the efficiency of a microfog lubricant system, the formation and impingement dynamics of lubricant drops seemed worthy of further attention.

In addition, the process of spraying a heated rotating body with a lubricant is widely used in many industrial applications. Despite this widespread use, knowledge of the factors which affect the wettability and heat transfer of the lubricant spray is conspicuously lacking.

These considerations prompted the direction of a part of the contract effort toward photographing the kinetic drop formation and the impaction (or collision) of individual drops impinging on a heated rotating disc.

a. Analysis

For a study of drop phenomena, it was first necessary to develop a dropwise lubricant system which would accurately project a drop of known size and velocity onto a predetermined area. In order to aid in designing such a system, which must be tailored to the physical limitations of the present test apparatus, and to select the proper ranges of operating variables, a theoretical model of kinetic drop formation in a forced gas flow has been reviewed.

The model to be investigated for this phase of the contract, as shown schematically in Figure 21, is a lubricant drop having a size of D_p, formed at the tip of a capillary tube with a diameter of D_o, situated horizontally in a forced flow of the gas stream which has velocity, U_∞. This model omits many details of the kinetic drop formation; however, it is very useful for scoping purposes.

A force balance around the drop formed at the tip of a capillary tube requires consideration of four different forces:

(a) Surface tension

(b) Lubricant inertia

(c) Gas drag

(d) Gravity

These forces can be expressed in the mathematical forms of:

$$\underbrace{\pi D_o \sigma g_c f(D_o/D_p)}_{(a)} = \underbrace{\frac{d}{dt}\left(\frac{1}{6}\pi D_p^3 \rho_\ell U\right)}_{(b)} + \underbrace{\frac{\pi C_D}{4}(D_p^2 - D_o^2)\left(\frac{\rho_g U_\infty^2}{2}\right)}_{(c)}$$

$$+ \underbrace{\frac{\pi}{4} D_p^2 D_o \rho_\ell g F(D_o/D_p)}_{(d)} \tag{40}$$

where C_D is a drag coefficient, $F(D_o/D_p)$ and $f(D_o/D_p)$ are correction factors, g and g_c are the gravitational force and constant, U is the lubricant velocity in a capillary tube, and σ is the surface tension of the lubricant. Rearrangement of Equation (40) gives:

$$D_p = \left[\frac{4D_o \sigma g_c f(D_o/D_p) - \frac{d}{dt}\left(\frac{3}{2} D_p^3 \rho_\ell U\right)}{C_D\{1-(D_o/D_p)^2\}\left(\frac{\rho_g U_\infty^2}{2}\right) + D_o \rho_\ell g F(D_o/D_p)}\right]^{1/2} \tag{41}$$

If lubricant feed rates become insignificant, the lubricant inertia force, $d/dt(3/2\ D_p^3 \rho_\ell U)$, plays a negligible role in the kinetic drop formation, and Equation (41) can be reduced to:

Figure 21

A THEORETICAL MODEL
OF KINETIC DROP FORMATION IN A GAS STREAM

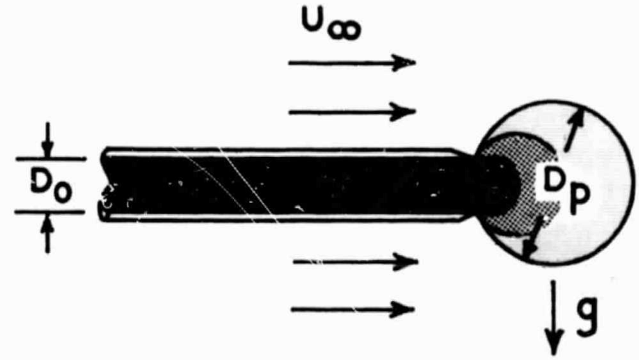

$$D_p = \left[\frac{4 D_o \, \sigma \, g_c \, f\,(D_o/D_p)}{C_D\{1 - (D_o/D_p)^2\} \left(\frac{\rho_g U_\infty^2}{2} \right) + \; D_o \, \rho_\ell \, g \, F\,(D_o/D_p)} \right]^{1/2} \tag{42}$$

Using Equation (42), after transforming it to an explicit equation of U_∞ in terms of D_p, the drop sizes of water, XRM 109 F, and Krytox 143 AC at 72°F (295°K) were calculated for D_o = 1 mm and for different gas stream velocities by estimating $C_D = 0.5$, $f(D_o/D_p) = 0.6$, and $F(D_o/D_p) = 0.2$, from the literature (22, 23, 24). The calculated results, depicted in Figure 22, show that the curves appear to asymptotically approach two distinctive regions where the drop sizes are predominantly controlled by either the gas inertia force, or the gravitational force, depending upon gas stream velocity. This behavior can be seen more clearly when Equation (42) is examined for two special cases, as follows:

- If $C_D\{1 - (D_o/D_p)^2\} \left(\frac{\rho_g U_\infty^2}{2} \right) \ll D_o \, \rho_\ell \, g \, F\,(D_o/D_p)$, then

Equation (42) becomes:

$$D_p = \left[\frac{4 \, \sigma \, g_c \, f\,(D_o/D_p)}{\rho_\ell \, g \, F\,(D_o/D_p)} \right]^{1/2} = 3.3 \left(\frac{\sigma}{\rho_\ell} \right)^{1/2} \tag{43}$$

Equation (43) was experimentally verified by Tamada and Shibaoka (24) for the case of the quasi-static drop formation of a liquid from a flat horizontal wetted surface.

- In the same manner, if

  $C_D \{ 1 - (D_o/D_p)^2\} \left(\frac{\rho_g U_\infty^2}{2} \right) \ll D_o \, \rho_\ell \, g \, F\,(D_o/D_p)$, then

Equation (42) becomes:

$$D_p = \left[\frac{8 D_o \, \sigma \, g_c \, f\,(D_o/D_p)}{C_D \{ 1 - (D_o/D_p)^2\} \, \rho_g \, U_\infty^2} \right]^{1/2} \tag{44}$$

Equation (44) further illustrates that if

$D_p \longrightarrow D_o$, then $U_\infty \longrightarrow \infty$

Equation (43) and (44) clearly define the limits of two extreme regions. For example, as the gas stream velocity approaches zero, the drop sizes of water, XRM 109 F, and Krytox 143 AC are 9.3, 6.6, and 3.4 mm, respectively; whereas high gas stream velocity is needed to produce drops having size equivalent to the capillary size.

Possible errors in the calculated drop sizes plotted in Figure 22 are largely empirical and arise from uncertainties of the values of three parameters used: C_D, $f(D_o/D_p)$, and $F(D_o/D_p)$. Regardless of these uncertainties, the calculated data show that water, XRM 109 F, and Krytox 143 AC, all behave similarly with varying gas stream velocity, although the curves for these fluids may be shifted right or left, depending on the selected values of the three parameters.

Figure 22 also reveals that the drop size decreases rapidly with the gas stream velocity between 1 and 20 m/s, but varies slightly as the velocity further increases. When the gas stream velocity, however, exceeds a point where the intensity of gas turbulence is a dominant factor, a new value of C_D must be selected, and a drop formed at the capillary tip may undergo a secondary breakup to form small drops. This phenomenon will be further discussed in a later section.

b. General Comments

Using a newly developed experimental technique, the kinetics of drop formation at the tip of a capillary tube, the sizes and velocities of lubricant drops suspended in a forced gas stream, and the dynamics of lubricant drops impinging on a heated rotating disc, were photographically recorded by the Hycam high-speed motion picture camera. In this series of experiments, the following test conditions with two lubricants, XRM 109 F and FN 2961, were chosen:

Disc temperature:	600 (589°K), 700 (644°K), and 800°F (700°K)
Angular velocity of disc:	52, 104, and 312 rad/s
Gas stream velocity:	11, 15, and 19 m/s
Lubricant feed rate:	1.67×10^{-2} cm^3/s
Capillary diameter:	1 mm (#1) and 0.5 mm (#2)

Although generally adequate for analysis of the photographic data, the image quality of the high-speed motion picture films often was less than ideal. This, together with other factors, made accurate determinations of the sizes and velocities of the lubricant drops a difficult and tedious process. Image quality was limited to some degree by the geometry of the test chamber,

Figure 22

DROP DIAMETER OF LIQUIDS
AS A FUNCTION OF GAS STREAM VELOCITY

$D_o = 1$ mm

$C_D = 0.5$

$f(D_o/D_p) = 0.6$

$F(D_o/D_p) = 0.2$

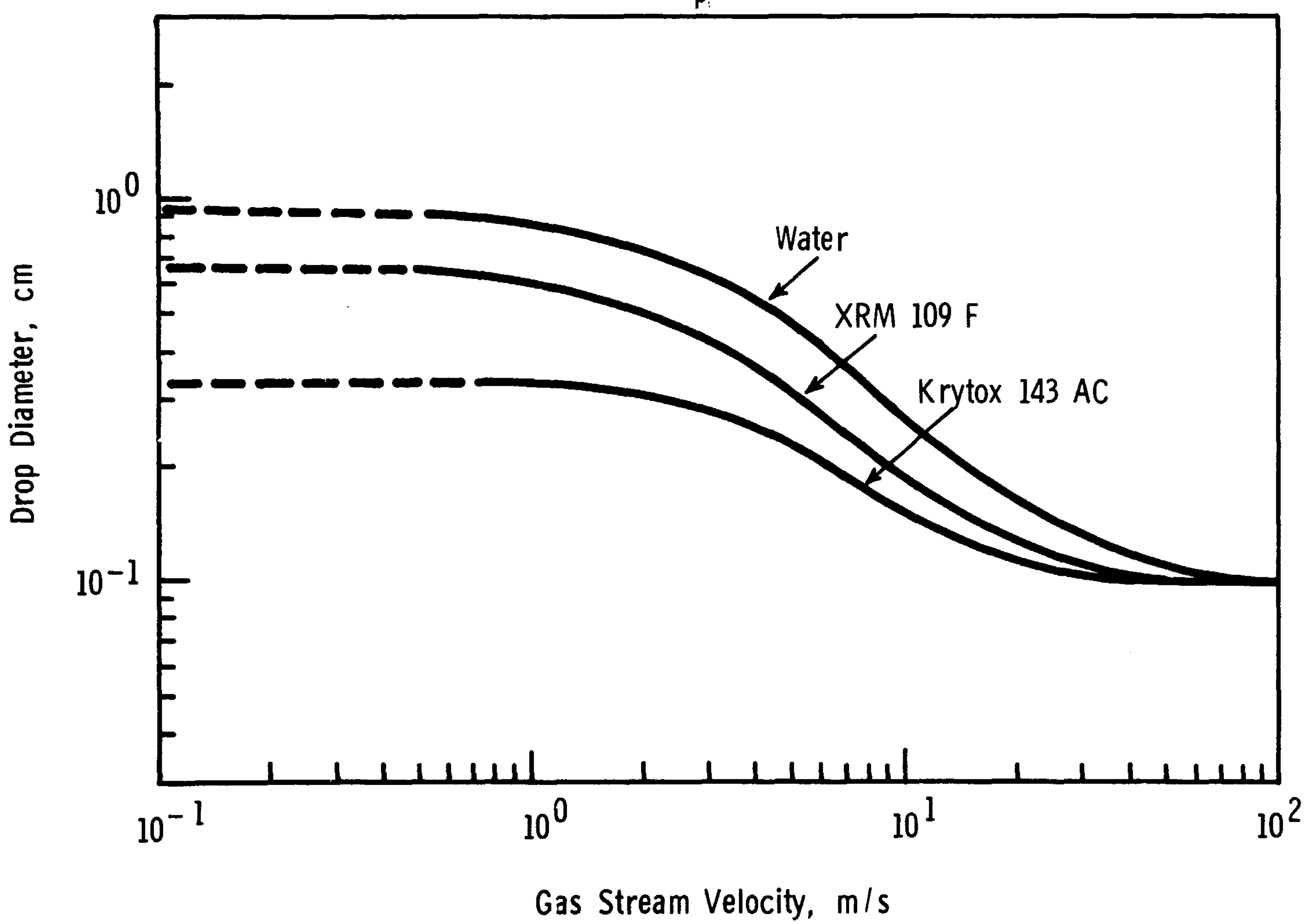

which, because it originally was designed for other studies, was incompatible with the optimum photographic magnifications and lighting angles. Analysis of the photographic data was further complicated by generally irregular shapes and random behavior of the drops photographed. Picture quality was often degraded by discrepancy between the projected path on which the camera was focused and the actual path taken by the drop. Hence, while some experimental error arose partly from uncertainties in the experimental conditions, most were probably due to variation of picture quality. Recognizing this, during the analysis of over 300,000 frames of high-speed motion pictures, the quality of the films was subjectively graded into three classes. Class A films were judged very sharp and easy to analyze. Class C films were difficult to evaluate, and the results obtained from them were of questionable value. The primary effect of poor quality was to increase scatter of the experimental data.

c. Drop Formation

Despite the difficulties in analyzing the motion picture films, their careful review reveals many interesting aspects of kinetic drop formation. Since lubricant is supplied at a finite rate by the infusion pump and continuously converted into drops, the drops must be formed at a predetermined rate. However, the motion picture films show that the rate (frequency) of drop formation for a given test condition seems to vary widely, and the drops formed at the tip in most cases are non-spherical and become highly deformed, presumably assuming a shape such that surface tension compensates for the pressure variations around the drops.

It is also observed from the motion pictures that the kinetics of drop formation, when the drops are produced at a certain predetermined rate, seem to involve the following sequential steps, although any specific step may be negligible or absent under some circumstances:

- The extension of the bulk lubricant into a jet by accelerating it through the capillary tube.
- The initiation of disturbances at the lubricant surface in the form of local ripples.
- The formation of a short ligament on the lubricant surface as the result of gas stream pressure or shear forces.
- The collapse of the short ligament into a drop as the result of surface tension.
- The breakup of the drop as it moves through the gaseous medium by the action of gas stream pressure or shear forces.

It is apparent from the sequential steps that the pendant drop is a special case for which the first and fourth steps alone are appreciable at negligibly low lubricant feed rate. For this case, only a balance between the gravitational field and surface tension is involved {refer to Equation (42)}. As soon as the flow rates of gas and lubricant become significant, the inertia forces generated by these fluids, together with any other forces arising as a result of the fluid motions, play a major role in controlling the sequential steps of drop formation.

Efforts to enlarge and print some frames of the high-speed films showing the mechanisms of the kinetic drop formation as described above failed to yield sufficient quality for use here. Hence, selected pictures drawn from the motion picture films are shown in Figures 23 and 24, which typify the mechanisms of drop formation for FN 2961 and XRM 109 F, respectively.

A brief literature survey was made with the hope of finding a theory or law for kinetic drop formation which would describe the mechanisms of drop formation. This would allow comparison of the mechanisms for different fluids by noting the changes in the parameters of the system instead of using the more cumbersome visual comparison. Unfortunately, no adequate drop formation law was found; and the observed results are, therefore, presented and compared in the form of Figures 23 and 24.

A comparison of these figures shows that the drops of FN 2961 follow more closely the aforementioned sequential steps of drop formation and that the drops of FN 2961 and XRM 109 F have markedly different shapes and sizes of the ligaments (thin filaments) formed on the drop surfaces when the drops are about to separate from the tip of capillary tube. The differences in the sequential steps of drop formation and in the elongation of the ligaments for these lubricants are caused most likely by a considerable difference in their viscosity, since their other physical properties, being nearly identical, cannot be considered as a contributing factor.

It is generally viewed from this study of drop formation that the effect of lower viscosity for FN 2961 is to produce more satellite drops. The ligaments formed on the drop surfaces seem to be less stable; and, hence, for a given gas stream velocity, more drops are free from ligaments, and the total number of drops formed seems to be generally more than in the corresponding case for more viscous XRM 109 F. In the nearly 200,000 motion picture frames analyzed during this study with XRM 109 F, drops completely free from ligaments are very scarce. A probable explanation for this is that the breakup distance of lubricant jets for viscous XRM 109 F is longer than the distance between the disc and the tip of the capillary table, whereas the breakup distance for less viscous FN 2961 is considerably shorter as compared with that for XRM 109 F. It is generally known that the viscosity of liquid jets has a great effect on the capillary instability of the jets (25, 26).

Figure 23

SCHEMATIC OF THE HIGH SPEED PHOTOGRAPHS
OF A KINETIC DROP FORMATION IN A GAS STREAM

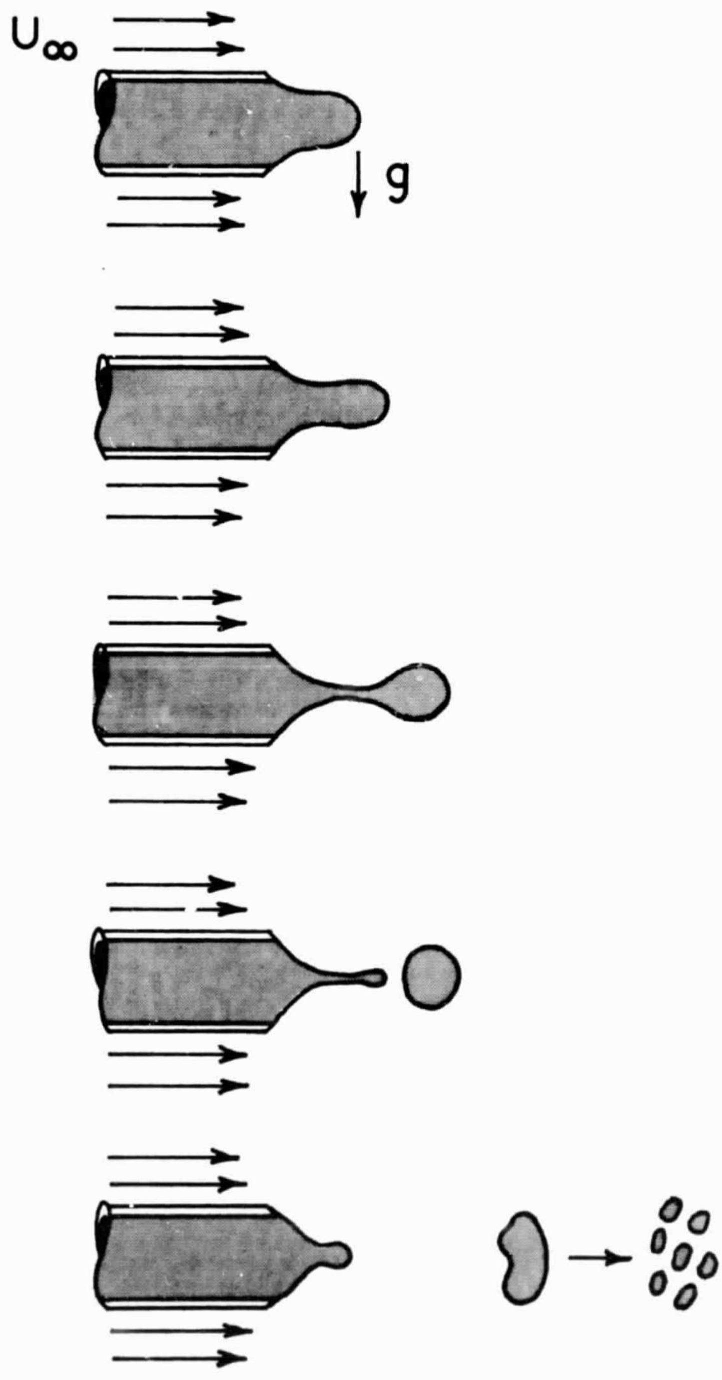

Figure 24

SCHEMATIC OF THE HIGH SPEED PHOTOGRAPHS OF A KINETIC DROP FORMATION IN A GAS STREAM

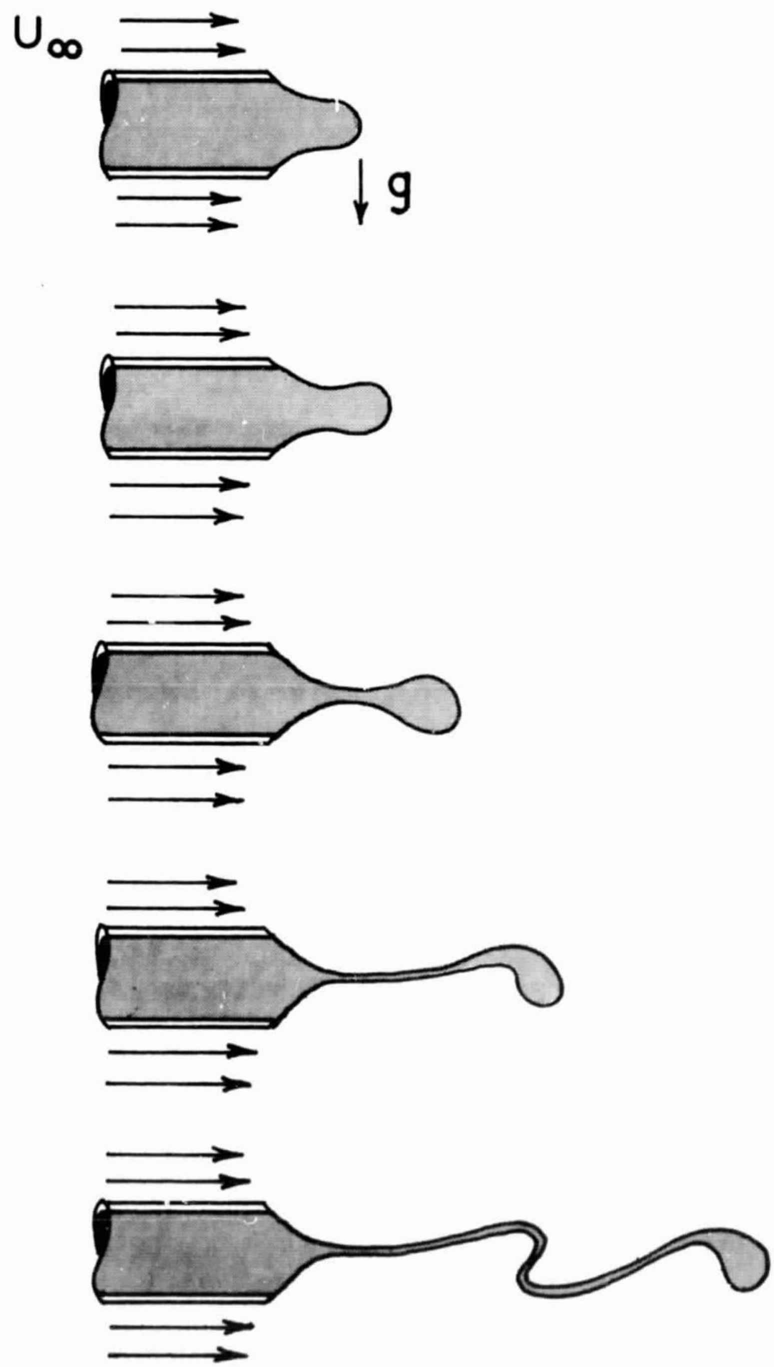

Although this study is useful in understanding the fomation of drops, it may not, however, provide a quantitative description adequate for use in designing and predicting performance of microfog lubricant spray systems.

d. Drop Size

As was previously pointed out, accurate determinations of the sizes of lubricant drops impinging on a rotating disc were very difficult. This difficulty was due largely to presence of the ligaments on the drop surfaces, but also to deformation of the drops. For these reasons, the sizes of drops were estimated before the formation of short ligaments on the drop surfaces for convenience.

The estimated values of drop size with a capillary tube of 1-mm diameter (#1) for FN 2961 and XRM 109 F range from 1.3 to 1.7 mm at the gas stream velocities of 11, 15, and 19 m/s. With a capillary tube of 0.5-mm diameter (#2), the drop sizes vary from 0.7 to 1.4 mm at the same gas stream velocities. For the effect of gas stream velocity on drop size, the general trend is for smaller drop sizes at the higher gas velocities than at the lower velocities, as indicated by Equation 41 and Figure 22. The differences, however, were small and often masked in experimental error; hence, no quantitative conclusions can be drawn. Highly deformed drops, in almost all cases, had an ellipsoidal shape with major and minor diameter about 1.8 and 1.0 mm, respectively.

When gas stream velocities less than 8 m/s were tried in order to generate large drops, the drops of XRM 109 F generally appeared highly deformed and in many cases failed to impact on the rotating disc.

e. Drop Velocity

The velocities of XRM 109 F and FN 2961 drops impinging on a heated rotating disc were determined with two different capillary tubes at gas stream velocities of 11, 15, and 19 m/s. The capillary tubes employed are #1 and #2. Selected velocity data obtained in this series are listed in Appendix E.

A typical result of XRM 109 F at a disc temperature of 600°F (589°K), listed in Table 6, is presented in Figure 25 by plotting distances traveled by lubricant drops versus time. Since the plot shows a definite curvature for each gas stream velocity, attempts were made to find a linear relationship which would conveniently describe the drop velocities in order to demonstrate the effect of gas stream velocity on the drop velocities. The inadequacy of a linear relationship is best illustrated by a log-log plot of a representative set of data shown in Figure 26. Since no adequate relationship was found, all the velocity data are presented and compared in graphical form. The velocities presented in the

Table 6

Relationship Between Time and Distance Traveled by Lubricant Drops

Run No.	Time sec x 10^2	Distance Traveled by Drops, cm x 10'				
XRM 25-1	0	0	0	0	0	0
-2	0.5	1.5	1.2	1.0	1.5	1.5
XRM 26-1	1.0	1.8	1.95	1.8	1.8	1.8
	1.5	2.1	2.7	2.0	2.4	2.4
	2.0	2.7	3.45	2.9	3.45	3.45
	2.5	4.25	4.65	3.9	5.4	4.95
	3.0	6.45	7.65	6.2	9.95	7.65
	3.5	9.2	13.5	8.2	14.0	12.0
	4.0	12.9	18.0	11.5	18.0	16.5
	4.5	17.5	20.0	15.5		
	5.0	21.8	25.2	20.5		
	5.5			25.0		

Gas Stream Velocity: 11 m/s
Disc Temperature: 600°F (589°K)
Capillary Tube: #1 (1 mm dia.)
Test Lubricant: XRM 109 F

Figure 25

RELATIONSHIP BETWEEN TIME AND DISTANCE TRAVELED BY LUBRICANT DROPS SUSPENDED IN GAS STREAMS

Test Lubricant : XRM 109 F
Disc Temp : 600 °F (589 °K)

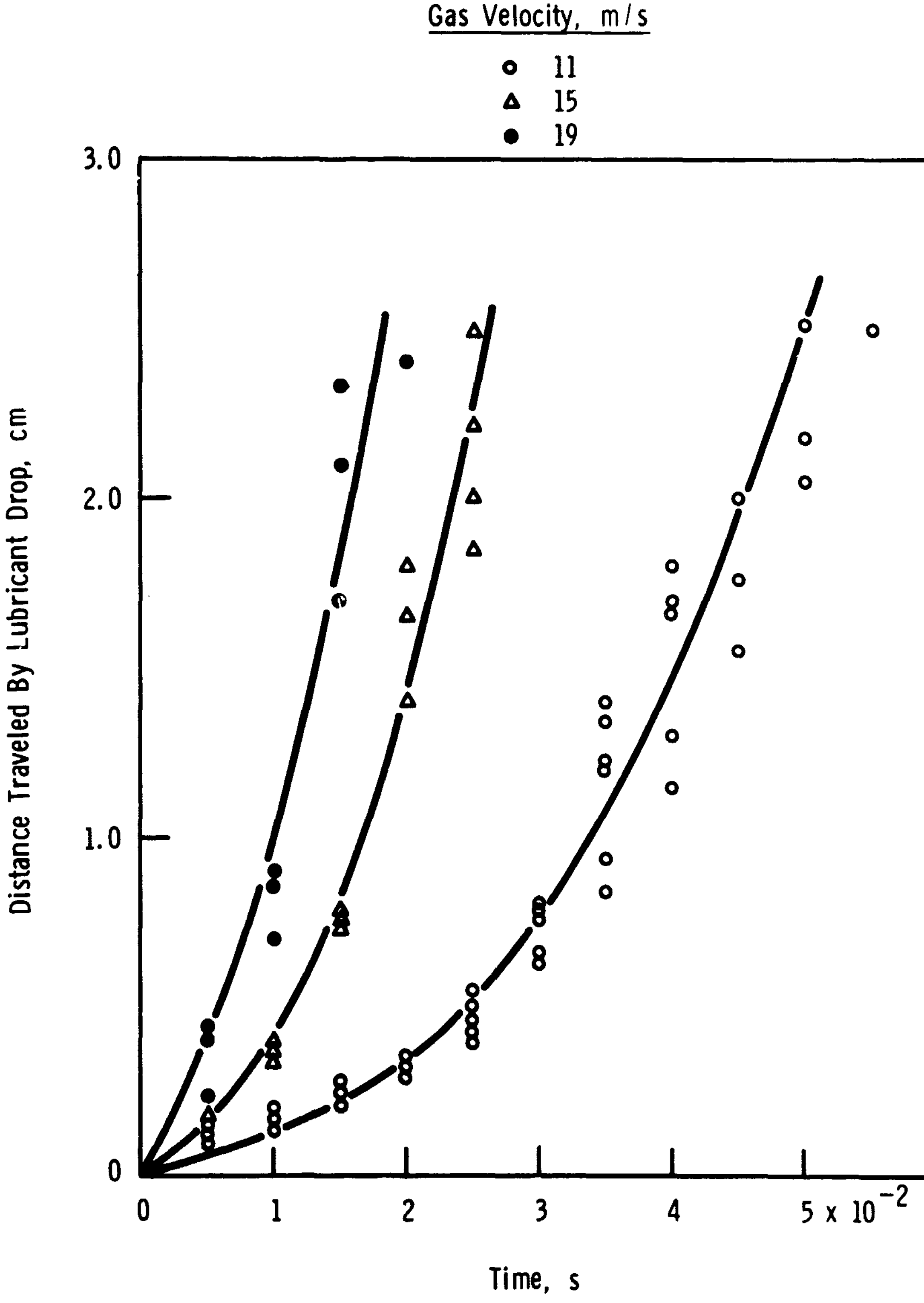

Figure 26

RELATIONSHIP BETWEEN TIME AND DISTANCE TRAVELED BY LUBRICANT DROPS SUSPENDED IN GAS STREAMS

(XRM 109 F; Disc Temp. : 589 °K)

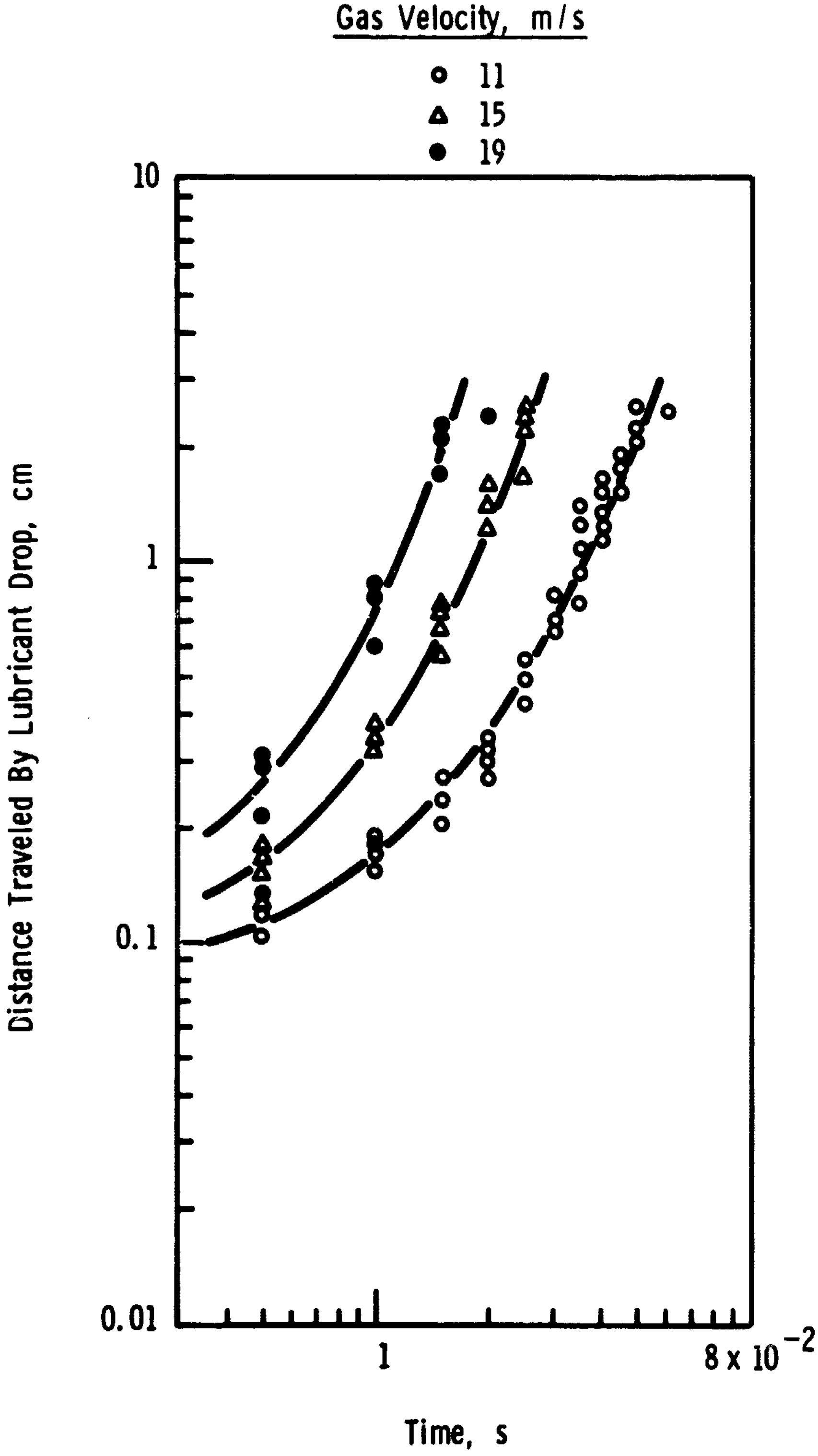

graphical form of Figure 25 are still useful for comparative purposes. In the same manner, the velocities of XRM 109 F drops at disc temperatures of 700 (644°K) and 800°F (700°K), and those of FN 2961 drops at a disc temperature of 600°F (589°K) are presented in Figures 27, 28, and 29, respectively.

The experimental results shown in Figure 25, though the data points scatter considerably, demonstrate that between time and distance traveled by lubricant drops there is a non-linear relationship similar to a parabolic curve, indicating that the drops are in acceleration stages and that, even just before impingement on the disc, they have not acquired the steady-state velocity of the gas stream.

To aid discussion of the drop velocity as a function of gas stream velocity, the terminal velocities of drops were graphically estimated by taking the straight lines at the linear portions of the curves presented in Figures 27, 28, and 29. These results, listed in Table 7, show that, as expected, the terminal velocity increases with increasing gas stream velocity, and an increase in terminal velocity is more apparent at a disc temperature of 600°F (589°K) than at one of 800°F (700°K). The measurable effect of disc temperature drop velocity, particularly at a gas stream velocity of 11 m/s, was surprising. However, the influence of disc temperature seems to diminish as the gas stream velocity further increases. This effect of disc temperature on drop velocity is most likely caused by variation of lubricant viscosity with its temperature, which in turn affects the shapes and sizes of the elongated ligaments of XRM 109 F drops. With the present experimental apparatus, the lubricant temperatures at the capillary tube could not be controlled accurately, because temperature differences between the disc and the lubricant in the tube were so large that the cooler, incoming lubricant was always affected by the convection and radiation of heat from the disc. For this reason, the effect of disc temperature on the drop velocity is construed as more a mechanical effect of the present system than a genuine physical effect.

Table 7 also shows that the terminal velocities acquired by XRM 109 F drops impinging on the disc are far lower than the gas stream velocities for the corresponding cases, indicating that the drops are not completely suspended in the gas streams. For example, at a disc temperature of 700°F (644°K), the terminal velocities of XRM 109 F drops are only 1.27 m/s for a gas stream velocity of 15 m/s and almost 1.6 m/s for 19 m/s.

For convenience in comparing the drop velocities of FN 2961 and XRM 109 F, their terminal velocities are again chosen for discussion. The terminal velocity of drops, taken from the curves presented in Figures 25 and 29, are listed on the next page:

Figure 27

RELATIONSHIP BETWEEN TIME AND DISTANCE TRAVELED BY LUBRICANT DROPS SUSPENDED IN GAS STREAMS

Test Lubricant : XRM 109 F
Disc Temp : 700 °F (644 °K)

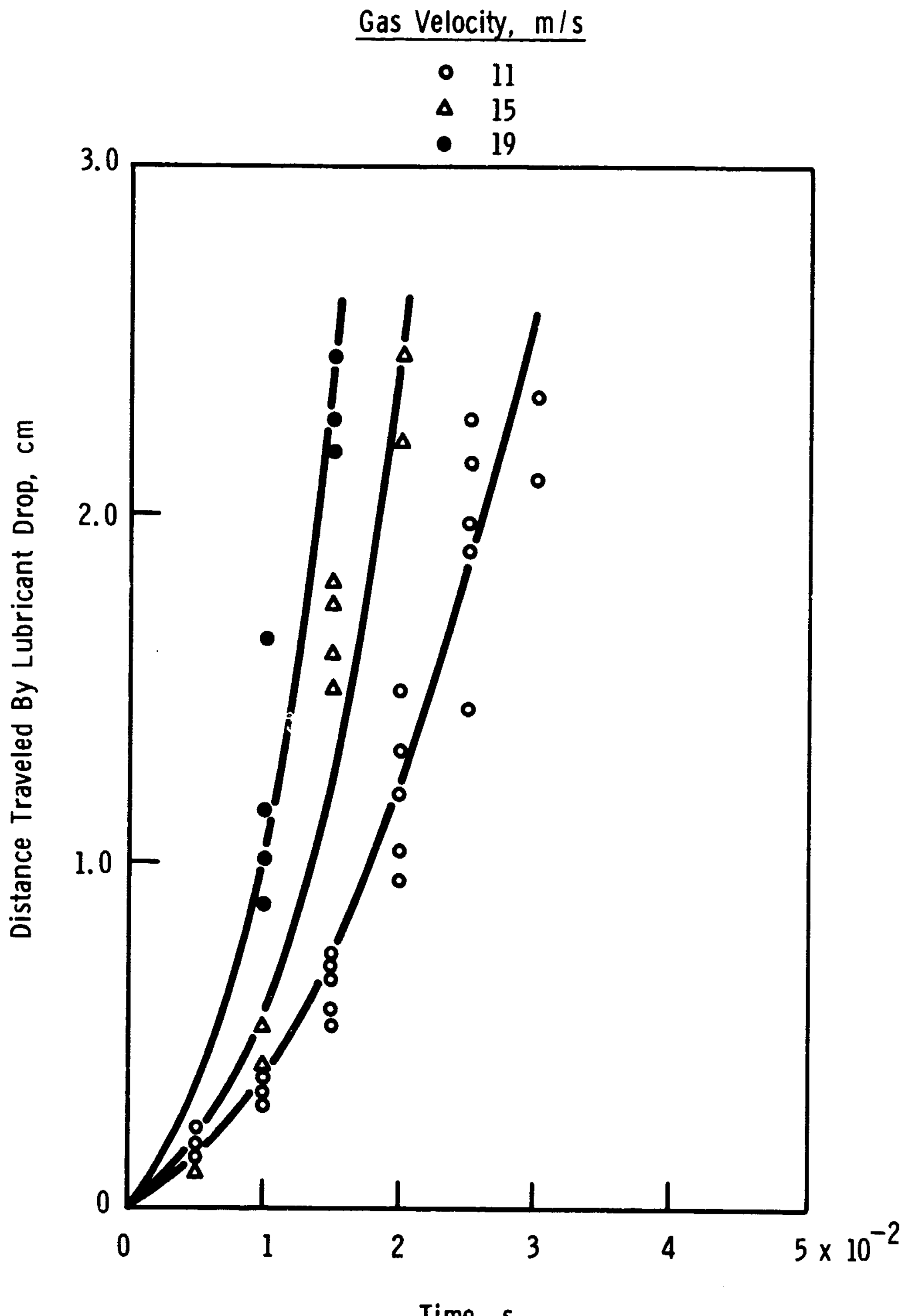

2E

Figure 28

RELATIONSHIP BETWEEN TIME AND DISTANCE TRAVELED BY LUBRICANT DROPS SUSPENDED IN GAS STREAMS

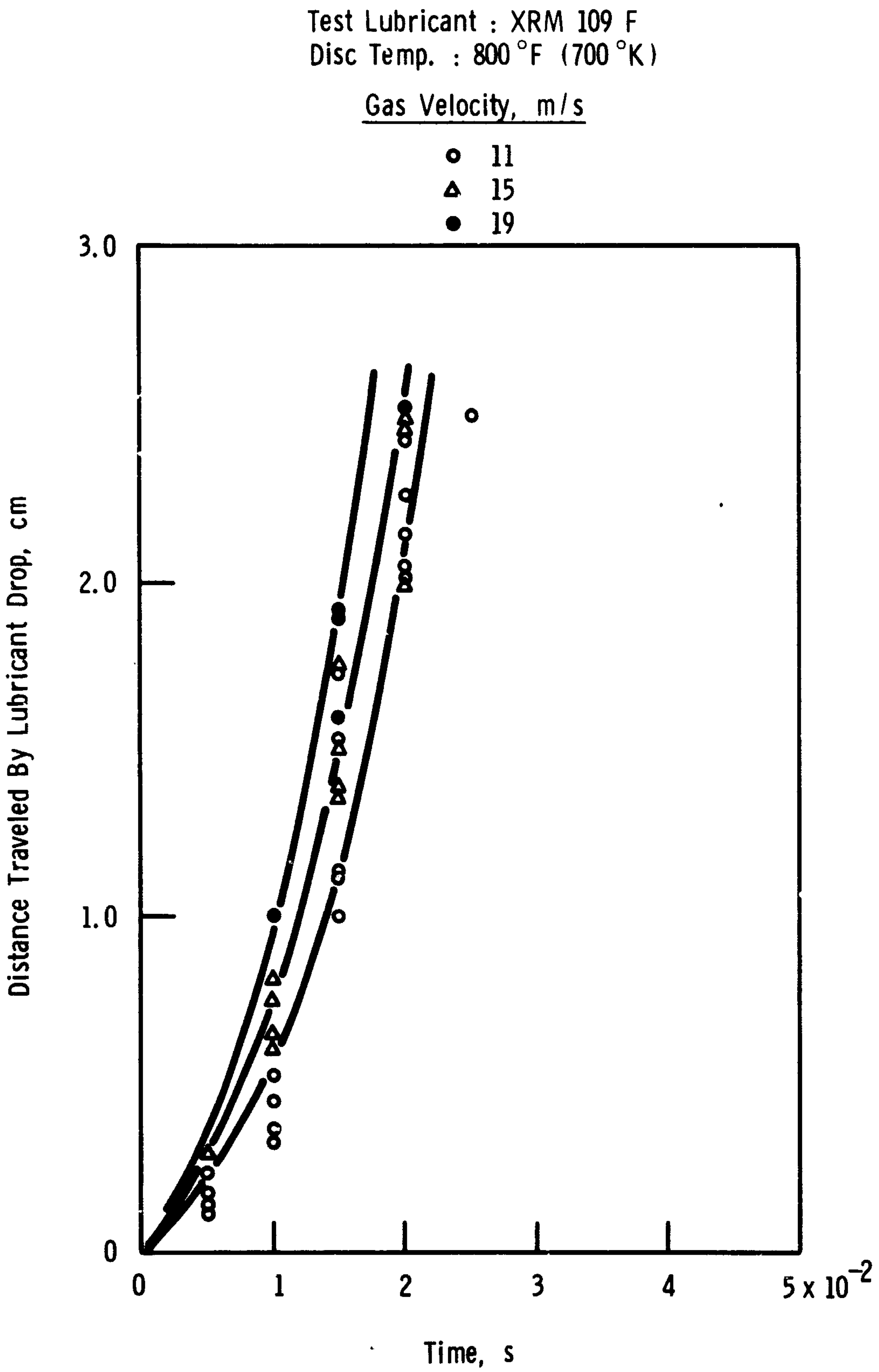

Figure 29

RELATIONSHIP BETWEEN TIME AND DISTANCE TRAVELED BY LUBRICANT DROPS SUSPENDED IN GAS STREAMS

Test Lubricant : FN 2961
Disc Temp : 600 °F (589 °K)

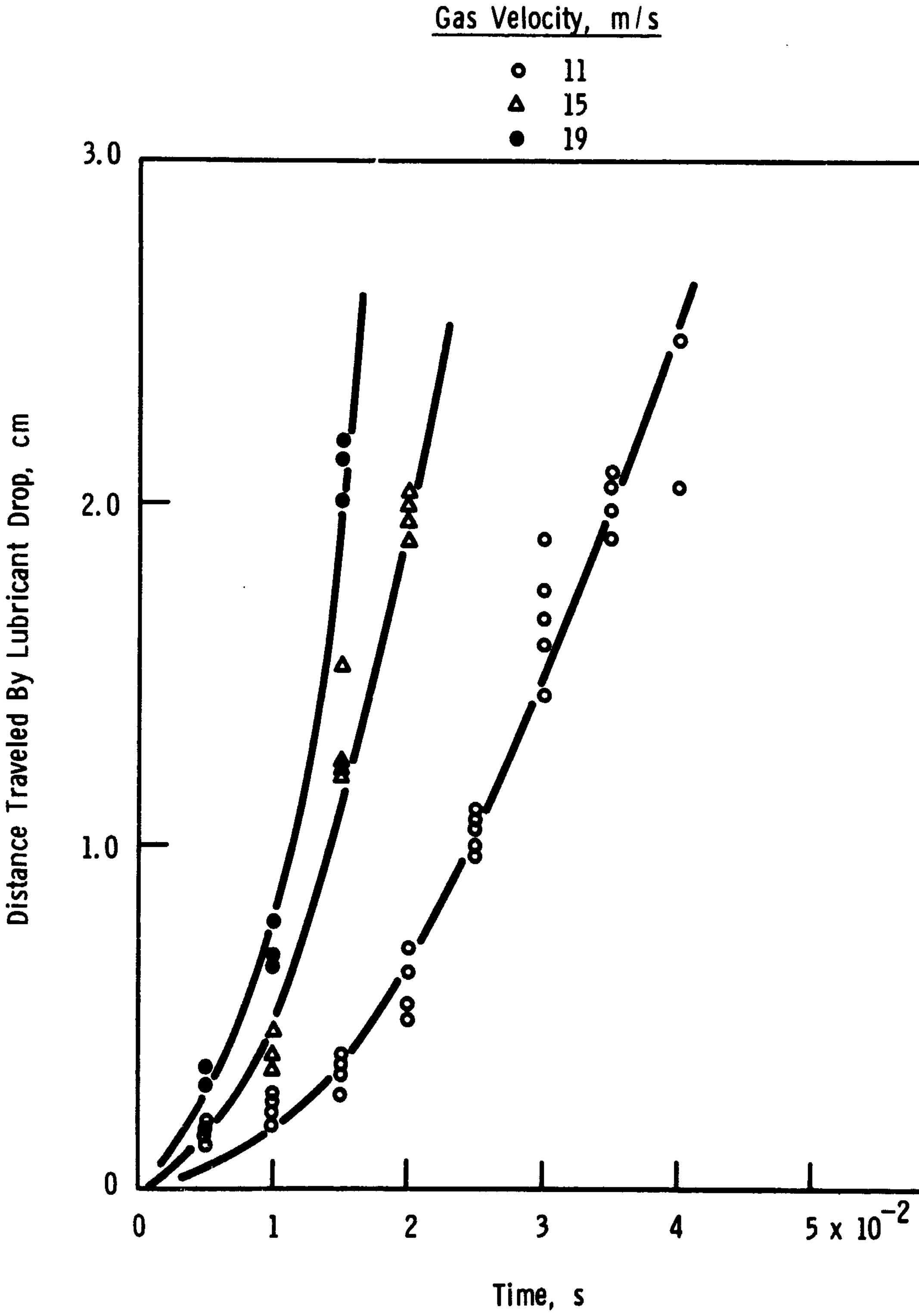

Table 7

Relationship Between Total Traverse Time and Gas Stream Velocity at Different Disc Temperatures

Gas Stream Velocity (m/s)	Total Traverse Time,* seconds x 10^2 600°F	700°F	800°F
11	5.0	3.0	2.2
15	2.6	2.0	2.0
19	1.9	1.6	1.7

*Total time taken by a lubricant drop to travel a distance of 2.54 cm.

Test Lubricant: XRM 109 F

Capillary Size: #1 (1 mm dia.)

Gas Stream Velocity (m/s)	Terminal Velocity of Drop, m/s FN 2961	XRM 109 F
11	0.63	0.51
15	1.15	0.98
19	1.50	1.34

Disc temperature: 600°F (589°K)

Capillary size: #1 (1-mm diameter)

It is apparent from the above comparison that the drops of FN 2961 travel faster than those of XRM 109 F for any corresponding gas stream velocity, although the differences are small. Once again, the differences in terminal velocity for these lubricants are probably due to nothing other than their viscosity differences under these test conditions. In analyzing the motion pictures for drop velocity, it was also observed that the drops of FN 2961 at disc temperatures of 700 (644°K) and 800°F (700°K), after detachment from the capillary tip, usually underwent a secondary breakup to form a shower of smaller drops after traveling breakup distances of 6 mm or longer (corresponding breakup time, 0.01 seconds). More detailed discussion of this behavior is included in the next section.

In an effort to examine the effect of capillary size on drop velocity, the capillary tube (#2) of 0.5-mm diameter was employed to measure the velocities of XRM 109 F drops at a disc temperature of 600°F (589°K). The gas stream velocities used were 11 and 15 m/s.

Figure 30 represents the effect of capillary size on the relationship between time and the distance traveled by lubricant drops. At a gas stream velocity of 11 m/s the values of the total traverse time taken by lubricant drops formed at the tips of #1 and #2 capillary tubes are 0.051 and 0.031 seconds, whereas at a gas stream velocity of 15 m/s, the total traverse time of the drops is nearly identical. The difference in the total traverse time for these capillary tubes at a gas stream velocity of 11 m/s can be related to both the drop size and the kinetic drop formation as would be expected from the previous analyses. In considering the effect of capillary size on drop size, it was generally observed from the drop size measurements that the effects of decreasing capillary size are that smaller drops are produced and the ligaments formed on drop surfaces appear to be smaller. Consequently, for a given gas stream velocity, more drops formed at the tip of the smaller capillary are free from ligaments. According to Equation (41), the capillary size not only has a direct influence on drop size, but also affects value of the correction factors, $f(D_o/D_p)$ and $F(D_o/D_p)$.

Figure 30

EFFECT OF CAPILLARY SIZE ON RELATIONSHIP BETWEEN TIME AND DISTANCE TRAVELED BY LUBRICANT DROPS

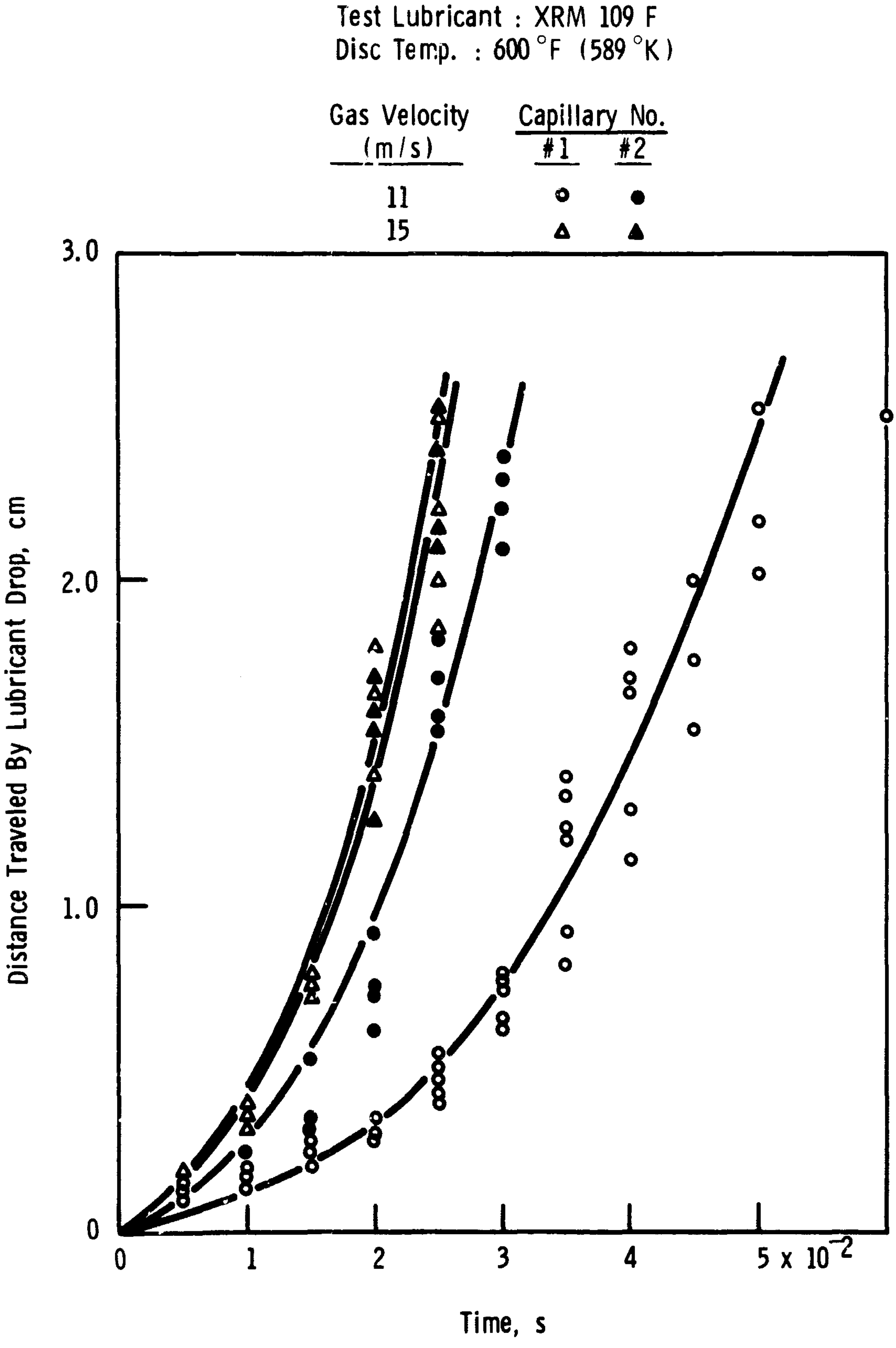

In analyzing the high-speed motion pictures for drop velocity, it was noted that angular velocity of the disc seemed to have no appreciable effect on the velocity of impinging drops. However, the velocities of the drops closely approaching the disc rotating at 312 rad/s were generally more difficult to determine and varied widely from run to run. As a result, divergence of the velocity data increased at 312 rad/s. This may be an indication that when the disc rotates at 312 rad/s, the tangential velocity of the surrounding gas near the disc is sufficiently large to influence the velocity of drops moving toward the disc. In addition to wide scattering of the experimental data, the effects of drop size, angular velocity of the disc, and velocity of gas jets impinging on the disc, particularly velocity of wall jets, are strongly coupled and difficult to separate. Therefore, with the limited results obtained in this series of experiments, it is very difficult to draw any quantitative conclusions on a possible windage effect generated by the actions of an impactor.

In summary, from the existing data, the only conclusions that can safely be drawn for this study are that:

- The terminal velocity of drops increases with increasing gas stream velocity.
- The drops generally are not fully entrained by turbulent eddies because of the significant differences in density between the gas and the lubricant drops.
- The velocities acquired by the drops seem to be largely dependent on the mechanisms of kinetic drop formation; i.e., the size and shape of ligaments on the drop surfaces greatly affect the velocity.

f. Drop Breakup

In analyzing the high-speed motion picture for drop velocity, we observed that drops of FN 2961, at disc temperatures of 700 (644°K) and 800°F (700°K), invariably underwent a secondary breakup after they were detached from the capillary tip. Similar behavior was observed with XRM 109 F only at a disc temperature of 800°F (700°K). Because of the limitation on photographic magnification imposed by the geometry of the experimental apparatus it was not possible to estimate the number and size of the satellite drops formed under these conditions. In order to have a better understanding of this phenomenon, a brief theoretical review has been made to examine the critical relative velocity at which a drop ruptures, and to estimate the size and number of the drops resulting from the breakup.

When a drop, detached from the tip of a capillary tube, is suspended and moving through a gas stream, there is imposed on the surface of the drop both a pressure and a shear distribution.

Because of the pressure distribution, the drop becomes deformed, assuming a shape such that surface tension compensates for the pressure distribution; while the shear induces a circulation within the drop, causing the pressure distribution to change. If the pressure variation becomes sufficiently great, there may be no stable shape that can compensate for the pressure variation; and the drop becomes increasingly deformed and will be broken up to produce a shower of very fine drops.

Knowing that this critical condition is achieved when the drag force just balances that of surface tension, the critical relative velocity, $(U_r)_{cr}$, at which a drop of size, D_p, will rupture is given by:

$$(U_r)_{cr} = \left(\frac{8\sigma}{C_D \rho_g D_p}\right)^{1/2} \tag{45}$$

Actually, Equation (45) cannot be derived on a rigorous basis, and can be considered only a crude approximation. Based on Equation (45), and the fluid properties of water and XRM 109 F at 72°F (295°K), drops of 1 mm diameter will deform and break up when the critical relative velocities reach 23.8 and 15.6 m/s respectively.

Equation (45) provides some basis for predicting under what conditions a drop will undergo breakup. It does not, however, give any basis for predicting the size and number of the drops resulting from the breakup. In an investigation of aerodynamic breakup of liquid drops, Wolfe and Anderson (27) have derived the following relationship for the average drop size, $\langle \bar{D}_p \rangle$, resulting from the aerodynamic breakup of a drop when exposed to a relative velocity, U_r:

$$\langle \bar{D}_p \rangle = \frac{5.14\, D_p^{1/6} \mu_\ell^{1/3} \sigma^{1/2}}{U_r^{4/3} \rho_\ell^{1/6} \rho_g^{2/3}} \tag{46}$$

This equation may be rearranged to the following form:

$$\frac{\langle \bar{D}_p \rangle}{D_p} = \frac{5.14 (\rho_\ell/\rho_g)^{2/3}}{\left(\frac{D_p U_r \rho_\ell}{\mu_\ell}\right)^{1/3} \left(\frac{D_p U_r \rho_\ell}{\sigma}\right)^{1/2}}$$

$$= \frac{5.14 (\rho_\ell/\rho_g)^{1/6}}{\left(\frac{D_p U_r \rho_\ell}{\mu_\ell}\right)^{1/3} \left(\frac{D_p U_r^2 \rho_g}{\sigma}\right)^{1/2}} \tag{47}$$

or Equation (46) is simply expressed as:

$$\frac{<\bar{D}_p>}{\bar{D}_p} = 5.14(\rho_\ell/\rho_g)^{1/6} \cdot (N_{Re})^{-1/3} \cdot (N_{We})^{-1/2}$$

Although it involved a large number of assumptions (drag coefficient assumed as unity; specific proportionality factors assumed in establishing fluid sheet thickness, breakup time, and shear stress; aerodynamic forces assumed large as compared with viscous and surface tension forces), the derivation of Equation (47) at least provides the basic information on how these various factors influence the aerodynamic breakup of a drop which is suspended in a high velocity gas stream. As a matter of interest, for a drop of 1.5-mm diameter and the fluid properties of XRM 109 F at 295°K $<\bar{D}_p>$ would be predicted from Equation (46) as 415 and 50 μm for relative velocities of 20 and 100 m/s, respectively.

g. Photographic Observation of Wetting Patterns

In order to obtain a better understanding of the impingement dynamics, part of the effort of this study was directed toward photographing the wetting patterns formed by drops impinging on a heated rotating disc.

For photographic purposes, the Hycam high-speed motion picture camera was directly focused on a predetermined area of the disc, on which the drops were to impact. The same drop-producing apparatus was used to provide the impinging stream of drops as was used in the previous studies.

With the magnification, illumination, and exposure time employed in this investigation, it was extremely difficult to obtain suitable photographs of the wetting patterns of lubricant films formed by the drops to illustrate different sequential stages of the impingement dynamics. Deformation and irregular impingement frequency of the drops also contributed to the problem.

Since efforts to print frames of the high-speed motion picture films showing the wetting patterns at disc temperatures of 600 (589°K), 700 (644°K), and 800°F (700°K) were unsuccessful, demonstrative photographs were prepared with XRM 109 F and #1 capillary tube by using a still camera. For this series of experiments, the disc, coated with flat wrought iron black paint in xylene and toluene, was sprayed with XRM 109 F drops at 295°K in the test chamber for 30 seconds, and then was photographed outside the chamber. The black coating was applied to the disc to raise the quality of the pictures by improving their tonal contrast.

Photographic results shown in Figures 31 and 32 represent the wetting patterns formed by XRM 109 F drops impinging on the rotating disc at 295°K and illustrate the effects of gas stream velocity and angular velocity on the wetting pattern. The photos reveal that as the drops strike the disc, they usually spread until their size is four or five times the original drop size, at which point the drops start to develop many small ligaments or streaks. Careful examination of these photographs also shows that as either the gas stream velocity or the angular velocity of the disc increases, the number of lubricant ligaments or streaks formed on the disc increases and their size decreases. The two variables tested - the gas stream velocity and the angular velocity - apparently have measurable effects on both the wetting pattern and the wetted area for a given lubricant flow and spraying time. The increase in wetted area and the difference in wetting pattern are probably caused by either the actions of high gas flows as wall jets, or the centrifugal forces generated by the rotating disc, or both. When this experiment was repeated at high disc temperatures, lubricant streaking was more violent and extensive, and the ligaments appeared to be much smaller. The photographic results also show that there is negligible variation of the total unwetted area at the center of the disc with increasing angular velocity. This implies that there probably is no measurable effect of windage from rotation on the radial displacement of drops impinging on the disc; however, this does not dismiss the possibility of tangential displacement of the drops. More detailed theoretical and experimental analyses are needed to secure information of this nature.

3. Evaluation of Reclassifying Nozzles and a Vortex Mist Generator

Wettability tests to evaluate novel or modified hardware related to microfog lubrication were carried out under test conditions specified under Task V. The hardware examined included a pneumatic reclassifying nozzle designed and fabricated by Mobil; a reclassifying nozzle designed and constructed by NASA, incorporating electrostatic principles to enhance particle collection; a reclassifying nozzle, designed and fabricated by Mobil, using electrostatic effects to improve particle size reclassification; and a microfog generator procured by NASA, featuring a pneumatic vortex atomizing nozzle.

The wetting rate data determined with these units are compared with those obtained with a conventional (convergent) nozzle, and with a venturi-type mist generator, in order to determine the effectiveness of the novel nozzles and the vortex mist generator. Advantages and limitations of these units are briefly discussed in terms of wetting rate and various critical parameters of microfog lubrication.

Figure 31

EFFECT OF GAS VELOCITY ON WETTING PATTERNS FORMED BY DROPLETS OF XRM 109 F IMPINGING ON A ROTATING DISC AT 295°K

Rotational Speed: 104 rad/s

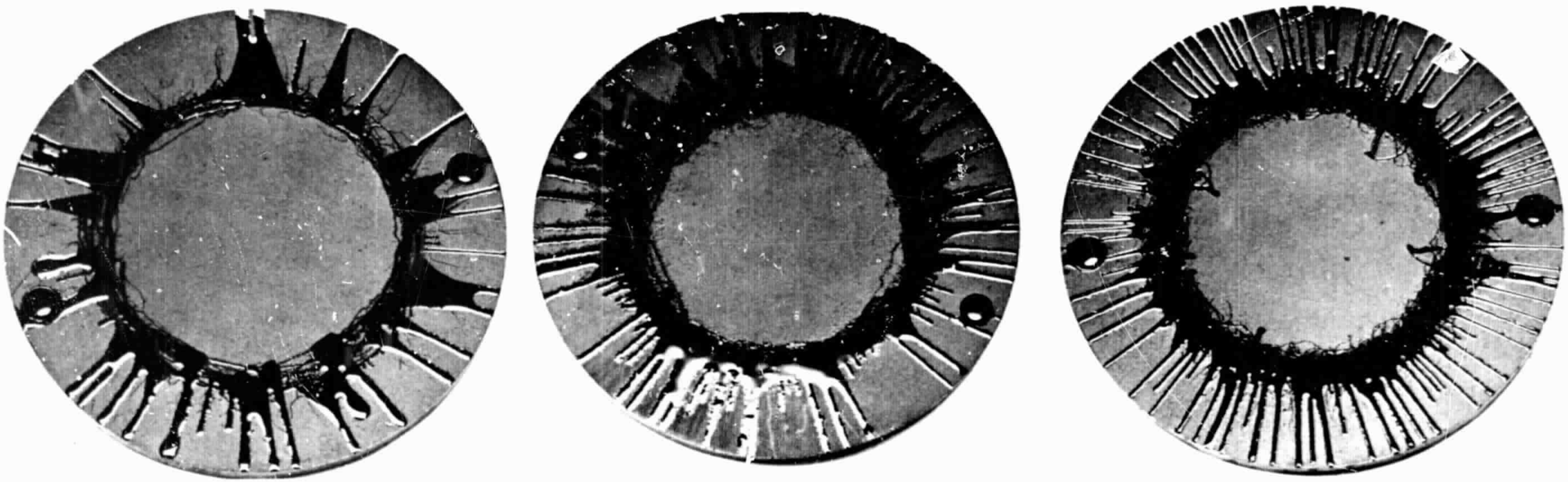

11 m/s　　15 m/s　　19 m/s

Figure 32

EFFECT OF ANGULAR VELOCITY ON WETTING PATTERNS FORMED BY DROPLETS OF XRM 109 F IMPINGING ON A ROTATING DISC AT 295°K

Gas Stream Velocity: 15 m/s

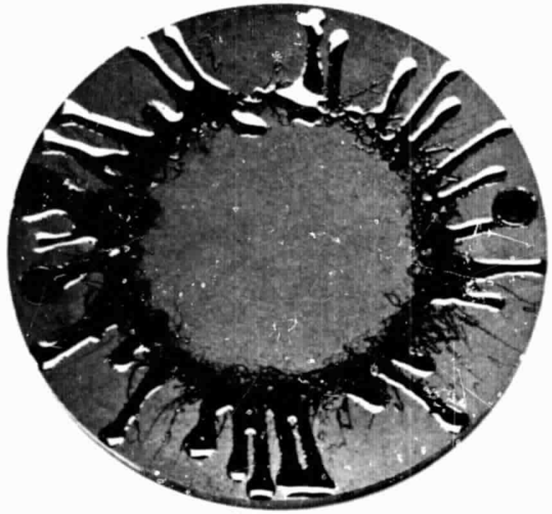

26 rad/s

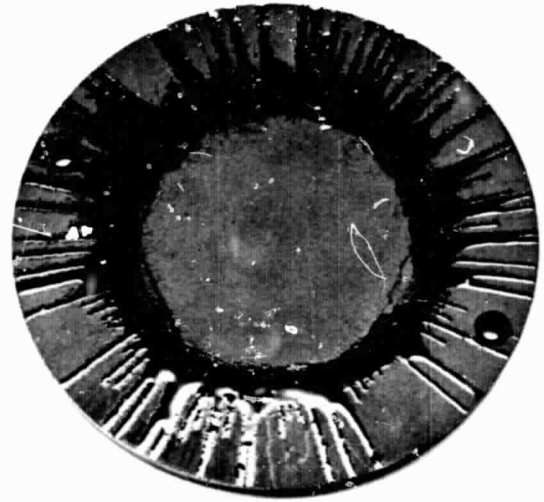

104 rad/s

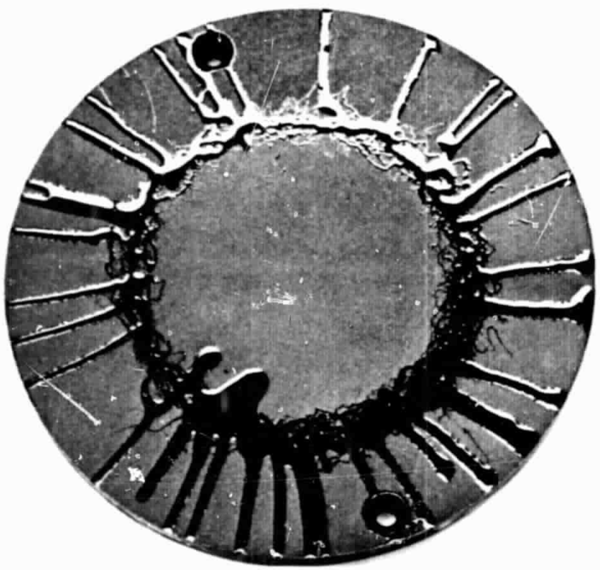

52 rad/s

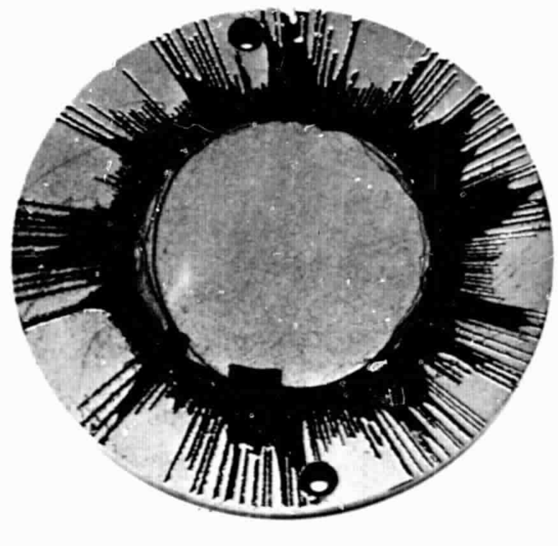

312 rad/s

a. Pneumatic Reclassifying Nozzle

A very simple way of increasing the coagulation of a microfog particle stream is to make the gas turbulent by mixing it with a means that may create eddies and swirls. Under this condition, the velocity of microfog particles relative to each other then becomes greater. The chance of collision of particles with one another must therefore be increased, and this implies an increased rate of coagulation. Microfog particles may also be indirectly converted to larger particles by wetting out on solid surfaces, followed by breakup and re-entrainment of the liquid film by the gas flow. This process may be enhanced by increasing the available solid surface and introducing turbulence to increase the probability of particle collisions with the solid surface. Keeping these mechanisms in mind, and combining the findings discussed in Section 2 and our earlier work (2), we have developed a novel pneumatic reclassifying nozzle which is schematically illustrated in Figure 33, and photographically presented in Figure 34. The nozzle basically consists of a conventional microfog nozzle with a layer of 150-mesh screen inserted in a converging section and a secondary gas nozzle which is mounted axially outside of the microfog nozzle. The nozzle is designed so that the primary microfog stream from the generator converges and expands through an orifice, and a secondary gas stream flows axially in the same direction as the microfog stream.

The wettabilities of XRM 109 F, using this nozzle, were determined with an angular velocity of 52 rad/s at gas flow rates to the microfog generator of 3, 4, and 5 cfm (1.4×10^{-3}, 1.9×10^{-3}, and 2.4×10^{-3} m^3/s). The secondary gas flow varied from 0 to 3 cfm (1.4×10^{-3} m^3/s), and the disc temperatures ranged from 600 to 800°F (589 to 700°K). Test results, reporting wetting time at different fractions of area covered, are summarized in Appendix F, with other related data including the wetting rates estimated graphically from the test results.

To illustrate improvement in wetting rate with this new nozzle, the wetting rate data for XRM 109 F at 600°F (589°K), without secondary gas flow through the nozzle, are compared with those obtained with a conventional convergent nozzle (No. 1). The comparison, shown in Figure 35, clearly indicates that the new pneumatic reclassifying nozzle increases the wetting rates of XRM 109 F for any given (oil/gas) mas flow ratios. Based on the specific wetting rate concept - wetting rate per unit (oil/gas) mass flow ratio, given by the slope of the straight-line plot - the new nozzle, even without a secondary gas stream, enhances wetting rate by 80 percent over the convergent nozzle. This is a strong indication that the presence of a fine screen alone greatly improves the efficiency of particle collection from a microfog stream through reclassification of the particles, which probably occurs primarily by the mechanism of wetting-out and re-atomization at the screen, but partly by coagulation. In a similar manner, the wetting rates at other disc temperatures can be compared to demonstrate effectiveness of this new nozzle in the improvement of wetting rate.

RF

Figure 33

SCHEMATIC OF
EXPERIMENTAL MICROFOG RECLASSIFYING NOZZLE

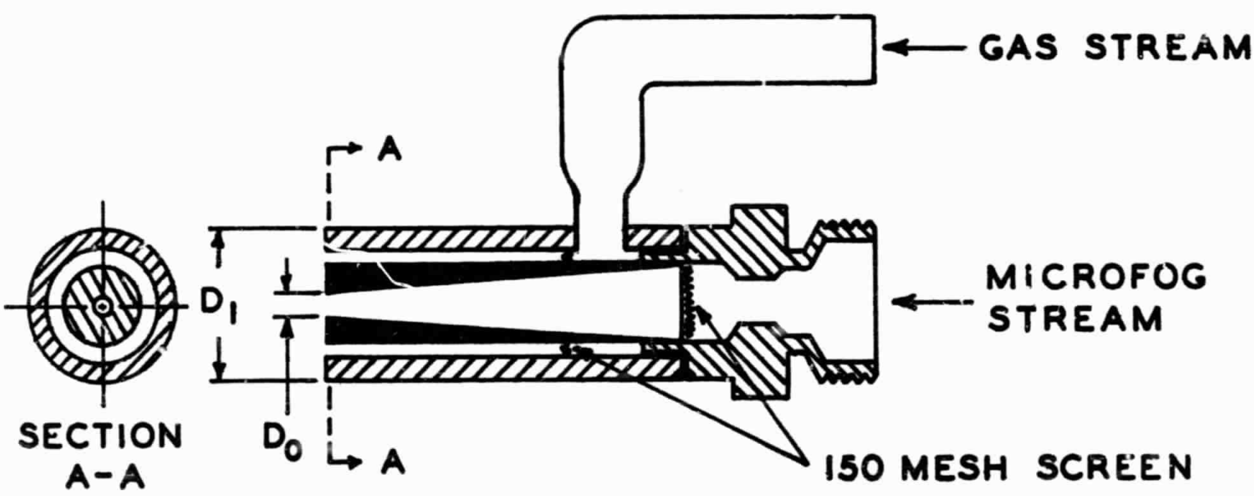

D_O : 0.171"

D_I : 0.830"

Figure 34

PHOTOGRAPHIC VIEW
OF EXPERIMENTAL RECLASSIFYING NOZZLE

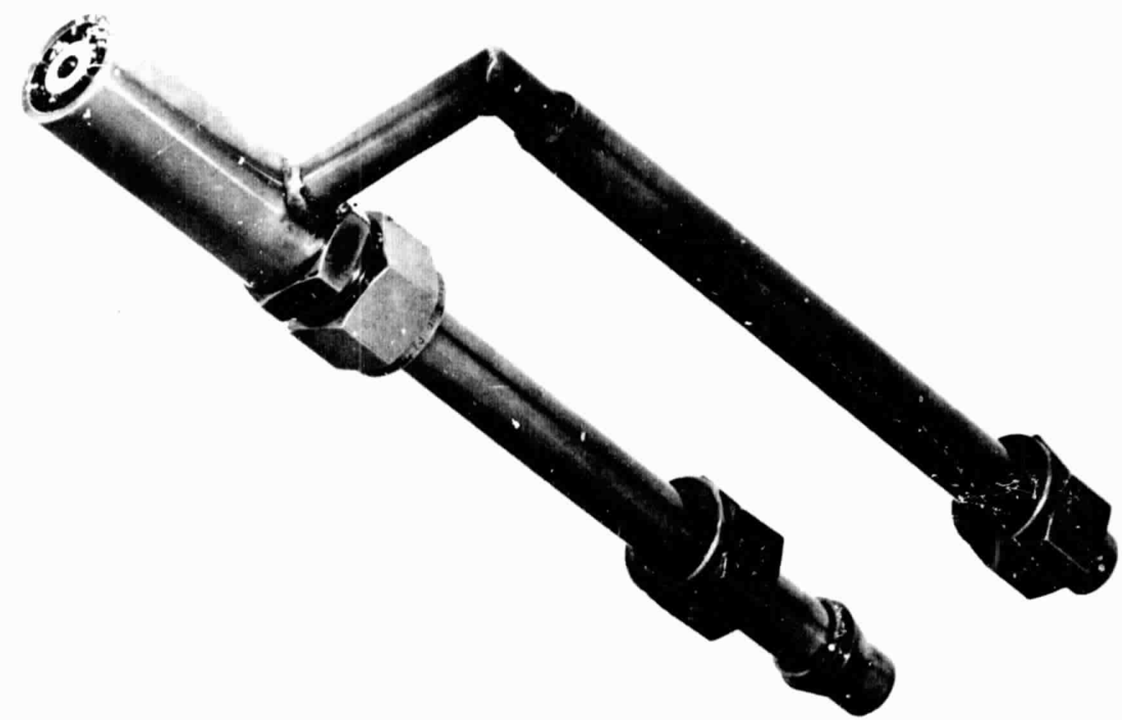

Figure 35

WETTING RATES OF XRM 109 F AS A FUNCTION OF (OIL/GAS)) MASS FLOW RATIO FOR DIFFERENT RECLASSIFYING NOZZLES

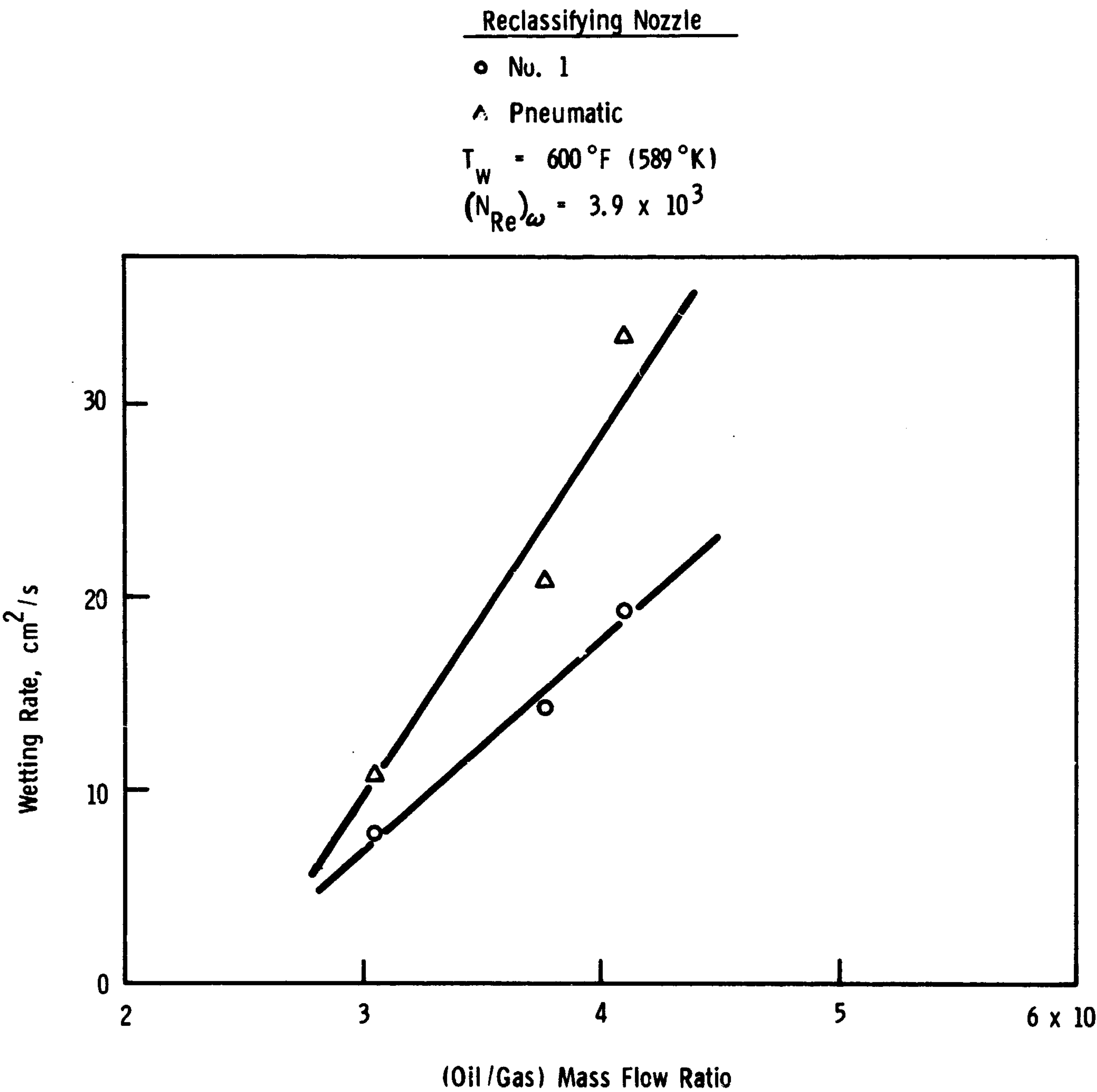

In order to investigate the effect of a secondary gas flow on wetting rate, the wettabilities of XRM 109 F were determined at primary gas flow rates of 3, 4, and 5 cfm (2.4×10^{-3} m^3/s) by progressively increasing secondary gas flow rate from 0 to 3 cfm (1.4×10^{-3} m^3/s). Test results with secondary gas flows, also reported in Appendix F, disappointingly fail to show any improvement over those without secondary gas flow. Instead, there is a slight decrease in wetting rate with increasing secondary gas flow rate, and excessive gas flow produces considerable streaking of the lubricant film.

In designing the pneumatic nozzle, the secondary gas flow was primarily intended to reduce loss of large lubricant drops, formed at the tips of reclassifying nozzles, by re-entraining the drops back into the primary microfog stream, and thereby increasing the overall collection efficiency. The test results, however, indicate that this anticipated advantage of the secondary gas flow is not realized under the present test conditions. A possible explanation is that spray time may not have been long enough for the large lubricant drops to be formed at the nozzle tip during a test run. If so, it is believed that the nozzle may still be effective in improving the collection of microfog particles when a microfog spray is applied continuously for an extended period, which is generally the case in most industrial applications. No attempt has been made to prove this point with the present test rig because extensive modification of the rig would be required. However, further examination of this type of nozzle could be of great value in advancing reclassification technology.

b. Electrostatic Reclassifying Nozzle

Although the fundamental idea of electrically separating particles suspended in gas streams was demonstrated many years ago, the development of adequate equipment and technology for coping with many problems associated with industrial application has been limited. Currently, the Cottrel precipitator and, to a lesser extent, the resin-wool charged filter developed from the modern theory of the electrostatic deposition process, are widely used in the field of industrial gas cleaning. Since deposition of microfog jets impinging on collecting surfaces may be viewed as the cleaning (or scrubbing) of a gas heavily laden with lubricant drops, it is of great interest to investigate how the collection of microfog particles may be affected by presence of electrostatic fields in reclassifying nozzles. Thus, a brief part of the contract effort has been aimed at testing this idea with simple reclassifying nozzles.

Physical Basis of Process

In the electrostatic deposition process, particles suspended in a gas are electrically charged and then driven to collecting electrodes under the forces of an electrical field. The process is distinguished from all mechanical or filtering processes in that the separating forces are exerted directly on the particles themselves rather than on the gas as a whole from a practical standpoint, the process is believed to be inherently efficient and economical in energy requirements (28).

Of the possible charging methods, corona discharge is the most practical and is universally used in electrostatic deposition practice. Cottrel's earliest work (29) on electrostatic deposition indicated the great superiority of the negative corona. A negative rather than a positive voltage is commonly used because with positive charges, periodic spark discharges occur even at low voltages (29,30).

Though particle charging mechanism in the corona discharge is not clearly understood, it is believed that the suspended particles are usually charged by ion bombardment under the forces of electrostatic field in the region between the corona wires and the collecting electrodes. The electrostatic separating forces acting on the particles, as might be expected, vary markedly with the strength of the electrostatic field to which the particles are exposed. The electrostatic field, in turn, is determined primarily by electrode geometry and by space-charge effects of the ionic current flow between the electrodes.

By visualizing this physical process of electrostatic phenomena with particulates, two electrostatic chargers (or reclassifying nozzles) have been developed to test the feasibility of applying this electrostatic depostion process to a microfog lubricant application system. These nozzles, with their electrostatic fields, might increase the collection efficiency of microfog particles by controlling either spray deposition or particle size. Figure 36 shows an external type reclassifying nozzle which consists of a pneumatic reclassifying nozzle attached with an aluminum electrode ring, while Figure 37 exhibits an internal electrostatic charger to be used with a conventional convergent reclassifying nozzle (No. 1 nozzle). After careful review of the test conditions involved and the physical limitations of the present test chamber, designs of the chargers were tailored accordingly, and test arrangements were made as follows:

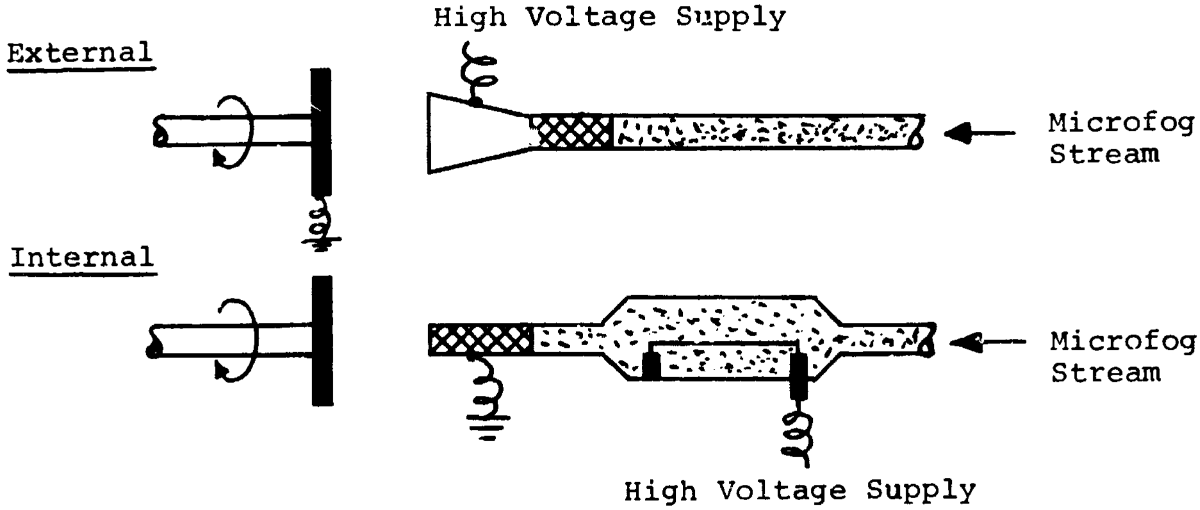

Figure 36

ADAPTER ASSEMBLY FOR ELECTROSTATIC RECLASSIFYING NOZZLE

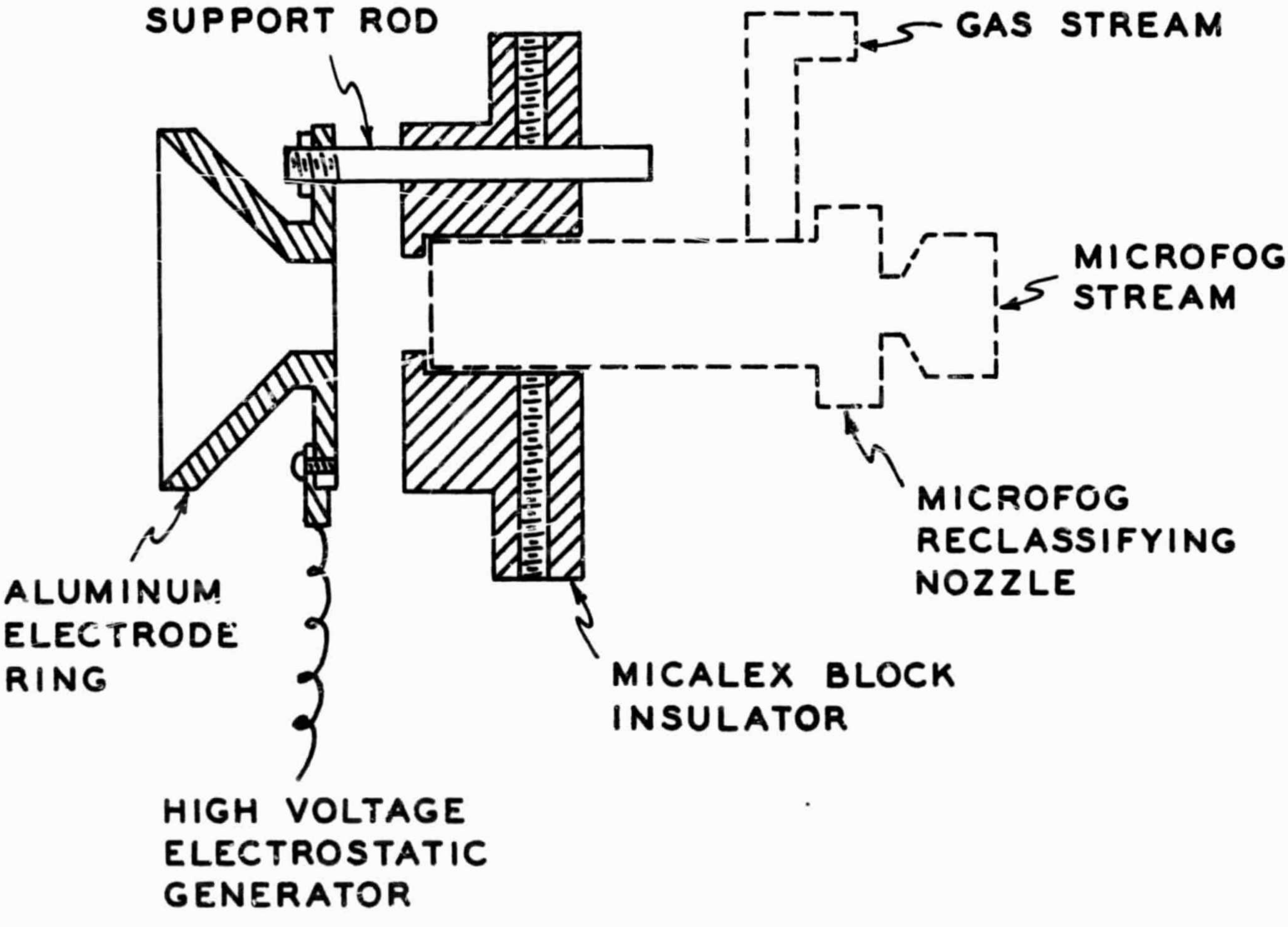

The basic difference between these test arrangements is the location where the applied electrostatic field is distributed in relation to the reclassifying nozzle - i.e., for the external type, the electrostatic field is externally distributed between the nozzle and the disc; whereas for the internal, it is distributed within the nozzle so that the disc may be free from the electrostatic charges. These arrangements are designed primarily to enhance the collection efficiency of microfog particles by controlling spray deposition in the first case, and by regulating particle size in the latter.

Wettability Determinations

In the wetting rate studies in Task III, wetting times of the microfog jets of XRM 109 F were relatively short at a spray distance of 1 in. (2.54 cm). Hence, to allow comparisons with electrostatic nozzles to be made under conditions where any improvement of the wettability of XRM 109 F through electrostatic effects could be readily demonstrated, preliminary wetting studies to a suitable range were made to increase the wetting time by varying spray distance. The preliminary wetting data, not reported here, suggested the spray distances of 1-3/8 in. (3.50 cm) for the external nozzle and 1 in. (2.54 cm) for the internal. After fixing the spray distances , the wettabilities of microfog jets of XRM 109 F were determined under various test conditions as specified in Section 1, Task V.

Test results showing the effects of electrostatic fields on wettability are summarized in Table 8 and Appendix G with other related data, including the wetting rates estimated graphically from the wetting data. Items (1) to (3) in Table 8 represent the wettabilities of microfog jets of XRM 109 F with a pneumatic reclassifying nozzle at a spray distance of 2-3/8 in., then at one of 1 in. (refer to Table 8) for corresponding (oil/gas) mass flow ratios.

In the series of test runs represented by Items (4) to (5), an effort was made to demonstrate the effect of the presence of the aluminum electrode ring on wettability, without any electrostatic charge, although attachment of the cone-shaped electrode ring to the pneumatic reclassifying nozzle changed the spray distance to 1-3/8 in. (3.5 cm). The test results in this series indicate that the presence of the electrode ring alone seems to have some effect on wetting rate; for a given (oil/gas) mass flow ratio the new external electrostatic nozzle (a combination of the pneumatic reclassifying nozzle with the electrode ring) increases wetting rate slightly. This increase in wetting rate was rather unexpected inasmuch as the electrode ring was designed to avoid interference with the flow characteristic of microfog jets impinging on the disc. Nevertheless, it is obvious from the wetting data that the impingement dynamics of microfog jets under the present test arrangement

Table 8

Wettability of Microfog Jets of XRM 109 F Through an Electrostatic Reclassifying Nozzle at 600°F (589°K)

Item	Run No.	Nozzle Type	Gas Flow Rate	Rate of Oil-Mist Output	Electrostatic Charge	Wetting Time (s)						Wetting Rate
			$(m^3/s) \times 10^3$ @ 40 N/cm^2 & 366°K	$(cm^3/s) \times 10^2$	(KV)	0.14	0.25	0.39	0.55	0.76	1.00	(cm^2/s)
1	XRM 45-1	Pneumati-	1.4 (3 cfm)	2.0	--	--	4.03	6.73	8.86	--	13.67	6.4
2	XRM 44-5	"	1.9 (4)	3.3	--	--	1.20	2.33	3.50	5.82	7.05	9.6
3	XRM 44-4	"	2.4 (5)	4.3	--	--	0.95	1.88	2.74	--	5.30	15.0
4	XRM 44-1	Electro-static	1.4	2.0	0	--	3.76	5.98	8.25	10.52	11.69	7.0
5	XRM 44-2		1.9	3.3	0	0.25	1.28	1.90	--	4.78	5.60	12.0
6	XRM 44-3	"	2.4	4.3	0	--	0.96	1.73	2.48	--	3.54	19.2
7	XRM 45-4	"	1.4	2.0	-15	2.30	Streaky flow to end of test run				12.33(?)	
8	XRM 45-3	"	1.9	3.3	-15	--	0.85	1.50	Streaky flcw		3.34 (?)	
9	XRM 45-2	"	2.4	4.3	-15	--	0.73	1.60	Streaky flow		3.07 (?)	
10	XRM 45-5	"	1.9	3.3	-5	--	1.37	2.08	Streaks		6.27 (?)	
11	XRM 46-1	"	"	"	-25	--	1.16	2.28	Streaks		3.98 (?)	
12	XRM 46-2	"	"	"	+15	--	1.46		Streaks		4.05 (?)	

Test Conditions - Oil Temperature: 200°F (366°K)
Angular Velocity: 52 rad/s
Spray Distance: 1-3/8" (3.5 cm) for electrostatic nozzle, and 2-3/8" (6.04 cm) for pneumatic nozzle

may have been affected by the electrode ring, possibly through a change in diffusion angle of either the impinging jets or the wall jets.

Items (7) to (9) represent an attempt to investigate the electrostatic effects on wettability by repeating the test runs indicated by Items (4) to (6) with a high voltage charge of -15KV to the electrode ring. Here, the electrostatic field was probably distributed between the ring and the disc, but its strength and distribution were not measured in this study, although the voltage input was known at the power supply (Beekman Instruments, Inc.). Careful analysis of the high-speed motion picture films taken in this series of tests reveals that the electrostatic field between these electrodes has a pronounced effect on the wetting patterns of thin lubricant films formed by impinging microfog jets of XRM 109 F, changing the uniform thin film flow to a streaky flow (see Ref. 2 and 3). This streaking of the lubricant films was so heavy, in fact, that no meaningful wetting data could be obtained for comparison.

In Items (10) to (12), the strength of the electrostatic field and the polarity of the electrodes were varied to determine whether these factors had any effect on wettability. These tests once again showed streaked wetting patterns very similar to that of the directly comparable test summarized by Item (8). Thus, with the present test results, it is difficult to draw any conclusion concerning electrostatic effects on wettability. While the exact cause of the observed is unknown, it may be reasoned that the electrostatic field, because of dielectric properties of the lubricant, may impose external stresses on the surface of the lubricant. Under the action of the electrostatic field, surface charges build up on the lubricant. These charges may, in certain circumstances, result in instability of the lubricant surface, as in the analogous case of electrostatic atomization. The circumstances under which the instability occurs probably depend, among other factors, on the surface tension, the dielectric constant, the film thickness, and the electrical conductivity of the lubricant. Unquestionably, extensive efforts are required to begin to understand the complex problems involved in dealing with electrostatic phenomena of particulates.

With the failure of the external nozzle to demonstrate any beneficial effects of an electrostatic field on the collection of microfog particles, a brief examination of the concept of electrostatic reclassification, for which the internal nozzle was designed, becomes of interest. Since the nozzle was made of a Pyrex glass tube with a discharge electrode, wettability tests were conducted under atmospheric pressure.

A review of the test results, presented in Appendix G, seems to indicate a definitive general trend toward increased wetting rate with the electrostatic field. Moreover, unlike results with the external electrostatic nozzle, the wetting pattern of the thin lubricant films is uniform. The difference in wetting pattern between these two nozzles may be due in part to the difference in the spray distance, but probably is caused predominantly by different distribution of the electrostatic fields. To prove this, the strength and distribution of the electrostatic field applied to the nozzle must be determined by measuring electrostatic potential with an electrometer. This has not been done in this study.

In summary, based on literature review and preliminary tests, there appears little doubt that electrostatic fields have potential importance in the collection of microfog particles. However, definitive values could not readily be demonstrated by the experimental data obtained with the present electrostatic nozzles. Further refinement of the nozzles, particularly the internal nozzle, and an improved physical arrangement of the disc and the nozzles, may be needed to achieve the original objective of demonstrating beneficial electrostatic effects on wettability.

c. <u>Vortex Mist Generator</u>

The rapid growth in acceptance of microfog lubricant application systems for industrial use has been accompanied by a steady demand for further improvements and refinements. In response, continuous efforts have been made by equipment builders to develop new hardware and by oil companies to provide lubricants specifically formulated for microfog lubrication. Recently, a microfog generator featuring a pneumatic vortex atomizing nozzle has become commercially available. The vortex generator, schematically shown in Figure 38, is claimed to offer significant advances toward low maintenance and highly efficient mist generation (31). Therefore, consistent with the objective of optimizing the overall performance of a microfog lubrication system, an effort was made to evaluate performance of the new generator.

Before making a series of wettability tests as specified in Task V, preliminary test runs had to be conducted to determine the rate of oil-mist output relative to gas flow rate to the generator, and size and distribution of the particles. During these tests, we learned that the vortex mist generator supplied through NASA is rated at only a 100 bearing inch (BI)* capacity instead of the 500 BI model needed for comparing with the venturi generator. Because of its restricted capacity, the maximum obtainable gas flow rate to the vortex atomizing chamber (nozzle) is limited to only 1.3 cfm (0.7×10^{-3} m^3/s) at 45 psig and 200°F (40 N/cm^2 and 366°K) at an inlet gas pressure of about 100 psig (78 N/cm^2).

*BI: An arbitrary unit of measurement used to rate the lubricant requirements of mechanisms lubricated by microfogs. For this report, <u>cfm</u> is preferred to the Bearing Inch as the design unit.

Figure 38

SCHEMATIC VIEW OF A VORTEX MIST GENERATOR

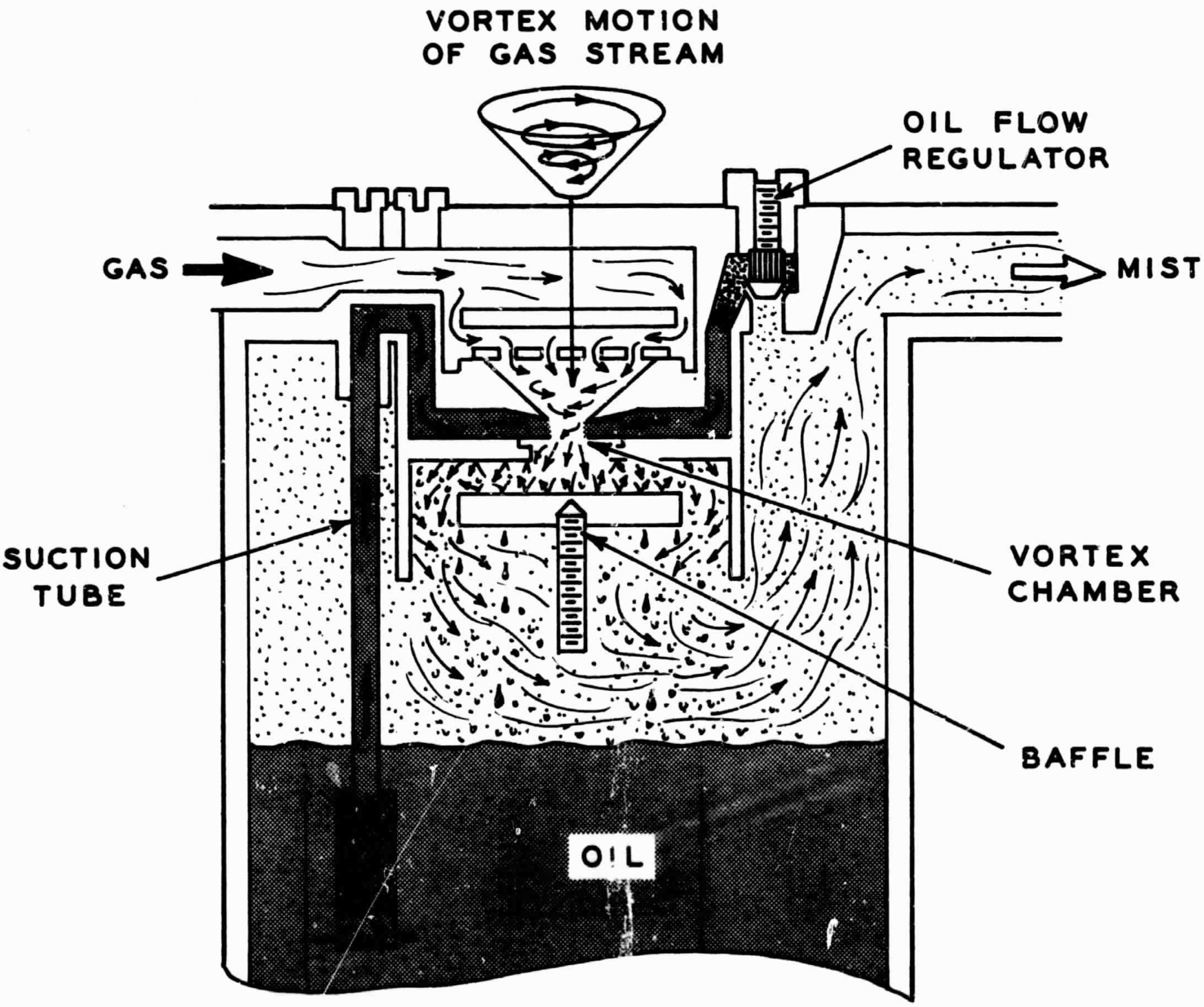

c3

Despite this shortcoming, and because there remained insufficient time to obtain a larger model, two series of wettability tests for XRM 109 F were made with the 100 BI vortex mist generator. In one series, a conventional convergent nozzle (No. 1) used in the previous tasks was used. The other series employed the new pneumatic reclassifying spray nozzle.

Test results, presented in Appendix H, reveal, as expected, basically the same relations of wetting rate to all of the basic parameters such as impaction velocity, particle size, (oil/gas) mass flow ratio, as those already established with a conventional Venturi-type generator. However, no attempt was made to compare results obtained with these two microfog generators of different types because of the difference in the relative sizes of their atomizing nozzles - i.e., 100 BI for the vortex generator and 500 BI for the Venturi-type generator. This difference has made characterization of the new vortex generator difficult, and its fair comparison with the conventional generator nearly impossible. This point is emphasized by the recognition that the sizes and distributions of particles from pneumatic atomizing nozzles are primarily a function of lubricant flow rate, gas flow rate (or dynamic forces of the atomizing gas), nozzle dimensions, (gas/oil) mass flow ratios, and physical properties, particularly viscosity of the lubricant. Obviously, the particle sizes and distributions have a pronounced effect on wetting rate (2). Consequently, use of the wetting rate criterion cannot properly or fairly compare the effectiveness of these atomizing nozzles of dissimilar capacity.

As a matter of interest, the particle size distributions of XRM 109 F with these two mist generators, determined at slightly different conditions for the reasons already given, are listed in Table 9. It is interesting to note from Table 9 that although the arithmetic mean diameters of the microfog particles from each generator are almost identical, there is a slight difference in the size distribution of the particles counted. Again, it is difficult to attribute the difference in $\sum_{i=1}^{N}$ Ni to any difference in the atomization principles of the classical Venturi nozzle and the new vortex atomizing nozzle. Instead, the difference may be the result of variation in the geometrical configuration of the nozzles, specifically the effect of impactor (baffle) design. Most atomizing nozzles commonly used in commercially available generators, including the new vortex mist generator, have in the generator a solid impactor, the purpose of which is to screen out large particles leaving the atomizing nozzle, allowing only particles below some maximum size to leave the generator. In our earlier work (2), the importance of impactor design in the Venturi-type atomizer has been discussed with the screen size, and the distance between nozzle and impactor, at various gas flow rates. In future work, it would be of considerable value to make a complete characterization of the new vortex mist generator.

Table 9

Particle Size Distributions of XRM 109 F Microfog With Different Generators

	Channel	Size Range (μm)	Particle Size Distribution* Venturi[(a)]	Vortex[(b)]
XRM 109 F				
Nozzle No. 1	1	0.5–0.7	486	573
	2	0.7–1.0	638	395
	3	1.0–1.4	357	193
	4	1.4–2.0	24	13
	5	2.0–2.8	1	0
	6	2.8–4.0	0	29
	7	4.0–5.6	0	1
	8	5.6–8.0	0	0
Arithmetic Mean Diameter (μm):			0.88	0.90

*The number of particles counted in 10-second period

(a) at gas flow rate of 2 cfm and atomizing pressure of 27 psig (28.4 N/cm^2)

(b) at gas flow rate of 1.3 cfm and atomizing pressure of 96 psig (75 N/cm^2)

IV. NOTATIONS

a	:	constant defined in Equation (12)
A	:	surface area
A_o	:	total cross-sectional area
A_1, A_2, A_3	:	surface area at reference 1, 2, and 3 respectively
b	:	constant defined in Equation (12)
C_D	:	drag coefficient
C_p	:	specific heat capacity at pressure constant
C_{p_1}, C_{p_2}	:	specific heat capacity of lubricant and gas, respectively
d	:	notation of differential
$\bar{d}$	:	average particle diameter
D	:	impactor size = $2R_o$
D_o	:	orifice diameter, capillary size
D_p, $\langle \bar{D}_p \rangle$	:	drop size, average drop size
$f(D_o/D_p)$	:	correction factor
$F(D_o/D_p)$	:	correction factor
g, g_c	:	gravitational force and constant, respectively
G	:	Mass flow rate of gas
h	:	convective heat transfer coefficient
hg	:	convective heat transfer coefficient of gas stream
k	:	thermal conductivity
kg	:	thermal conductivity of gas stream
K	:	constant defined in Equation (34)
M_ℓ	:	amount of lubricant evaporated
N_i	:	number of microfog particles
N	:	total number of microfog particles
N_{Nu}	:	Nusselt number = (hD_o/k_g)
N_{Pr}	:	Prandtl number = $(C_{p_2}\mu/kg)$
$(N_{Re})_m$	:	mass-flow Reynolds number = $(D_oG/\mu g)$
$(N_{Re})_\omega$	:	rotational Reynolds number = $(\omega R_o^2 \rho_g/\mu_g)$
N_{st}	:	Stanton number = $(h/C_{p_2}G)$ = $(h/C_{p_2}\rho_g U_\infty)$
N_{stk}	:	Stokes number = $[2(N_{Re})_m \rho_g \bar{d}^2/72\rho_\ell D2]$
N_{we}	:	Weber number = $(D_p U_r \rho_g/\sigma)$
P	:	pressure
q	:	heat flux, $q = h\Delta T$

IV. NOTATIONS (Cont'd)

Q	:	heat flow rate $Q = q \cdot A$
Q_f, Q_g	:	heat flux of microfog and gas stream, respectively
Q'_g, Q''_g	:	reference heat flux of gas stream at different times
r	:	radial distance, radius
r_1, r_2	:	radial distance at reference 1 and 2, respectively
$R_.$	:	radius of rotating disc
t	:	time
T	:	temperature
T_B	:	temperature at boiling point
T_G	:	outlet gas temperature
T_H	:	temperature at a transducer junction
T_i	:	temperature at interface, film temperature
T_m	:	mean temperature
T_w	:	wall temperature, temperature at disc surface
T_∞	:	inlet gas temperature, gas temperature at ∞
u	:	velocity, lubricant velocity in a capillary tube
u_r	:	radial velocity of lubricant film
$\langle \bar{u}_r \rangle$	:	average (log-mean) surface velocity of lubricant film
U_r	:	relative velocity, $U_r = U_\infty - u$, radial velocity of microfog stream
U_∞	:	gas stream velocity at ∞
V	:	volumetric flow rate of lubricant
W	:	total mass flow rate of microfog stream
z	:	z-direction

GREEK LETTERS

α	:	constant in Equation (34)
β	:	constant in Equation (34)
γ	:	constant in Equation (34)
Γ	:	total specific flow rate
δ	:	film thickness, constant in Equation (34)
δ_t	:	thickness of thermal boundary layer
Δ	:	denoting a difference
η	:	collection efficiency, $\eta = (\omega/\nu)^2 \cdot Z$
θ	:	dimensionless temperature = $(T - T_\infty/T_W - T_\infty)$
λ	:	latent heat of evaporation
μ	:	dynamic viscosity
μ_g, μ_ℓ	:	dynamic viscosity of gas and liquid, respectively
μ_B, μ_W	:	viscosity at bulk and wall temperature
ν	:	kinematic viscosity
π	:	3.14
ρ	:	density
ρ_g, ρ_ℓ	:	density of gas and liquid, respectively
σ	:	surface tension
Σ	:	denoting summation
τ_i	:	interfacial shear = $\mu\left(\frac{\partial u}{\partial r}\right)$
ϕ_1, ϕ_2	:	functions defined in Equations (30), (31), and (32)
χ	:	dimensionless velocity = $(\omega R_O/U_\infty)^2$
ω	:	angular velocity

V. REFERENCES

1. Shim, J. and S. J. Leonardi; "Microfog Lubricant Application System for Advanced Turbine Engine Components", Task I Report, NASA CR-72291, Sept. (1967).

2. Shim, J. and S. J. Leonardi; "Microfog Lubricant Application System for Advanced Turbine Engine Components", Final Report, NASA CR-72489, Sept. (1968).

3. Shim, J. and S. J. Leonardi; "Microfog Lubricant Application System for Advanced Turbine Engine Components", Task I and II Report, NASA CR-72743, May (1970).

4. Rhoads, W. L.; "Supersonic Transport Lubrication Systems Investigation" NASA CR-73496, Dec. (1968).

5. Hodgson, J. W., R. T. Saterback, and J. E. Sunderland; J. of Heat Transfer, Trans ASME, Series C, 90, 457 (1968).

6. Thomas, W. C. and J. E. Sunderland; Ind. Eng. Chem. Fundamental 9, 368 (1970).

7. Coon, C. W. and H. C. Perkin; J. of Heat Transfer, Trans ASME, Series C 92, 506 (1970).

8. Pohlhausen, E.; Zeitschr. f. Math. u. Mech., 1, 115 (1921).

9. Colhurn, A. P.; Trans. AICh.E., 29, 174 (1933).

10. Wagner, C.; J. of Applied Physics, 19, 837 (1948).

11. Kreith, F., E. Doughman, and H. Kozlowski; J. of Heat Transfer, Trans ASME, Series C, 85, 153 (1963).

12. Millsaps, K. and K. Pohlhausen; J. of Aeronautical Sci., 19, 120, (1952).

13. Sparrow, E. M. and J. L. Grigg; J. of Heat Transfer, Trans. ASME, Series C, 82, 294 (1960).

14. Tien, C. L. and I. J. Tsuji; J. of Heat Transfer, Trans. ASME, Series C, 87, 184 (1965).

15. Schrader, H.; Forschungsch. Ver. Dtsch. Ing., 484 (1961).

16. Schliechting, H.; "Boundary Layer Theory", 4th Ed., Pergamon Press, London (1960) Pg 78-83.

17. Scholtz, M. T. and O. Trass; AICh.E. Journal, 16, 81 (1970).

18. Gardon, R. and J. C. Akfirat; Int. J. of Heat and Mass Transfer, 8, 1261 (1965).

19. Gardon, R. and J. C. Akfirat; J. of Heat Transfer, Trans. ASME, Series C, 88, 101 (1966).

20. Sieder, E. N. and G. E. Tate; Ind. Eng. Chem., 28, 1429 (1936).

21. McAdams, W. H.; "Heat Transmission", 2nd Ed., McGraw-Hill, New York (1942) Pg 168.

V. REFERENCES (Cont'd)

22. Hughes, R. R. and E. R. Gilliland; Chem. Eng. Progr., 48, 497 (1952).

23. Hawkins, W. D. and R. C. Brown; J. Am. Chem. Soc., 499 (1919).

24. Tamada, K. and Y. Shibaoka; J. of Phys. Soc., Japan, 16, 2149 (1961).

25. Rayleigh, Lord; Proc. London Math. Soc., 10 (1878).

26. Lane, W. R.; Ind. Eng. Chem., 43, 1312 (1951).

27. Wolfe, H. E. and W. H. Anderson; Aerojet-General Corp., Report No. 0395-04 (18) SP., April (1964).

28. White, H. J.; "Industrial Electrostatic Precipitation" Addison-Wesley Publishing Co., Mass. (1963) Pg. 126.

29. Cottrell, F. G.; U.S. Patent 895,729 (1908).

30. Faith, L. E., et.al.; Ind. Eng. Chem. Fundamentals, 6, 519 (1967).

31. Lyth, W.; "The Vortex Generator - Newest Approach to Oil-Mist," presented at the 26th ASLE Annual Meeting in Boston, Mass. May 3-6, (1971) Pg. 115.

VI. APPENDICES

APPENDIX A

APPENDIX A

Statement of Work
Contract NAS3-13207

I. SCOPE OF WORK

The Contractor shall furnish the necessary personnel, facilities, services, and materials (except the Government Furnished Property as specified in Article XIV) and otherwise do all things necessary for, or incident to, the work described below:

A. Task I - Mist Generator Tests

The Contractor shall investigate the wettability of five test lubricants under a range of ambient conditions and in a manner as prescribed in this task.

1. Test Lubricants

The following five lubricants shall be used in this investigation:

a. Dupont Krytox 143 AC perfluorinated fluid (non-formulated).

b. Monsanto MCS-293 modified polyphenyl ether.

c. Mobil XRM-109F synthetic paraffinic hydrocarbon.

d. Mobil XRM-209A, pentaerythritol ester.

e. Humble FN-2961 super refined (deep-dewaxed) naphthenic mineral oil (base for Humble FN-3158).

Substitution of items in this list shall be made if recommended by the Contractor and approved by the NASA Project Managers.

2. Test Rig and Instrumentation

The Contractor shall provide the microfog lubricant applicator test rig, test specimens, and instrumentation that were designed, fabricated, and used under NASA Contract NAS3-9400. This equipment is described in Task I of Appendix I, Statement of Work, and subsequent amendments of that contract.

3. Test Procedure and Conditions

The Contractor shall perform a series of wettability tests using each of the five test lubricants listed in Task I, paragraph A.1 under each set of standard test conditions. These standard test conditions are as listed below and shall be used throughout this contract unless otherwise specified.

a. Standard Test Conditions

(1) Oil and gas temperatures in generator: 200 (± 10) °F.

(2) Test specimen temperature: 600, 700, and 800 (± 10) °F.

(3) Nitrogen flow rate: 3, 4, and 5 cfm (at 45 psig and 200°F).

(4) Spray nozzle: converging type, orifice diameter of 0.171 in. and 0.281 in.

(5) Spray distance between nozzle and test plate: 1 inch.

(6) Test chamber pressure: 45 (± 5) psig.

(7) Test specimen: 2 (± 1/2) in. x 2 (± 1/2) in. x 1/4 (± 1/16) in. made of hardened CVM WB-49 material and finished circumferentially ground to 4 to 8 μin. RMS.

b. Wettability shall be determined using the photographic technique developed in Contract NAS3-9400.

c. Prior to the start of each run, the test chamber and specimen shall be brought to the required temperature. A stream of pure nitrogen, at the same rate as the nitrogen stream to be introduced from the microfog generator, shall then be sprayed through the nozzle. The run shall be started by switching to the nitrogen stream carrying fog from the microfog generator when the specimen temperature has recovered to the control temperature, and the nozzle temperature has reached equilibrium.

RC

d. All lubricants shall be degassed for a 72-hour period immediately before running by means of a mechanical vacuum pump capable of maintaining a pressure of 10^{-3} mm Hg, while vibrating the fluid. The test chamber shall be pumped down with a mechanical pump prior to a run and then purged with nitrogen during the run.

e. Test Runs

(1) Metal test specimens shall be cleaned before each test in the following manner:

(a) Rinsed with acetone.

(b) Scrubbed with moist levigated alumina and a soft polishing cloth.

(c) Thoroughly rinsed with tap water.

(d) Rinsed briefly with distilled water.

(e) Rinsed with ethyl alcohol.

(2) A run shall consist of operating the generator with a test lubricant under a set of conditions while impinging the mist on the specimen. After reaching equilibrium conditions of pressure, temperature, and flow, the wettability shall be recorded by measuring the time required to cover the entire metal specimen with a complete film of oil. Similarly, the particle size and velocity shall be determined under the identical conditions. A minimum of 90 runs shall be made to include all test conditions in Task I.

B. Task II - Optimization of Microfog Lubrication

The Contractor shall investigate the effects of various factors on wetting rate in microfog lubrication. These shall include the effect of gas and oil temperature on wettability, modification oil properties by additives, and the effect of test plate surface condition. Two reference test fluids common to both the Task I and Task II shall be selected, one of which will be Mobil XRM-109F synthetic paraffinic hydrocarbon. Selection of the second fluid by the Contractor shall be subject to approval by the NASA Project Manager. One spray nozzle, selected by the Contractor and approved by the NASA Project Manager, shall be used in this task. The test procedure and equipment of Task I shall be used.

1. <u>Effect of Gas and Generator Temperature</u>

   The Contractor shall perform two series of wettability tests under the standard test conditions as listed in Task I, paragraph C, with the exception that the gas and generator temperature shall be 100 and 300 (± 10) °F. A minimum of 36 runs shall be made to include all these conditions.

2. <u>Effect of Additives</u>

   The Contractor shall perform a series of wettability tests under the standard test conditions as listed in Task I, paragraph 3, with the following exceptions:

   a. Test plate temperature shall be held at 700 (± 10) °F only.

   b. Nitrogen flow rate shall be held at 3 cfm only.

   c. Four blended fluids shall be tested. The blended fluids shall consist of: (1) Mobil XRM-109F plus 10 weight percent of Kendall paraffinic resin (20,000 SUS), (2) Mobil XRM-210A, formulated pentaerythritol ester, (3) Monsanto MCS-2931 and (4) DuPont additive No. 9530-49. Substitution of any of these fluids shall be made if recommended by the Contractor and approved by the NASA Project Manager. A minimum of 4 runs shall be made to include all these conditions.

3. <u>Effect of Test Plate Surface</u>

   The Contractor shall perform a series of wettability tests using two fluids (XRM-109F and another fluid common to Task I and Task II selected by the Contractor and approved by the NASA Project Manager) with varying surface roughnesses of test plate under the standard test conditions as described in Task I, paragraph 3 except that the test plate temperature shall be held at 700 (± 10) °F and the nitrogen flow rate held at 3 cfm during all the runs. The surface roughness of test plate shall include two finish types (i.e., honed and lapped) and two coating types (i.e., black oxide and fluid decomposition product). A minimum of 8 runs shall be made to include all these conditions.

C. <u>Task III - Wettability of Lubricants on a Rotating Disk</u>

The Contractor shall investigate the stability of a thin oil film on a heated rotating metal disk and its effect on wettability.

1. <u>Test Chamber</u>

The Contractor shall design and fabricate a test chamber with a rotating, flat disk or test specimen. Test chamber design shall be approved by the NASA Project Manager prior to its fabrication. The disk shall be 4 inches in diameter, made of CVM WB-49 tool steel circumferentially ground to 4~8 μinches RMS, and shall be capable of variable rotative speeds up to 5,000 rpm and higher as limited by the power requirement for a driving motor. The disk shall be mounted in a vertical position in the test chamber with a flat side facing the spray nozzle, positioned at a right angle to the disk surface and at one inch from that surface. The chamber shall be a thermostatically and pressure controlled oven for simulation of pressures up to 80 psia and temperatures up to 1000°F. The chamber shall have an observation port through which visual and photographic observations of the test specimen can be made. A heater mounted closely behind the rotating disk shall be capable of maintaining the required temperature during operation. The disk shall also be equipped with a thermal flux transducer by which the rate of heat transfer through the disk can be measured during operation. A dropwise oil feed system shall be provided as well as the microfog spray system.

2. <u>Film Formation and Wettability Tests on a Rotating Disk</u>

The Contractor shall perform two series of wettability tests under the standard conditions as described in Task I, Section 3, using the test chamber and test disk described in Section A of this Task. One spray nozzle, selected by the Contractor and approved by the NASA Project Manager, shall be used in this Task. In one series the dropwise oil feed system shall be used and in the other the microfog spray system. The oil feed shall be located at a one inch horizontal distance from the disk surface and directed normal to that surface. The oil feed shall be directed at a radial distance of one-half inch to one inch from the center of the disk as recommended by the Contractor and approved by the NASA Project Manager. Two reference test fluids, the same as tested in Task II, shall be used in both series of tests. These tests shall be conducted while the test disk is under static condition and at two different speeds up to 5,000 rpm or higher as recommended by the Contractor and approved by the NASA Project Manager. A minimum of 108 runs shall be made to include all these conditions.

D. Task IV - Surface Cooling Studies

Using the microfog lubricant applicator test rig specified in Task III, the Contractor shall measure the cooling effect of oil-fog sprays on the heated rotating disk for four different oils or formulations. The disk shall be maintained at the required temperature while spraying each of four test fluids on the disk. After reaching steady state conditions of temperature, pressure, and flow, the rate of heat transfer through the disk shall be measured by using a thermal flux transducer in conjunction with a recording potentiometer. Test conditions shall be used as defined in Task III, Section 2, except that the dropwise feed system shall not be used, with two blended fluids. The blended fluids shall consist of: (1) Mobil XRM-109F synthetic paraffinic hydrocarbon plus 10 weight percent of Mobil XRM-126A fluid. A minimum of 108 runs shall be made to include all these conditions.

E. Task V - Evaluation of a Novel Reclassifying Nozzle and a Mist Generator

Using the test equipment and test conditions as specified in Task III for the microfog feed system, the Contractor shall perform a series of wettability tests with one reference base fluid and one rotative speed to be selected by the Contractor and approved by the NASA Project Manager, with the novel reclassifiers and flight weight-mist generator as described in the following sections.

1. Tests shall be made with two new reclassifier nozzles in conjunction with the microfog generator supplied in Task I. The Government will provide one of these nozzles, and the Contractor shall design and fabricate the second nozzle which shall be capable of delivering a secondary gas stream to the test specimen, in addition to a primary microfog stream from the generator. Nozzle design shall be approved by the NASA Project Manager prior to its fabrication. A minimum of 18 runs shall be made to include all these conditions.

2. Two series of wettability tests shall be made with a new flight weight mist generator to be supplied by NASA. In one series, one conventional nozzle from Task I shall be used selected by the Contractor and approved by the NASA Project Manager, and in the other series the new reclassifier nozzles specified in Section A of this task shall be used. A minimum of 18 runs shall be made to include all these conditions.

Physical Properties of Test Lubricants

Property	Primol 355 (FN-2961)	XRM 109 F	XRM 109 F + 10% K-Resin	XRM 109 F + 10% XRM 126 A
Chemical Type	Super-refined Mineral Oil	Synthetic Non-aromatic Hydrocarbon	XRM 109 F Containing Kendall Paraffinic Resin (20,000 SUS)	XRM 109 F Containing Synthetic Hydrocarbon
Flash Point, °F	485	520	535	485
Fire Point, °F	510	595	610	540
Pour Point, °F	-30	<-35	<-35	<-35
Autogenous Ignition Point, °F	690	760	750	730
Kinematic Viscosity, cs				
@ 400°F	1.65	5.98	6.50	5.05
@ 210°F	8.31	39.8	46.3	30.77
@ 100°F	78.0	443	555	305.1
@ 0°F	9,677	38,524	57,008	21,577
Density @ 20°C, g/cm^3	0.882	0.847	0.851	0.843
Surface Tension @ 25°C, dynes/cm	30.9	30.8	31.5	31.5
Specific Heat, BTU/lb/°F				
@ 300°F	0.60	0.65	0.64	0.65
@ 400°F	0.65	0.67	0.68	0.67
@ 500°F	0.72	0.73	0.73	0.71
Thermal Conductivity,* BTU/hr - ft^2 (°F/ft)				
@ 300°F	0.070	0.075		
@ 500°F	0.066	0.070		

*The values of thermal conductivity were furnished by the suppliers of test oils.

APPENDIX B

Engineering Drawings of Rotating Specimen Chamber and Drive Mechanism

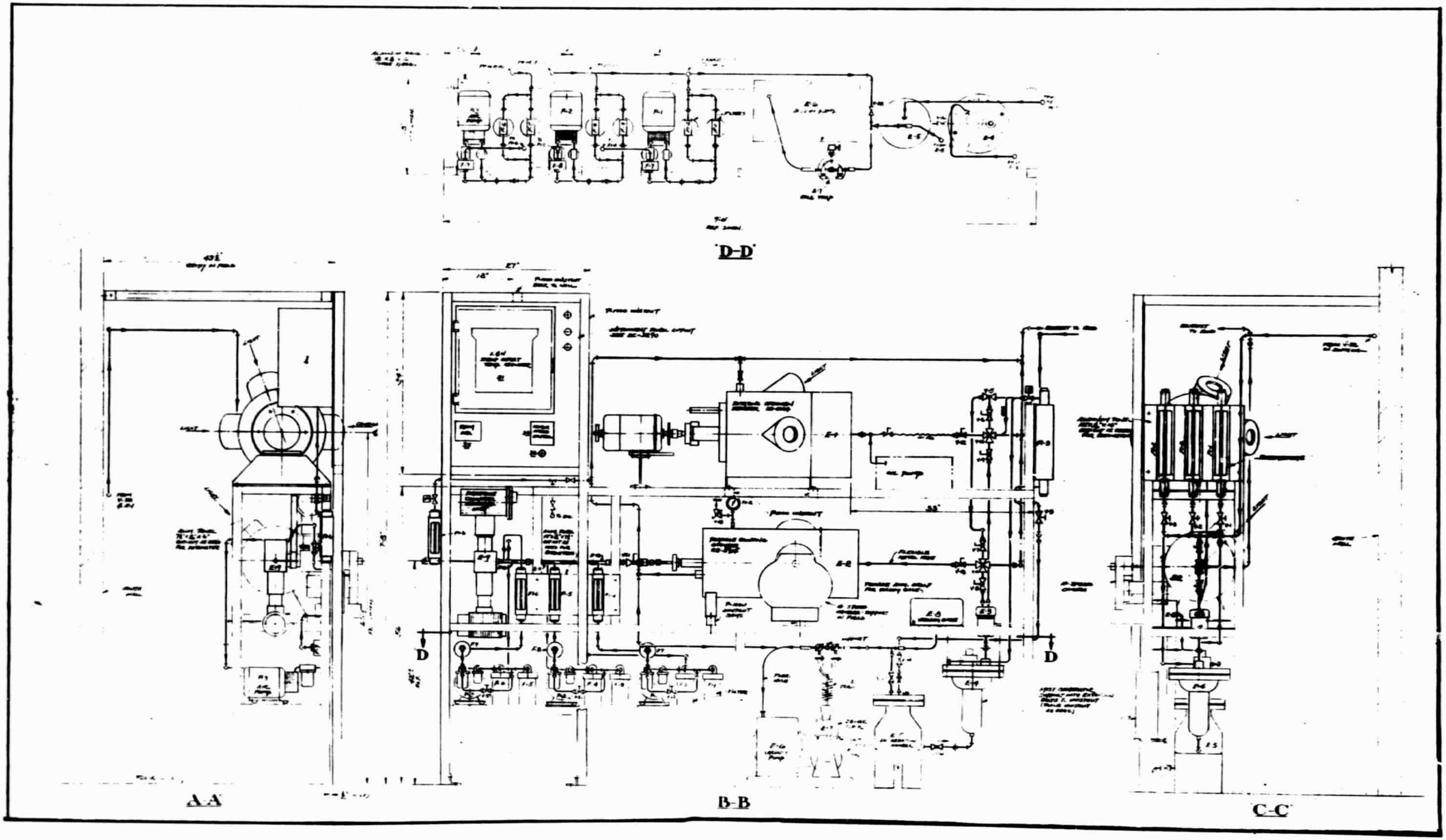

Attachment 1 - Flow Diagram and Piping Arrangement

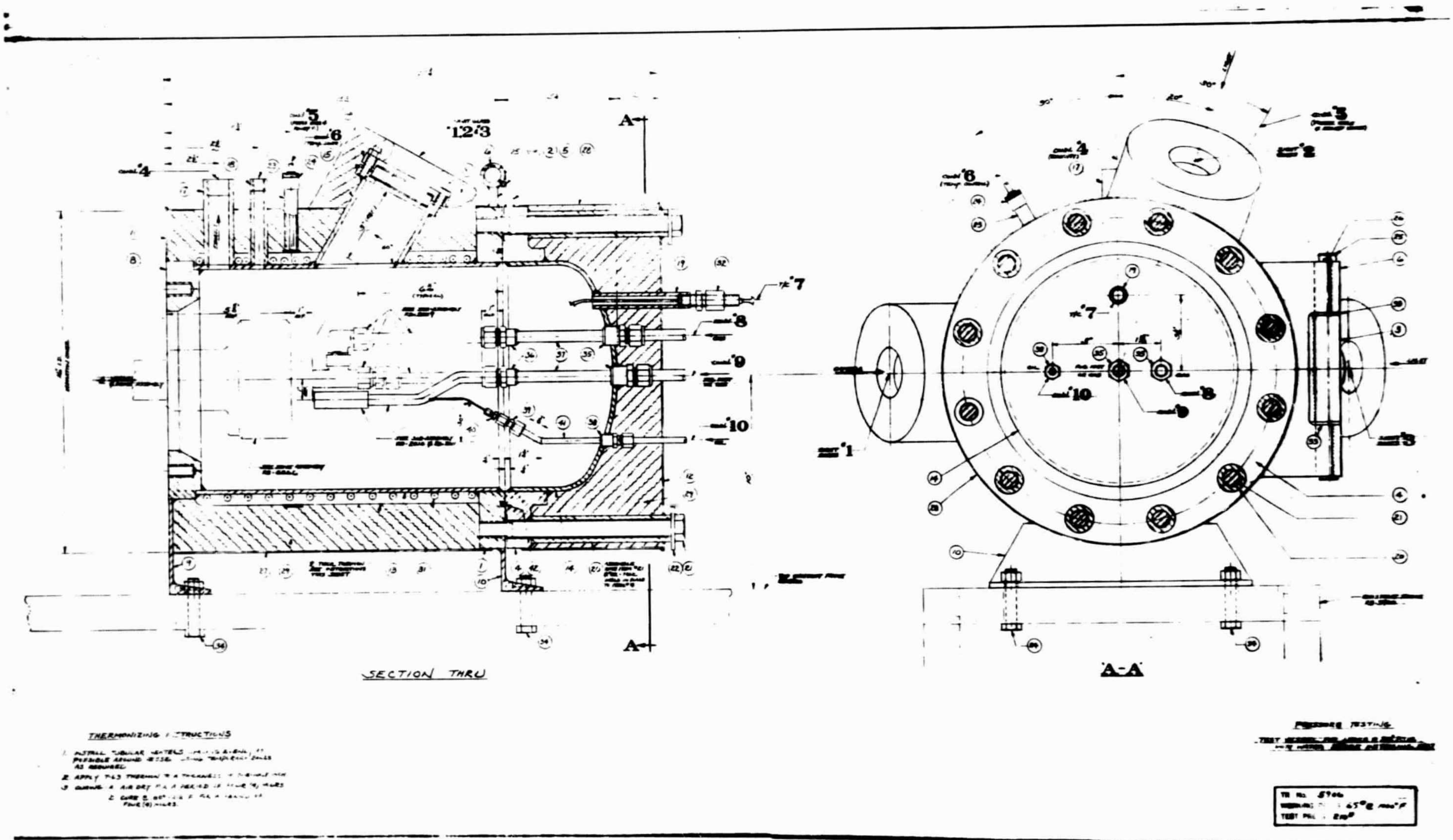

Attachment 2 - Rotating Specimen Chamber Assembly

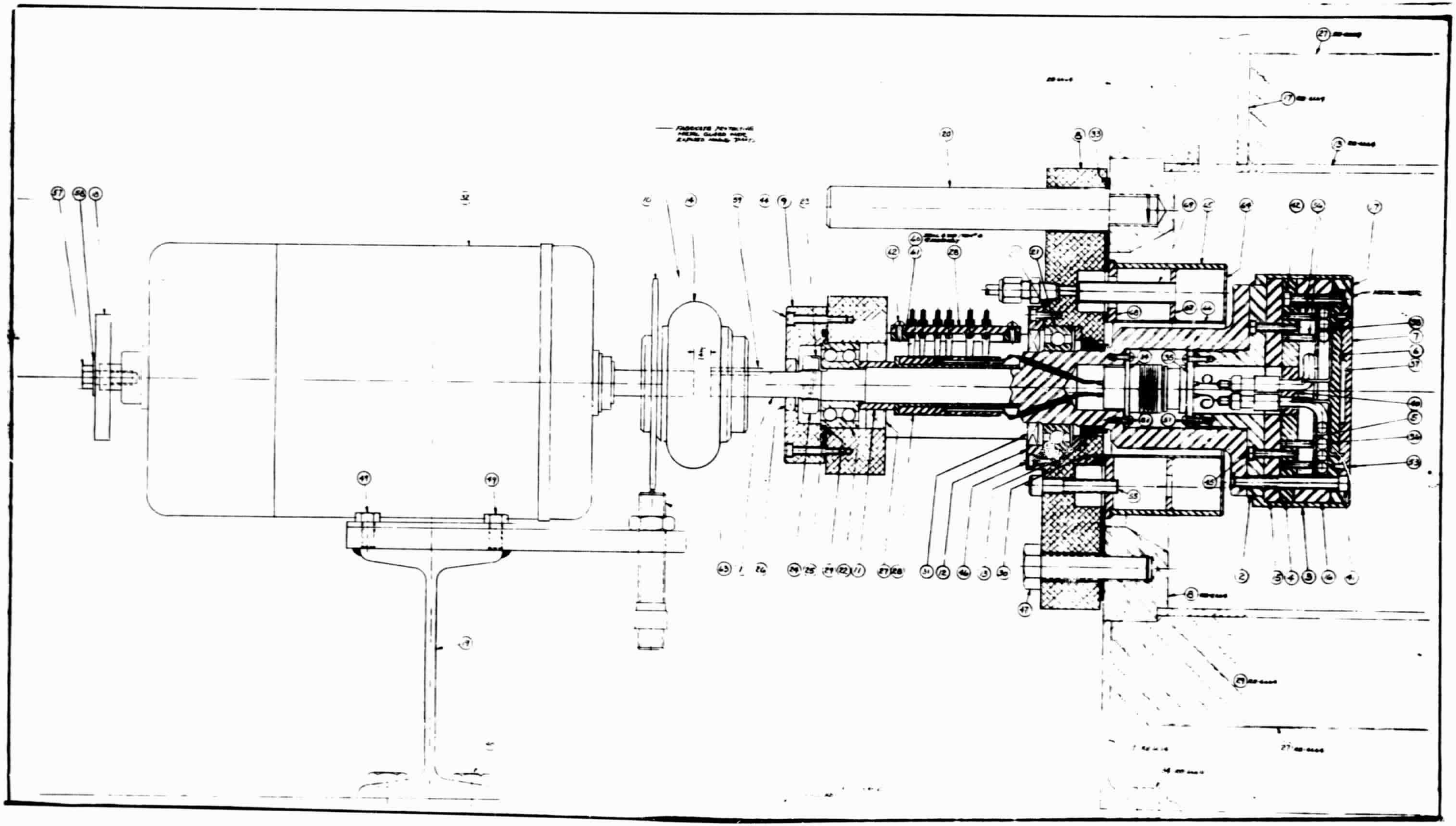

Attachment 3 - Rotating Specimen Drive Mechanism Assembly

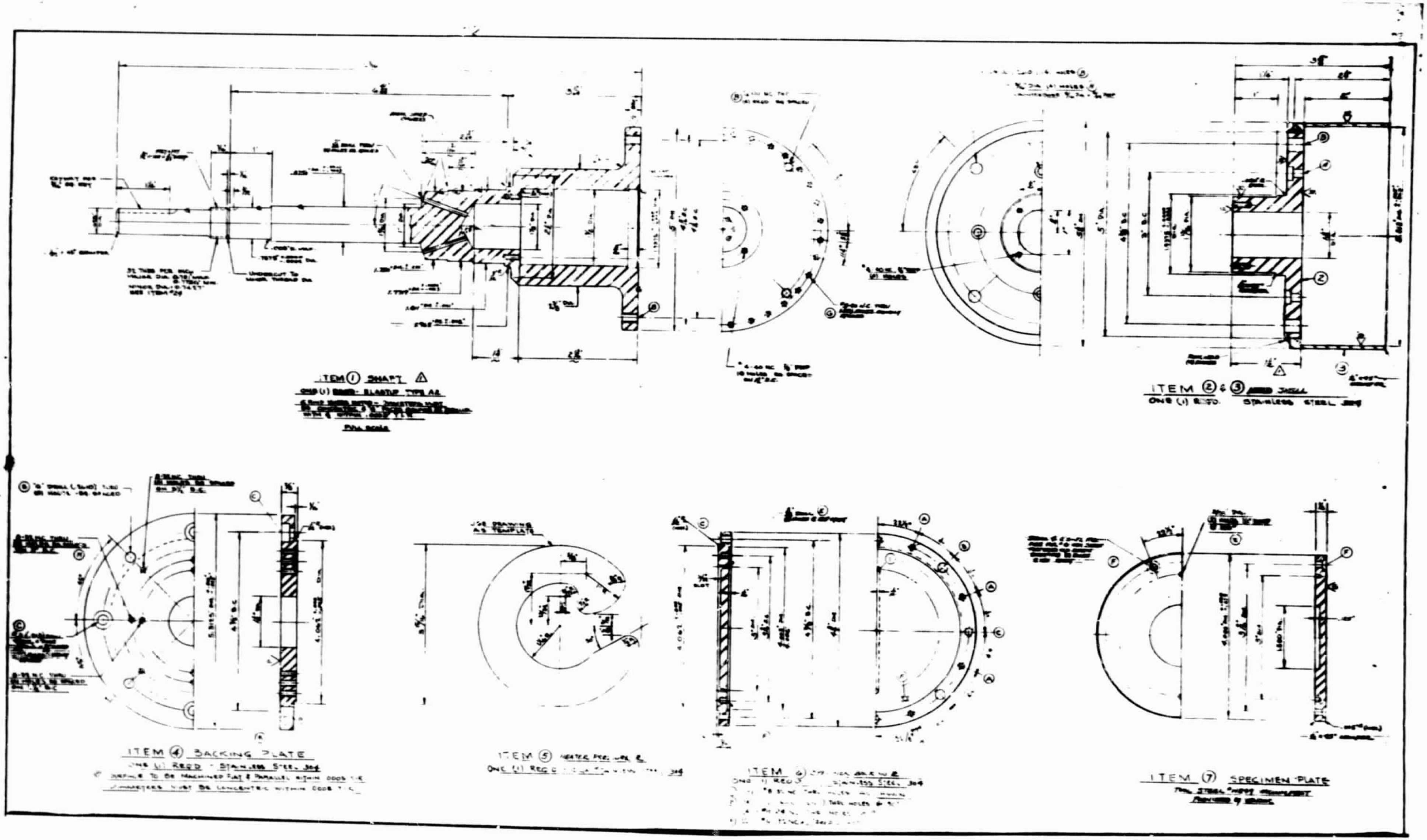

Attachment 4 - Rotating Specimen Drive Mechanism, Detail Sheet No. 1

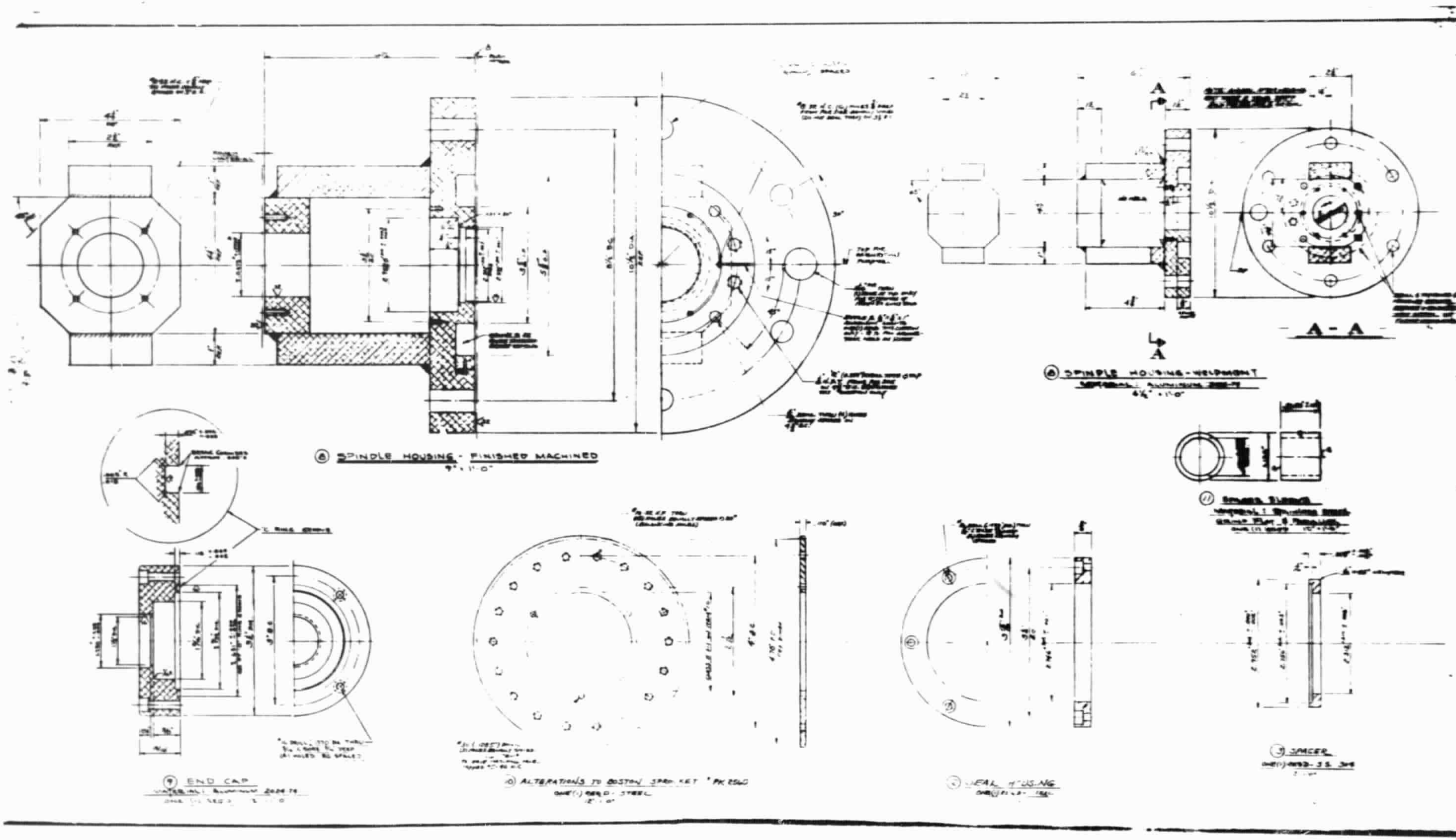

Attachment 5 - Rotating Specimen Drive Mechanism, Detail Sheet No. 2

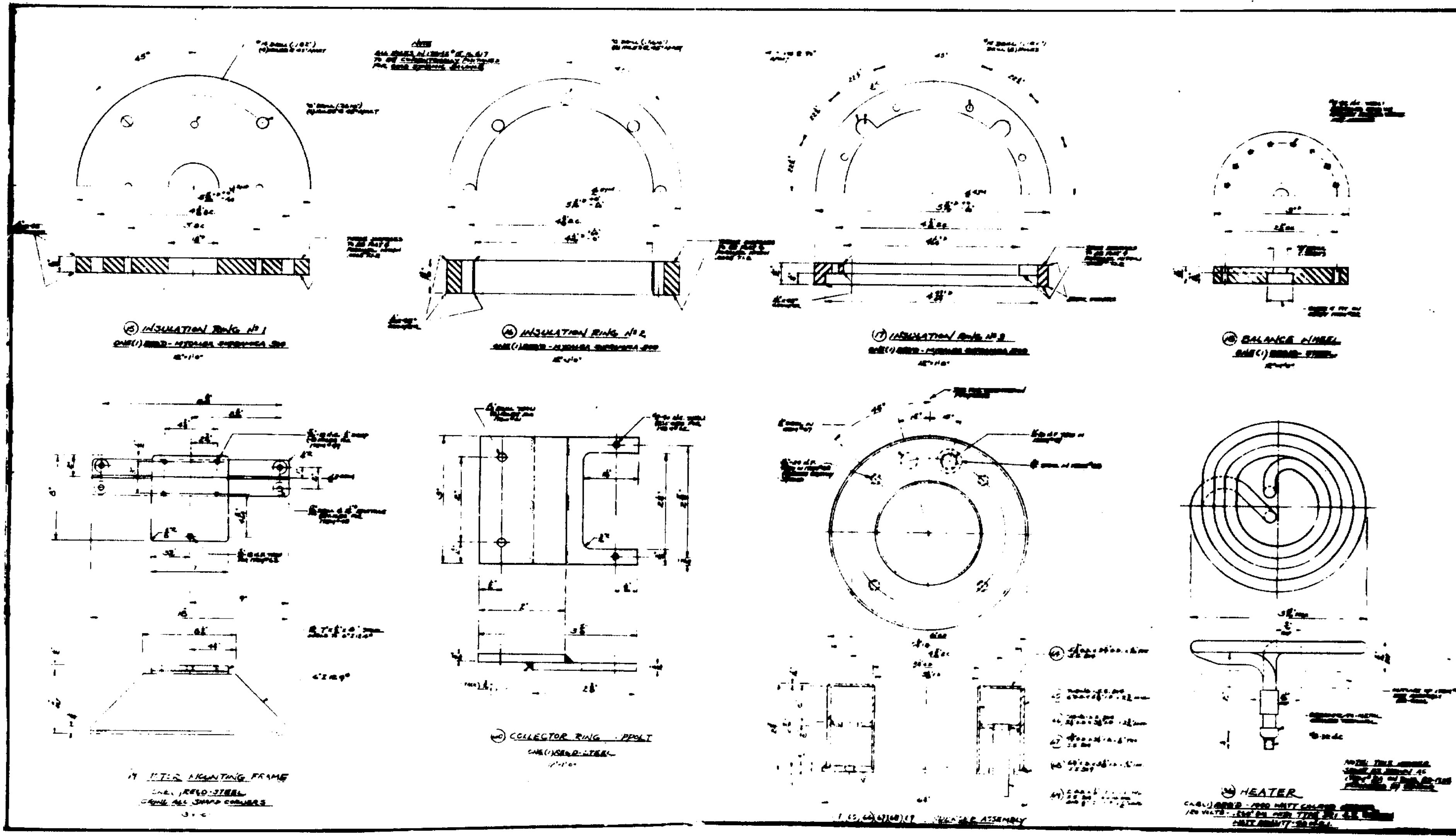

Attachment 6 - Rotating Specimen Drive Mechanism, Detail Sheet No. 3

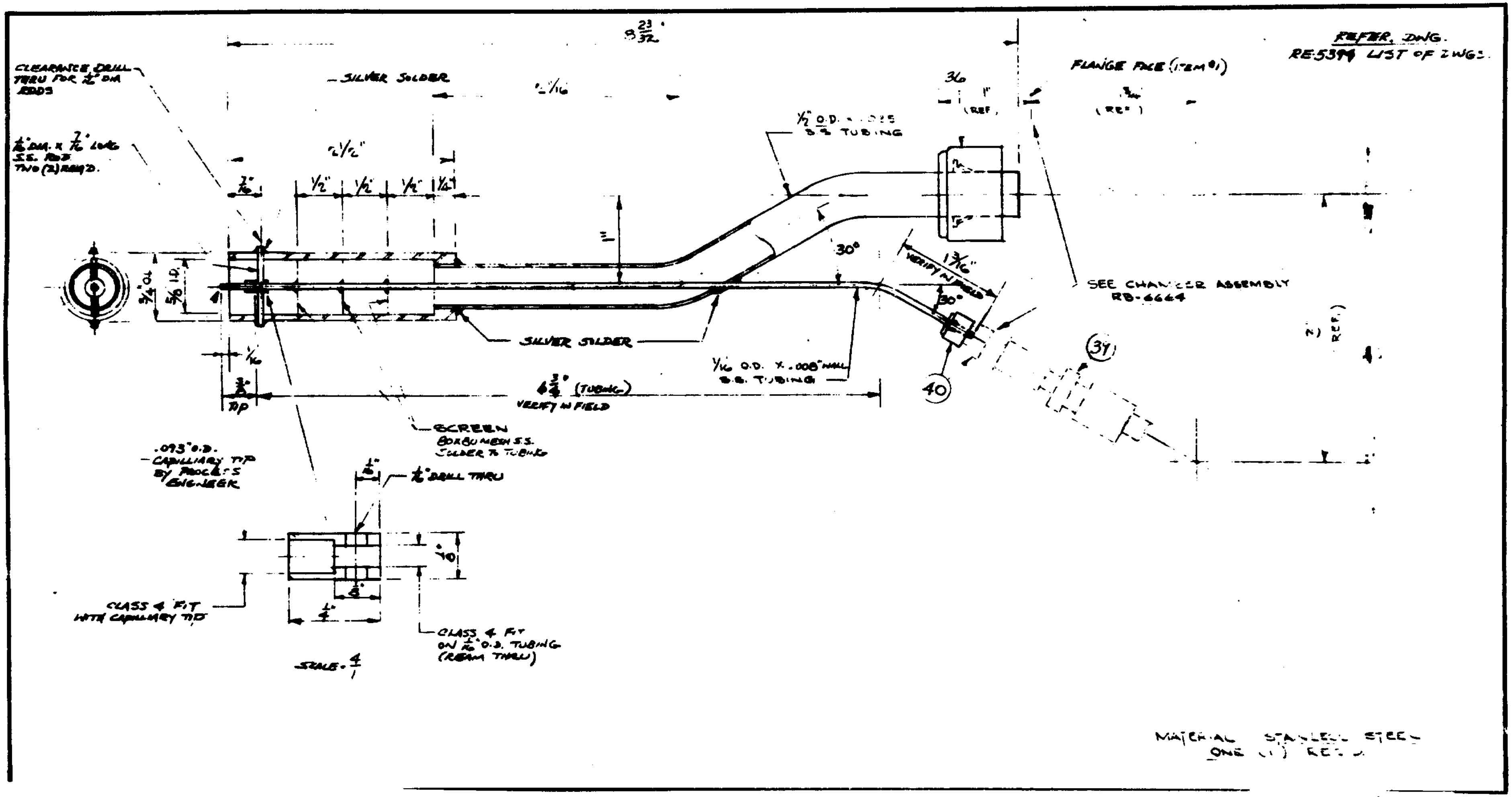

Attachment 7 - Nozzle Assembly for a Dropwise Oil Feed System

Attachment 8

Material List for Rotating Specimen Chamber

Item No.	No. Req'd	Description
1	1	Stationary Flange - 16" O.D. x 10-7/8" I.D. x 1-1/4" thk. S.S. 304
2	1	Hinge PL 1-1/8" x 3/8" x 5" - Steel
3	1	Tube - 1-1/8" O.D. x 3/4" I.D. x 5" long - Steel (Cut from Item #6 after welding)
4	1	10" - 150# Slip-on Flange - S.S. Type 304
5	1	Hinge PL 3" x 3/8" x 10" - Steel
6	1	Tube - 1-1/8" O.D. x 3/4" I.D. x 10" long - Steel
7		
8	1	Drive Mounting Flange - 11-1/4" O.D. x 6-1/2" I.D. x 1-1/2" thk. - S.S. 304
9	1	Vessel Left End Support - 6" [8.2# x 12" long - Steel
10	1	" Right " " - 6" [8.2# x 12" long - Steel
11	1	Left End Insulation Cover PL - 16-1/4" O.D. x 11-9/32" I.D. x 24 Ga Steel
12	1	Right " " " " - 16-1/4" O.D. x 24 Ga. Steel
13	1	Pipe - 10" Sched. 10 - S.S. Type 304 - 14" long
14	1	Cap, Weld, 10" I.P.S., light weight - 165" wall, 5" long
15	3	Pipe - 3" Sched. 40 - S.S. Type 304 - 4" long - Cut one end to fit 10" pipe @ 60°∠
16	3	Sight Window - 2-3/8" D window opg., Weld Type Jacoby-Tarbox Style 5200, Size #3
17	1	Tube 1-1/4" O.D. x 7/8" I.D. x 4" long - S.S. 321 - Tap one end 3/4" N.P.T.
18	1	Tube 9/16" O.D. x 5/16" I.D. x 4" long - S.S. 304 - Tap one end 1/4" N.P.T.
19	1	" " " " " x 4-1/2" - " " " " " " "
20	12	Pipe, 3/4" I.P.S. S.S. 304 - Weld to Item #4 with Item #21 in place - Ream pipe 29/32" I.D.
21	12	Cap Screw - 7/8" - 9" N.C. x 9" long - Hex Hd, Steel
22	12	Washer, plain 7/8", Steel
23	1	Bayonet T/C Pipe Clamp Adapter
24	1	Bayonet T/C
25	1	Bar 3/4" ø x 10-1/2" long, Steel - Drill hole for item #26 at 1/4" from one end 1/32" x 45° chamfer both ends
26	1	Cotter Pin - 1/8" x 1" long, Steel
27	1	Insulation Cover Tube - 16" I.D. x 24 Ga x 14-5/8" long - Steel (Cut out as req'd & weld to Item #1, #9 & #11)
28	1	" " " - 16" I.D. x 24 Ga x 6-1/2" long - Steel (Cut out as req'd & weld to Item #4, #12)
29	As req'd	Insulation - 10" I.P.S. x 3" thick x 20" long (approx)
30	"	Insulation - 1" thick
31	1	Heater, 3200 W @ 208 V, Beaded, 26 to 28 ft long (Order as Item #36 RC-2978)
32	1	Transducer Gland - Conax #TG-20-B-2-1
33	2	Washer - 23/32" I.D. x 1-1/8" O.D. x 1/8" thk - Lap to suit - Steel
34	4	Cap Screq - 1/2" - 13 N.C. x 2-1/2" long, Hex Hd, Steel, with Nuts
35	2	Swagelok to Butt Weld Connector - Swagelok #810-1-8W-316 (Drill thru for 1/2" Tube)
36	2	Swagelok to Socket Weld Union - Swagelok #810-6-8SW-316
37	2	Tube - 1/2" O.D. x .035" wall - S.S. 304 - 24" long (Cut to suit in field)
38	1	Swagelok to Butt Weld Connector - Swagelok #400-1-4W-316 (Drill thru for 1/4" Tube)
39	1	Reducing Union 1/4" Tube x 1/8" Tube - Swagelok #400-6-2-316
40	1	Reducer - 1/8" Tube x 1/16" Tube - Swagelok #100-R-2-316
41	1	Tube - 1/4" O.D. x .035" wall - S.S. 304 - 24" long (Cut to suit in field, bend as shown)
42	1	"O" Ring, Metal, .125" dia., 12" O.D. Nom. - Advanced Product Co.

Attachment 9

Material List for Rotating Specimen Drive Mechanism

Item No.	No. Req'd	Description
1	1	Shaft - 5" dia. x 12-9/16" - Elastuf Type A2
2	1	Head Shell Shaft PL - 5" dia. x 1-5/8" - S.S. 304
3	1	Head Shell Ring - Tubing 5-9/16" O.D. x .258" wall x 2-1/2" long - S.S. 304
4	1	Backing PL - 5.3125" dia. x 3/8" thk - S.S. 304
5	1	Heater Pressure PL - 3-15/16" dia. x 16 Ga. S.S. 304
6	1	Specimen Backing PL - 4-3/4" dia. x 5/16" S.S. 304
7	-	Specimen PL - 4.000" dia. x 1/4" thk - Tool Steel #WB49 Vacuum Melt
8	1	Spindle Housing - Aluminum 2024-T4 (1 pc 10-1/2" dia. x 1-1/2"; 1 pc 4-1/4" x 1-1/2" x 4-1/4"; 2 pcs 2-1/2" x 1" x 4-3/4")
9	1	End Cap - 3-1/2" dia. x 15/16" Aluminum 2024-T4
10	1	Sprocket - Boston #PK2560 Type "A" - 60 teeth - 4.78 P.D. - Steel (Modify as shown)
11	1	Spacer Sleeve - .8750" I.D. x 1.1250" O.D. x .8650" S.S. 304
12	1	Seal Housing - 3-15/16" O.D. x 3/8" thk - Steel
13	1	Spacer - 2.952" O.D. x 2.312" I.D. x .245" thk - S.S. 304
14	1	Coupling - Poly-Flex Taper Lock #D1709 - 5/8" bore both ends
15	1	Insulation Ring No. 1 - 5-5/16" O.D. x 1-1/8" I.D. x 3/8" thk - Mycalex Supramica 500
16	1	Insulation Ring No. 2 - 5-5/16" O.D. x 4-1/16" I.D. x 13/16" thk - " " "
17	1	Insulation Ring No. 3 - 5-5/16" O.D. x 4-1/64" I.D. x 1/2" thk - " " "
18	1	Balance Wheet - 3" dia. x 11/32" thk - Steel
19	1	Motor Mounting Frame - PL 7" x 1/2" x 8" & 6" I 12.4# x 18" long
20	1	Guide Stud - 1"ϕ x 7-1/2" long - Turn & thread one end 3/4" - 10 N.C. x 1" long; Chamfer other end
21	1	Bearing - New Departure #993L09
22	1	Bearing - New Departure #45304 Double Row
23	1	Lock Washer - New Departure #W-04
24	1	Lock Nut - New Departure #N-04
25	1	"O" Ring - Parker No. 143
26	1	Shaft Seal - Victoprene No. 63243
27	1	Shaft Seal - " No. 60325
28	1	Collector Ring Assembly - E.T.C.
29	1	Snap Ring - Furnished with Bearing Item #22
30	1	Seal Assembly - Magnetic Seal Corp. - Dwg #69069
31	1	Oil Seal - Victor Mfg. & Gasket Co. #64646 Type K-3
32	1	Motor - Century Electric Co. (Furnished as part of Boston Ratiotrol Equipment - See Item #34 RC-2978)
33	1	Gasket - 10" O.D. x 3-1/4" I.D. x 1/16" thk - Bi-Metalic - Hi Temp.
34	1	Electrical Connector, Female - Amphenol #17-3102A-18-443S (23)
35	1	" " , Male - " #97-5105-18-443P (496)
36	1	Heater, Disc - 1000 Watt, Watt Density 40 W.S.I. - GE Calrod

Attachment 9 (Cont'd)

Material List for Rotating Specimen Drive Mechanism

Item No.	No. Req'd	Description
37	1	Transducer - 1-1/2" O.D. x 1/8" nominal -
38	2	Thermocouple -
39	2	Male Connector 1/8" M.P.T. x 1/4" tube - Swagelok #400-1-2-316 (S.S.)
40	As req'd	Insulation - Sauerize
41	4	Hex Socket Hd. Cap Screw - 1/4" - 20 N.C. x 2-1/2" long - Steel
42	4	" " " " " - 1/4" - 20 N.C. x 1-1/4" long - Steel
43	1	Gasket - 3-15/16" O.D. x 2-3/4" I.D. x 1/16" thk Teflon - Holes to match Item #12
44	4	Hex Socket Hd. Cap Screw - #8 - 32 N.C. x 1-1/4" long - Steel
45	4	" " " " " - #8 - 32 N.C. x 1" long - Steel
46	6	" " " " " - #8 - 32 N.C. x 1/2" long - Steel
47	6	Hex Hd. Cap Screw - 5/8" - 11 N.C. x 2-1/2" long - Steel
48	4	" " " " - 1/2" - 13 N.C. x 1-1/2" long - Steel
49	4	" " " " - 5/16" - 18 N.C. x 1/2" long - Steel
50	8	Rd. Hd. Screw - #8 - 32 N.C. x 1/2" long - S.S.
51	8	" " " - #4 - 40 N.C. x 1/2" long - Steel
52		
53	2	Flat Countersunk Socket Hd. Cap Screw - #6 - 32 N.C. x 3/8" long - Steel
54	3	Flat Hd. Mach Screw - #8 - 32 N.C. x 3/8" long - Brass
55	4	Hex Socket Hd. Cap Screw - #5/16" - 24 N.F. x 1-1/2" long - Steel
56	8	Set Screw, Allen Head, Cup Point - #8 - 32 N.C. x 5/8" long - Steel
57	1	Hex Hd. Cap Screw - 5/16" - 18 N.C. x 3/4" long - Steel
58	1	5/16" Flat Washer - Steel
59	2	Coupling Keys 3/16" sq. x 1" long
60	1	Collector Ring Bracket - 1 pc 2" x 3/16" x 3" & 1 pc 2-3/8" x 3/16" x 3" - Steel
61	2	" " " Mtg. Screws - #8 - 32 N.C. x 3/8" long - R.H. - Steel
62	2	" " Mtg. Screws - #5 - 40 N.C. x 1/2" long - R.H. - Steel
63	1	Electromagnetic Pickup - Airpax Electronics Model #700-0941-B (Long Reach)
64	1	Ring - 5-7/8" O.D. x 3-1/4" I.D. x 1/16" thk. S.S. 304
65	1	Tubing - 6" O.D. x 5-3/4" I.D. x 2-9/16" long - S.S. 304
66	1	Tubing - 3-1/4" O.D. x 3-1/8" I.D. x 2-9/16" long - S.S. 304
67	1	Ring - 5-3/4" O.D. x 3-1/4" I.D. x 1/8" thk. S.S. 304
68	1	Ring - 6-1/4" O.D. x 3-1/8" I.D. x 3/16" thk. S.S. 304
69	1	Tube - 1/2" O.D. x 3/8" I.D. x 2-1/4" long - S.S. 304 - Thread one end 1/2" - 20 N.F. x 1/8" long

APPENDIX C

Wettability of Microfog Jets Impinging on a Heated Rotating Disc

Figure 39

PICTURE FREQUENCY VERSUS FILM LENGTH

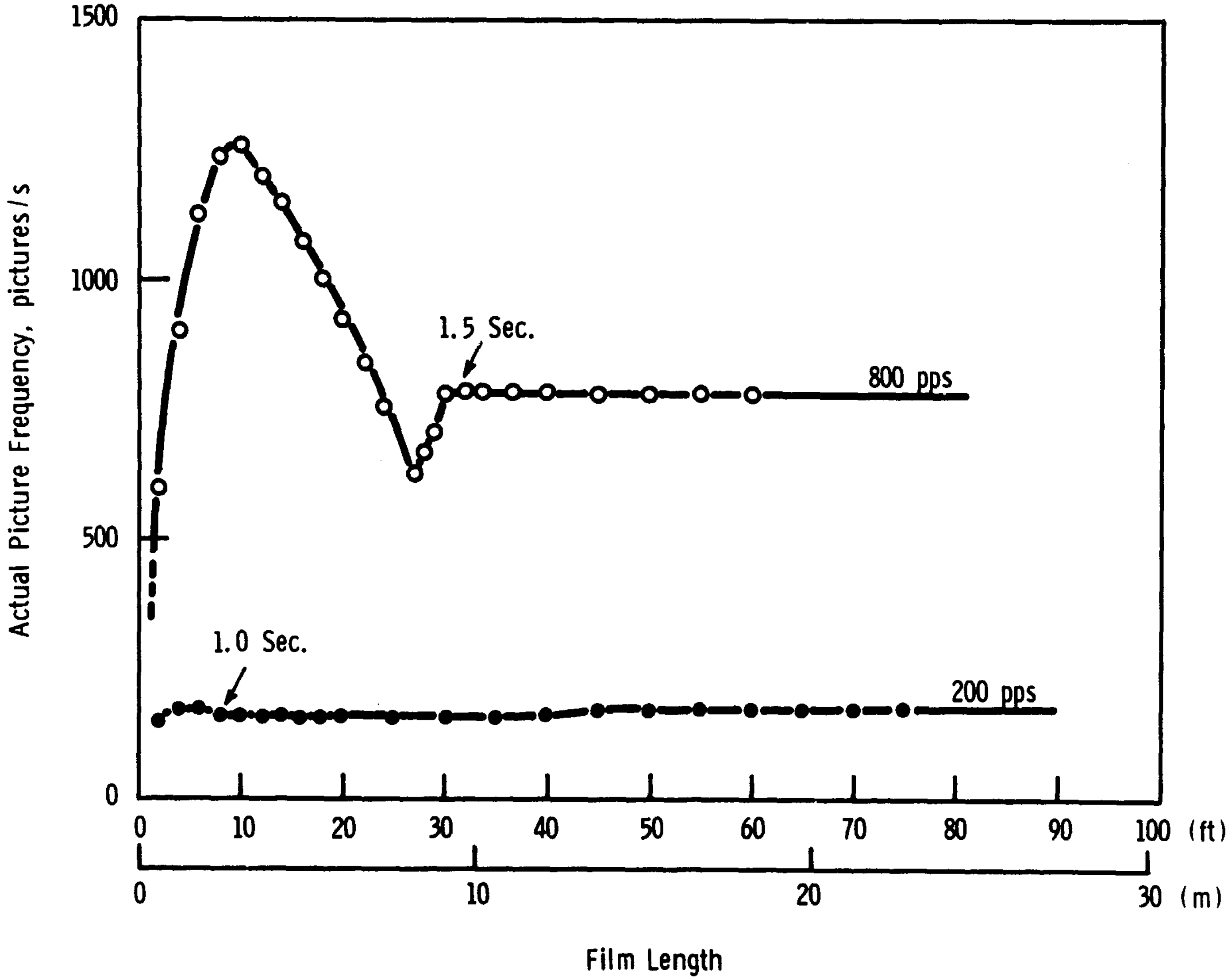

Wetting Rate Study

Item	Run No.	Plate Temp. (°F)	Gas Flow Rate (cfm at 45 psig & 200°F)	Rate of Oil-Mist Output (cc/min)	Wetting Time, sec.					
					3/4"	1"	1-1/4"	1-1/2"	1-3/4"	2"
1	XRM 15-1	600	3	1.2	2.75	4.10	6.80	9.25	14.30	17.90
2	XRM 15-2	600	4	2.0	2.50	3.80	5.65	7.20	9.10	11.70
3	XRM 15-3	600	5	2.6	2.00	3.70	5.70	6.85	8.70	10.70
4	XRM 15-4	700	3	1.2	5.05	8.00	10.25	13.20	14.50	17.70
5	XRM 15-5	700	4	2.0	2.70	4.40	6.60	10.20	10.90	12.00
6	XRM 15-6	700	5	2.6	1.70	3.20	5.60	8.90	10.70	11.80
7	XRM 15-7	800	3	1.2	4.60	8.70	12.40	14.00	16.20	19.30
8	XRM 15-8	800	4	2.0	2.70	5.00	9.10	12.00	13.10	14.30
9	XRM 15-9	800	5	2.6	1.90	4.00	7.30	10.50	12.80	14.30

Test Conditions - Test Oil: XRM 109 F
Oil Temp.: 200°F
Nozzle: No. 1 (0.171" dia.)
Rotational Speed: 0 rpm

Wetting Rate Study

Item	Run No.	Plate Temp. (°F)	Gas Flow Rate (cfm at 45 psig & 200°F)	Rate of Oil-Mist Output (cc/min)	Wetting Time, sec. 3/4"	1"	1-1/4"	1-1/2"	1-3/4"	2"
1	XRM 16-1	600	3	1.2	1.29	2.29	4.46	6.55	9.16	--
2	XRM 16-2	600	4	2.0	1.08	1.58	2.03	3.36	4.24	5.47
3	XRM 16-3	600	5	2.6	0.98	1.34	1.81	2.56	3.64	4.40
4	XRM 18-1	700	3	1.2	1.14	1.80	3.58	6.22	8.64	10.68
5	XRM 17-6	700	4	2.0	1.10	1.58	2.16	3.32	4.24	4.93
6	XRM 17-5	700	5	2.6	0.77	1.11	1.50	2.59	3.16	3.44
7	XRM 19-3	800	3	1.2	1.32	2.08	3.66	5.78	8.32	9.77
8	XRM 19-5	800	4	2.0	0.79	1.17	1.80	3.00	3.96	4.62
9	XRM 19-6	800	5	2.6	0.70	0.98	1.44	2.31	3.02	3.74

Test Conditions - Test Oil: XRM 109 F
Oil Temp.: 200 °F
Nozzle: No. 1
Rotational Speed: 250 rpm

Wetting Rate Study

Item	Run No.	Plate Temp. (°F)	Gas Flow Rate (cfm at 45 psig & 200°F)	Rate of Oil-Mist Output (cc/min)	Wetting Time, sec. 3/4"	1"	1-1/4"	1-1/2"	1-3/4"	2"
1	XRM 17-1	600	3	1.2	1.44	2.31	4.43	7.77	9.20	10.68
2	XRM 16-5	600	4	2.0	0.94	1.41	2.03	3.38	4.33	
3	XRM 16-4	600	2.6	0.69	0.96	1.62	2.63			
4	XRM 18-2	700	3	1.2	1.37	2.39	4.00	6.35	9.30	11.50
5	XRM 18-3	700	4	2.0	0.72	1.41	1.96	3.09	3.98	4.55
6	XRM 18-4	700	5	2.6	0.77	1.14	1.53	2.18	2.98	3.59
7	XRM 20-1	800	3	1.2	1.21	2.02	3.67	6.50	8.85	--
8	XRM 19-8	800	4	2.0	0.93	1.35	2.02	3.00	3.88	4.70
9	XRM 19-7	800	5	2.6	0.73	1.04	1.47	2.26	2.91	3.52

Test Conditions - Test Oil: XRM 109 F
Oil Temp.: 200°F
Nozzle: No. 1
Rotational Speed: 500 rpm

Wetting Rate Study

Item	Run No.	Plate Temp. (°F)	Gas Flow Rate (cfm at 45 psig & 200°F)	Rate of Oil-Mist Output (cc/min)	Wetting Time, sec. 3/4"	1"	1-1/4"	1-1/2"	1-3/4"	2"
1	XRM 17-2	600	3	1.2	1.20	2.16	4.30	6.87	8.78	10.78
2	XRM 17-3	600	4	2.0	0.79	1.30	1.84	2.94		4.72
3	XRM 17-4	600	5	2.6	0.68	1.04	1.45	2.22	2.68	3.44
4	XRM 19-2	700	3	1.2	1.26	2.12	3.98	6.10	8.12	10.50
5	XRM 19-1	700	4	2.0	0.44	1.09	1.78	2.59	3.30	4.13
6	XRM 18-5	700	5	2.6	0.79	1.08	1.58	2.26	3.02	3.52
7	XRM 20-4	800	3	1.2	1.50	2.66	4.57	6.69	9.26	--
8	XRM 20-3	800	4	2.0	0.69	1.11	1.71	2.69	3.72	4.43
9	XRM 20-2	800	5	2.6	0.37	0.69	1.08	1.71	2.43	3.20

Test Conditions - Test Oil: XRM 109 F
Oil Temp.: 200°F
Nozzle: No. 1
Rotational Speed: 1000 rpm

Wetting Rate Study

Item	Run No.	Plate Temp. (°F)	Gas Flow Rate (cfm at 45 psig & 200°F)	Rate of Oil-Mist Output (cc/min)	Wetting Time, sec. 3/4"	1"	1-1/4"	1-1/2"	1-3/4"	2"
1	XRM 20-5	600	3	1.2	1.41	2.23	2.75	4.24	5.15	7.30(?)
2	XRM 21-1	600	4	2.0	1.39	1.63	2.24	2.90	--	4.36
3	XRM 21-2	600	5	2.6	0.82	1.15	1.51	2.20	2.66	3.22
4	XRM 23-1	700	3	1.2	1.90	2.28	3.68	4.82	6.33	8.87(?)
5	XRM 22-2	700	4	2.0	0.96	1.26	1.60	2.06	2.99	3.74
6	XRM 22-1	700	5	2.6	0.99	1.23	1.53	1.90	2.68	3.14
7	XRM 24-2	800	3	1.2	1.56	2.48	4.06	6.04	7.98	10.10
8	XRM 24-1	800	4	2.0		1.40	1.93	2.83	3.70	4.63
9	XRM 23-2	800	5	2.6	0.63	0.92	1.27	2.01	2.45	3.01

Test Conditions - Test Oil: XRM 109 F
Oil Temp.: 200°F
Nozzle: No. 1
Rotational Speed: 3000 rpm

Wetting Rate Study

Item	Run No.	Plate Temp. (°F)	Gas Flow Rate (cfm at 45 psig & 200°F)	Rate of Oil-Mist Output (cc/min)	Wetting Time, sec. 3/4"	1"	1-1/4"	1-1/2"	1-3/4"	2"
1	FN 4-1	600	3	2.1		10.6	20.0	Streaks		
2	FN 4-2	600	4	4.2		8.05		Streaks		
3	FN 4-3	600	5	5.4		8.20	13.68	14.7	Streaky flow	
4	FN 7-3	700	3	2.1		21.8				
5	FN 7-2	700	4	4.2		18.0	No further wetting, but heavy streaks			
6	FN 7-1	700	5	5.4		9.2				
7	FN 8-6	800	3	2.1		23.1				
8	FN 8-5	800	4	4.2		22.4	No further wetting, but heavy streaks			
9	FN 8-4	800	5	5.4		15.3				

Test Conditions - Test Oil: FN 2961
Oil Temp.: 200°F
Nozzle: No. 1 (0.171" dia.)
Rotational Speed: 0 rpm

R.2

Wetting Rate Study

Item	Run No.	Plate Temp. (°F)	Gas Flow Rate (cfm at 45 psig & 200°F)	Rate of Oil-Mist Output (cc/min)	Wetting Time, sec. 3/4"	1"	1-1/4"	1-1/2"	1-3/4"	2"
1	FN 5-3	600	3	2.1		17.05				
2	FN 5-2	600	4	4.2		8.07	No further wetting			
3	FN 5-1	600	5	5.4	6.80	7.32				
4	FN 7-9	700	3	2.1	16.5					
5	FN 7-8	700	4	4.2	8.75		No further wetting			
6	FN 7-7	700	5	5.4	7.90					
7	FN 9-3	800	3	2.1	18.8					
8	FN 9-2	800	4	4.2	11.40		No further wetting			
9	FN 9-1	800	5	5.4	6.80					

Test Conditions - Test Oil: FN 2961
Oil Temp.: 200°F
Nozzle: No. 1 (0.171" dia.)
Rotational Speed: 500 rpm

Wetting Rate Study

Item	Run No.	Plate Temp. (°F)	Gas Flow Rate (cfm at 45 psig & 200°F)	Rate of Oil-Mist Output (cc/min)	Wetting Time, sec. 3/4"	1"	1-1/4"	1-1/2"	1-3/4"	2"
1	FN 5-6	600	3	2.1		26.0				
2	FN 5-5	600	4	4.2		9.34	No further wetting			
3	FN 5-4	600	5	5.4		8.34				
4	FN 7-6	700	3	2.1	19.2					
5	FN 7-5	700	4	4.2	9.75		No further wetting			
6	FN 7-4	700	5	5.4	7.02					
7	FN 9-6	800	3	2.1	19.6					
8	FN 9-5	800	4	4.2	9.9		No further wetting			
9	FN 9-4	800	5	5.4	8.2					

Test Conditions - Test Oil: FN 2961
Oil Temp.: 200°F
Nozzle: No. 1 (0.171" dia.)
Rotational Speed: 1000 rpm

Wetting Rate Study

Item	Run No.	Plate Temp. (°F)	Gas Flow Rate (cfm at 45 psig & 200°F)	Rate of Oil-Mist Output (cc/min)	Wetting Time, sec. 3/4"	1"	1-1/4"	1-1/2"	1-3/4"	2"
1	FN 6-3	600	3	2.1	6.45					
2	FN 6-2	600	4	4.2	2.05	2.12	No further wetting			
3	FN 6-1	600	5	5.4	0.20	0.53				
4	FN 8-3	700	3	2.1	5.14					
5	FN 8-2	700	4	4.2	1.70		No further wetting			
6	FN 8-1	700	5	5.4	0.47					

Test Conditions - Test Oil: FN 2961
Oil Temp.: 200°F
Nozzle: No. 1 (0.171" dia.)
Rotational Speed: 3000 rpm

APPENDIX C-3

Summary of the Wetting Rate Data for XRM 109 F

Wettability of XRM 109 F at Disc Temperature of 600°F (589°K)

Item	Run No.	Gas Flow Rate	Rate of Oil-Mist Output	Angular Velocity	Wetting Time (s)						Wetting Rate
		$(m^3/s) \times 10^3$ @ 40 N/cm^2 & 366°K	$(cm^3/s) \times 10^2$	(rad/s)	0.14	0.25	0.39	0.55	0.76	1.00	(cm^2/s)
1	XRM 15-1	1.4 (3 cfm)	2.0	0	2.75	4.10	6.80	9.25	14.30	17.90	4.4
2	XRM 16-1	1.4	2.0	26	1.29	2.29	4.46	6.55	9.16	--	5.7
3	XRM 17-1	1.4	2.0	52	1.44	2.31	4.43	7.77	9.20	10.68	6.2
4	XRM 17-2	1.4	2.0	104	1.20	2.16	4.30	6.87	8.78	10.78	7.1
5	XRM 20-5	1.4	2.0	312	1.41	2.23	2.75	7.24	5.15	7.30(?)	11.8
6	XRM 15-2	1.9 (4 cfm)	3.3	0	2.50	3.80	5.65	7.20	9.10	11.70	7.5
7	XRM 16-2	1.9	3.3	26	1.08	1.58	2.03	3.36	4.24	5.47	14.5
8	XRM 16-5	1.9	3.3	52	0.94	1.41	2.03	3.38	4.33	--	14.3
9	XRM 17-3	1.9	3.3	104	0.79	1.30	1.84	2.94	--	4.72	17.2
10	XRM 21-1	1.9	3.3	312	0.87	1.39	1.63	2.24	2.90	4.36	22.2
11	XRM 15-3	2.4 (5 cfm)	4.3	0	2.00	3.70	5.70	6.85	8.70	10.78	8.8
12	XRM 16-3	2.4	4.3	26	0.98	1.34	1.81	2.56	3.64	4.40	17.5
13	XRM 16-4	2.4	4.3	52	0.69	0.96	1.62	2.63	3.37	--	19.2
14	XRM 17-4	2.4	4.3	104	0.68	1.04	1.45	2.22	2.68	3.44	24.2
15	XRM 21-2	2.4	4.3	312	0.82	1.15	1.51	2.20	2.66	3.22	28.4

Test Conditions - Oil Temp.: 200°F (366°K)
Nozzle: No. 1 (4.34 mm orifice dia.)
Disc Size: 10.2 cm dia.

Wettability of XRM 109 F at Disc Temperature of 700°F (644°K)

Item	Run No.	Gas Flow Rate	Rate of Oil-Mist Output	Angular Velocity	Wetting Time (s)						Wetting Rate
		$(m^3/s) \times 10^3$ @ 40 N/cm^2 & 366°K	$(cm^3/s) \times 10^2$	(rad/s)	0.14	0.25	0.39	0.55	0.76	1.00	(cm^2/s)
1	XRM 15-4	1.4 (3 cfm)	2.0	0	5.05	8.00	10.25	13.20	14.50	17.70	4.7
2	XRM 18-1	1.4	2.0	26	1.14	1.80	3.58	6.22	8.64	10.68	7.1
3	XRM 18-2	1.4	2.0	52	1.37	2.39	4.00	6.35	9.30	11.50	6.0
4	XRM 19-2	1.4	2.0	104	1.26	2.12	3.98	6.10	8.12	10.50	7.3
5	XRM 23-2	1.4	2.0	312	1.90	2.28	3.68	4.82	6.33	8.87(?)	10.6
6	XRM 15-5	1.9 (4 cfm)	3.3	0	1.42	2.70	4.40	6.60	10.90	12.00	6.3
7	XRM 17-6	1.9	3.3	26	1.10	1.58	2.16	3.32	4.24	4.93	15.6
8	XRM 18-3	1.9	3.3	52	0.72	1.41	1.96	3.09	3.98	4.58	16.2
9	XRM 19-1	1.9	3.3	104	0.44	1.09	1.78	2.59	3.30	4.13	19.3
10	XRM 22-2	1.9	3.3	312	0.96	1.26	1.60	2.06	2.99	3.74	24.1
11	XRM 15-6	2.4 (5 cfm)	4.3	0	1.70	3.20	5.60	8.90	10.70	11.80	6.8
12	XRM 17-5	2.4	4.3	26	0.79	1.17	1.80	3.00	3.96	4.62	16.2
13	XRM 18-4	2.4	4.3	52	0.77	1.14	1.53	2.18	2.98	3.59	22.8
14	XRM 18-5	2.4	4.3	104	0.79	1.08	1.58	2.26	3.02	3.52	23.4
15	XRM 22-1	2.4	4.3	312	0.99	1.23	1.53	1.90	2.68	3.14	28.9

Test Conditions - Oil Temp.: 200°F (366°K)
Nozzle: No. 1 (4.34 mm orifice dia.)
Disc Size: 10.2 cm dia.

Wettability of XRM 109 F at Disc Temperature of 800°F (700°K)

Item	Run No.	Gas Flow Rate	Rate of Oil-Mist Output	Angular Velocity	Wetting Time (s)						Wetting Rate
		$(m^3/s) \times 10^3$ @ 40 N/cm^2 & 366°K	$(cm^3/s) \times 10^2$	(rad/s)	0.14	0.25	0.39	0.55	0.76	1.00	(cm^2/s)
1	XRM 15-7	1.4 (3 cfm)	2.0	0	4.60	8.70	12.40	14.00	16.20	19.30	3.2
2	XRM 19-3	1.4	2.0	26	1.32	2.08	3.66	5.78	8.32	9.77	8.1
3	XRM 20-1	1.4	2.0	52	1.21	2.02	3.67	6.50	8.85	--	6.8
4	XRM 20-4	1.4	2.0	104	1.50	2.66	4.57	6.69	9.26	?	6.5
5	XRM 24-2	1.4	2.0	312	1.56	2.48	4.06	6.04	7.98	?	8.0
6	XRM 15-8	1.9 (4 cfm)	3.3	0	2.70	5.00	9.10	12.00	13.10	14.30	4.8
7	XRM 19-5	1.9	3.3	26	0.79	1.17	1.80	3.06	3.96	4.84	15.9
8	XRM 19-8	1.9	3.3	52	0.93	1.35	2.02	3.00	3.88	4.70	17.2
9	XRM 20-3	1.9	3.3	104	0.69	1.11	1.71	2.69	3.72	4.43	18.3
10	XRM 24-1	1.9	3.3	312	--	1.40	1.93	2.83	3.70	4.63	18.8
11	XRM 15-9	2.4 (5 cfm)	4.3	0	1.90	4.00	7.30	10.50	12.80	14.30	4.8
12	XRM 19-6	2.4	4.3	26	0.70	0.98	1.44	2.31	3.02	3.74	20.2
13	XRM 19-7	2.4	4.3	52	0.73	1.04	1.47	2.26	2.91	3.52	23.1
14	XRM 20-2	2.4	4.3	104	0.69	0.89	1.38	1.91	2.43	3.20	24.3
15	XRM 23-2	2.4	4.3	312	0.63	0.92	1.27	2.01	2.45	3.11	26.2

Test Conditions - Oil Temp.: 200°F (366°K)
Nozzle: No. 1 (4.34 mm orifice dia.)
Disc Size: 10.2 cm dia.

APPENDIX D

Heat Transfer of Microfog Jets
Impinging on a Heated Rotating Disc

D-1. Operating Principle of Heat Flux Transducer (HFT)

The principle of operation of what might be called the "heat-flow meter" is schematically illustrated in Figure 40. Heat flux is absorbed at the sensor surface of HFT and is transferred to a heat sink which thermally remains at a temperature above or below that of the sensor surface. The difference in temperature, ΔTm, between two well defined points along the path of the heat flow from the sensor to the sink, ΔZ, is proportional to the heat being transferred. This can be equally stated in the mathematical form with the Fourier's first law:

$$q = \frac{Q}{A} = -k\left(\frac{\Delta Tm}{\Delta Z}\right) \tag{48}$$

and, therefore, knowing the values of thermal conductivity of the HFT media, the heat flux being absorbed, Q/A, is simply proportional to ($\Delta Tm/\Delta Z$).

At two such points, the heat flux transducer has thermocouple junctions which form differential thermoelectric circuits (i.e., the emf between the two output leads directly measures a temperature gradient; neither power source nor reference junction is needed). In this manner, the transducer provides a self-generated (thermoelectric) signal which is directly proportional to heat flux absorbed at the sensor surface. This relatively small self-generated signal is suitably amplified by means of a miniature thermopile which makes it possible to measure the heat flow without additional amplification equipment, thereby maintaining high accuracy. The transducer output signal (in milivolts) is read with the aid of a simple galvanometer or indicating or recording potentiometer. Also, the transducer is designed in such a way that it automatically averages heat fluxes that are not uniform.

D-2. Calibration of Heat Flux Transducer

When the heat flux transducer was purchased, the complete system calibration was performed at the factory. The method used at the factory requires the use of an auxiliary standardized heat flow meter or a heat transfer apparatus with well-defined heat fluxes. In brief, to calibrate a heat flux transducer at a given temperature range, the transducer is simply subjected to the heat transfer apparatus at known heat fluxes and its output signals are read or recorded on a calibrated potentiometer. The calibrated heat flux data for the present transducer are shown in Figure 41. The calibrated transducer has high temperature stability, short time constant (about 1 sec. response time), accuracy of ±3%, maximum flux density of 15 W/cm^2, and output electrical resistance of 78 ohms.

Figure 40

PRINCIPLE OF OPERATION
OF HEAT FLUX TRANSDUCER (HFT)

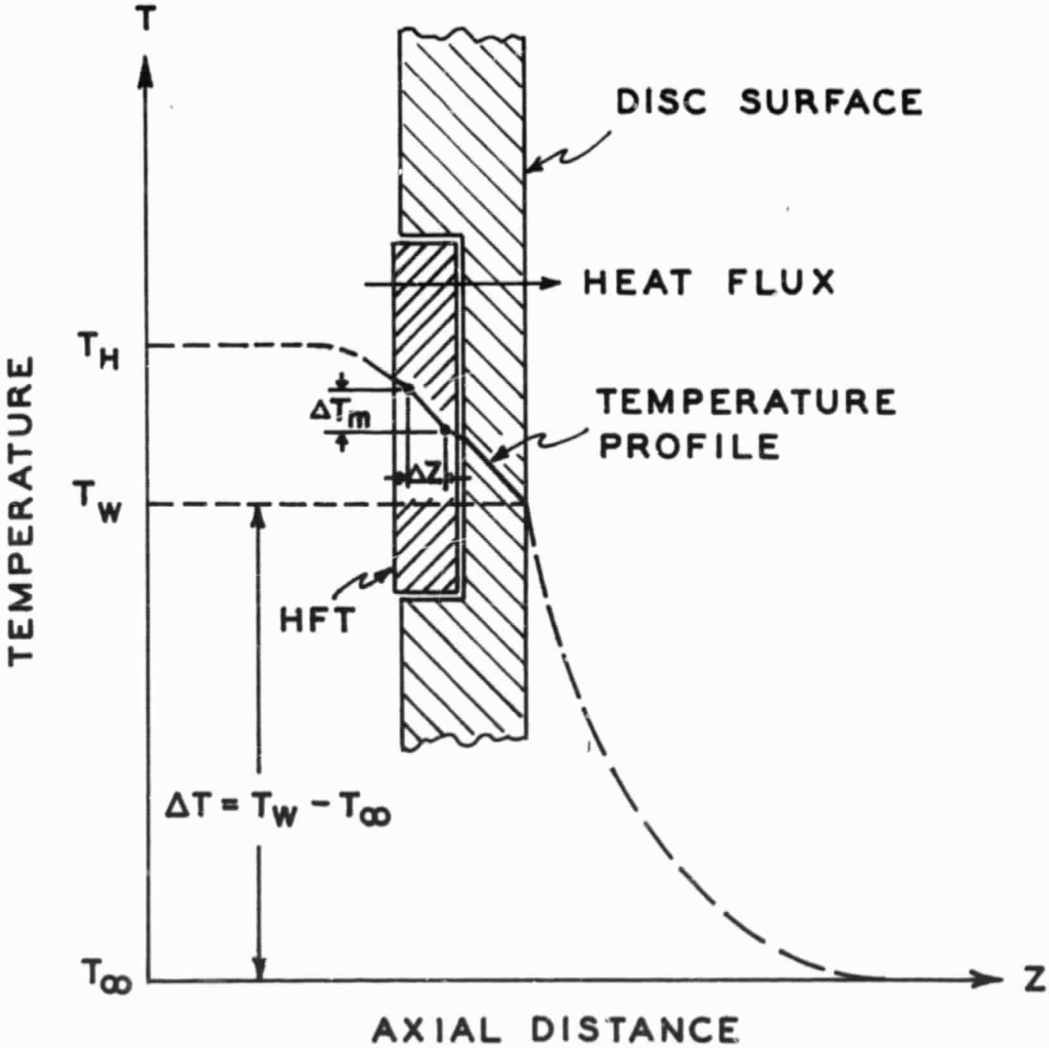

Figure 41

HEAT FLUX DATA FOR CALIBRATION OF THE HEAT FLUX TRANSDUCER

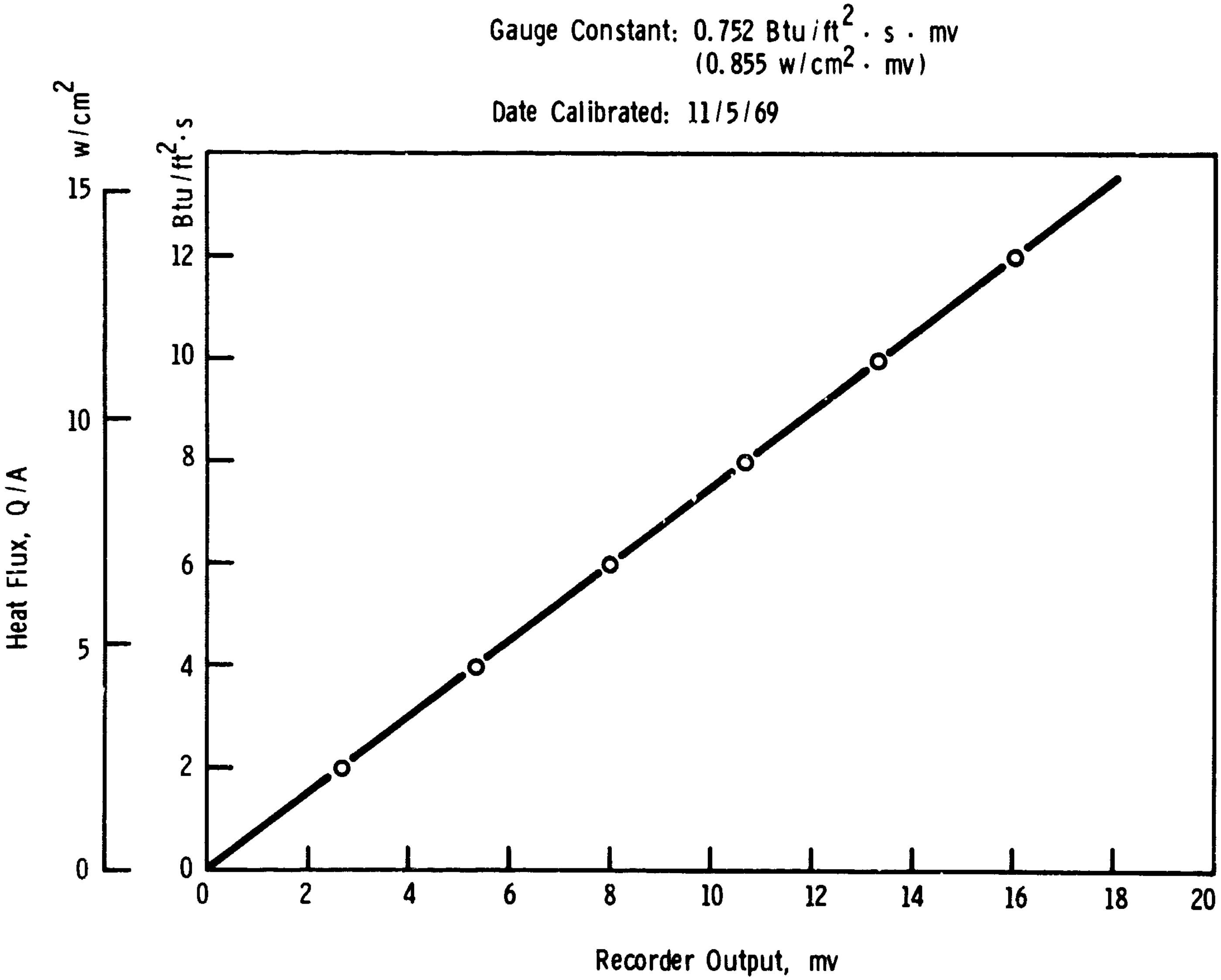

Figure 42

A CALIBRATION CURVE FOR EMF RECORDER

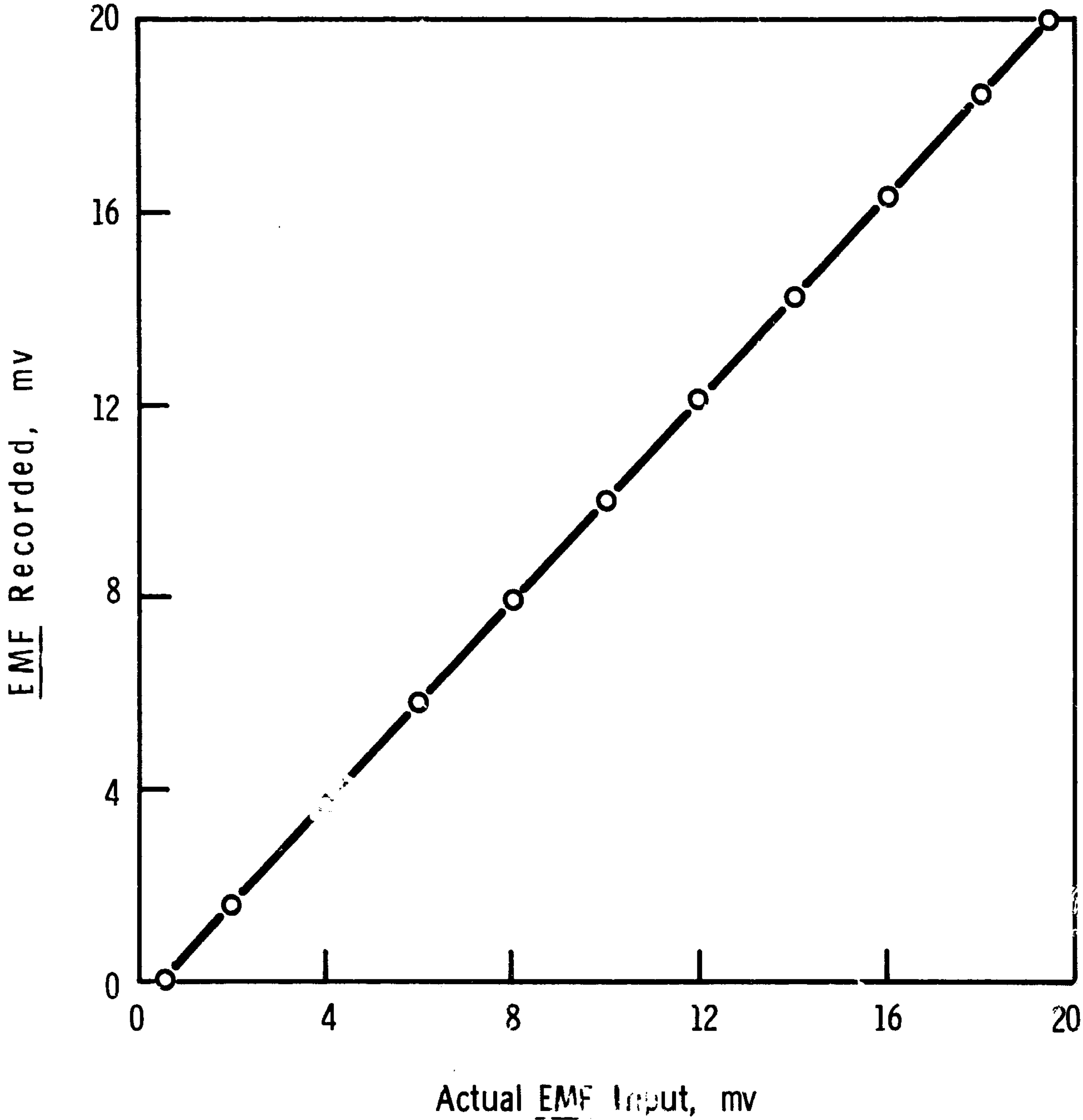

APPENDIX D-3

Heat Transfer Data of Microfog Jets of Different Lubricants

Heat Transfer Rates of XT'' 109 F Microfog Jets Impinging on a Heated Rotating Disc

Item	Run No.	Gas Flow Rate	Rate of Oil-Mist Output	Angular Velocity	Temperature (°F)		Heat Energy Transferred (mv)			Total Heat Flux	Heat Transfer Coefficient
		$(m^3/s) \times 10^3$ @ 40 N/cm^2 & 366°K	$(cm^3/s) \times 10^2$	(rad/s)	T_w	T_∞	Q_f	Q_g	ΔQ	$(Btu/hr - ft^2) \times 10^{-3}$	$(Btu/hr - ft^2 - °F)$
1	TX-16	1.4 (3 cfm)	2.0	0	700 (644°K)	200 (366°K)	10.2	9.7	0.5	27.6 (88×10^3 W/m^2)	55.3 (313 $W/m^2 - °K$)
2	TX-17	1.9 (4)	3.3	0	710	200	10.2	9.6	0.6	27.6	54.0
3	TX-18	2.4 (5)	4.3	0	705	185	11.3	10.7	0.6	30.5	58.7
4	TX-19	1.4	2.0	26	700	200	10.4	9.8	0.6	28.1	56.3
5	TX-20	1.9	3.3	26	707	200	10.4	9.9	0.5	28.1	55.5
6	TX-21	2.4	4.3	26	705	200	10.6	10.1	0.5	28.6	56.7
7	TX-22	1.4	2.0	52	705	190	10.4	9.5	0.9	28.1	54.5
8	TX-23	1.9	3.3	52	710	200	11.0	10.2	0.8	29.7	58.3
9	TX-24	2.4	4.3	52	705	220	10.5	9.9	0.6	28.4	58.5
10	TX-25	1.4	2.0	104	700	220	9.8	9.4	0.4	26.5	55.2
11	TX-26	1.9	3.3	104	695	220	10.4	9.9	0.5	28.1	59.1
12	TX-27	2.4	4.3	104	705	200	11.0	10.4	0.6	29.7	58.8
13	TX-28	1.4	2.0	312	695	230	10.1	9.6	0.5	27.3	58.6
14	TX-29	1.9	3.3	312	700	190	11.0	10.2	0.8	29.7	58.3
15	TX-30	2.4	4.3	312	690	210	11.0	10.4	0.6	29.7	61.9

Test Conditions - Oil Temp.: 200°F (366°K)
Nozzle: No. 1 (4.34 mm orifice dia.)

Heat Transfer Rates of XRM 109 F Microfog Jets Impinging on a Heated Rotating Disc

Item	Run No.	Gas Flow Rate (m^3/s) x 10^3 @ 40 N/cm^2 & 366°K	Rate of Oil-Mist Output (cm^3/s) x 10^2	Angular Velocity (rad/s)	Temperature (°F) T_w	Temperature (°F) T_∞	Heat Energy Transferred (mv) Q_f	Heat Energy Transferred (mv) Q_g	Heat Energy Transferred (mv) ΔQ	Total Heat Flux (Btu/hr - ft^2) x 10^{-3}	Heat Transfer Coefficient (Btu/hr - ft^2 - °F)
1	TX-31	1.4 (3 cfm)	2.0	0	790 (694°K)	200 (366°K)	11.2	10.9	0.3	30.2 (95.1 x 10^3 W/m^2)	51.2 (290 W/m^2-°K)
2	TX-32	1.9 (4)	3.3	0	795	190	11.4	11.0	0.4	30.8	51.0
3	TX-33	2.4 (5)	4.3	0	785	200	12.0	11.5	0.5	32.4	55.4
4	TX-34	1.4	2.0	26	795	220	11.0	10.7	0.3	29.7	51.7
5	TX-35	1.9	3.3	26	798	200	11.4	11.1	0.3	30.8	51.5
6	TX-36	2.4	4.3	26	792	230	11.8	11.3	0.5	31.9	56.8
7	TX-37	1.4	2.0	52	800	225	11.1	10.7	0.4	30.0	522
8	TX-38	1.9	3.3	52	795	200	11.5	11.2	0.3	31.0	52.2
9	TX-39	2.4	4.3	52	798	225	11.0	10.6	0.4	29.7	51.8
10	TX-40	1.4	2.0	104	800	200	10.9	10.8	0.1	29.4	49.0
11	TX-41	1.9	3.3	104	790	210	11.0	10.6	0.4	29.7	51.3
12	TX-42	2.4	4.3	104	787	200	11.4	11.0	0.4	30.8	52.5
13	TX-43	1.4	2.0	312	790	230	10.6	10.4	0.2	28.6	51.1
14	TX-44	1.9	3.3	312	795	220	11.2	10.9	0.3	30.2	52.5
15	TX-45	2.4	4.3	312	775	205	11.2	11.1	0.1	30.2	53.0

Test Conditions - Oil Temp.: 200°F (366°K)
Nozzle: No. 1 (4.34 mm orifice dia.)

Heat Transfer Rates of FN 2961 Microfog Jets Impinging on a Heated Rotating Disc

Item	Run No.	Gas Flow Rate (m^3/s) x 10^3 @ 40 N/cm^2 & 366°K	Rate of Oil-Mist Output (cm^3/s) x 10^2	Angular Velocity (rad/s)	Temperature (°F) T_w	Temperature (°F) T_∞	Heat Energy Transferred (mv) Q_f	Heat Energy Transferred (mv) ΔQ	Total Heat Flux (Btu/hr - ft^2) x 10^{-3}	Heat Transfer Coefficient (Btu/hr - ft^2 - °F)
1	TFN-1	1.4 (3 cfm)	3.5	0	600 (589°K)	200 (366°K)	8.4	0.3	22.6 (71.2 x 10^3 W/m^2)	56.5 (319 W/m^2 - °K)
2	TFN-2	1.9 (4)	7.0	0	600	195	8.7	0.5	23.5	58.0
3	TFN-3	2.4 (5)	9.0	0	600	190	9.0	0.6	24.3	59.3
4	TFN-4	1.4	3.5	26	608	200	8.6	0.3	23.2	56.9
5	TFN-5	1.9	7.0	26	605	200	8.9	0.6	24.0	59.3
6	TFN-6	2.4	9.0	26	600	210	9.1	0.5	24.6	63.1
7	TFN-7	1.4	3.5	52	610	210	8.4	0.2	22.7	56.8
8	TFN-8	1.9	7.0	52	610	210	8.6	0.4	23.2	58.0
9	TFN-9	2.4	9.0	52	610	210	8.9	0.3	24.0	60.0
10	TFN-10	1.4	3.5	104	600	200	8.5	0.2	23.0	57.5
11	TFN-11	1.9	7.0	104	600	190	8.8	0.5	23.8	58.0
12	TFN-12	2.4	9.0	104	600	210	9.2	0.7	24.8	63.6
13	TFN-13	1.4	3.5	312	605	205	8.5	0.3	23.0	57.5
14	TFN-14	1.9	7.0	312	605	200	9.0	0.7	24.3	60.0
15	TFN-15	2.4	9.0	312	605	205	9.4	0.9	25.4	63.5

Test Conditions - Oil Temp.: 200°F (366°K)
Nozzle: No. 1 (4.34 mm orifice dia.)

Heat Transfer Rates of FN 2961 Microfog Jets Impinging on a Heated Rotating Disc

Item	Run No.	Gas Flow Rate	Rate of Oil-Mist Output	Angular Velocity	Temperature (°F)		Heat Energy Transferred (mv)		Total Heat Flux	Heat Transfer Coefficient
		$(m^3/s) \times 10^3$ @ 40 N/cm^2 & 366°K	$(cm^3/s) \times 10^2$	(rad/s)	T_w	T_∞	Q_f	ΔQ	$(Btu/hr-ft^2) \times 10^{-3}$	$(Btu/hr-ft^2-°F)$
1	TFN-16	1.4 (3 cfm)	3.5	0	700 (644°K)	200 (366°K)	9.8	0.2	26.5 (83.5×10^3 W/m^2)	53.0 (300 W/m^2 - °K)
2	TFN-17	1.9 (4)	7.0	0	695	200	10.0	0.6	27.0	54.5
3	TFN-18	2.4 (5)	9.0	0	690	195	10.4	0.5	28.1	56.8
4	TFN-19	1.4	3.5	26	705	210	10.1	0.4	27.3	55.2
5	TFN-20	1.9	7.0	26	710	210	10.2	0.4	27.5	55.0
6	TFN-21	2.4	9.0	26	710	200	10.5	0.5	28.4	55.7
7	TFN-22	1.4	3.5	52	700	195	10.2	0.4	27.5	54.5
8	TFN-23	1.9	7.0	52	705	200	10.5	0.5	28.4	56.2
9	TFN-24	2.4	9.0	52	695	190	10.6	0.8	28.6	56.6
10	TFN-25	1.4	3.5	104	710	200	10.3	0.6	27.8	54.5
11	TFN-26	1.9	7.0	104	705	205	10.3	0.4	27.8	55.6
12	TFN-27	2.4	9.0	104	695	190	10.4	0.5	28.1	55.6
13	TFN-28	1.4	3.5	312	700	200	10.0	0.3	27.0	54.0
14	TFN-29	1.9	7.0	312	710	195	10.6	0.9	28.6	55.5
15	TFN-30	2.4	9.0	312	690	190	10.6	0.7	28.6	57.2

Test Conditions - Oil Temp.: 200°F (366°K)
Nozzle: No. 1 (4.34 mm orifice dia.)

Heat Transfer Rates of FN 2961 Microfog Jets Impinging on a Heated Rotating Disc

Item	Run No.	Gas Flow Rate (m^3/s) x 10^3 @ 40 N/cm^2 & 366°K	Rate of Oil-Mist Output (cm^3/s) x 10^2	Angular Velocity (rad/s)	Temperature (°F) T_w	Temperature (°F) T_∞	Heat Energy Transferred (mv) Q	Heat Energy Transferred (mv) Δq	Total Heat Flux ($Btu/hr - ft^2$) x 10^{-3}	Heat Transfer Coefficient ($Btu/hr - ft^2 - °F$)
1	TFN-31	1.4 (3 cfm)	3.5	0	800 (700°K)	200 (366°K)	11.5	0.2	31.1 (98.0 x 10^3 W/m^2)	51.8 (293 W/m^2 - °K)
2	TFN-32	1.9 (4)	7.0	0	790	200	11.3	0.0	30.5	51.7
3	TFN-33	2.4 (5)	9.0	0	795	190	11.8	0.3	31.9	52.7
4	TFN-34	1.4	3.5	26	790	205	11.3	0.0	30.5	52.1
5	TFN-35	1.9	7.0	26	790	200	11.4	0.1	30.8	52.2
6	TFN-36	2.4	9.0	26	800	195	12.0	0.5	32.4	53.6
7	TFN-37	1.4	3.5	52	795	210	11.0	0.0	29.7	50.8
8	TFN-38	1.9	7.0	52	790	210	11.2	0.2	30.2	52.1
9	TFN-39	2.4	9.0	52	790	200	11.6	0.3	31.3	53.1
10	TFN-40	1.4	3.5	104	785	200	11.1	--	30.0	51.3
11	TFN-41	1.9	7.0	104	795	205	11.3	0	30.5	51.7
12	TFN-42	2.4	9.0	104	790	190	11.5	0.2	31.1	51.8
13	TFN-43	1.4	3.5	312	795	220	10.8	0.1	29.2	50.8
14	TFN-44	1.9	7.0	312	790	215	11.0	0.3	29.7	51.7
15	TFN-45	2.4	9.0	312	790	190	11.7	0.2	31.6	52.7

Test Conditions - Oil Temp.: 200°F (366°K)
Nozzle: No. 1 (4.34 mm orifice dia.)

Heat Transfer Rates of (XRM 109 F + K-Resin) Microfog Jets Impinging on a Heated Rotating Disc

Item	Run No.	Gas Flow Rate $(m^3/s) \times 10^3$ @ 40 N/cm^2 & 366°K	Rate of Oil-Mist Output $(cm^3/s) \times 10^2$	Angular Velocity (rad/s)	Temperature (°F) T_w	Temperature (°F) T_∞	Heat Energy Transferred (mv) Q_f	Heat Energy Transferred (mv) ΔQ	Total Heat Flux $(Btu/hr - ft^2) \times 10^{-3}$	Heat Transfer Coefficient $(Btu/hr - ft^2 - °F)$
1	TXK-1	1.4 (3 cfm)	2.5	0	600 (589°K)	200 (366°K)	8.5	0.3	23.0 (72.5×10^3 W/m^2)	57.5 (325 W/m^2 - °K)
2	TXK-2	1.9 (4)	4.0	0	605	200	9.0	0.5	24.3	60.0
3	TXK-3	2.4 (5)	5.1	0	600	195	9.3	0.6	25.1	62.0
4	TXK-4	1.4	2.5	26	605	210	8.9	0.4	24.0	60.8
5	TXK-5	1.9	4.0	26	605	210	9.0	0.5	24.3	61.5
6	TXK-6	2.4	5.1	26	610	200	9.3	0.7	25.1	61.2
7	TXK-7	1.4	2.5	52	600	205	8.8	0.4	23.8	60.3
8	TXK-8	1.9	4.0	52	600	195	8.9	0.6	24.0	59.3
9	TXK-9	2.4	5.1	52	600	190	9.0	0.6	24.3	59.3
10	TXK-10	1.4	2.5	104	610	210	8.5	0.3	23.0	57.5
11	TXK-11	1.9	4.0	104	605	210	8.8	0.5	23.8	60.3
12	TXK-12	2.4	5.1	104	595	205	9.1	0.7	24.6	63.1
13	TXK-13	1.4	2.5	312	600	205	8.7	0.4	23.5	59.5
14	TXK-14	1.9	4.0	312	590	210	9.1	0.6	24.6	64.7
15	TXK-15	2.4	5.1	312	595	210	9.5	0.7	25.7	66.8

Test Conditions - Oil Temp.: 200°F (366°K)
Nozzle: No. 1 (4.34 mm dia.)

Heat Transfer Rates of (XRM 109 F + K-Resin) Microfog Jets Impinging on a Heated Rotating Disc

Item	Run No.	Gas Flow Rate	Rate of Oil-Mist Output	Angular Velocity	Temperature (°F)		Heat Energy Transferred (mv)		Total Heat Flux	Heat Transfer Coefficient
		$(m^3/s) \times 10^3$ @ 40 N/cm^2 & 366°K	$(cm^3/s) \times 10^2$	(rad/s)	T_w	T_∞	Q_f	ΔQ	$(Btu/hr - ft^2) \times 10^{-3}$	$(Btu/hr - ft^2 - °F)$
1	TXK-16	1.4 (3 cfm)	2.5	0	695 (641°K)	200 (366°K)	10.0	0.4	27.0 (85.1×10^3 W/m^2)	54.5 (308 W/m^2 - °K)
2	TXK-17	1.9 (4)	4.0	0	700	200	10.2	0.4	27.5	55.0
3	TXK-18	2.4 (5)	5.1	0	700	190	11.0	0.9	29.7	58.2
4	TXK-19	1.4	2.5	26	690	210	9.9	0.4	26.7	55.6
5	TXK-20	1.9	4.0	26	705	210	10.2	0.6	27.5	55.6
6	TXK-21	2.4	5.1	26	695	200	10.8	0.7	29.2	59.0
7	TXK-22	1.4	2.5	52	710	195	10.6	0.5	28.6	55.5
8	TXK-23	1.9	4.0	52	710	200	10.9	0.8	29.4	57.6
9	TXK-24	2.4	5.1	52	695	190	11.2	0.7	30.2	59.8
10	TXK-25	1.4	2.5	104	700	220	9.8	0.3	26.5	55.2
11	TXK-26	1.9	4.0	104	690	220	10.2	0.5	27.5	58.5
12	TXK-27	2.4	5.1	104	690	210	10.6	0.5	28.6	59.6
13	TXK-28	1.4	2.5	312	705	210	10.3	0.5	27.8	56.2
14	TXK-29	1.9	4.0	312	700	210	10.7	0.6	28.9	59.0
15	TXK-30	2.4	5.1	312	690	200	11.2	0.6	30.2	61.6

Test Conditions - Oil Temp.: 200°F (366°K)
Nozzle: No. 1 (4.34 mm dia.)

Heat Transfer Rates of (XRM 109 F + E-Resin) Microfog Jets Impinging on a Heated Rotating Disc

Item	Run No.	Gas Flow Rate	Rate of Oil-Mist Output	Angular Velocity	Temperature (°F)		Heat Energy Transferred (mv)		Total Heat Flux	Heat Transfer Coefficient
		$(m^3/s) \times 10^3$ @ 40 N/cm^2 & 366°K	$(cm^3/s) \times 10^5$	(rad/s)	T_w	T_∞	e_f	Δe	$(Btu/hr-ft^2) \times 10^{-3}$	$(Btu/hr-ft^2-°F)$
1	TXK-31	1.4 (3 cfm)	2.5	0	795(697°K)	200(366°K)	11.3	0.4	30.5 (96.1×10^3 W/m^2)	51.3 ([illegible])
2	TXK-32	1.9 (4)	4.0	0	790	190	11.6	0.6	31.3	52.0
3	TXK-33	2.4 (5)	5.1	0	790	190	12.2	0.7	32.9	54.8
4	TXK-34	1.4	2.5	26	800	210	11.1	0.3	30.0	50.8
5	TXK-35	1.9	4.0	26	790	210	11.2	0.2	30.2	52.1
6	TXK-36	2.4	5.1	26	790	195	12.1	0.6	32.7	55.0
7	TXK-37	1.4	2.5	52	795	200	11.2	0.3	30.2	50.8
8	TXK-38	1.9	4.0	52	785	190	11.3	0.3	30.5	51.3
9	TXK-39	2.4	5.1	52	790	210	11.8	0.4	31.9	55.0
10	TXK-40	1.4	2.5	104	800	220	11.0	0.3	29.7	51.2
11	TXK-41	1.9	4.0	104	790	215	11.1	0.2	30.0	52.2
12	TXK-42	2.4	5.1	104	790	210	11.9	0.4	32.1	55.3
13	TXK-43	1.4	2.5	312	795	210	11.0	0.1	29.7	50.8
14	TXK-44	1.9	4.0	312	785	200	11.3	0.2	30.5	52.1
15	TXK-45	2.4	5.1	312	790	195	12.0	0.3	32.4	54.5

Test Conditions - Oil Temp.: 200°F (366°K)
Nozzle: No. 1 (4.34 mm dia.)

Heat Transfer Rates of (XRM 109 F + XRM 126 A) Microfog Jets Impinging on a Heated Rotating Disc

Item	Run No.	Gas Flow Rate $(m^3/s) \times 10^3$ @ 40 N/cm^2 & 366°K	Rate of Oil-Mist Output $(cm^3/s) \times 10^2$	Angular Velocity (rad/s)	Temperature (°F) T_w	Temperature (°F) T_∞	Heat Energy Transferred (mv) Q_t	Total Heat Flux $(Btu/hr - ft^2) \times 10^{-3}$	Heat Transfer Coefficient $(Btu/hr - ft^2 - °F)$
1	TXX-1	1.4 (3 cfm)	2.3	0	605 (591°K)	210 (372°K)	8.4	22.7 (71.5×10^3 W/m^2)	57.5 (326 $W/m^2 - °K$)
2	TXX-2	1.9 (4)	3.8	0	600	200	8.7	23.5	58.8
3	TXX-3	2.4 (5)	4.7	0	590	195	8.9	24.0	60.8
4	TXX-4	1.4	2.3	26	600	200	8.7	23.5	58.8
5	TXX-5	1.9	3.8	26	605	210	8.9	24.0	60.8
6	TXX-6	2.4	4.7	26	600	200	9.3	25.1	62.8
7	TXX-7	1.4	2.3	52	605	210	8.5	23.0	58.2
8	TXX-8	1.9	3.8	52	600	210	8.7	23.5	60.3
9	TXX-9	2.4	4.7	52	600	205	9.2	24.8	62.8
10	TXX-10	1.4	2.3	104	610	230	8.4	22.7	59.7
11	TXX-11	1.9	3.8	104	600	210	8.9	24.0	61.5
12	TXX-12	2.4	4.7	104	590	195	9.1	24.6	62.3
13	TXX-13	1.4	2.3	312	600	200	8.7	23.5	58.8
14	TXX-14	1.9	3.8	312	595	190	9.0	24.3	60.0
15	TXX-15	2.4	4.7	312	595	190	9.4	25.4	52.7

Test Conditions - Oil Temp.: 200°F (366°K)
Nozzle: No. 1 (4.34 mm dia.)

Heat Transfer Rates of (XRM 109 F + XRM 126 A) Microfog Jets Impinging on a Heated Rotating Disc

Item	Run No.	Gas Flow Rate (m^3/s) x 10^3 @ 40 N/cm^2 & 366°K	Rate of Oil-Mist Output (cm^3/s) x 10^2	Angular Velocity (rad/s)	Temperature (°F) T_w	T_∞	Heat Energy Transferred (mv) Q_f	Total Heat Flux (Btu/hr - ft^2) x 10^{-3}	Heat Transfer Coefficient (Btu/hr - ft^2 - °F)
1	TXX-16	1.4 (3 cfm)	2.3	0	700 (644°K)	200 (366°K)	10.2	27.5 (86.6 x 10^3 W/m^2)	55.0 (312 W/m^2 - °K)
2	TXX-17	1.9 (4)	3.8	0	695	190	10.5	28.4	56.2
3	TXX-18	2.4 (5)	4.7	0	690	190	11.1	30.0	60.0
4	TXX-19	1.4	2.3	26	705	210	10.3	27.8	56.2
5	TXX-20	1.9	3.8	26	700	210	10.4	28.1	57.3
6	TXX-21	2.4	4.7	26	700	200	11.0	29.7	59.4
7	TXX-22	1.4	2.3	52	710	220	10.2	27.5	56.1
8	TXX-23	1.9	3.8	52	700	220	10.3	27.8	57.9
9	TXX-24	2.4	4.7	52	690	210	10.8	29.2	60.8
10	TXX-25	1.4	2.3	104	705	210	10.1	27.3	55.2
11	TXX-26	1.9	3.8	104	690	200	10.3	27.8	56.7
12	TXX-27	2.4	4.7	104	700	210	10.7	28.9	59.0
13	TXX-28	1.4	2.3	312	710	230	9.8	26.5	55.2
14	TXX-29	1.9	3.8	312	700	220	10.2	27.5	57.3
15	TXX-30	2.4	4.7	312	695	200	10.8	29.2	59.0

Test Conditions - Oil Temp.: 200°F (366°K)
Nozzle: No. 1 (4.34 mm dia.)

Heat Transfer Rates of (XRM 109 F + XRM 126 A) Microfog Jets Impinging on a Heated Disc

Item	Run No.	Gas Flow Rate $(m^3/s) \times 10^3$ @ 40 N/cm^2 & 366°K	Rate of Oil-Mist Output $(cm^3/s) \times 10^2$	Angular Velocity (rad/s)	Temperature (°F) T_w	Temperature (°F) T_∞	Heat Energy Transferred (mv) q_f	Total Heat Flux $(Btu/hr\text{-}ft^2) \times 10^{-3}$	Heat Transfer Coefficient $(Btu/hr\text{-}ft^2\text{-}°F)$
1	TXX-31	1.4 (3 cfm)	2.3	0	790 694°K)	220 377°K)	10.8	29.2 (92×10^3 W/m^2)	51.2 (290 W/m^2-°K)
2	TXX-32	1.9 (4)	3.8	0	785	205	11.1	30.0	51.7
3	TXX-33	2.4 (5)	4.7	0	785	205	11.7	31.6	54.5
4	TXX-34	1.4	2.3	26	800	220	11.2	30.2	52.1
5	TXX-35	1.9	3.8	26	790	210	11.4	30.8	53.1
6	TXX-36	2.4	4.7	26	790	210	11.6	31.3	54.0
7	TXX-37	1.4	2.3	52	800	210	11.4	30.8	52.2
8	TXX-38	1.9	3.8	52	790	195	11.4	30.8	51.8
9	TXX-39	2.4	4.7	52	785	190	11.8	31.9	53.6
10	TXX-40	1.4	2.3	104	790	200	11.0	29.7	50.3
11	TXX-41	1.9	3.8	104	790	195	11.2	30.2	50.8
12	TXX-42	2.4	4.7	104	775	180	10.9	29.4	49.4
13	TXX-43	1.4	2.3	312	795	210	11.2	30.2	51.6
14	TXX-44	1.9	3.8	312	785	205	11.3	30.5	52.6
15	TXX-45	2.4	4.7	312	785	195	11.7	31.6	53.6

Test Conditions - Oil Temp.: 200°F (366°K)
Nozzle: No. 1 (4.34 mm dia.)

APPENDIX D-4

Axial Variation of Heat Transfer Coefficients of Nitrogen Gas Jets Impinging on a Heated Disc

Axial Variation of Heat Transfer Coefficients of Nitrogen Gas Jets Impinging on a Heated Disc

Item	Run No.	Spray Distance (in)	Gas Flow Rate $(m^3/s) \times 10^3$ @ 10 N/cm^2 & 294°K	Temperature (°F) T_w	Temperature (°F) T_∞	Heat Energy Transferred (mv)	Total Heat Flux $(Btu/hr - ft^2) \times 10^{-3}$	Heat Transfer Coefficient $(Btu/hr - ft^2 - °F)$	Spacing Ratio (Z/D_o)	$(N_{Re})_m$ $(D_oG/\mu_g)_B \times 10^{-3}$	N_{Nu} $(hD_o/k_g)_f$	$N_{Nu} \times N_{Pr}^{-1/3}$
1	X2-1	0.5 (1.27 cm)	0.5 (1 cfm)	452 (507°K)	70 (294°K)	3.6	9.7 (30.6×10^3 W/m^2)	25.4 (143 W/m^2 - °K)	2.92	7.8	18.7	21.2
2	X2-2		1.0	448	70	4.2	11.3	29.9	"	15.6	22.0	24.9
3	X2-3		1.9	440	70	4.9	13.2	35.7	"	31.2	26.3	29.7
4	X2-4	1.0 (2.54 cm)	0.5	260	70	3.55	9.6	24.6	5.85	7.8	18.1	20.4
5	X2-5		1.0	450	70	4.1	11.1	29.2	"	15.6	21.5	24.2
6	X2-6		1.9	443	70	4.8	13.0	35.2	"	31.2	25.9	29.3
7	X2-7	2.0 (5.08 cm)	0.5	455	70	2.6	7.0	18.2	11.70	7.8	13.4	15.2
8	X2-8		1.0	447	70	3.2	8.6	22.8	"	15.6	16.8	19.0
9	X2-9		1.9	440	70	3.8	10.3	27.8	"	31.2	20.5	23.2
10	X2-10	4.0 (10.16 cm)	0.5	457	70	2.8	7.6	19.6	23.4	7.8	14.4	16.3
11	X2-11		1.0	450	70	3.4	9.2	24.2	"	15.6	17.8	20.1
12	X2-12		1.9	445	70	4.1	11.1	29.6	"	31.2	21.8	24.6

Spray Nozzle: No. 1 (4.34 mm dia.)

Axial Variation of Heat Transfer Coefficients of Nitrogen Gas Jets Impinging on a Heated Disc

Item	Run No.	Spray Distance (in)	Gas Flow Rate $(m^3/s) \times 10^3$ @ 10 N/cm^2 & 294°K	Temperature (°F) T_w	Temperature (°F) T_∞	Heat Energy Transferred (mv)	Total Heat Flux $(Btu/hr - ft^2) \times 10^{-3}$	Heat Transfer Coefficient $(Btu/hr - ft^2 - °F)$	Spacing Ratio (Z/D_o)	$(N_{Re})_m$ $(D_oG/\mu_g)_B \times 10^{-3}$	N_{Nu} $(hD_o/k_g)_f$	$N_{Nu} \times N_{Pr}^{-1/3}$
1	X3-1	0.5 (1.27 cm)	0.5 (1 cfm)	455 (508°K)	70 (294°K)	3.00	8.1 $(25.5 \times 10^3\ W/m^2)$	21.0 $(119\ W/m^2 - °K)$	1.78	5.5	25.4	28.7
2	X3-2		1.0	450	70	3.50	9.5	25.0	"	11.0	30.3	34.2
3	X3-3		1.9	457	70	4.35	11.7	30.2	"	22.0	36.5	41.2
4	X3-4	1.0 (2.54 cm)	0.5	467	70	3.05	8.2	20.7	3.56	5.5	25.0	28.2
5	X3-5		1.0	455	70	3.45	9.3	24.1	"	11.0	29.2	33.0
6	X3-6		1.9	458	70	4.25	11.5	29.6	"	22.0	35.8	40.5
7	X3-7	2.0 (5.08 cm)	0.5	460	70	2.45	6.6	16.9	7.12	5.5	20.4	23.0
8	X3-8		1.0	452	70	2.90	7.9	20.7	"	11.0	25.0	28.2
9	X3-9		1.9	453	70	3.70	10.0	26.1	"	22.0	31.6	35.7
10	X3-10	4.0 (10.16 cm)	0.5	460	70	2.70	7.3	18.7	14.23	5.5	22.6	25.6
11	X3-11		1.0	457	70	3.10	8.4	21.7	"	11.0	26.3	29.7
12	X3-12		1.9	458	70	3.90	10.5	27.1	"	22.0	32.8	37.0

Spray Nozzle: No. 3 (7.13 mm dia.)

APPENDIX E

Wettability of Lubricant Drops Impinging on a Heated Rotating Disc

Relationship Between Time and Distance Traveled by Lubricant Drops

Run No.	Time sec x 10^2	Distance Traveled by Drops, cm x 10'			
XRM 26-2	0	0	0	0	0
-3	0.5	1.5	1.4	1.6	1.5
-4	1.0	3.6	3.2	3.8	3.8
	1.5	7.35	--	7.5	7.8
	2.0	18.0	14.0	16.5	18.0
	2.5	22.2	18.5	20.0	25.0
	3.0				

Gas Stream Velocity: 15 m/s
Disc Temperature: 600°F (589°K)
Capillary Tube: #1 (1 mm dia.)
Test Lubricant: XRM 109 F

Relationship Between Time and Distance Traveled by Lubricant Drops

Run No.	Time sec x 10^2	Distance Traveled by Drops, cm x 10'		
XRM 26-5	0	0	0	0
XRM 27-1	0.5	3.0	3.2	2.2
-2	1.0	9.0	8.5	6.9
	1.5	23.4	21.0	17.0
	2.0			24.0

Gas Stream Velocity: 19 m/s
Disc Temperature: 600°F (589°K)
Capillary Tube: #1 (1 mm dia.)
Test Lubricant: XRM 109 F

Relationship Between Time and Distance Traveled by Lubricant Drops

Run No.	Time sec x 10^2	Distance Traveled by Drop, cm x 10'				
XRM 27-3	0	0	0	0	0	0
-4	0.5	2.25	1.80	1.35	1.35	1.35
-5	1.0	3.75	3.75	3.00	3.30	3.15
	1.5	5.40	6.90	6.60	7.20	5.10
	2.0	9.30	13.20	12.0	15.0	10.5
	2.5	14.4	21.6	22.8	19.8	19.1
	3.0	21.0				23.4

Gas Stream Velocity: 11 m/s

Plate Temperature: 700°F (644°K)

Capillary Tube : #1 (1 mm dia.)

Test Lubricant: XRM 109 F

Relationship Between Time and Distance Traveled by Lubricant Drops

Run No.	Time sec x 10^2	Distance Traveled by Drops, cm x 10'			
XRM 28-1	0	0	0	0	0
-2	0.5	1.35	1.5	1.1	0.9
-3	1.0	5.25	3.0	4.05	3.30
	1.5	15.0	18.0	16.0	17.5
	2.0	22.2		24.5	
	2.5				

Gas Stream Velocity: 15 m/s
Plate Temperature: 700°F (644°K)
Capillary Tube: #1 (1 mm dia.)
Test Lubricant: XRM 109 F

Relationship Between Time and Distance Traveled by Lubricant Drops

Run No.	Time sec x 10^2	Distance Traveled by Drops, cm x 10'			
XRM 28-4	0	0	0	0	0
XRM 28-5	0.5	1.2	1.1	1.5	2.4
XRM 29-1	1.0	10.5	11.5	8.6	16.5
	1.5	24.5	21.8	22.6	Lost
	2.0				

Gas Stream Velocity: 19 m/s

Plate Temperature: 700°F (644°K)

Capillary Tube: #1 (1 mm dia.)

Test Lubricant: XRM 109 F

Relationship Between Time and Distance Traveled by Lubricant Drops

Run No.	Time sec x 10^2	Distance Traveled by Drop, cm x 10'				
XRM 29-2	0	0	0	0	0	0
-3	0.5	1.80	1.20	1.50	1.5	2.25
-4	1.0	3.75	4.35	3.75	3.30	5.25
	1.5	11.5	15.3	11.2	10.1	17.2
	2.0	21.5	22.6	20.1	20.4	24.2
	2.5				25.0	

Gas Stream Velocity: 11 m/s

Plate Temperature: 800°F (700°K)

Capillary Tube: #1 (1 mm dia.)

Test Lubricant: XRM 109 F

Relationship Between Time and Distance Traveled by Lubricant Drops

Run No.	Time sec x 10^2	Distance Traveled by Drop, cm x 10'			
XRM 29-5					
XRM 30-1	0	0	0	0	0
-2	0.5	3.0	2.55	1.65	0.9
	1.0	8.25	6.45	7.50	6.0
	1.5	17.4	13.2	13.8	15.0
	2.0	20.0	24.8	--	24.6

Gas Stream Velocity: 15 m/s

Plate Temperature: 800°F (700°K)

Capillary Tube: #1 (1 mm dia.)

Test Lubricant: XRM 109 F

Relationship Between Time and Distance Traveled by Lubricant Drops

Run No.	Time sec x 10^2	Distance Traveled by Drop, cm x 10'			
XRM 30-3	0	0	0	0	0
-4	0.5	1.95	3.3	1.2	2.40
-5	1.0	4.05	10.2	5.25	6.75
	1.5	17.5	19.2	19.0	15.9
	2.0				25.2

Gas Stream Velocity: 19 m/s

Plate Temperature: 800°F (700°K)

Capillary Tube: #1 (1 mm dia.)

Test Lubricant: XRM 109 F

Relationship Between Time and Distance Traveled by Lubricant Drops

Run No.	Time sec x 10^2	Distance Traveled by Drop, cm x 10'			
XRM 31-1	0	0	0	0	0
-2	0.5	1.5	1.2	1.8	1.5
-3	1.0	1.95	1.95	2.4	1.8
	1.5	5.25	3.15	3.45	3.3
	2.0	9.15	6.15	7.35	7.20
	2.5	18.5	15.5	15.9	17.1
	3.0	22.2	23.0	21.0	23.7
	3.5				

Gas Stream Velocity: 11 m/s

Plate Temperature: 600°F (589°K)

Capillary Tube: #2 (0.5 mm dia.)

Test Lubricant: XRM 109 F

Relationship Between Time and Distance Traveled by Lubricant Drops

Run No.	Time sec x 10^2	Distance Traveled by Drop, cm x 10'			
XRM 31-4	0	0	0	0	0
XRM 32-1	0.5	1.2	1.2	1.1	1.5
-2	1.0	2.1	1.95	2.55	2.25
	1.5	7.5	8.1	5.7	7.05
	2.0	15.3	17.1	12.5	15.8
	2.5	25.2	23.9	21.5	21.0
	3.0				

Gas Stream Velocity: 15 m/s

Plate Temperature: 600°F (589°K)

Capillary Tube: #2 (0.5 mm dia.)

Test Lubricant: XRM 109 F

Relationship Between Time and Distance Traveled by Lubricant Drops

Run No.	Time sec x 10^2	Distance Traveled by Drop, cm x 10'				
FN 10-1	0	0	0	0	0	0
-2	0.5	1.35	1.8	1.95	1.5	1.5
-3	1.0	1.8	2.55	2.7	2.4	2.1
-4	1.5	2.7	3.45	3.45	3.75	3.9
	2.0	5.55	5.4	4.8	6.3	7.05
	2.5	10.8	10.4	9.6	9.9	11.1
	3.0	19.0	16.6	17.1	14.3	15.8
	3.5	20.4	19.0	21.0	19.0	19.8
	4.0				20.3	24.8

Gas Stream Velocity: 11 m/s

Plate Temperature: 600°F (589°K)

Capillary Tube: #1 (1.0 mm dia.)

Test Lubricant: FN 2961

Relationship Between Time and Distance Traveled by Lubricant Drops

Run No.	Time sec x 10^2	Distance Traveled by Drop, cm x 10'			
FN 11-1	0	0	0	0	0
-2	0.5	0.9	1.8	1.8	1.5
-4	1.0	3.45	4.50	3.90	3.3
	1.5	15.3	12.1	12.5	12.3
	2.0	19.5	19.8	18.8	20.2

Gas Stream Velocity: 15 m/s
Plate Temperature: 600°F (589°K)
Capillary Tube: #1 (1.0 mm dia.)
Test Lubricant: FN 2961

Relationship Between Time and Distance Traveled by Lubricant Drops

Run No.	Time sec x 10^2	Distance Traveled by Drop, cm x 10'		
FN 12-1	0	0	0	0
-2	0.5	2.1	3.6	3.0
-3	1.0	6.45	7.65	6.7
	1.5	20.1	21.8	21.3

Gas Stream Velocity: 19 m/s

Plate Temperature: 600°F (589°K)

Capillary Tube: #1 (1.0 mm dia.)

Test Lubricant: FN 2961

APPENDIX F

Wettability Data of XRM 109 F with a Pneumatic Reclassifying Nozzle

Wettability of XRM 109 F with a Pneumatic Reclassifying Nozzle

Item	Run No.	Disc Temp. (°F)	Gas Flow Rate (m^3/s) x 10^3 @ 40 N/cm^2 & 366°K		Rate of Oil-Mist Output (cm^3/s) x 10^2	Wetting Time (s)						Wetting Rate (cm^2/s)
			Primary	Secondary		0.14	0.25	0.39	0.55	0.76	1.00	
1	XRM 34-3	600 (589°K)	1.4 (3 cfm)	0	2.0	0.36	1.72	3.23	4.29	6.10	7.25	10.8
2	XRM 34-2	600	1.9 (4)	0	3.3	0.48	0.76	1.41	2.13	2.92	3.59	20.6
3	XRM 34-1	600	2.4 (5)	0	4.3	0.24	0.50	1.05	1.47	1.92	2.29	33.7
4	XRM 35-4	700 (644°K)	1.4	0	2.0	0.85	1.41	2.17	3.22	4.24	5.37	14.2
5	XRM 35-5	700	1.9	0	3.3	0.36	0.55	0.91	1.48	--	2.48	29.4
6	XRM 35-6	700	2.4	0	4.3	0.23	0.41	0.70	1.20	1.58	2.29	33.8
7	XRM 36-7	800 (700°K)	1.4	0	2.0	0.50	0.91	1.52	2.75	3.75	4.88	15.2
8	XRM 36-6	800	1.9	0	3.3	0.22	0.46	0.82	1.31	1.86	2.49	29.3
9	XRM 36-5	800	2.4	0	4.3	0.12	0.33	0.57	0.95	1.27	1.92	39.2

Test Conditions - Oil Temperature: 200°F (366°K)
Angular Velocity: 52 rad/s

Wettability of XRM 109 F with a Pneumatic Reclassifying Nozzle

Item	Run No.	Disc Temp. (°F)	Gas Flow Rate $(m^3/s) \times 10^3$ @ 40 N/cm^2 & 366°K		Rate of Oil-Mist Output $(cm^3/s) \times 10^2$	Wetting Time (s)						Wetting Rate (cm^2/s)
			Primary	Secondary		0.14	0.25	0.39	0.55	0.76	1.00	
1	XRM 34-6	600 (589°K)	1.4 (3 cfm)	0.5 (1 cfm)	2.0	1.14	1.96	3.04	4.28	5.87	7.26	10.5
2	XRM 34-5	600	1.9 (4)	0.5	3.3	0.48	0.78	1.31	2.06	3.04	3.75	19.9
3	XRM 34-4	600	2.4 (5)	0.5	4.3	0.37	0.62	0.96	1.60	2.12	2.93	27.9
4	XRM 36-1	700 (644°K)	1.4	0.5	2.0	0.73	1.41	2.10	2.80	4.10	5.46	15.0
5	XRM 35-8	700	1.9	0.5	3.3	0.36	0.61	1.05	1.51	2.26	2.85	27.4
6	XRM 35-7	700	2.4	0.5	4.3	0.19	0.41	0.69	1.27	1.57	2.17	36.4
7	XRM 37-2	800 (700°K)	1.4	0.5	2.0	0.53	1.08	1.66	2.43	3.58	5.12	15.2
8	XRM 37-1	800	1.9	0.5	3.3	0.30	0.59	1.07	1.44	--	2.99	25.9
9	XRM 36-8	800	2.4	0.5	4.3	0.35	0.58	0.91	1.34	1.84	2.64	30.5

Test Conditions - Oil Temperature: 200°F (366°K)
Angular Velocity: 52 rad/s

Wettability of XRM 109 F with a Pneumatic Reclassifying Nozzle

Item	Run No.	Disc Temp. (°F)	Gas Flow Rate (m^3/s) x 10^3 @ 40 N/cm^2 & 366°K		Rate of Oil-Mist Output (cm^3/s) x 10^2	Wetting Time (s)						Wetting Rate (cm^2/s)
			Primary	Secondary		0.14	0.25	0.39	0.55	0.76	1.00	
1	XRM 35-1	600 (589°K)	1.4 (3 cfm)	1.0 (2 cfm)	2.0	0.47	1.30	2.98	4.10	6.95	Streaks	8.3
2	XRM 35-2	600	1.9 (4	1.0	3.3	0.28	0.65	1.30	2.13	3.40	4.37	17.7
3	XRM 35-3	600	1.4	1.4	2.0	1.04	1.83	3.04	4.71	6.40	Streaks	9.1
4	XRM 36-2	700 (644°K)	1.4	1.0	2.0	0.36	0.83	1.41	2.06	2.84	6.05(?)	18.7
5	XRM 36-3	700	1.9	1.0	3.3	0.20	0.49	0.83	1.38	1.90	2.62(?)	29.8
6	XRM 36-4	700	1.4	1.4	2.0	0.50	0.90	1.74	2.41	3.59	Streaks	17.1
7	XRM 37-3	800 (700°K)	1.4	1.0	2.0	0.53	0.95	1.55	2.21	3.37	4.51(?)	18.0
8	XRM 37-5	800	1.9	1.0	3.3	0.32	0.56	0.86	1.33	2.10	2.70(?)	30.5
9	XRM 37-4	800	1.4	1.4	2.0	0.66	1.02	1.53	2.30	3.12	Streaks	19.0

Test Conditions - Oil Temperature: 200°F (366°K)
Angular Velocity: 52 rad/s

APPENDIX G

Wettability Data of XRM 109 F
with an Electrostatic Reclassifying Nozzle

Wettability of XRM 109 F with an Electrostatic Charger

Item	Run No.	Disc Temp. (°F)	Gas Flow Rate $(m^3/s) \times 10^3$ @ 40 N/cm^2 & 366°K	Rate of Oil-Mist Output $(cm^3/s) \times 10^2$	Electrostatic Charge (KV)	Wetting Time (s) 0.14	0.25	0.39	0.55	0.76	1.00	Wetting Rate (cm^2/s)
1	XRM 38-1	600 (589°K)	1.4 (3 cfm)	2.0	0	0.28	0.81	1.47	2.15	2.93	4.26	17.3
2	XRM 38-3	600	1.9 (4)	3.3	0	0.24	0.53	0.83	1.38	2.24	2.99	24.3
3	XRM 38-2	600	1.4	2.0	-10	0.23	0.57	1.00	1.68	2.46	3.63	20.8
4	XRM 38-4	600	1.9	3.3	-10	0.25	0.51	0.80	1.32	--	2.74	27.6
5	XRM 39-1	700 (644°K)	1.4	2.0	0	0.32	0.64	1.04	1.94	2.72	3.68	19.7
6	XRM 39-3	700	1.9	3.3	0	0.23	0.51	0.86	1.27	1.78	2.63	30.4
7	XRM 39-2	700	1.4	2.0	-10	0.24	0.61	1.00	1.83	2.57	3.40	22.4
8	XRM 39-4	700	1.9	3.3	-10	0.29	0.53	0.78	1.28	1.84	2.37	34.5
9	XRM 40-2	800 (700°K)	1.4	2.0	0	0.38	0.75	1.25	1.90	2.83	3.77	19.4
10	XRM 39-5	800	1.9	3.3	0	0.29	0.65	1.07	1.37	1.80	2.46	31.7
11	XRM 40-3	800	1.4	2.0	-10	0.25	0.56	1.06	1.81	2.70	3.67	20.7
12	XRM 40-1	800	1.9	3.3	-10	0.22	0.52	1.09	1.52	1.85	2.55	30.5
13	XRM 40-4	600	1.9	3.3	-5	0.31	0.56	0.88	1.34	2.27	3.08	25.1
14	XRM 40-5	600	1.9	3.3	-15	0.36	0.66	1.00	1.47	2.09	2.75	30.0

Test Conditions - Oil Temperature: 200°F (366°K)
Angular Velocity: 52 rad/s
Nozzle: No. 1 (4.34 mm orifice dia.)

APPENDIX H

Wettability Data of XRM 109 F
with a Vortex Mist Generator

Wettability of XRM 109 F with a Vortex Mist Generator

Item	Run No.	Disc Temp. (°F)	Gas Flow Rate $(m^3/s) \times 10^3$ @ 40 N/cm^2 & 366°K	Rate of Oil-Mist Output $(cm^3/s) \times 10^2$	Wetting Time (s) 0.14	0.25	0.39	0.55	0.76	1.00	Wetting Rate (cm^2/s)
1	XRM 41-1	600 (589°K)	1.4 (3 cfm)	0.6	1.75	3.52	5.89	9.01	12.82	16.22	4.7
2	XRM 41-2	600	1.9 (4)	0.6	--	1.79	3.78	6.22	8.34	11.32	6.7
3	XRM 41-3	600	2.4 (5)	0.6	--	1.47	2.41	4.02	6.19	8.27	9.1
4	XRM 42-6	700 (644°K)	1.4	0.6	1.62	3.35	5.88	8.58	11.79	15.91	4.9
5	XRM 42-5	700	1.9	0.6	0.92	1.89	3.44	5.08	7.40	9.87	7.5
6	XRM 42-4	700	2.4	0.6	0.56	1.13	1.96	3.13	4.36	5.75	12.8
7	XRM 43-3	800 (700°K)	1.4	0.6	1.67	3.60	6.16	10.27	13.73	Streaks	4.2
8	XRM 43-2	800	1.9	0.6	0.64	1.39	2.48	3.91	--	8.03	9.3
9	XRM 43-1	800	2.4	0.6	0.66	1.35	2.12	3.15	4.60	6.05	13.1

Test Conditions - Oil Temperature: 200°F (366°K)
Nozzle: No. 1 (4.34 mm orifice dia.)
Angular Velocity: 52 rad/s

Wettability of XRM 109 F with a Vortex Mist Generator

Item	Run No.	Disc Temp. (°F)	Gas Flow Rate $(m^3/s) \times 10^3$ @ 40 N/cm^2 & 366°K	Wetting Time (s) 0.14	0.25	0.39	0.55	0.76	1.00	Wetting Rate (cm^2/s)
1	XRM 41-4	600 (589°K)	1.4 (3 cfm)	2.47	4.00	6.01	8.42	11.21	--	6.0
2	XRM 41-5	600	1.9 (4)	1.35	2.23	3.83	5.67	6.95	9.26	8.6
3	XRM 41-6	600	2.4 (5)	0.92	1.46	2.75			7.72	10.2
4	XRM 42-1	700 (644°K)	1.4	2.13	3.88	5.56	7.90	10.64	13.42	6.0
5	XRM 42-2	700	1.9	1.00	1.72	2.67	3.71	--	6.41	11.9
6	XRM 42-3	700	2.4	0.83	1.36	2.20	3.25	4.60	5.68	14.2
7	XRM 43-6	800 (700°K)	1.4	2.55	3.50	5.05	7.08	9.18	11.99	7.2
8	XRM 43-5	800	1.9	1.28	1.89	2.89	4.27	5.85	7.68	10.5
9	XRM 43-4	800	2.4	0.47	0.82	1.42	2.29	--	4.39	18.5

Test Conditions - Oil Temperature: 200°F (366°K)
Nozzle: Pneumatic Reclassifier
Angular Velocity: 52 rad/s

Mobil Research and Development Corporation

RESEARCH DEPARTMENT
PAULSBORO, NEW JERSEY 08066

J F SOCOLOFSKY
MANAGER
PRODUCTS RESEARCH AND
TECHNICAL SERVICE

August 25, 1972

Gentlemen:

FINAL REPORT - CONTRACT NAS3-13207

Attached is Report NASA CR-120843, entitled "Microfog Lubricant Application System for Advanced Turbine Engine Components - Phase II, Final Report - Wettability and Heat Transfer of Microfog Jets Impinging on a Heated Rotating Disc, and Evaluation of Reclassifying Nozzles and a Vortex Mist Generator."

This report, issued under contract NAS3-13207, is sent to you at the request of the National Aeronautics and Space Administration.

Very truly yours,

E A Oberright

E. A. Oberright, Manager
Process Products,
Aviation & Special Oils

JShim:md
Attachment